Université de Valenciennes et du Hainaut-Cambrésis

Thèse de doctorat

Pour obtenir le grade de Docteur de l'Université de

VALENCIENNES ET DU HAINAUT-CAMBRESIS

Discipline, spécialité selon la liste des spécialités pour lesquelles l'Ecole Doctorale est accréditée :
Matériau

Présentée et soutenue par Olivier COUSIGNE.

Le 29/11/2013, à Valenciennes

Ecole doctorale :
Sciences Pour l'Ingénieur (SPI)

Equipe de recherche, Laboratoire :
Laboratoire d'Automatique, de Mécanique et d'Informatique Industrielles et Humaines (LAMIH)

Contribution au développement de la simulation numérique des matériaux composites à renforts tissés pour l'application au crash

JURY

Président du jury
- ABRATE, Serge. Professeur. Southern Illinois University. Carbondale, États-Unis.

Rapporteurs
- GUILLAUMAT, Laurent. Professeur. Ecole Nationale Supérieure d'Arts et Métiers, Angers, France.
- FERRERO, Jean-François. Professeur. Université Paul Sabatier, Toulouse, France.

Examinateurs
- CAMANHO, Pedro P. Professeur. Faculdade de Engenharia Universidade do Porto, Portugal.
- ABRATE, Serge. Professeur. Southern Illinois University. Carbondale, Etats-Unis.

Directeur de thèse
- COUTELLIER, Daniel. Professeur. LAMIH UMR CNRS 8201, Valenciennes, France.

Co-directeur de thèse
-NACEUR, Hakim. Professeur. LAMIH UMR CNRS 8201, Valenciennes, France.

Tuteur industriel
-MONCAYO, David. Ingénieur. Daimler AG, Sindelfingen, Allemagne.

Université de Valenciennes et du Hainaut-Cambrésis

Thèse de doctorat

Pour obtenir le grade de Docteur de l'Université de

VALENCIENNES ET DU HAINAUT-CAMBRESIS.

Numéro d'ordre: 13/35

Spécialité: **Matériau**

Présentée et soutenue par Olivier COUSIGNE.

Le 29/11/2013, à Valenciennes.

Ecole doctorale: Sciences Pour l'Ingénieur (SPI).

Equipe de recherche, Laboratoire :

Laboratoire d'Automatique, de Mécanique et d'Informatique Industrielles et Humaines (LAMIH).

Contribution to the development of the numerical simulation of woven composites for crash applications

JURY

Président du jury: Prof. Serge ABRATE, Southern Illinois University, Carbondale, Etat-Unis.

Rapporteurs

- Prof. Laurent GUILLAUMAT, Ecole Nationale Supérieure d'Arts et Métiers, Angers, France.
- Prof. Jean-François FERRERO, Université Paul Sabatier, Toulouse, France.

Examinateurs

- Prof. Pedro P. CAMANHO, Faculdade de Engenharia Universidade do Porto, Porto, Portugal.
- Prof. Serge ABRATE, Southern Illinois University, Carbondale, Etat-Unis.

Directeur de thèse: Prof. Daniel COUTELLIER, LAMIH UMR CNRS 8201, Valenciennes, France.

Co-directeur de thèse: Prof. Hakim NACEUR, LAMIH UMR CNRS 8201, Valenciennes, France.

Tuteur industriel: Dipl.-Ing. David MONCAYO, Daimler AG, Sindelfingen, Allemagne.

To my lovely mother.

Synthesis - Synthèse

This study presents the development of an experimental and numerical material characterization method relying on the investigation of the material behavior of woven composites, from the microscopic scale up to the macroscopic level by increasing progressively the complexity of the geometries and load cases. Taking into account the different limitations imposed by the industrial and engineering fields, a new numerical mesh-insensitive material model has been developed as a UMAT for the explicit finite elements solver LS-DYNA. This model accounts for nonlinearity, plasticity, failure and post-failure damage in order to predict the macroscopic behavior and the damage tolerance of woven laminated composites. It includes also a smeared formulation to avoid undesirable localization phenomena. The first step of the validation process relies on the simulation of quasi-static coupon tests, which allows to set the fundamental numerical parameters corresponding to the effective material properties and to the macroscopic behavior observed experimentally. Then, the post-failure material degradation models have been investigated using the simulations of impact tests on elementary plates and on representative parts. A satisfying agreement has been obtained for the different load cases.

Keywords: Woven composites, nonlinearity, plasticity, damage, impact, UMAT, FE-simulation.

Cette étude présente le développement d'une méthode expérimentale et numérique de caractérisation du comportement d'un matériau composite à renforts tissés, depuis l'échelle microscopique jusqu'au niveau macroscopique, en augmentant progressivement la complexité des géométries et des cas de chargement. Un nouveau modèle matériau numérique a été développé sous la forme d'un UMAT pour le logiciel éléments finis LS-DYNA. Ce modèle est capable de prédire un comportement linéaire ou non-linéaire, la déformation plastique, la rupture et l'endommagement progressif du matériau après rupture, tout en respectant les différentes restrictions imposées par le domaine industriel. Une formulation non-locale a été implémentée afin d'éviter les phénomènes indésirables de localisation de l'endommagement et d'offrir l'indépendance du modèle à la finesse du maillage. La première étape du processus de validation est la simulation des essais quasi-statiques sur des échantillons, ce qui permet de définir les paramètres numériques fondamentaux correspondant aux propriétés mécaniques et au comportement macroscopique du matériau étudié. Ensuite, les simulations d'impact assurent l'étude des modèles de dégradation. Une bonne corrélation a été obtenue pour les différents cas de chargement.

Mots clés: Composites à renforts tissés, nonlinéarité, plasticité, endommagement, impact, UMAT, simulation par éléments finis.

Acknowledgments

This study has been conducted at Daimler AG in the department "Rohbau Vorentwicklung" in Sindelfingen, Germany. For this great experience, I would like to thank many people, who brought their contribution in this work.

I would like to express my deep gratitude to my advisor Professor Daniel Coutellier, Director of the ENSIAME, for supervising my work, the quality of his advice and our regular and friendly communication.

Special thanks are also addressed to my advisor Dipl.-Ing. David Moncayo at Daimler AG for his generous support and encouragement for the past years. He has always provided me with the best opportunities and help whenever I needed it.

I would like to thank Professor Hakim Naceur for his support and his participation in this work.

Many thanks to Professor Pedro Camanho from the University of Porto (Faculdade de Engenharia Universidade do Porto, FEUP) for his availability, his kindness and his contribution in my work.

Acknowledgments are also given to my team leader Dipl.-Ing. Steffen Hampel for giving me the opportunity to conduct my work in his team. In the same time I would like to thank all my colleagues at Daimler AG for their help and their contribution in this study.

I would like to give many thanks to my French colleagues Benoit, Sylvain, Julien, Jeremy and Laetitia for their kindness and our interesting collaboration.

I would like to thank all my friends in Germany Pauline, Christian, Maxime and Georg for their support and friendship.

Special thanks are given to my best friend Christophe for our collaboration and for its generous support during the difficult moments.

Greatest thanks are adressed to Florence for her contribution in this work. This thesis could not be possible without her unconditional support, her patience and her love.

Finally, many thanks are given to my family for her encouragements.

Abstract

Due to their draping, stiffness, improved ductility and damage tolerance properties woven composites are increasingly used for the design of crash-relevant automotive structural parts. In order to limit the number of expensive experiments, reliable numerical simulations are required in order to predict the behavior of woven composites under different loading paths. A deep analysis and an optimal understanding of the material behavior are necessary and the suitable modeling techniques have to be validated. In this way, an experimental and numerical characterization method has been developed and it relies on the investigation of the material behavior from the microscopic scale up to the full-size car model by increasing progressively the complexity of the geometries and load cases.

Throughout this material characterization process, different modeling techniques are investigated and assessed. Most of the numerical material models aiming at predicting the macroscopic behavior of composites are based on linear constitutive laws up to failure onset. However, woven composites are likely to present a nonlinear behavior in each material direction, in function of the textile structure. Taking in consideration the different limitations imposed by the industrial and engineering fields, a new numerical mesh-insensitive material model has been developed as a UMAT for the explicit finite element solver LS-DYNA. This model accounts for nonlinearity, plasticity, failure and post-failure damage to predict the behavior of woven laminated composites under several loading paths. The implementation includes a smeared formulation and it has been adapted for shell, thick shell and solid elements, as both thin and relatively thick structures are likely to be designed to fulfill the different crash regulations.

The validation of the model relies first on the simulation of elementary coupon tests, which allows to validate the in-plane and bending effective material properties observed experimentally. Then, based on the previous validated material parameters, the post-failure material degradation models are assessed using the simulation of impact tests. The correlation relies here on quantitative and qualitative analysis corresponding to the comparison between experimental and numerical results regarding repectively the material response and the damage/delamination propagation. Finally, the modeling techniques and material parameters are assessed and validated on the simulation of representative component tests, which corresponds to the last step in the characterization process before starting the investigations on real structural parts or on full-size car models (not conducted in this study). A satisfying correlation has been obtained for both considered RTM and PREPREG carbon/epoxy woven composites.

Résumé

De par leur rigidité, leur ductilité, leur tolérance à l'endommagement et leurs propriétés de mise en forme, les matériaux composites à renforts tissés sont de plus en plus utilisés pour la conception de pièces structurelles dans le domaine automobile. Cependant, en plus des différentes fonctions qu'elles devront assurer en service, ces pièces doivent remplir le cahier des charges et les règles de sécurité imposés par les tests de crash. Afin de limiter le nombre et le coût des essais expérimentaux, l'utilisation de simulations numériques pouvant prédire de manière fiable le comportement, sous différents cas de chargement, des matériaux composites à renforts tissés est indispensable. Une analyse détaillée et une parfaite compréhension du comportement du materiau sont alors nécessaires, ainsi que l'existence et la validation de techniques de modélisation adéquates. Dans cette optique une méthode de caractérisation a été développée. Elle repose sur une analyse du matériau à l'échelle microscopique jusqu'à une étude à l'échelle du véhicule complet en augmentant progressivement la complexité des géométries et des cas de chargement.

Différentes techniques de modélisation sont étudiées et évaluées tout au long de ce processus de caractérisation. La plupart des modèles matériau numériques visant à prédire le comportement macroscopique d'un composite repose généralement sur une évolution linéaire avant rupture. Cependant, les composites à renforts tissés peuvent présenter un comportement non-linéaire dans chaque direction, en fonction de la structure du tissé. En tenant compte des différentes restrictions en terme de modélisation imposées par le domaine industriel, un nouveau modèle matériau numérique a été développé sous la forme d'un UMAT pour le logiciel éléments finis LS-DYNA. Ce modèle est capable de prédire un comportement linéaire ou non-linéaire, la déformation plastique, la rupture et l'endommagement progressif du matériau après rupture. L'implémentation comprend une formulation particulière pour la répartition de l'endommagement et elle a été adaptée pour des modélisations impliquant des éléments coques, des coques épaisses ou des éléments solides. En effet, des structures plus ou moins épaisses peuvent être conçues afin de remplir les différents critères de crash tests.

La validation du modèle repose tout d'abord sur la simulation d'essais sur échantillons, ce qui permet de corréler les propriétés mécaniques du matériau dans le plan et en flexion. Ensuite, en utilisant les paramètres matériau validés précédemment, l'endommagement après rupture est étudié en simulant les essais d'impact. La corrélation se base ici sur une analyse qualitative et quantitative, ce qui se traduit par une comparaison des résultats numériques avec les résultats expérimentaux en ce qui concerne les différentes courbes représentant la réponse du matériau et l'évaluation des zones endommagées/délaminées. Enfin, les techniques de modélisation et les paramètres matériau sont validés

grâce à la simulation des essais de puits de chute sur les profils chapeau. Cela représente la dernière étape du processus de caractérisation avant le début des études de réelles pièces automobiles ou du véhicule complet. Les résultats obtenus pour les deux compositess RTM et PREPREG à renforts tissés en fibres de carbone et résine époxy montrent une bonne corrélation.

Zusammenfassung

Die Gewebe faserverstärkten Kunststoffe (FVK) werden in der Konstruktion von Crash-relevanten Strukturbauteilen immer mehr verwendet. Diese zeigen eigentlich sehr gute Steifigkeits-, Festigkeits-, Duktilitäts- und Schädigungstoleranzeigenschaften. Diese FVK Bauteile müssen nicht nur funktionsfähig sein, sondern sie müssen die verschiedenen Crashanforderungen erfüllen. Um den Anzahl und die Kosten der experimentellen Versuche zu reduzieren, sind zuverlässige und effiziente numerische Simulationen, die das makroskopische Verhalten von Gewebe FVK prognostizieren können, notwendig. Eine detaillierte Analyse, ein vertieftes Verständnis des Materialverhaltens und die Verfügbarkeit adäquaten Modellierungstechniken sind dann erforderlich. Auf diese Art und Weise wurde eine Charakterisierungsstrategie entwickelt. Sie basiert auf der progressiven Erhöhung der Komplexität der Geometrie und der Randbedingungen von der mikroskopischen Analyse des Materials bis auf der Gesamtfahrzeugebene.

Verschiedene Modellierungstechniken werden durch den gesamten Charakterisierungsprozess untersucht und bewertet. Die meisten aktuellen numerischen Materialmodelle bilden oft nur ein lineares Verhalten bis zum Versagen ab. Jedoch können Gewebe FVK in Abhängigkeit von der Gewebestruktur ein nicht-lineares Verhalten zeigen. Unter Beachtung der verschiedenen Einschränkungen im industriellen Bereich, wurde ein neu numerisches Materialmodel als UMAT für den finiten Elementen Solver LS-DYNA entwickelt. Das Model ist in der Lage, die Nichtlinearität, die Plastizität, das Versagen und die progressive Schädigung des Materials im Nachbruchbereich zu prognostizieren. Eine spezielle Formulierung für die Verteilung der Schädigung wurde verwendet. Außerdem wurde die Implementierung an Schalen, dicke Schalen und Volumenelementen angepasst, da die Dicke der Strukturen schnell steigen kann, um die Crashanforderungen zu erfüllen.

Die Validierung des Models beginnt mit der Simulation der Versuche auf elementaren Proben. Damit werden die effektiven Materialeigenschaften mit den experimentellen Ergebnissen korreliert. Dann wird die Untersuchung der Schädigung im Nachbruchbereich durch die Simulation der Impaktversuche durchgeführt. Die Korrelation basiert auf einer quantitativen und qualitativen Analyse, die einem Vergleich der Materialantwort und der beschädigten/delaminierten Flächen entspricht. Schließlich werden die Modellierungstechniken und alle Materialparametern durch die Simulation der Fallturmversuche auf Prinzipkomponente validiert. Diese Validierung ist die letzte Stufe in dem Materialcharakterisierungsprozess vor der Untersuchungen von realen Bauteilen oder auf Gesamtfahrzeugebene. Die numerischen Ergebnisse zeigen eine befriedigende Übereinstimmung mit den experimentellen Daten für beide RTM und PREPREG (Kohlenfaser und Epoxy Harz) Gewebe faserverstärkten Kunststoffe.

Contents

Acknowledgments iii

Abstract v

Résumé vii

Zusammenfassung ix

List of Figures xxv

List of Tables xxv

Nomenclature xxvii

1 Introduction 1

1.1 Context of the study . . . 1

1.1.1 General context . . . 1

1.1.2 Automotive field . . . 1

1.2 Use of composite materials for automotive applications . . . 2

1.2.1 Why? . . . 2

1.2.2 Where and how? . . . 2

1.2.3 Introduction to the crash behavior of composite materials for automotive applications 3

1.3 Motivation and objectives of the thesis . . . 4

1.3.1 Presentation of the challenge and motivation . . . 4

1.3.2 Description of the objectives . . . 5

1.4 Structure of the study . . . 5

1.4.1 Characterization method applied to composite materials . . . 5

1.4.2 Milestone of the thesis . . . 7

2 State of the Art - Literature review 9

2.1 Introduction . . . 9

2.2 Constituents and manufacturing processes of composite materials . . . 9

2.2.1 Constituents . . . 9

2.2.1.1 General overview . . . 9

2.2.1.2 Textile reinforcements . . . 10

2.2.2 Manufacturing processes . . . 10

2.2.2.1 Manufacturing process of a dry fabric . . . 10
2.2.2.2 Manufacturing processes of a composite laminate . . . 11
2.2.2.3 Additional remarks . . . 12
2.3 Study of fibrous composites from the lamina to the laminate . . . 12
2.3.1 Multiscale analysis . . . 12
2.3.2 Prediction of failure . . . 13
2.3.2.1 Intralaminar failure . . . 13
2.3.2.2 Interlaminar failure . . . 13
2.4 Models for textile composite materials . . . 14
2.4.1 Effect of fiber waviness . . . 14
2.4.2 Analytic models . . . 14
2.4.2.1 Prediction of the extensional effective material properties . . . 15
2.4.2.2 Prediction of the bending properties . . . 18
2.4.3 Numerical models . . . 18
2.4.4 Extension to the mesoscopic and macroscopic levels . . . 20
2.4.5 Discussion . . . 20
2.5 Material behavior, prediction of failure and damage . . . 21
2.5.1 Observation and prediction of the material behavior of textile composites . . . 21
2.5.2 Failure and damage . . . 24
2.5.2.1 Analytic models . . . 24
2.5.2.2 Numerical models . . . 26
2.5.2.3 Notched textile composites . . . 27
2.5.2.4 Focus on damage . . . 27
2.5.3 Discussion . . . 28
2.6 Impact behavior and strain rate-dependency of woven composites . . . 29
2.6.1 Impact on woven composites . . . 29
2.6.2 Strain rate dependency . . . 29
2.7 Modeling of composite materials using the crash-solver LS-DYNA . . . 31
2.7.1 Explicit time integration . . . 31
2.7.1.1 Equation of motion . . . 31
2.7.1.2 Central difference method . . . 32
2.7.1.3 Time integration in LS-DYNA . . . 33
2.7.1.4 Determination of the time step . . . 33
2.7.1.5 Governing equations . . . 34
2.7.1.6 Application to the spatial discretization . . . 36
2.7.1.7 Milestone for the resolution . . . 37
2.7.2 Elements available to model FRP-Materials . . . 37
2.7.2.1 Shell elements . . . 37
2.7.2.2 Solid elements . . . 38
2.7.2.3 Thick shell elements . . . 38
2.7.2.4 Hourglass control . . . 39
2.7.3 Material models available to model FRP-Materials . . . 39

2.7.3.1 *MAT_022 . . . 39
2.7.3.2 *MAT_054-055 . . . 40
2.7.3.3 *MAT_058 . . . 40
2.7.3.4 *MAT_059 . . . 41
2.7.3.5 *MAT_118 . . . 41
2.7.3.6 *MAT_261 . . . 42
2.7.3.7 *MAT_262 . . . 42
2.7.3.8 *MAT_161-162 . . . 42
2.7.4 Discretization and modeling of a woven ply . . . 43
2.8 Discussion and synthesis of the literature review . . . 43

3 Experimental observations: quasi-static, impact and representative component tests on carbon woven reinforced plastics 47
3.1 Experimental tests on a RTM carbon plain weave presenting outer glass mat layers . . . 48
3.1.1 Longitudinal tensile tests . . . 48
3.1.2 Longitudinal compressive tests . . . 50
3.1.3 Shear tests . . . 51
3.1.3.1 Tensile shear tests . . . 51
3.1.3.2 Compressive shear tests . . . 52
3.1.4 Three-point bending tests . . . 53
3.1.4.1 Longitudinal three-point-bending . . . 53
3.1.4.2 Diagonal three-point-bending . . . 53
3.2 Experimental tests on a RTM carbon plain weave without glass mat . . . 55
3.2.1 Experimental determination of the effective material properties . . . 55
3.2.1.1 Longitudinal tensile tests . . . 55
3.2.1.2 Longitudinal compressive tests . . . 56
3.2.1.3 Tensile shear tests . . . 57
3.2.1.4 Compressive shear tests . . . 57
3.2.1.5 Longitudinal four-point bending tests . . . 59
3.2.1.6 Diagonal four-point bending tests . . . 60
3.2.2 Impact tests and representative component tests . . . 60
3.2.2.1 Impact tests on elementary plates . . . 60
3.2.2.2 Representative component tests: drop tower tests on hat-profiles . . . 66
3.3 Experimental tests on a PREPREG carbon twill weave . . . 67
3.3.1 Experimental determination of effective material properties . . . 67
3.3.1.1 Unidirectional tensile tests . . . 69
3.3.1.2 Multidirectional tensile tests . . . 70
3.3.1.3 Shear tensile tests . . . 70
3.3.1.4 Unidirectional compressive tests . . . 71
3.3.1.5 Multidirectional compressive tests . . . 72
3.3.1.6 Unidirectional bending tests . . . 73
3.3.1.7 Multidirectional bending tests . . . 74

3.3.2 Impact tests on elementary plates . . . 76
3.3.3 Representative component tests: drop tower tests on hat-profiles . . . 79
3.3.3.1 Impact on 2mm thick hat-profiles . . . 81
3.3.3.2 Impact on 4mm thick hat-profiles . . . 81
3.4 Partial conclusions . . . 83

4 Development of a user-defined material model: theory and implementation 85
4.1 Introduction . . . 85
4.2 Behavior before failure . . . 86
4.2.1 Linear behavior and incremental implementation . . . 86
4.2.2 The Ramberg-Osgood model . . . 88
4.2.3 User-defined load curve . . . 88
4.2.4 Stiffness in compression . . . 89
4.2.5 Unidimensional plasticity formulation . . . 89
4.3 Failure criterion . . . 93
4.3.1 Maximal stress failure criterion . . . 93
4.3.2 The 2D Tsai-Wu failure criterion . . . 93
4.4 Post-failure behavior and damage . . . 94
4.4.1 Smeared formulation . . . 94
4.4.2 Determination of the energy before failure onset Γ_1 . . . 96
4.4.3 Post-failure material degradation models . . . 96
4.4.3.1 Linear damage . . . 96
4.4.3.2 Step-based material degradation . . . 97
4.4.3.3 Constant stress level material degradation . . . 98
4.4.3.4 Nonlinear damage . . . 98
4.4.4 Mesh dependency . . . 99
4.4.5 Critical element length . . . 99
4.5 Input data of the model . . . 101
4.6 Analysis of the results . . . 102
4.6.1 Failure indicators . . . 102
4.6.2 Damage indicators . . . 103
4.7 Partial conclusions . . . 103

5 Numerical results and validation on carbon plain-weave RTM specimens 105
5.1 Introduction . . . 105
5.2 RTM carbon plain-weave with outer glass mat layers . . . 107
5.2.1 Simulations with four current composite material models . . . 107
5.2.2 Numerical results obtained with the UMAT . . . 109
5.2.3 Investigation of the bending stiffness . . . 112
5.2.3.1 Influence of the mesh size on the bending behavior . . . 112
5.2.3.2 Numerical results using the *MAT_118 model . . . 113
5.2.3.3 Consideration of the fiber waviness . . . 114
5.2.3.4 Modeling of the outer glass mat layers . . . 116

5.2.4 Partial conclusions . . . 117
5.3 RTM carbon plain-weave without glass mat . . . 119
5.3.1 Longitudinal tensile tests . . . 119
5.3.2 Longitudinal compressive tests . . . 119
5.3.3 Tensile and compressive shear . . . 120
5.3.4 Four-point Bending tests . . . 121
5.3.4.1 Longitudinal four-point bending tests . . . 121
5.3.4.2 Diagonal four-point bending tests . . . 122
5.3.5 Impact tests on elementary plates . . . 122
5.3.5.1 Introduction . . . 122
5.3.5.2 Modeling with shell elements . . . 124
5.3.5.3 Modeling with thick shell elements . . . 129
5.3.6 Drop tower tests on hat-profiles . . . 139
5.3.7 Partial conclusions . . . 142

6 Numerical results and validation on carbon twill-weave PREPREG specimens 147
6.1 Quasi-static tests on a unidirectional stacking sequence . . . 147
6.1.1 Tensile tests . . . 148
6.1.2 Compressive tests . . . 148
6.1.3 Shear tests . . . 149
6.1.4 Longitudinal four-point bending tests . . . 149
6.1.5 Diagonal four-point bending tests . . . 149
6.2 Quasi-static tests on a multidirectional stacking sequence . . . 151
6.2.1 Tensile tests on a multidirectional stacking sequence . . . 151
6.2.1.1 Longitudinal tensile tests on a multidirectional stacking sequence . . . 151
6.2.1.2 Diagonal tensile tests on a multidirectional stacking sequence . . . 151
6.2.2 Compressive tests on a multidirectional stacking sequence . . . 152
6.2.2.1 Longitudinal compressive tests on a multidirectional stacking sequence . . . 152
6.2.2.2 Diagonal compressive tests on a multidirectional stacking sequence . . . 152
6.2.3 Four-point bending tests on a multidirectional stacking sequence . . . 153
6.2.3.1 Longitudinal four-point bending tests on a multidirectional stacking sequence . . . 153
6.2.3.2 Diagonal four-point bending tests on a multidirectional stacking sequence 153
6.3 Impact tests on elementary plates . . . 154
6.3.1 Modeling with shell elements . . . 154
6.3.2 Modeling with thick shell elements . . . 160
6.4 Drop tower tests on hat-profiles . . . 162
6.4.1 Drop tower tests on 2mm thick hat-profiles . . . 163
6.4.2 Drop tower tests on 4mm thick hat-profiles . . . 166
6.4.2.1 Impact energy of 350J . . . 166
6.4.2.2 Impact energy of 500J . . . 169
6.5 Partial conclusions and outlooks . . . 171

Conclusion **173**

Bibliography **177**

List of Figures

1.1 Three vehicles developed by Daimler AG equipped with new generations of powertrains: SLS Electric Drive (left), the new E-Class hybrid (middle) and the Smart Brabus Electric Drive (right) . . . 2

1.2 Building-block approach for the experimental and numerical characterization of composites 6

2.1 Illustration of the plain-weave (left) and twill-weave (right) textile structures . . . 11

2.2 Illustration of the relative shift between adjacent plain-weave layers . . . 20

2.3 Single degree of freedom dynamic system . . . 32

2.4 Central difference method (left) and time integration used in LS-DYNA (right) . . . 32

2.5 Time dependent deformation of a 3D body in a Cartesian space and the Lagrangian formulation. . . . 35

2.6 Overview of four composite material models regarding the macroscopic behavior . . . 40

2.7 Comparison of the potential discretization of a non-crimp laminated structure and of a plain-weave textile structure . . . 44

3.1 Experimental results for the quasi-static longitudinal tension . . . 49

3.2 Analysis of the failure modes for the longitudinal tension: a) overview of the specimen, b) zoom on the failure location, c) view of the failure location from the left side, d) view of the failed cross-section . . . 49

3.3 Analysis of the failure modes for the longitudinal tension: failure of the yarns (left) and view of some crack propagation away from the failure location (right) . . . 49

3.4 Experimental results for the quasi-static longitudinal compression . . . 50

3.5 Analysis of the failure mode for the longitudinal compression: a) macroscopic failure of two specimens, b) micrographs of the failure location for two specimens . . . 50

3.6 Experimental results for the quasi-static shear tension . . . 51

3.7 Analysis of the failure modes for the tensile shear: a) representative macroscopic failure, b) and c) zoom on the failure location, d) micrograph of the failure location . . . 51

3.8 Experimental results for the quasi-static shear compression . . . 52

3.9 Analysis of the failure mode for the compressive shear: a) representative macroscopic failure, b) zoom on the representative failure location, c) micrograph of the failure location 52

3.10 Experimental results for the quasi-static longitudinal three-point-bending . . . 53

3.11 Analysis of the failure modes for the longitudinal three-point bending: photography of the compressive fracture of the specimen (top left), micrograph of the compressive fracture (bottom left), photography of the full-fracture of the specimen (top right) and micrograph of the full-fracture (bottom right) 54
3.12 Experimental results for the quasi-static diagonal three-point bending 54
3.13 Failure analysis for the diagonal bending 55
3.14 Experimental results for the longitudinal tension: representative failure (top) and stress vs. strain material response (bottom) 56
3.15 Experimental results for the longitudinal compression: representative failure (top) and stress vs. strain material response (bottom) 57
3.16 Experimental results for the shear tensile tests: representative failure (top) and shear stress vs. shear strain material response (bottom) 58
3.17 Experimental results for the shear compressive tests: representative failure (top) and shear stress vs. shear strain material response (bottom) 58
3.18 Experimental results for the longitudinal bending: representative failure (top) and flexural stress vs. flexural strain material response (bottom) 59
3.19 Experimental results for the diagonal bending: representative failure (top) and flexural stress vs. flexural strain material response (bottom) 60
3.20 Cutting plan of the test specimen (left) and experimental set up (right) 61
3.21 Experimental results of the 5J impact tests for the 0° and 45° orientations 62
3.22 Experimental results of the 25J impact tests for the 0° and 45° orientations 63
3.23 Experimental results of the 50J impact tests for the 0° and 45° orientations 64
3.24 Comparison of the experimental results (material response and damaged surfaces) for the three impact energies and for both 0° and 45° orientations 65
3.25 Experimental set-up for the 200J drop tower tests on hat-profiles: dimensions of the specimen (left), experimental set-up and specimen preparation (right) 67
3.26 Experimental results for the 200J drop tower tests on hat-profiles: displacement vs. time and force vs. time (top), a) side view of the hat-profile after impact - b) side view and zoom on failure - c) top view and zoom on failure 68
3.27 Experimental results for the longitudinal tension: representative failure (top) and stress vs. strain material response (bottom) 69
3.28 Experimental results for the longitudinal tension on a multidirectional stacking sequence: representative failure (top) and stress vs. strain material response (bottom) 70
3.29 Experimental results for the diagonal tension on a multidirectional stacking sequence: representative failure (top) and stress vs. strain material response (bottom) 71
3.30 Experimental results for the shear tensile tests: representative failure (top) and shear stress vs. shear strain material response (bottom) 71
3.31 Experimental results for the longitudinal compression: representative failure (top) and stress vs. strain material response (bottom) 72
3.32 Experimental results for the longitudinal compression on a multidirectional stacking sequence: representative failure (top) and stress vs. strain material response (bottom) . . . 73

3.33 Experimental results for the diagonal compression on a multidirectional stacking sequence: representative failure (top) and stress vs. strain material response (bottom) 73
3.34 Experimental results for the longitudinal bending: representative failure (top) and flexural stress vs. flexural strain material response (bottom) 74
3.35 Experimental results for the diagonal bending: representative failure (top) and flexural stress vs. flexural strain material response (bottom) 74
3.36 Experimental results for the longitudinal bending on a M.D. stacking sequence: representative failure (top) and flexural stress vs. flexural strain material response (bottom) . . . 75
3.37 Experimental results for the diagonal bending on a M.D. stacking sequence: representative failure (top) and flexural stress vs. flexural strain material response (bottom) 75
3.38 Experimental results of the 5J impact tests for the 0° and 45° orientations 76
3.39 Experimental results of the 25J impact tests for the 0° and 45° orientations 77
3.40 Experimental results of the 50J impact tests for the 0° and 45° orientations 78
3.41 Comparison of the experimental results (material response and damaged surfaces) for the three impact energies and for both 0° and 45° orientations 79
3.42 Experimental set-up for the drop tower tests on PREPREG hat-profiles: dimensions of the specimen (top) and experimental set-up (bottom) 80
3.43 Experimental results for the 100J drop tower tests on 2mm thick PREPREG hat-profiles: displacement vs. time and force vs. time (top), a) side view of the hat-profile after impact - b) side view and zoom on failure - c) top view and zoom on failure 81
3.44 Experimental results for the 350J drop tower tests on 4mm thick PREPREG hat-profiles: displacement vs. time and force vs. time (top), a) side view of the hat-profile after impact - b) side view and zoom on failure - c) top view and zoom on failure 82
3.45 Experimental results for the 500J drop tower tests on 4mm thick PREPREG hat-profiles: displacement vs. time and force vs. time (top), a) side view of the hat-profile after impact - b) side view and zoom on failure - c) top view and zoom on failure 83

4.1 Material coordinate system for a unidirectional composite ply 86
4.2 Illustration of the influence of the shape parameter n_i on the nonlinear behavior until the failure onset 89
4.3 Schematic representation of the 1D plasticity formulation with linear hardening 90
4.4 Failure surfaces of the maximum stress (black curve) and Tsai-Wu (dotted blue curve) failure criteria 94
4.5 a) Fracture plane for a load in the direction 2 - b) Example of a material law with a linear post-failure material degradation 95
4.6 Overview and schematic representation of the four post-failure material degradation models: a) linear damage - b) nonlinear damage - c) constant stress level post-failure material degradation - d) steps-based post-failure material degradation 97
4.7 Mesh-size independence of the regularized linear a) and nonlinear b) damage 100
4.8 Final strain update for the regularized constant stress level a) and step-based b) post-failure material degradation 101

5.1 Description of the numerical models for the tensile (top) and compressive tests (bottom) . 106

5.2 Description of the numerical models for the three-point bending (top) and four-point bending (bottom) tests . . . 106
5.3 Comparison of the numerical results obtained for four composite material models: a) longitudinal tension - b) longitudinal compression - c) shear tension - d) shear compression 108
5.4 Comparison of the numerical results obtained for four composite material models: a) longitudinal bending - b) diagonal (shear) bending . . . 109
5.5 Numerical results obtained with the UMAT and a modeling with shell and thick shell elements: a) longitudinal tension - b) longitudinal compression - c) shear tension - d) shear compression . . . 110
5.6 Numerical results obtained with the UMAT and a modeling with shell and thick shell elements: a) longitudinal bending - b) diagonal (shear) bending . . . 111
5.7 Comparison between the evolution of the macroscopic and plastic strains: a) Longitudinal compressive tests - b) Shear tensile tests - c) Maximal shear strain distribution over the specimen for the shear tensile test . . . 112
5.8 Influence of the mesh size on the longitudinal bending behavior for the *MAT_054 model: a) Using under-integrated shell elements - b) Using full-integrated shell elements . . . 113
5.9 Numerical results obtained with the *MAT_118 model and under-integrated shell elements: a) Longitudinal tension - b) Longitudinal bending . . . 114
5.10 Analytic evaluation of the effect of fiber waviness on the compressive longitudinal Young's modulus of a wavy ply . . . 115
5.11 Numerical results obtained with the *MAT_054 model, a bidirectional stacking sequence and material properties accounting for fiber waviness: a) longitudinal tension and compression - b) longitudinal three-point bending . . . 115
5.12 Numerical results obtained with the *MAT_054 and the UMAT models with shell and thick shell elements and the modeling of the outer glass mat layers: a) longitudinal bending - b) diagonal bending . . . 117
5.13 Numerical results obtained with the *MAT_054 and the UMAT model with shell and thick shell elements and the modeling of the outer glass mat layers: a) longitudinal tension - b) longitudinal compression - c) shear tension - d) shear compression . . . 118
5.14 Correlation for the carbon plain-weave RTM composite: longitudinal tension . . . 119
5.15 Correlation for the carbon plain-weave RTM composite: longitudinal compression . . . 120
5.16 Distribution of the maximal macroscopical compressive strain and its corresponding plastic strain . . . 120
5.17 Correlation for the carbon plain-weave RTM composite: tensile and compressive shear . . . 121
5.18 Distribution of the maximal macroscopical tensile shear strain and its corresponding shear plastic strain . . . 121
5.19 Correlation for the carbon plain-weave RTM composite: longitudinal four-point bending . . . 122
5.20 Correlation for the carbon plain-weave RTM composite: diagonal four-point bending . . . 123
5.21 Correlation for the carbon plain-weave RTM composite: 25J and 50J impact and modeling with shell elements but without post-failure material degradation . . . 124
5.22 Correlation for the carbon plain-weave RTM composite: 5J impact, linear damage and a modeling with shell elements . . . 125

5.23 Correlation for the carbon plain-weave RTM composite: 25J impact, linear damage and a modeling with shell elements . . . 126
5.24 Correlation for the carbon plain-weave RTM composite: 50J impact, linear damage and a modeling with shell elements . . . 127
5.25 Correlation for the carbon plain-weave RTM composite: 5J, 25J, 50J impact energies, a 2.5mm mesh size, a linear damage, a modeling with shell elements and the 45° orientation 128
5.26 Correlation for the carbon plain-weave RTM composite: 25J, 50J impact energies, a 5mm mesh size, a step-based post-failure material degradation and a modeling with shell elements 128
5.27 Correlation for the carbon plain-weave RTM composite: 25J, 50J impact energies, a 5mm mesh size, a constant-stress level post-failure material degradation and a modeling with shell elements . . . 129
5.28 Correlation for the carbon plain-weave RTM composite: 25J impact, nonlinear damage and a modeling with shell elements . . . 130
5.29 Correlation for the carbon plain-weave RTM composite: 50J impact, nonlinear damage and a modeling with shell elements . . . 130
5.30 Comparison of the numerical results for the four post-failure material degradation models for a 25J impact and a modeling with shell elements . . . 131
5.31 Comparison of the numerical results for the four post-failure material degradation models for a 50J impact and a modeling with shell elements . . . 132
5.32 Correlation for the carbon plain-weave RTM composite: 5J impact, linear damage and a modeling with thick shells . . . 133
5.33 Correlation for the carbon plain-weave RTM composite: 25J impact, linear damage and a modeling with thick shells . . . 134
5.34 Correlation for the carbon plain-weave RTM composite: 50J impact, linear damage and a modeling with thick shells . . . 134
5.35 Comparison between a modeling with ten layers of thick shell and ten layers of under-integrated brick elements: 50J impact and linear damage . . . 136
5.36 Correlation for the carbon plain-weave RTM composite: 25J, 50J impact energies, a 5mm mesh size, a step-based post-failure material degradation and a modeling with thick shell elements . . . 136
5.37 Effect of the post-failure number of steps on the material response: 50J impact and a modeling with thick shells . . . 137
5.38 Correlation for the carbon plain-weave RTM composite: 25J, 50J impact energies, a 5mm mesh size, a constant stress level post-failure material degradation and a modeling with thick shell elements . . . 137
5.39 Effect of the post-failure stress level on the material response: 50J impact and a modeling with thick shells . . . 138
5.40 Correlation for the carbon plain-weave RTM composite: 25J, 50J impact energies, a 5mm mesh size, a nonlinear post-failure damage and a modeling with thick shell elements . . . 138
5.41 Comparison of the numerical results for the four post-failure material degradation models for both 25J and 50J impact energies and a modeling with thick shell elements . . . 139

5.42 Correlation for the carbon plain-weave RTM hat-profile: 200J impact energy, a 5mm mesh size, a linear post-failure damage, a modeling with shell elements and the previous validated material parameters . . . 140
5.43 Correlation for the carbon plain-weave RTM hat-profile: 200J impact energy, a 5mm mesh size, a linear post-failure damage, a modeling with shell elements and updated material parameters . . . 141
5.44 Correlation for the carbon plain-weave RTM hat-profile: 200J impact energy, a 5mm mesh size, a nonlinear post-failure damage, a modeling with shell elements and the previous validated material parameters . . . 142
5.45 Correlation for the carbon plain-weave RTM hat-profile: 200J impact energy, a 5mm mesh size, a nonlinear post-failure damage, a modeling with shell elements and updated material parameters . . . 143

6.1 Correlation for the carbon twill-weave PREPREG composite: longitudinal unidirectional tension . . . 148
6.2 Correlation for the carbon twill-weave PREPREG composite: longitudinal unidirectional compression . . . 148
6.3 Correlation for the carbon twill-weave PREPREG composite: shear tension . . . 149
6.4 Correlation for the carbon twill-weave PREPREG composite: longitudinal unidirectional four-point bending . . . 150
6.5 Correlation for the carbon twill-weave PREPREG composite: diagonal unidirectional four-point bending . . . 150
6.6 Correlation for the carbon twill-weave PREPREG composite: longitudinal multidirectional tension . . . 151
6.7 Correlation for the carbon twill-weave PREPREG composite: diagonal multidirectional tension . . . 152
6.8 Correlation for the carbon twill-weave PREPREG composite: longitudinal multidirectional compression . . . 152
6.9 Correlation for the carbon twill-weave PREPREG composite: diagonal multidirectional compression . . . 153
6.10 Correlation for the carbon twill-weave PREPREG composite: longitudinal multidirectional four-point bending . . . 153
6.11 Correlation for the carbon twill-weave PREPREG composite: diagonal multidirectional four-point bending . . . 154
6.12 Correlation for the carbon twill-weave PREPREG composite: 5J impact and a modeling with shell elements . . . 155
6.13 Correlation for the carbon twill-weave PREPREG composite: 25J impact and a modeling with shell elements . . . 156
6.14 Influence of nonlinearity on the correlation for the carbon twill-weave PREPREG composite: 25J impact, a modeling with shell elements and of a linear elastic behavior . . . 157
6.15 Correlation for the carbon twill-weave PREPREG composite: 50J impact and a modeling with shell elements . . . 158

6.16 Correlation for the carbon twill-weave PREPREG composite: overview of the 5J, 25J and 50J impacts for the 45° orientation and a modeling with shell elements 159
6.17 Correlation for the carbon twill-weave PREPREG composite: 5J impact and a modeling with thick shell elements 160
6.18 Correlation for the carbon twill-weave PREPREG composite: 25J impact and a modeling with thick shell elements 161
6.19 Correlation for the carbon twill-weave PREPREG composite: 50J impact and a modeling with thick shell elements 161
6.20 Correlation for the carbon twill-weave PREPREG composite: overview of the 5J, 25J and 50J impacts for the 45° orientation and a modeling with thick shell elements 162
6.21 Correlation for the carbon twill-weave 2mm thick PREPREG hat-profiles: 100J impact, comparison between the linear and nonlinear post-failure damages using the previous validated material parameters 163
6.22 Failure and damage distribution for the 100J impact on 2mm thick PREPREG hat-profiles and a linear post-failure damage model 164
6.23 Failure and damage distribution for the 100J impact on 2mm thick PREPREG hat-profiles and a nonlinear post-failure damage model 164
6.24 Correlation for the carbon twill-weave 2mm thick PREPREG hat-profiles: 100J impact, the linear post-failure damage using the previous validated material parameters and a 25% reduction of the compressive strength in the corners 165
6.25 Correlation for the carbon twill-weave 2mm thick PREPREG hat-profiles: updated strains at ultimate failure 166
6.26 Correlation for the carbon twill-weave 4mm thick PREPREG hat-profiles: 350J impact, comparison between the linear and nonlinear post-failure damages using the previous validated material parameters 167
6.27 Correlation for the carbon twill-weave 4mm thick PREPREG hat-profiles: 350J impact, the linear post-failure damage using the previous validated material parameters and a 50% reduction of the compressive strength in the corners 168
6.28 Correlation for the carbon twill-weave 4mm thick PREPREG hat-profiles: updated strains at ultimate failure for the 350J impact 169
6.29 Correlation for the carbon twill-weave 4mm thick PREPREG hat-profiles: 500J impact, comparison between the linear and nonlinear post-failure damages using the previous validated material parameters 170
6.30 Correlation for the carbon twill-weave 4mm thick PREPREG hat-profiles: updated ultimate strains at failure for the 500J impact 171

List of Tables

3.1 Coefficients of variation (in %) for the effective material properties in longitudinal tension 56
3.2 Coefficients of variation (in %) for the effective material properties in longitudinal compression 57
3.3 Coefficients of variation (in %) for the flexural stiffness, strength and strain at failure for the longitudinal four-point bending tests 59
3.4 Coefficients of variation (in %) concerning the bending stiffness, maximal flexural stress and maximal flexural strain for the diagonal four-point bending tests 60
3.5 Overview of the impact energies and the corresponding impacting mass and impact velocity 61
3.6 Coefficients of variation (in %) concerning the maximal impactor's displacement, the maximal force peak and the damaged surfaces for the impact tests on the RTM material and the 0° orientation 66
3.7 Coefficients of variation (in %) concerning the maximal impactor's displacement, the maximal force peak and the damaged surfaces for the impact tests on the RTM material and the 45° orientation 66
3.8 Coefficients of variation (in %) concerning the maximal impactor's displacement, the maximal force peak and the damaged surfaces for the impact tests on the PREPREG material and the 0° orientation 80
3.9 Coefficients of variation (in %) concerning the maximal impactor's displacement, the maximal force peak and the damaged surfaces for the impact tests on the PREPREG material and the 45° orientation 80

Nomenclature

Greek symbols

α	Internal hardening variable in the 1D plasticity formulation
α_{n+1}	Internal hardening variable at the step $n+1$
α_{n+1}^{trial}	Trial value of the internal hardening variable at the step $n+1$
α_n	Internal hardening variable at the step n
β	Parameter in the exponential formulation of the nonlinear damage representing a value close to 0
Δt	Time step
Δt_0	Initial time step
Δt_n	Time step at time t_n
$\Delta t_{\text{critical}}$	Critical time step
$\Delta t_{n+\frac{1}{2}}$	Time step at time $t_{n+\frac{1}{2}}$
$\Delta t_{n-\frac{1}{2}}$	Time step at time $t_{n-\frac{1}{2}}$
δx_i	Arbitrary virtual displacement and displacement at a point inside an element in the direction i
δx_{ki}	Displacement at the node k in the direction i
$\Delta\lambda$	Increment of the internal hardening variable
$\Delta\varepsilon_n$	Increment of the total strain
$\dot{\sigma}$	Stress rate
$\dot{\varepsilon}$	Total strain rate
$\dot{\varepsilon}^e$	Elastic strain rate
$\dot{\varepsilon}^p$	Plastic strain rate
Γ	Fracture toughness (energy per unit area)

Γ^{ref}	Fracture toughness reference
Γ_1	Area under the stress-strain curve before failure onset
Γ_2	Area under the stress-strain curve between failure onset and ultimate failure
Γ_1^{L}	Energy before failure onset for a linear elastic behavior
Γ_1^{NLP}	Energy before failure onset for a nonlinear plastic behavior
Γ_2^{level}	Energy between failure onset and ultimate failure for a constant stress level post-failure material degradation
Γ_2^{L}	Energy between failure onset and ultimate failure for a linear damage
λ	Absolute value of the slip rate in the 1D plasticity formulation
ν_{ij}	Poisson's ratio $(i, j = 1, ..., 6)$
ρ	Material density
σ	General expression of the stress
σ^{ud}	Undamaged stress considered for the damage models
σ_i^a	Asymptotic stress level in the Ramberg-Osgood formulation
σ_i^o	Stress at failure onset
σ_i	Stress in the material direction i $(i = 1, ..., 6)$
σ_{n+1}	Stress at the step $n + 1$
σ_{n+1}^{trial}	Trial value of the stress at the step $n + 1$
σ_y	Yield stress in the 1D plasticity formulation
ε	General expression of the strain and total strain
ε^f	Final strain at ultimate failure
ε^i	Plastic strain at failure onset
ε_i^o	Strain at failure onset
$\varepsilon_{\text{new}}^f$	Update of the final strain at ultimate failure
ε_i	Strain in the material direction i $(i = 1, ..., 6)$
ε_{n+1}	Strain at the step $n + 1$
ε_{n+1}^p	Plastic strain at the step $n + 1$
ε_n	Strain at the step n
ε_n^p	Plastic strain at the step n

Roman symbols and abbreviations

$\bar{x}_0$	Initial geometry at time t_0
$\ddot{u}$	Acceleration of the single degree of freedom system
$\ddot{u}_n$	Acceleration at time t_n
$\ddot{x}_0$	Initial acceleration of the complete geometry at time t_0
$\ddot{x}_i$	Velocity of each particle of a 3D body (for the study of the LS-DYNA formulation)
$\ddot{x}_n$	Acceleration of the complete geometry at time t_n
$\dot{u}$	Velocity of the single degree of freedom system
$\dot{u}_n$	Velocity at time t_n
$\dot{u}_{n+\frac{1}{2}}$	Velocity at time $t_{n+\frac{1}{2}}$
$\dot{u}_{n-\frac{1}{2}}$	Velocity at time $t_{n-\frac{1}{2}}$
$\dot{x}_0$	Initial velocity of the complete geometry at time t_0
$\dot{x}_i$	Velocity of each particle of a 3D body (for the study of the LS-DYNA formulation)
$\dot{x}_{n+\frac{1}{2}}$	Velocity of the complete geometry at time $t_{n+\frac{1}{2}}$
$\dot{x}_{n-\frac{1}{2}}$	Velocity of the complete geometry at time $t_{n-\frac{1}{2}}$
$\{\ddot{u}\}_n$	Acceleration vector of an arbitrary degree of freedom system at cycle number n
$\{\dot{u}\}_n$	Velocity vector of an arbitrary degree of freedom system at cycle number n
$\{F^{\text{ext}}\}_n$	External forces vector of an arbitrary degree of freedom system at cycle number n
$\{F^{\text{int}}\}_n$	Internal forces vector of an arbitrary degree of freedom system at cycle number n
$\{u\}_n$	Displacement vector of an arbitrary degree of freedom system at cycle number n
C	Coefficient of damping of an arbitrary degree of freedom system
c	Coefficient of damping of the single degree of freedom system
C_{ij}	Terms of the orthotropic stiffness matrix $(i, j = 1, ..., 6)$
c_s	Wave or sound speed
$coef_{xx}$	Coefficient multiplied (between 0 and 1) by the strength to determine the post-failure stress level
d	General expression of the damage variable
d_i	Displacements prescribed on the surface of a 3D body (for the study of the LS-DYNA formulation)

$d_{\mathrm{L}}^{\mathrm{inst}}$	Instantaneous value of the linear damage
d_{NL}	Nonlinear damage evolution law based on the exponential formulation
d_{NL}^{1}	Nonlinear damage evolution law based on the nth-root formulation
d_i	Strain increment in the material direction i $(i = 1, ..., 6)$
E_i	Young's modulus in the material direction i $(i = 1, ..., 6)$
F^{ext}	External forces of the single degree of freedom system
$F_{\mathrm{stat}}^{\mathrm{ext}}$	External forces from static loading
F_n^{ext}	External forces at time t_n
F^{int}	Internal forces of the single degree of freedom system
f_i	External forces density acting on a 3D body (for the study of the LS-DYNA formulation)
F_0^{ext}	Initial external forces
F_0^{int}	Initial internal forces
F_{d}	Damping forces of the single degree of freedom system
F_{i}	Inertia forces of the single degree of freedom system
f_{n+1}^{trial}	Trial value of the yield function f at the step $n+1$
G_{ij}	Shear modulus in the material direction ij $(i, j = 1, 2, 3)$
K	Plastic modulus (UMAT theory) and stiffness of an arbitrary degree of freedom system (for the study of the LS-DYNA formulation)
k	Stiffness of the single degree of freedom system
l^*	Element characteristic length
l_{ref}^*	Element characteristic length reference
l^{crit}	Critical element length
l_{c}	Characteristic length of an element (for the determination of the critical time step)
M	Mass of an arbitrary degree of freedom system
m	Mass of the single degree of freedom system
n_i	Shape parameter in the Ramberg-Osgood formulation or exponent for the nth-root damage formulation
S_{d}	Surface a 3D body where the displacements d_i are prescribed (for the study of the LS-DYNA formulation)

S_{t}	Surface a 3D body where the traction forces t_i are applied (for the study of the LS-DYNA formulation)
S_{12}	Shear strength
t_i	Traction forces density acting on the surface of a 3D body (for the study of the LS-DYNA formulation)
t_0	Initial time at the cycle 0
t_{n+1}	Time at cycle $n+1$
$t_{n+\frac{1}{2}}$	Time at cycle $n+\frac{1}{2}$
t_{n-1}	Time at cycle $n-1$
$t_{n-\frac{1}{2}}$	Time at cycle $n-\frac{1}{2}$
t_n	Time at the current cycle n
U	Total energy absorbed after failure by one element
u	Displacement of the single degree of freedom system
u_n	Displacement at time t_n
u_{stat}	Initial displacement from static loading
u_{n+1}	Displacement at time t_{n+1}
$u_{n+\frac{1}{2}}$	Displacement at time $t_{n+\frac{1}{2}}$
u_{n-1}	Displacement at time t_{n-1}
$u_{n-\frac{1}{2}}$	Displacement at time $t_{n-\frac{1}{2}}$
U_{vol}	Total energy absorbed per unit volume
V_m	Volume of an element (for the study of the LS-DYNA formulation)
x_0	Initial displacement of the complete geometry at time t_0
x_i	Spatial coordinates of each particle of a 3D body (for the study of the LS-DYNA formulation)
x_n	Displacement of the complete geometry at time t_n
X_{c}	Longitudinal compressive strength
X_{t}	Longitudinal tensile strength
x_{n+1}	Displacement of the complete geometry at time t_{n+1}
x_{n-1}	Displacement of the complete geometry at time t_{n-1}
Y_{c}	Transverse compressive strength

Y_t	Transverse tensile strength
Z_c	Through the thickness compressive strength
Z_t	Through the thickness tensile strength
$C-SCAN.$	Ultra-sound analysis
$C.A.I$	Compression After Impact
$C.D.M$	Continuum Damage Mechanics
$C.L.T$	Classical Laminate Theory
$D.I.C$	Digital Image Correlation
$M.D.$	Multidirectional
$R.U.C$	Representative unit cell
$U.D.$	Unidirectional

Chapter 1

Introduction

1.1 Context of the study

1.1.1 General context

Over few decades the global population increased considerably and the development of some countries like China or India in terms of economic growth and urbanization has been considerably accelerated. It leads to a considerable increase of the general global consumption. More particularly, the fossil energy consumption exploded due to the escalation of the global air traffic and ground means of transport. Unfortunately, it implies a dramatically raise of polluting emissions and greenhouse gases [1–3]. The general increase of gas emissions and energy consumption is mainly responsible for the well-known global warming phenomenon. Some studies investigated the causes and consequences of climate changes concerning the environmental and economic impacts for the future years at global and regional scales [1, 4, 5] and they studied the corresponding potential risks on the human health and on ecosystems [1, 6–10]. Additionally to these environmental and human aspects, the increasingly price of the fossil energy forced the diverse manufacturers of the transport field to develop fuel-save engines and powertrains. Given that the present study has been conducted at Daimler AG, a special focus will be ported on the automotive industry.

1.1.2 Automotive field

European regulations set some limits for the different gas emissions in function of the category of vehicles (passenger cars, light commercial vehicles, lorries, buses, etc.). Since September 2009, the Euro 5 regulation has to be respected and the Euro 6 regulation will be then in service in September 2014 for the passenger cars [11]. Most of the car manufacturers makes huge efforts to develop environment-friendly vehicles. Based on the well-known combustion engines, Daimler developed innovative technologies to improve the efficiency of the engines and to reduce the fuel consumption. The labels "BlueEfficiency" and "BlueTec" characterize these new engine and powertrain generations. Hybrid vehicles, which combine electric powertrain and combustion engine, have already been commercialized. Daimler developed also fuel-cell and full-electric emission-free vehicles, as for example the Smart Electric Drive and more recently the new concept of the SLS Electric Drive (see Fig. 1.1).

Until now, the weight increase due to the rising number of comfort and safety instrumentations has been often compensated by the improved efficiency of the combustion engines in order to avoid a fuel

Figure 1.1: Three vehicles developed by Daimler AG equipped with new generations of powertrains: SLS Electric Drive (left), the new E-Class hybrid (middle) and the Smart Brabus Electric Drive (right)

over-consumption. However, the current electric powertrains are relatively heavy, which tends to limit the cruising range of these vehicles. Consequently, it is necessary to save weight using light materials and structures. A first concept in the automotive lightweight construction is for example to replace heavy metallic parts in steel by aluminum, as it has been recently successfully made for the last generation of the Mercedes-Benz SL-Class. Another concept is the use of composite materials, which are well-known for their strength to weight ratio. However, the design and the dimensioning of automotive structural parts using composite materials represent still a considerable challenge, as it is detailed in the next sections.

1.2 Use of composite materials for automotive applications

1.2.1 Why?

First, as mentioned previously, the use of composite material for automotive applications aims at the design of lightweight structures. On one side, it allows to reduce the weight of the current cars featured with a common combustion engine, and on another side it will allows to limit the impact of the weight increase due to the alternative powertrains. Then, the design and the fabrication of geometrically complex parts may be possible, due to the large number of composite types and manufacturing processes. Moreover, the composites represent a new generation of materials, which were until now mainly used in the prestigious aeronautic and aerospace industries, for race cars or for small serial vehicle production. Consequently, these materials refer often to the idea of new concept, technological innovation, advanced engineering, sport, exclusivity and cutting-edge technologies. These aspects could convince a potential customer to buy a car equipped with such materials instead of getting another one more conventional. It means that composite materials could have also a non-negligible commercial aspect in the automotive field. Finally, composite materials are now increasingly used in different engineering fields, which induced a non-negligible reduction of their costs. Indeed, material costs are drastically limited in the automotive industry, which was until now one of the main obstacles to the application of composite materials in this field.

1.2.2 Where and how?

Composite materials are often used for the body of race cars but they are employed too for the design and the manufacturing of structural parts in the Formula 1 motor racing field [12]. Due to their relatively

suitable energy absorbing properties, composite materials ensure the safety of sport cars. Regarding more conventional vehicles adapted for large serial productions, plastic materials have been until now mainly applied for non-structural parts or some car body parts. Carbon fiber reinforced plastics have been then sometimes used for non-structural or decorative parts due to their attractive optical properties.

Crash studies require materials that are able to absorb energy. For automotive crash applications, an adequate material has to absorb as much energy as possible before breaking, as the rupture of the material represents generally a large reduction of energy dissipation. It explains that ductile materials are more adapted for crash applications than brittle material. Long fiber reinforced plastics loaded in shear, short fiber reinforced plastics or glass fiber composites show generally a ductile behavior but they also present a too low stiffness. A minimal rigidity is required to avoid a too weak behavior in bending or in torsion of the car structure. Consequently, the compromise between rigidity, ductility and energy dissipation is one of the major challenges for the design of crash-safe automotive structural parts in composite.

Due to confidentiality reasons, no real example of composite structural parts developed at Daimler AG will be mentioned. However, the well-known application possibilities of composite materials will be detailed. First, composites can be used as a local reinforcement on a large structural part. Thus, very thin structures can be manufactured and a local reinforcement in the critical zones allows to fulfill the requirements list. Then, composite materials can be used in the design of complete structural parts, which contribute to the overall rigidity of the car, even if they are not really crash-relevant. Composite materials can be also used to replace steel or aluminum in the main structural parts of the vehicle. In this case, the design of the part has to account for the validation of the different crash regulations. The main challenge is here to find the compromise between lightweight potential and energy absorption. Finally, composite parts presenting hybrid structures (use of different materials over the thickness) can be considered for structural parts, but the present study is limited to the common fiber reinforced composites. Considering the previous remarks, it is necessary to adapt the design of the part to composite materials. The replacement of a metallic material by a composite without adapting the geometry, the thickness or the orientation and location of the reinforcements does not allow to capture the full lightweight potential of these materials.

1.2.3 Introduction to the crash behavior of composite materials for automotive applications

Crash studies consist in the assessment of the progressive absorption and dissipation of kinetic energy in deformable zones or in energy absorbing elements, in order to ensure the occupants' safety. All these systems used to absorb the kinetic energy of a vehicle in crash refer to the passive safety of the car. In addition, some active safety systems are used to help the driver in avoiding an accident or preparing the vehicle and its passengers to the crash. In this way, one of the main certification steps in the development and commercialization process of a new vehicle is the validation of crash-tests. Global standards for car safety have been set as for example the European New Car Assessment Program (EuroNCAP) [13–15]. The crash behavior of each new car is assessed and awarded referring to a particular star rating. Consequently, each crash-relevant structural part made up with composite material has to fulfill the different crash regulations and requirements.

The crushing behavior and crashworthiness of fiber reinforced materials have already been investigated

particularly regarding crash boxes or energy absorbing elements [16–21], automotive [21–27] and aircraft applications [28–30]. In [31], composite tubes have been found to absorb more energy than heavier aluminum tubes. Composite materials have been thus identified as a promising investigation way for systems offering a suitable compromise between lightweight and energy absorption capability.

An explosive failure with a complete loss of material integrity is generally observed by crushing loads of composite tubes. In this case the destruction, progressive fragmentation and pulverization of the composite material dissipate a large amount of energy. Regarding the automotive applications, such a behavior is acceptable for crash-boxes or energy absorbing elements. However, the structural parts of a vehicle do not have to loss their overall integrity in order to ensure the occupant's safety. In this situation, composite materials have to absorb the adequate amount of kinetic energy, undergoing deformations and distributing eventually the load to other energy absorbing and deformable parts. Consequently, the total disintegration of the composite material is here generally not wished. Finally, in order to catch the full benefit of the lightweight potential of composite material, it is very important to assess their damage tolerance and energy dissipation capability.

Structural parts are likely to present a considerable thickness and relatively complex geometries. For these reasons and due to their draping, stiffness, improved ductility and damage tolerance properties woven composites are being increasingly used for the design of crash-relevant structural parts. Consequently, the behavior of carbon fiber woven composites under different quasi-static and impact load cases will be the main focus of the present study.

1.3 Motivation and objectives of the thesis

1.3.1 Presentation of the challenge and motivation

If the crash behavior of the main isotropic metallic materials like steel or aluminum is relatively well-known, the one of composite materials requires still many investigations. Indeed, due to the complex internal structure of the long fiber reinforced plastic and their anisotropic properties, their mechanical behavior is relatively difficult to assess and to predict.

Regarding the considerable costs induced by experimental tests on composite materials, numerical simulations are very helpful to investigate the mechanical behavior of composites. Thus, the main challenge of the present study is to develop and validate characterization methods and modeling techniques, in order to predict numerically the behavior of composite materials under different load cases. Some experimental tests will be used to validate the models. The behavior of composite materials has to be predicted in terms of stiffness, failure and post-failure material degradation, which allows to assess the damage tolerance of the material in order to avoid over-dimensioning. The numerical models and modeling techniques developed in this study will be thereafter used in the development process of vehicle to assess the crash-behavior of structural parts made of composite materials. However, simulations on a full-scale car model have not been conducted in this work.

The industrial field imposes some limitations regarding the discretization and the costs of numerical models. To limit the computing time, element sizes between 3mm and 5mm have to be respected to mesh the different parts. Moreover, a unique layer of under-integrated shell, brick or thick shell elements have to be used to model the complete material. The stacking sequence of the composite is defined through

the different integration points over the thickness of each element. The objective is to represent one elementary composite ply by only one point of integration. A maximum of two points of integration is authorized for the modeling of an elementary woven ply. Finally, an acceptable compromise has to be found between the different experimental and numerical costs and the accuracy of the predictions regarding stiffness, failure and damage propagation in the material.

The main motivation is to design safer lightweight structures in order to accelerate the development of environment-friendly vehicles and to extend their range of use. These kinds of vehicles have to be commercialized as soon as possible to limit the polluting emissions and to improve the life quality of the people and of the next generations. It will also allow to reduce the number of experimental tests being replaced by numerical simulations, which will reduce the costs of the vehicles increasing their attractiveness for the customers.

1.3.2 Description of the objectives

The main objective of the study is to develop and validate modeling techniques for finite elements simulations, that contribute to improve the numerical predictions regarding the behavior of carbon fiber woven composite laminates under different load cases. According to the experimental observations, the first step consists in assessing the current existing modeling techniques available in the explicit finite element solver LS-DYNA. In function of the different deficiencies, that are likely to be identified, solutions will be proposed, developed and validated to improve the reliability of the predictions regarding the macroscopic behavior of composite materials, with a special focus on woven laminates. Post-failure material degradation and permanent deformation should be taken in consideration, as they play a major role in the crash behavior of a material. Finally, the solutions mentioned previously have to respect the limitations and conditions imposed by the industrial field.

1.4 Structure of the study

1.4.1 Characterization method applied to composite materials

In order to limit the costs of expensive experiments on large composite structures, a consistent methodology has been developed to characterize the macroscopic mechanical behavior of a composite under different load cases. This method is based on a building-block approach [32, 33] beginning with a micromechanical approach up to full-car crash tests via coupon and representative component tests (see Fig. 1.2). The experimental tests and their corresponding numerical validation evolve in a parallel way. The number of experimental tests decreases but the costs of each test increase by going up through the pyramid.

The method begins at the bottom of the pyramid with the micromechanical investigation of the material aiming at a more intimate understanding of its internal structure. The experimental tests consist here in the observation of the structure based for example on computational tomography analysis or micrographs. From a modeling point of view, this steps consists in the investigation of the different material theories. It concerns particularly the determination of the homogenized material properties using the different homogenization rules or numerical micromechanical FE-analysis, based on the mechanical properties of the material's constituents. Having reliable predictions of the effective properties, the

quasi-static tests on elementary coupons (next step of the building-block approach) are no more required, which can lead to considerable costs savings. If no micromechanical numerical investigations have been achieved, experiments on coupons are required to determine the effective material properties of the material under different load paths as tension, compression or bending in the different directions. The numerical simulations consist here in the modeling of these experimental tests to assess and eventually to validate the corresponding modeling techniques.

As composite parts have to be assembled with other vehicle components, the third step of the building-block approach investigates the joining techniques, that are suitable for composite materials as mechanical or adhesive joints. Experimental tests are here conducted to characterize the behavior of the joints under different load cases. The numerical modeling of these tests allows to assess and validate particular modeling techniques to predict the behavior of the different joining techniques.

The fourth level involves impact tests and representative component tests to investigate the effect of the part geometry and to evaluate the propagation of damage and delamination within the material under crash load cases. Once validated, the numerical models should be here able to predict the delamination propagation and the damage tolerance of the considered composite material. Based on reliable predictions, few expensive experimental tests on real automotive composite parts are required, reducing thus the development costs of a vehicle. Finally, full-car crash simulations validated using full-car crash tests complete the method.

The validation of all these steps has to follow a consistent methodology. Each material parameter or modeling technique validated at one step is used for the next steps without any change. Once these simulations are validated, the numerical models should be able to predict efficiently the behavior of the investigated composite material in crash configurations with an suitable reliability.

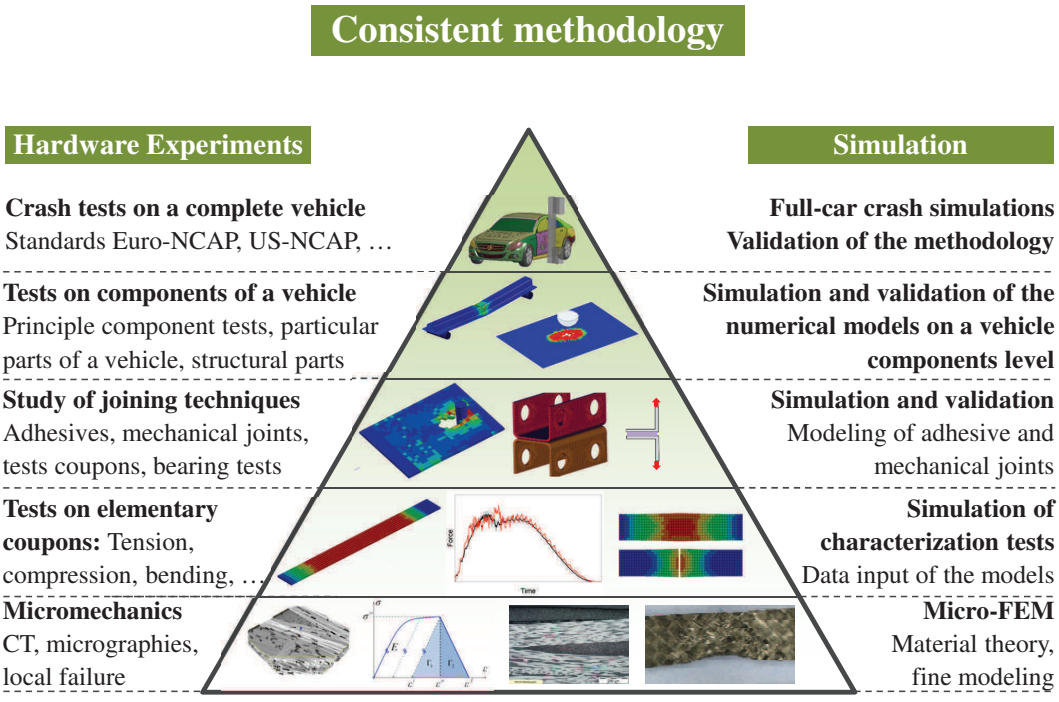

Figure 1.2: Building-block approach for the experimental and numerical characterization of composites

1.4.2 Milestone of the thesis

In the next chapter, a state of the art concerning the characterization and the numerical modeling of woven composites will be presented. The current modeling used to predict the effective material properties and the mechanical behavior of such materials will be reviewed and discussed. Current capabilities and limits will be identified leading to the proposition of solutions. Then, experimental results conducted on a carbon plain-weave RTM composite and on a carbon twill-weave PREPREG composite will be presented. It consists first in quasi-static tests on elementary coupons aiming at the determination of the effective material properties and of the characterization of the macroscopic material behavior under different load cases. Then, the experimental observations made for impact tests on elementary composite plates will be reported and discussed. These tests investigate the damage and delamination propagation in the material. They allow also to evaluate the damage tolerance of the material under impact loads, which represents a very important step for the dimensioning of crash-relevant structural parts designed with composite materials. The experimental results obtained for the drop tower tests on hat-profiles will be then presented. Hat-profiles specimens are used here as a representative component or a representative part to validate the modeling techniques and the characterization methods, before starting with experiments and simulations on real automotive composite parts. The fourth chapter will present the development of a new material model for the explicit FE-solver LS-DYNA. The different features of this new material model have to bring a solution to the main weaknesses identified in the state of the art. They will also offer suitable numerical modeling techniques to predict the macroscopic material behavior observed experimentally. Finally, the new material model developed in this study will be assessed and validated based on the simulations of the experimental tests described previously. A discussion of the results will be made opening to the final conclusion and the future works.

Chapter 2

State of the Art - Literature review

2.1 Introduction

In this chapter, the literature dealing with the prediction of material properties and failure of textile reinforced composites is reviewed in order to identify weaknesses in current approaches and to highlight exploration ways overcoming some of the discovered limitations. First, an introduction about textile composites and their manufacturing processes is presented. Thereafter, analytic and numerical models to determine the elastic properties and failure of textile composites are reviewed. Then, the main studies about the impact of woven composites are described including the strain rate dependency of such materials. The modeling techniques and material models available in the crash solver LS-DYNA will be reviewed and discussed to identify the potential requirements in order to better predict the mechanical behavior of textile composites.

2.2 Constituents and manufacturing processes of composite materials

2.2.1 Constituents

2.2.1.1 General overview

At the macroscopic level, composite materials are the combination of at least two non-miscible constituents, which remain distinct and separate within the finished structure. Each composite material is constituted by two types of components [33–35]. The first constituent is a reinforcement, fiber or particle, which assures the mechanical behavior, the stiffness and the strength of the composite material. In the present study, the focus is on reinforcements constituted by "infinite" fibers in unidirectional arrangement or in a textile structure. Among the different types of fibers, carbon fibers are particularly investigated for their lightweight, stiffness, strength and flexibility properties. The second constituent is a matrix which supports and links the reinforcements by maintaining their relative position. It distributes the stresses all over the material, assures the chemical protection and gives the form to the material. Considering their high strength and modulus, excellent adhesion, low shrinkage, good chemical resistance, and ease of processing properties, epoxy resins are the main point of interest in the present study.

The mechanical properties of the fibers are generally very different than those of the matrix. Thus, each composite presents its own material properties that depend on those of the constituents and on the intimate junction between the reinforcements and the matrix. Defining adequate techniques of homogenization, the effective mechanical and physical properties of a composite can be predicted. The reliability of the prediction depends on several parameters: the method of homogenization (analytic or numerical using finite element simulations), the knowledge of the reinforcement distribution in the matrix and the knowledge of the constituents material properties. Moreover, several material deficiencies or characteristics are likely to affect the material properties as for example porosity, fiber waviness, fiber tension, fiber misalignment, chemical heterogeneity in the resin, heterogeneity in the fibers arrangement and distribution, resin-rich regions and local fiber debonding. It naturally increases the difficulties to predict accurately the material properties and the mechanical behavior of composites and it underlines the large scatter of parameters affecting the mechanical and physical properties of such materials.

2.2.1.2 Textile reinforcements

Textile composites can be classified into three basic categories: the woven fabrics, the knitted fabrics and the braided fabrics. Woven fabrics can be then divided into the opened-packing weaves where there are gaps between the adjacent yarns, and the closed packing weaves, where there are no gap between the adjacent yarns. Moreover, balanced weaves offer similar properties and geometric dimensions in the warp and weft directions, whereas unbalanced weaves does not present these symmetries [36]. An organization in quasi-laminar and non-laminar textile has been proposed by Cox [37]: quasi-laminar textile behaves similarly to laminates (2D woven and braided), whereas non-laminar textiles presents generally though-thickness reinforcements to reduce delamination and have to respond to complex part geometry or triaxial loads (3D woven and braided). Tools have been developed to study and represent the internal structure of woven composites [38] or to assist the design of woven composite parts [39].

Models and theories are developed to predict the behavior and the mechanical properties of dry fabrics: they are based on experimental observations [40, 41], using numerical constitutive models and/or finite element methods [42–45], probabilistic theories [46], multiscale approaches [47] or the behavior under impact [48, 49]. Several modeling techniques of textiles have been recently reviewed by Vassiliadis *et al.* [50].

2.2.2 Manufacturing processes

2.2.2.1 Manufacturing process of a dry fabric

The manufacturing process of dry fabrics for fibrous composite materials begins with the choice of the type of fibers. Then, the fibers are grouped together to form an assemblage of filaments called a yarn. A yarn is generally constituted by several continuous, discontinuous, or twisted filaments, and it is commonly characterized by its number of filaments, their diameter and their packing density. Then, the yarns are interlocked and bonded together following specific patterns giving the final dry textile structure. Different textile processes are used to create woven, knitted, or braided fabrics. It relies on the use of particular interlacing patterns inducing the corresponding and characteristic yarn undulation. The regular interlacing of warp (0°) and weft (90°) yarns leads to the production of woven fabrics. Knits

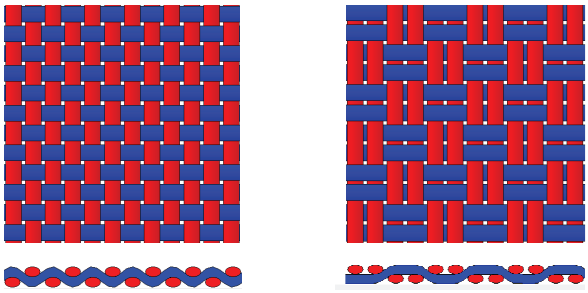

Figure 2.1: Illustration of the plain-weave (left) and twill-weave (right) textile structures

fabrics are usually made by interlooping one or more yarns. Braided fabrics are manufactured using a cylindrical mandrel leading to a tubular preform. The braided angle is a particular characteristic of the braided fabrics and it can be influenced by the controlling the different velocities of the braiding process [37, 51].

The present study is mainly focused on the 2D carbon fiber plain-weave and twill-weave fabrics (see Fig. 2.1). During the manufacturing process, a warp (0°) and a weft (90°) directions are defined. In the case of a well-balanced textile, the effective material properties of the composite material are similar. If different types of filaments are used for each direction, which refers to hybrid textiles, each direction will present particular mechanical properties.

2.2.2.2 Manufacturing processes of a composite laminate

Several processes are available to manufacture composite materials, as for example the pultrusion, the fiber winding, or the vacuum assisted resin injection (VARI), but both RTM and Prepreg processes are considered in the present study.

RTM manufacturing process The Resin Transfer Molding (RTM) manufacturing process of a composite material is a low pressure closed mold process. Dry fiber reinforcements are placed into a mold cavity being then closed and clamped. A catalyzed liquid resin is then injected into the closed mold impregnating thus the reinforcements preform. Then, the next step is the cure and eventually a post cure of the material at the suitable temperatures depending on the constituents. The main advantages of this manufacturing process are the fast cycle times, good tolerances of the parts, smooth sides and production capacity suitable for mid-volume production rates [35, 52, 53].

PREPREG manufacturing process Prepregs are composite materials, in which the reinforcements are pre-impregnated with a thermoplastic or thermoset resin matrix [54]. The complete PREPREG manufacturing process can be divided into two steps.

A first step consists in producing the pre-impregnated tape using one of the both following processes. The hot melt process allows to produce both fabric and unidirectional prepregs. It begins by placing a thin film of a heated resin on a paper substrate. Then, the reinforcement are laid on this film and after application of pressure and heat, the resin is impregnated into the reinforcement resulting in the final prepreg tape. This prepreg material is then wound on a cylinder to facilitate its storage and handling.

The second process, named the solvent dip process, consists in dissolving the resin in a solvent and dipping the dry fabric in this bath (process not suitable for unidirectional prepreg). Then, the solvent is evaporated using a drying oven resulting in the final prepreg tape [54].

The second step consists in achieving the lay-up of the final prepreg component by automated tape-laying or by hand lay-up processes.

The third step is represented by the cure of the laminate. The two main methods to manufacture prepreg composites are the vacuum bag/oven and the autoclave processes. For the vacuum bag technique, a vacuum bag is placed and sealed over the composite lay-up. The air under the bag is then completely evacuated. The system is afterwards placed inside an oven and the final composite material is produced after some curing cycles. A similar set up is used for the autoclave curing process but the oven is replaced by the autoclave. An autoclave can be defined as a pressure vessel allowing to control the different curing conditions. However, higher cure cycles are here required due to the thermal inertia of the system. This cure process allow to apply high pressures, which are required for the manufacturing of thick composites or complex shapes [55].

The main advantages of prepregs is their low manufacturing costs, a good control of the fiber content, of the resin impregnation and of the laminate thickness. It contributes in the production of a material presenting consistent performances.

2.2.2.3 Additional remarks

An interesting review of the resin impregnation of braided composites is proposed in [56]. The complexity of the woven internal structure coupled with the characteristics of the fabrication processes is likely to lead to inconsistencies in the material behavior. The effects of the RTM process deficiencies, characterized by local variations in the fiber volume fraction and change in the fiber orientation during the resin infusion have been studied in [57] particularly for the interlaminar toughness and delamination. For a plain weave composite laminate, the tension/transverse shear coupling can present a considerable effect on the stiffness properties of the laminate between in-phase or out-of-phase laminated woven structure see Fig. 2.2. In the reality, woven laminated composites present a random-phase structure where each layer can behaves as a single-lamina composite due to the growth of the interfacial debonding [58]. Prepreg laminates should minimize the presence of waviness in unidirectional composite tape. However, ply drops and ply joints could lead to a considerable loss of compressive strength of the material [59]. The effect of thermo-forming induced deformation on thermoplastic woven laminates has been experimentally [60] and numerically [61, 62] investigated by Hofstee. Fabrication process of fabrics can be also numerically simulated. It allows for example to study the influence of fabrication parameters or to predict accurately the geometry of the resulting material [63]. Once the geometry of the fabrics being known, micromechanical analysis can be conducted to determine the material properties of the composite as described below.

2.3 Study of fibrous composites from the lamina to the laminate

2.3.1 Multiscale analysis

A composite material can be investigated at three different levels: the microscopic, the mesoscopic and the macroscopic scales. Either a single lamina or the complete laminate can be investigated at each of

these scales. However, only a lamina or a single elementary ply is generally concerned by the microscopic level.

The micromechanical level of study of textile composites is represented by the observation of the local fiber bundle and the fiber arrangement in the R.U.C of an impregnated yarn [64, 65]. This step investigates the distribution of the constituents and it aims generally at determining the effective material properties of the material based on the different rules of mixture [66].

Then, at the mesoscale, impregnated yarns defining the architecture of the textile are considered [64]. It defines also the internal structure of the reinforcement (textile architecture and deformations applied during the part forming or loading), variations of the fiber direction and the fiber volume fraction inside the yarns [65]. The mesoscopic level is commonly characterized by the definition of R.U.C based on microscopic observations to predict material properties used on the macroscopic level. This level is essential to link together the microstructure of the material and its macroscopic behavior.

Regarding a single lamina, the macroscopic level investigates its macroscopic behavior. It defines for example its constitutive relations linking the stresses to the strains in each direction. It takes also into account the different conditions of symmetry (e.g. isotropy, orthotropy, anisotropy) to simplify the equations. Consequently, the elementary ply is seen here as a "unique" material having particular homogenized mechanical properties. Regarding the complete laminate, the macroscopic level investigates the behavior of the structure accounting for the different plies orientations and thicknesses. The macroscopic behavior of thin laminates can be predicted using the well-known Classical Laminate Theory (C.L.T) [67].

2.3.2 Prediction of failure

Laminated composite materials suffer from two main failure types: the intralaminar and the interlaminar failure. One of the main challenges for the dimensioning of structural composite parts is the prediction of failure and the identification of the failure modes.

2.3.2.1 Intralaminar failure

The intralaminar failure corresponds to the failure of the elementary plies, when the loads exceed the admissible strength. Different failure modes in tension, compression or shear can be observed and have to be identified. They depend naturally on the nature of the constituents and on the structure of the reinforcements. To predict failure of a lamina, failure criteria have been developed generally based on the effective strengths of the elementary plies. Excellent reviews have been published about the failure theories developed for fibrous composite materials [68–71]. The World Wide Failure Exercise [72] offers an interesting comparison between several failure theories for unidirectional and multi-directional laminated composites. Their capabilities and limits have been highlighted through comparisons with a large amount of on-axis, off-axis or bi-axial experimental tests. Considering textile composites, the failure criteria developed for non-crimp fabrics are not always able to account for all the effects leading to ultimate failure and few studies have a special focus on woven composites [65, 73, 74].

2.3.2.2 Interlaminar failure

The interlaminar failure, which refers generally to delamination, consists in the separation of two elementary plies at their interface. Delamination occurs, when too large out-of-plane stress (Mode I), shear

stresses (Mode II) or a combination of these both loads (mixed-mode) propagate in the structure. As a unique element layer modeling is used in the present study, no deep investigation of the interlaminar failure of textile composites will be made. Several studies have been conducted about the resistance to delamination of 3D textile composites but few works are published about the delamination in 2D woven composites. It is clear that further investigations should be conducted to assess the resistance to delamination of 2D laminated textile composites. The common double cantilever beam and end-notched flexure tests should allow to make some preliminary comparisons with the non-crimp fabric laminates regarding the different fracture energies leading to delamination.

2.4 Models for textile composite materials

2.4.1 Effect of fiber waviness

Fiber waviness is one of the major characteristic of a woven composite. The degree of waviness has an influence on the material behavior and different studies reported these effects. The effect of fiber waviness has been studied not only for woven, but for unidirectional tapes or laminates too. Different approaches have been used to study the effect of fiber waviness like analytic or statistic theories [75] as well as FE-models. In [76] it has been concluded that the degree of waviness affected the stress at which damage initiated but also the type of damage occurring in the material leading to the complex progressive failure process of a woven composite. Fiber waviness has a considerable influence on the compressive behavior of composites [59, 77]. It has been noticed that the compressive failure mode tends to become a matrix dominated mode due to the change of the fiber orientations induced by the wave amplitude. The compressive strength of unidirectional lamina seems to be more affected by the through-thickness waviness, than the one of woven composites.

Using FEM simulations, it is observed in [78] that elastic moduli, in-plane shear modulus and Poisson's ratio decrease almost linearly with increased waviness, probably due to the increase of resin pockets and resin content as waviness increases. On the contrary, the transverse shear modulus and Poisson's ratios increased almost linearly with increased waviness. Finally, the influence of the yarn waviness is more pronounced on the axial stiffnesses and strengths. The shear behavior being more resin dominated is less affected by the undulations [37].

2.4.2 Analytic models

As mentioned previously, a composite material presents its own mechanical properties, called effective material properties. Different analytic homogenization techniques are available to predict the stiffness and the strength of the material, as for example the well-known "rule of mixture". However, the particular complexity of a fabric architecture requires enhanced theories to predict the behavior of such materials. As the mechanical properties of textile composites mainly depend on microscopic parameters, micromechanical modelings are commonly used to determine them. Different methods have been used to predict the stiffness properties of woven composites. The most common method is based on R.U.C eventually coupled with the lamination theory [79–81] or accounting for manufacturing effects [82]. Other methods use a statistical approach like the Mori-Tanaka method [83].

2.4.2.1 Prediction of the extensional effective material properties

Three analytic models have been developed by Ishikawa and Chou [84]: the mosaic model, the fiber undulation model and the bridging model. In the one-dimensional "mosaic model", the impregnated woven fabric is considered as an assembly of asymmetrical cross-ply laminates but it does not account for the yarn undulation and yarn continuity. The "fiber undulation model" considers the fiber undulation and continuity, and the C.L.T is applied on each infinitesimal piece of the unit cell, where the local stiffness depends on the local off-axis angle. These two models are adapted for plain weave fabrics, whereas the "bridging model" has been developed to study of mechanical properties of satin composites. In this last model, the hexagonal shape of the satin weave unit cell is simplified by a square shape. Then, this R.U.C is divided in several regions assimilated to either cross-ply laminates or interlaced structure. Through these models it has been concluded that the in-plane elastic stiffness of fabric composites is lower than the one of cross-ply laminates. The non-interlaced regions linking the interlaced regions together in a satin composites are called "bridging regions", because they play the role of "load transferring bridges", which increases the elastic stiffness of the material compared to plain weave composites. An important feature of the "bridging model" is that the stress states in the constituents are correlated with the overall applied load on the material.

In [85] Naik and Ganesh developed two 2D analytic models to predict the elastic properties of plain weave composites, considering the undulation and continuity of strand in both warp and weft directions, as well as the gaps between adjacent strands. One model divides a R.U.C into slices along the loading direction (referring to the slice array model). The different slices are analyzed separately and their properties are then assembled under iso-strain conditions to determine the elastic properties of the R.U.C. The second model divides the R.U.C either along or across the loading direction into slices. The slices are subdivided into elements that are separately analyzed and then assembled in series to obtain the slices' elastic properties (referring to the element array model). Finally, these slices properties are assembled to determine the elastic properties of the R.U.C.

In [86] N.K. Naik proposed a two-dimensional analytic model to predict the thermo-elastic properties of a plain weave fabric laminae. He considers the undulation and continuity in warp and weft directions, the volume fraction and the gap between the yarns. From a representative unit cell , an idealized unit cell is defined being constituted by a three-plies laminate, one layer as a pure matrix ply and two layers as unidirectional (U.D.) laminae with the adequate orientation. The cross-section and the undulation of the yarns are defined by shape functions, where the parameters account for the potential gaps between the yarns. Local compliance constants depending on the undulation angle are averaged over the length to obtain the effective compliance of the yarns. The C.L.T is applied to the unit cell but the theory considers only extensional deformation (no bending). Circular and sinusoidal yarn paths are investigated and it comes that the sinusoidal function model was more realistic. The method requires the material properties of the constituents and geometrical parameters, that can be observed using a microscope. In [87] a "NDPROP" model has been developed based on photomicrographs and being able to account for the through-the-thickness material characteristics.

An analytic 3D geometric model has been developed by Vandeurzen *et al.* [88] and implemented in a

Microsoft Excel Office Application to predict the stiffness and strength of woven composites. The model is based on three types of geometrical parameters that are the "know-group" parameters coming from the textile manufacturer, the "measure-group" parameters coming from experimental observations and measurements, and the "calculated-group" parameters being calculated using analytic equations involving the two previous parameters groups. A R.U.C of textile composite is then divided in macro-cells (macro-partition of the unit-cell) and it is split into two layers in the thickness direction. Then, macro-cells are divided into micro-cells (micro-partition process) to better analyze the variations of mechanical properties in the unit-cell. Finally, libraries of macro-cells have been created to serve as basis for the study of complex material structure, even if the authors recognize themselves, that some of their assumptions are not always representative of the reality. They used the model to predict stiffness engineering constants, local fiber volume fraction and yarn orientation reporting good results for the Young's moduli but difficulties to obtain accurate shear moduli [89].

In [90] Walsh and Ochoa developed three-dimensional surface equations to represent the fill and warp tows. The R.U.C is segmented and the different coefficients of the stiffness matrix are determined analytically and then homogenized to obtain the properties of the unit-cell. In [91] a selective averaging method is developed to predict the stiffness matrix of a woven composite. It is based on a division into slices of the R.U.C for a mesoscale representation and each slice is divided into sub-elements for a microscopic analysis. The different columns of the macroscopic stiffness matrix are then determined successively. The results show a good prediction for the extensional matrix but over- and underestimations for the bending matrix.

In [92–94] Naik and Shembekar study the effect of lamina thickness and fiber undulation on the in-plane elastic constants of woven fabric composites. The two-dimensional models give good correlation with the experimental results, whereas one-dimensional models show discrepancies. Huang [95] uses a bridging model [96–99] to characterize the elasto-plastic and ultimate strength behavior of composites reinforced with woven and braided fabrics. The composite failure is reached, when one of the constituents failed. The assembly for the full composite of the overall stress states in the different subdivisions is made using the iso-stress assumption (overall stress in each sub-element is the same) and a good correlation with experimental data is obtained. Each sub-element is constituted by at most four layers: pure matrix at the top and the bottom and two yarns in the middle. The sub-element is then sufficiently small to be regarded as a U.D. composite ply in its local coordinate system. The assembly of the U.D. composite properties leads to those of the sub-elements before the second assembly determines the properties of the R.U.C [100]. It is noticed that the inter-yarn gaps have a considerable effect on the effective stiffness of woven composites.

Donadon *et al.* [79] develop a 3D analytic micromechanical model for the prediction of the elastic behavior of a hybrid carbon/glass plain weave. The model is based on the C.L.T, on the shape functions developed by Naik [92] and it is adapted to account for the asymmetrical structure of the material. A good correlation with experiments is obtained for the in-plane properties but the out-of-plane stiffness is overestimated. On one side, some limits in the C.L.T due to the lack of assumption regarding the through-the-thickness behavior could be responsible for these discrepancies. On the other side distortions in the fabric layers and microscopic defects could explain the small differences in the prediction of the in-plane properties. As a conclusion it seems that the C.L.T is not able to predict through the thickness behaviors

and the use of a simple rule of mixtures is suggested.

Scida *et al.* [101] develop the MESOTEX analytic micromechanical model to predict the in-plane properties of hybrid and non-hybrid woven composites. It is based on the crimp model developed by Ishikawa and Chou and the R.U.C is divided in many slice regarded as small pieces of U.D. lamina. A good correlation is found with experiments for plain, satin and twill weave structures and a enhancement of the model to the prediction of out-of-plane properties has been proposed [102].

Homogeneous stress and strain distributions are generally assumed in the micromechanical theories mentioned above but non-uniform stress states determined using the C.L.T have been considered by Karkkainen in [80]. Extensions and curvatures (with consideration of bending moments) lead to the calculation of the strain and stiffness coefficients of a R.U.C. The failure analysis is made by defining a quadratic failure criterion close to the Tsai-Wu theory but based on the corresponding maximal forces. The results show a significant influence of the moment resultants and fiber tow failure is identified as a major failure mode among the failure envelope.

Longitudinal and transverse stiffness and strength are often the main focus of micromechanical theories but the shear stiffness and strength have to be investigated too. In [103] Ganesh study the influence of strand width, strand thickness, inter-strand gap and the corresponding fiber volume fractions on the both shear properties.

Matsuda *et al.* [104] developed a method to reduce the domain of analysis for plain-woven laminates. They used the point-symmetry of in-phase and out-of-phase woven. The viscoplastic behavior of the studied GFRP woven composite material was found to be affected by the differences of phase in the material structure. In [105] Gupta reported that the unit cell length and the undulation length were higher for a woven composite ply embedded in a multi-layer laminated structure than in the case of a single ply lamina. Moreover, the lamina thickness and the gap length were also lower in multi-ply laminate due to consolidation and nesting from the adjacent plies. Consequently, the overall fiber volume fraction in a unit cell is likely to vary considerably for multi-ply woven composites.

Special tools conglomerate integrating meso- and macro-analysis are developed, based on Wise Tex and TexComp packages as reported in [106]. Moreover, Lomov *et al.* propose a "road map" to conduct meso-analysis [65]. It begins with the construction of the internal geometry of the reinforcement (using for example Wise Tex) before transferring to a volume description and meshing. Then, local material properties of impregnated yarns and matrix are assigned and a R.U.C is defined based on symmetry properties. Finally, boundary conditions are applied before starting the homogenization (ANSYS) and eventually a study of damage initiation and propagation. In this paper damage initiation is predicted using the Hoffman's criterion. An anisotropic damage model is defined for the fiber bundles, whereas an isotropic one is used for the resin. Good correlation with experiments is obtained for the damage onset prediction but a non-physical behavior is observed in the study of damage propagation because damage propagates across the yarn instead of only along the yarns.

Finally, interesting reviews about some developments of numerical methods and models for the prediction of the textile composites material properties have been published by Tan *et al.* [36] or Cox [37].

2.4.2.2 Prediction of the bending properties

As reported above the in-plane and more rarely out-of-plane properties of woven composites are studied using different analytic models and methods but the bending behavior of textile composite is not so extensively investigated. Soykasap [107, 108] shows, that significant errors appeared in the flexural properties of thin plain-weave composites, when the C.L.T is applied. An error up to 200% is found for the bending stress and strains, whereas an error up to 400% occurred in the prediction of the bending stiffness. A potential cause of this phenomenon is that the C.L.T assumes a uniform fiber and matrix distribution in each lamina. However, a thin fabric lamina consists in fiber bundles much thinner than the overall thickness and in a non-homogeneity through the thickness. Under high curvatures, longitudinal fibers undergo localized deformations leading to nonlinear behavior of the bending stiffness and strains. Thicker laminates having more than two plies show a better correlation between the prediction and the experiments. In [109] Allison remarks a variation in the bending strength in function of the waviness and it has been reported that the dominant failure mode of U.D. wavy composites under bending is an interlaminar shear leading to microbuckling. The stiffness reduction under bending is more significant if the waviness occurs in plies playing a major role under this loading path [110]. In [111] it has been remarked that for GFRP-woven the flexural strength determined from 4-point bending test is higher than that from the 3-point bending test. For a "unidirectional" woven, the failure started at the tension side and in the case of 4-point bending specimen the cracks initiated at one load point and then propagated toward the second one.

2.4.3 Numerical models

Finite element methods (FEM) are also regularly used in order to solve complex structural engineering problems. A conventional method to predict the mechanical properties of textile composites using FEM consists in dividing the composite structure into unit cells and then reconstructing the entire reinforcement geometry through the assembly of unit cells [36]. In [112] and [113] Cox *et al.* develop for ABAQUS a finite element model called the '"binary model" to simulate the elastic behavior of 3D textile composites. Line elements with axial rigidity represent the axial properties of the tows, whereas solid elements can model Poisson's, transverse and shear stiffness effects. However, anisotropy and heterogeneity of the material structure caused by voids or resin concentrations are not considered. In [114] the authors describe a double homogenization procedure based first on the yarns with the assumption of a regular fiber distribution in the yarn and then extended to a representative volume, where a regular arrangement of the yarns is assumed. Whitcomb [78] develops finite element models to determine the effect of tow waviness on effective moduli, Poisson's ratios, and internal strain distributions. The use of coarse models does not show differences in the prediction of elastic moduli in comparison with fine models but more discrepancies are observed for the study of the Poisson's ratios. In addition to the observations made on the effect of fiber waviness (see 2.4.1), he notices large strain gradients in the material, which suggests that damage initiation occurs at a significantly lower global strain than for a traditional cross-ply laminate.

Based on global average strains, local/global finite element methods are developed to determine the global stress state. It starts from global average strains of a R.U.C and it computes local strain and stress states in subcell systems before a homogenization to return then on the global scale of the R.U.C [115].

In [116] a simplified model is proposed but under- and overestimations in the prediction of the engineering constants are observed. The increase of the number of subcells (until a minimum about 10 subcells) improved the convergence of the results. A global-local approach is well defined and detailed by Whitcomb in [117]. It consists basically in solving a global model, which defines the boundary conditions (generally displacements) for the local model. Corrections for the update of the global displacements can be applied.

In [118] a finite element analysis model is developed to determine the elastic constants of plain weave composites using a sinusoidal yarn model and an analytic model is presented to predict the failure strength of such materials. It has been noticed that the elastic constants are related to the overall fiber volume fraction, whereas the failure strength can be related to the fiber volume fraction of the yarns.

In [119] a 3D micromechanical finite element model is presented to predict the material properties of twill-weave composites. The analysis is conducted using ANSYS. The model is based on the definition of a R.U.C of the material and it incorporates a thin matrix layer between the warp and weft yarns. A homogenization procedure is then used to predict the different elastic properties as follow: only one constant non-zero component of strain is applied on a particular surface of the R.U.C that leads to nodal forces. An average macroscopic stress is then obtained dividing the sum of the nodal forces by the corresponding surface, where they act. Putting the calculated stress and initial strain condition in the stress-strain relations allows to find progressively all the stiffness coefficients of the material.

In [120] the authors develop a micromechanical model in Abaqus to study the behavior of twill-weave composites under bi-axial loading. In the R.U.C, tows and resin are modeled using 3D elements. The resin material is assumed to be isotropic and is modeled using a linear Drucker-Prager model to capture the pressure-dependent yield and the different yield responses under tensile and compressive loading. The model accounts for a possible debonding between tows and matrix and a quadratic stress criterion (based on normal and shear tractions at the interface) is used to detect the damage initiation. Failure is predicted using a maximum stress criterion and/or a physically-based kinking model for the longitudinal compression. The study of out-of-phase (OP) and in-phase (IP) laminated structures (see figure 2.2) shows that the support provided by the adjacent layers has a more significant effect on strength than on stiffness, and the effect is more remarkable for the compressive strength than for the tensile one. A stiffer behavior is noticed for OP structures with a difference about 5-6% compared to the IP case. Finally, the model is used to predict the in-plane bi-axial failure envelope of the material, where the scatter in the predictions between IP and OP cases (particularly when compressive loads are involved) should rely on the lack of control on the shifting between adjacent plies. In [121] the authors make with ABAQUS two-dimensional (length over thickness) micromechanical finite element analysis neglecting the effect of through-width variations. They report a lower stiffness for out-of-phase laminates than for in-phase laminates with an intermediate stiffness for staggered laminates, which differ from the conclusion reported in [120]. They also remark an increase of the energy release rates associated with crack formation if bending deformations occur in the laminates. In the case of large degrees of bending, a nonlinear analysis seems to be required to accurately predict the energy release rate.

In [122] Barbero *et al.* use ANSYS to determine the elastic moduli of plain weave composite. It based on photomicrographs and a mesh is constructed starting from geometric models and using solid elements. Transversely isotropic material properties are assigned to the tow elements and isotropic properties are assigned to the matrix elements. The material properties of the tows are calculated using micromechanics

(a) In-phase (IP) (b) Out-of-phase (OP) (c) Random-stacked

Figure 2.2: Illustration of the relative shift between adjacent plain-weave layers

depending on whether the fibers are isotropic or transversely isotropic.

2.4.4 Extension to the mesoscopic and macroscopic levels

As reported above, microscopic analysis of textile composites are extensively used to predict the mechanical properties of such materials. However, to capture the global behavior of textile composites, mesoscopic up to macroscopic investigations have to be conducted. One of the main aims of such works is a study based on unit-cells coupled with the capability to consider additional effects like voids or initial damage without increasing the geometry complexity of the model. In [123] a X-Ray tomography is used as experimental basis and the authors put in evidence the importance of the initial geometrical model, the precautions to respect in order to conduct mesoscopic experiments and the interest to obtain numerical results on a mesoscopic and macroscopic scale, what is very interesting for the engineering and industrial applications. Mesoscopic analysis coupled with FEM and damage mechanics work successfully as reported in [124] highlighting also the challenges in mesh building and local phenomenons.

Some authors make multi-scales approach to predict the mechanical behavior of composite materials. In his PhD [125], Couegnat develops a numerical model based on the material properties of the constituents and he implements it in the finite elements solver ZeBuLoN. A microscopic analysis of the material leads to the construction of the woven preform geometries. R.U.C are then generated and meshed defining thus the mesoscopic study of the material. Effective properties are determined for a damaged state and a periodic homogenization procedure allows the calculation on large meshes.

2.4.5 Discussion

As described above, analytic and numerical micro-mechanical studies are often based on R.U.C. Its geometrical characteristics can be determined from microscopical observations or/and using results from draping simulations [126]. Different techniques of homogenization and analysis approaches have been reviewed. It has been noticed, that most of them are focused on the determination of elastic modulus, of the strength and of the influence of diverse material or geometrical parameters on the effective material properties. Few of them are studying the material behavior including progressive failure. From an industrial point of view, micro-mechanical analyses are useful to understand the progressive failure phenomenon occurring in complex material internal structures like textile composites. They can also be used to predict stiffness and strength properties of the textile composites reducing the number and consequently the costs of experimental campaigns. However, the study of such material under crash loads requires the knowledge of additional material properties or characteristics (delamination, post-failure damage, strain-rate dependency, fragmentation or matting effects). Moreover, structural parts, particularly in the automotive field suffer from complex geometries, that are influencing considerably the reinforcements shapes and/or the material behavior at these locations. Due to the limitations imposed by the industrial

field such effects can only be represented on a macroscopic scale because micro-mechanical investigations are too expensive. That is why specific tools and analysis have to be developed to capture numerically the mechanical behavior of textile composites on a macroscopic level. The different smoothing effects on the stiffness inducing nonlinearity, or on the strength modifying the failure envelope of the material have to be considered in a global approach aiming at finding an adequate compromise between efficiency, accuracy and reliability of the predictions.

2.5 Material behavior, prediction of failure and damage

In this section, the particular material behavior of textile composites observed in different studies is described. It has to put in evidence the validity or the obsolescence of the modeling of such materials using linear elastic constitutive laws. A review of the main theories and criteria used for the prediction of the failure of textile composites is also presented. A discussion about the modeling of the mechanical behavior, failure, damage and permanent deformation will follow keeping in mind the application in the industrial field and crashworthiness.

2.5.1 Observation and prediction of the material behavior of textile composites

On one side, woven fabric composites present generally a good dimensional stability in the two main in-plane direction, and high out-of-plane strength. They are thus able to carry the secondary loads due to multi-directional load paths or buckling. On the other side, they show anisotropy and they exhibit generally a low shear rigidity and resistance contributing to their good draping capability [36]. The frequent yarn's changes of position from top to bottom in a plain weave composite reduce their overall strength and stiffness [37]. In [127], experimental tests on a plain weave composite show a linear behavior of the material under tension and a characteristic nonlinear behavior in shear controlled by the properties of the matrix. It is also remarked for plain weave composites, that the elastic modulus increases with the laminate ply number [128]. In [129], the authors study the effect of stacked layers on the stiffness of woven composites. In the case of a carbon plain weave with unsaturated polyester resin, a more linear behavior is observed for the multi-layered material compared to a single layer coupon that depicts a clear nonlinear behavior. It is due to the fact that multi-layered composites have unconstrained deformations in the through-the-thickness direction. Consequently, for micromechanical analysis and material properties predictions, such composites can be studied under iso-strain assumptions for the in-plane deformations and iso-stress assumptions in the third direction.

In [37] on-axis and off-axis tensile tests show the particular stress-strain behaviors of plain weave carbon/epoxy laminates under tension: a linear behavior is observed for a tension in the warp and weft directions, whereas a clear nonlinear plastic behavior is captured for the off-axis direction of tension. It is also reported that textile composites offer generally a notch insensitivity in both tension and compression because the material structure seems to redistribute loads from the notch to the entire material reducing stress concentration and minimizing the degradation of the ultimate strength. If carbon woven laminates exhibit a linear behavior in longitudinal tension, glass fibers woven composites can show a noticeable nonlinearity under longitudinal loads and a knee in the stress-strain curves caused by the start of trans-

verse cracking of the matrix [130]. It leads to a macroscopic nonlinear behavior, that has to be properly characterized and predicted.

The behavior of different Kevlar and glass fiber woven epoxy composites is investigated in [131]. The authors put in evidence the undesirable effects on the material properties induced by resin rich regions comparing the interlaminar fracture toughness of classical woven composite with the one of materials containing microfiber inclusions. Kevlar woven composites exhibit a quite-linear tensile behavior, whereas glass fibers textile composites depict a strong nonlinear behavior. It has been concluded that due to the anisotropy of the Kevlar fibers the transverse yarns does not play an important role. On the contrary, progressive matrix damage and debonding occurs in the transverse direction for glass woven composites leading to the stiffness softening. For bending load, a failure on the tensile side is observed for glass fibers, whereas a failure on the both sides characterizes the Kevlar woven composites.

Multiple sources of nonlinearity can be identified for woven composites: a material nonlinearity due to nonlinear constitutive behavior of the matrix constituent, a material nonlinearity due to progressive failure and stiffness reduction, and a geometrical nonlinearity due to straightening of the wavy tows under tensile loading [132, 133]. Moreover, Ryou *et al.* reports that woven composites are generally characterized by an asymmetric behavior between tension and compression, a rate dependency and an anisotropic and nonlinear material behavior [45]. The nonlinear behavior coupled with plastic deformation is found being larger for glass fiber than carbon fiber for a 2x2 twill weave braided composite [134]. This plasticity has to be distinguished from nonlinear elasticity because it does not arise from the motion of dislocations as in a metal but it results from microcracking due to the noncrystalline structure of a polymer [37]. The importance of plasticity on the strength of composite materials, particularly for off-axis loading or low-stiffness reinforcements has been also studied in [135]. A transversely-isotropic elastic-plastic constitutive model for unidirectional fiber reinforced plastics has been developed in [136]. The model is able to represent the fully nonlinear mechanical behavior under multi-axial loading conditions. The yield surface material parameter could be identified using the hardening curves (yield stress vs. plastic strain) of each stress state. Then, in order to predict failure onset and propagation, a three-dimensional smeared crack model has been developed [137].

Few macroscopic material models are developed to predict the nonlinear behavior of woven materials. In [138] an orthotropic plastic material model is proposed to capture the nonlinear stress-strain behavior observed for off-axis tensile tests on GFRP-woven composites. It is based on a three-parameter plasticity formulation, where a plastic deformation is detected using a quadratic yield function. A simplification to a one-parameter plasticity model is also proposed. The theory is inspired from the model developed in [139] but assuming plasticity in all directions including in the direction of the fibers. The results put in evidence a considerable contribution of shear stress in producing plastic deformation and highlight similarities for the warp and weft directions. In [140] Hochard *et al.* adapt models based on damage mechanics that are developed for unidirectional plies to predict the mechanical behavior of textile composites up to failure. An elastic brittle behavior is defined for the warp and weft directions, whereas a nonlinear with progressive damage model coupled with inelastic strains (plastic hardening model) is used for the shear. The input data of this one-damage-parameter model is based on material characterization tests.

Finally, glass fibers textile composites depict a more nonlinear behavior in all directions than the

carbon fibers woven laminates that present a linear or a light nonlinear evolution in the main two in-plane warp and weft directions. This nonlinearity should be coupled to a permanent deformation definition to account for the irreversible damage occurring in the material. A review about the progressive failure and damage theories for textile composites is proposed in the next section 2.5.2.

In [141] a continuum model for the macromechanical prediction of the elastic-plastic behavior of woven composite is presented. The Tsai-Wu failure criterion is used as yield function and instead of degrading the effective undamaged stress, a scalar hardening parameter function of the applied stress state is defined but it has to be determined experimentally. In [40] an experimental and theoretical investigation of the shearing properties of plain weave fabrics and prepreg is conducted. It is remarked that the changes in the resin properties modify the shear behavior, but that both dry and impregnated fabrics depict a similar parabolic shear deformation behavior. An analytic shear model, where yarns are modeled with beams is proposed. It gives good results for the prediction of the elastic modulus but it seems to be very sensitive to the yarn thickness and to the empirical spring constant. In [133] d'Amato studies the nonlinear behavior of a triaxial textile composites. A 3D representation of the textile structure puts in evidence the progressive variation of the yarn waviness and it shows the textile global stiffness variations. Based on this results global models of textile are developed based on beam elements and the elastic properties of the yarns.

Tabiei [142] develops a micromechanical finite element model as UMAT in Abaqus to determine the behavior of woven composites. Based on R.U.C approach the model divided the R.U.C in subcell in order to determine the characteristics of an equivalent homogeneous anisotropic material, which constitute the input data for simulations with the commercial code. The nonlinearity is induced by the properties of the resin. The model relies on a stress/strain averaging procedure, where the aim is to determine the total stresses in the subcells starting from the global average strain. Then, the strain increment and the total strains in each subcell are calculated and total stress for each constituents of the subcell can be determined leading to the determination of total stresses of the subcell.

The study of the stiffness and stress-strain behavior of a material is generally based on coupon tests like tensile tests. Until now, strain gauges have been extensively used to measure the strains. However, particularly for heterogeneous materials like textile composites it is likely to capture too localized strain measurements, whereas the strain distribution over the material is more complex causing discrepancies between the behavior observed on small specimens and the one observed on larger parts. Nicoletto *et al.* [143] use thus the digital image correlation technique (D.I.C) to study the full-field strain distribution in a twill-weave CFRP under in-plane loading. The results show a considerable strain non-uniformity with local strain concentrations correlated to the yarn architecture, what requires to define homogenization procedure to determine the macroscopic longitudinal strain representative of the lamina response [144]. The experimental results have been compared to numerical results of fine finite element model of a unit cell (more than $80,000$ brick elements) showing a good correlation.

2.5.2 Failure and damage

Some authors [145] reported that matrix cracking in a resin pocket on the fiber/matrix interface could be the first form of damage found in textile composites. If the load increases the crack propagates to neighboring tows, which causes high stress concentrations at the interface responsible then for tow rupture. This capacity to bear load even after rupture indicates that significant deformation can develop without catastrophic failure. It can explain the difficulties encountered and reported in several aforementioned papers to predict the failure of woven composites. Consequently, specific failure criteria and damage models have to be developed for this kind of materials to better predict their both mechanical and failure behavior. Analytic and numerical damage and failure models are reviewed in this part.

2.5.2.1 Analytic models

In [146, 147] Naik and Ganesh develop 2D models to predict the failure strength of plain weave fabric laminates under on-axis uniaxial tensile loading and they study the effect of fabric geometry on the failure behavior. Different types of failure such as warp strand transverse failure, fill strand shear /transverse failure, pure matrix block failure and the failure of matrix and fiber in the fill strand in longitudinal tension are considered, as well as material and geometrical nonlinearity. They notice that the fabric geometry (yarn width, yarn thickness or yarn gaps) can affect significantly the shear strength and modulus. Moreover, an increase in the overall fiber volume fraction leads to an increase of the strength. On the contrary, a large crimp of yarn increases strain concentrations leading to a reduced strength especially for glass fiber and less for carbon fiber. Kim *et al.* [148] study the in-plane tensile and compressive strengths of carbon/epoxy plain, twill and satin weave composites fabricated by employing a vacuum infusion process. The dominant compressive fracture mode of laminate and textile composite is identified as a fiber microbuckling, but the authors noticed a detaching of the longitudinal and transverse yarns occurring at a stress level lower than the critical stress causing fiber microbuckling. Under tensile loads the longitudinal yarns are compelled to decrease the amplitude of waviness. The failure is not induced by the detachment of yarns but it takes place, when the multiaxial stresses in the material satisfy a failure criterion. To predict the strength of the woven, the authors developed two equations as increasing functions of the radius of curvature of yarns:

$$\sigma_{\mathrm{c}} = k\frac{\rho_{\mathrm{m}}}{\pi a}\sigma_{\mathrm{m}} \text{ the compressive strength} \tag{2.1}$$

$$\sigma_{\mathrm{t}} \simeq \sigma_{\mathrm{t0}}\left[1 - \frac{1}{8}\left(\frac{\pi\sigma_{\mathrm{t0}}a}{\sigma_{\mathrm{y0}}\rho_{\mathrm{m}}}\right)^2\right] \text{ the tensile strength (based on the Tsai-Hill fracture criterion)} \tag{2.2}$$

$$\rho_{\mathrm{m}} = \frac{L^2}{a\pi^2} \text{ the radius of curvature of yarns} \tag{2.3}$$

where k is the areal fraction of the longitudinal yarns in the cross section of the woven laminate perpendicular to the loading direction, a the radius of the yarns, $2L$ the wavelength of the yarn undulation, A the amplitude of the yarn undulation, σ_{m} the tensile strength of the matrix, and σ_{t0} and σ_{y0} the strengths of the U.D. composite under pure longitudinal tensile and transverse compressive loadings. Both strengths increase when ρ_{m} increases.

The detaching of the yarn mentioned in [148] is assimilated to a delamination failure mode in [149], where Yang *et al.* remark also a compressive strength 15% higher for non-crimp [0/90°] laminates than for woven fabric induced by the yarn waviness. A kinking phenomenon [150–152] is observed for braided composite under compressive loads in addition to microbuckling [153]. The compressive strength is although influenced by the geometrical imperfections of the axial tows and matrix nonlinearity. *In situ* matrix property corresponding to residual stresses and heterogeneity of the material properties due to non-uniform temperature distribution by matrix curing (particularly for resin molding fabrication processes) would give a softer compressive behavior of the material. Naik *et al.* [154] develop an analytic model for the compressive behavior of plain-weave fabric composites under uni-axial on-axis loading based on curved beam elements in an elastic state. They study thus the influence of different model and geometrical material parameters on the elastic modulus and compressive strength. The plastic microbuckling of the load bearing tows is identified in [155] as the major failure mechanism in woven composites. The authors showed although the high damage tolerance of woven and their low compressive strength due to a large fiber misalignment. To summarize, it seems that quasi-laminar textile composites presents a complex compressive failure as a combination of shear plasticity or kink band formation with delamination and buckling [37]. It could explain the common difficulties encountered to measure the compressive stiffness and strength of woven composites [156].

Gao *et al.* [157] propose a closed-form formula to determine the effective Young's modulus of damaged woven laminates. Three damage modes are considered (transverse yarn cracking, interface debonding and sliding with friction) and the complexity of the formula depicts the difficulty to predict the stiffness reduction in a quantitative manner. Naik [158] remarks that the tensile strength is not significantly influenced by the use of twisted yarns up to a certain twisting angle.

R.A. Naik [159] implemented in the TEXCAD code an analytic formulation to predict the three-dimensional thermal and mechanical properties, damage initiation and progression and the strength of woven and braided fabric reinforced composites. The technique is based on repeating R.U.C assuming a lenticular cross-section of the yarn. The R.U.C is then divided into slice depending on the geometry and iso-strain states have been assumed. Fiber dominated failures are predicted using a maximum strain criterion, whereas matrix dominated failures are determined using a maximum stress criterion. The stiffness reduction scheme described in [127] has been applied to model the damage. The material failure occurs, when axial yarns failed or if all yarn slices fail in the same failure mode. The nonlinear shear behavior is depicted using a three-parameter equation having a close formulation to the Ramberg-Osgood equation. The results showed, that a small variation in the fiber volume fraction does not affect the shear strength, but it had an influence on the tensile and compressive strengths. Moreover, it is reported that the composite stiffness and strength properties are governed by weave architecture, yarn sizes, yarn spacing, yarn crimp, stacking orientation, overall fiber volume fraction and the constituents' properties.

Starting from the development of a new geometrical modeling method [160], the thermo-elastic material constants, progressive failure behavior, and strength of 2D woven are investigated using analytic/numerical models [132]. The in-plane stiffness coefficients are evaluated using iso-strain assumption in the R.U.C. The progressive failure analysis is based on an element stiffness reduction procedure and the strength is determined based on the maximum stress criterion. The theory assumes iso-stress load distribution in a bending restrained R.U.C. The methods seems able to predict the influence of the sensitive and linked-together parameters that are the fiber volume fraction and the gaps. In [51], Chretien

determines the equivalent three-dimensional elastic moduli of plain weave and other textile composites using unit-cell and constitutive models. He implemented different predictive models as UMAT in Abaqus to compare them and he considered a progressive failure analysis [161] to study the different material failure mechanisms.

2.5.2.2 Numerical models

Progressive failure theories are also used at the micromechanical level to predict the behavior of woven composite [162]. In [163] a progressive failure model is implemented in Abaqus. The Tsai-Hill criterion detects the failure onset and a ply-discount method is defined as progressive failure of the laminate. Acceptable results are obtained in terms of maximal load peak and nonlinear behavior. A good review and discussion about the progressive failure theories of composites materials have been presented by Tay *et al.* [164].

In [165] the authors propose a three-dimensional heterogeneous finite element model coupled with an anisotropic damage model based on the reduction of the effective stress in the fictitious undamaged configuration. The damage parameter is correlated to the effective area reduction caused by cracks and voids and it is initiated by reaching the Hoffman's failure criterion [166]. Tabiei and Ivanov [167] develop a computationally-efficient micro-mechanical material model for woven composites based on a repeated R.U.C approach. The R.U.C of the woven composite is extracted from the deformed material pattern with consideration of fiber reorientation and it is divided into four sub-cells. When failure is detected, a degradation scheme [127] is applied on the stiffness of the constituents. Then, the homogenization procedure, implemented first in MATLAB [168], begins with the homogenization of the constituents properties at the sub-cell level and it goes on with the homogenization of the material properties of each sub-cell on the R.U.C level. Finally, the material response of the material can be calculated. The shear nonlinearity is accounted for using a Ramberg-Osgood formulation. The material model is implemented in LS-DYNA for shell and solid elements as user defined subroutine and a good correlation with experimental results is obtained.

In his thesis, Ivanov [64] uses the Puck's failure criterion to predict the damage initiation. He defines then a damage propagation law based on the energy release rate theories and meso stress-strain analysis. He concludes, that the definition of a critical stress is not clear for woven composite due to the combination of many failure and deformation mechanisms. The heterogeneity and complexity of the structure can induce cracks at small deformation and it implies, that they propagate in "short shots but not crossing the full length of the specimen" as observed in unidirectional laminates. It implies also, that the prediction of a failure mode requires the modeling of damage development. For textile composites, plasticity and micro-damage are linked together and difficult to separate experimentally despite their different physical origin and they represent the first level of damage process. Then, matrix intra-ply and intra-yarn cracking occur followed by inter-yarn and inter-ply delamination until the catastrophic failure caused by the rupture of the fibers. Ivanov reports that the random shift between the layers during the fabrication should be accounted for because it resulted in significant differences in the local stress distributions.

In [74] the authors present a novel orthotropic failure criterion to model non-crimp fabric single textile layers. The criterion is based on an orthotropic elasticity law and invariant coefficients. It leads to a system of nine equations with nine independent parameters, that can be experimentally determined. A progressive failure analysis is proposed following a multiscale approach [73], where fiber and matrix are

modeled at the microscale using a randomized distribution in the R.U.C. Homogenized properties are obtained and they are then used as an input for the mesoscale, where the influence of reinforcement shapes is studied, leading to the determination of the stiffnesses and strengths of one single layer. Finally, the failure criterion is applied at the macroscale coupled with a damage and degradation model to predict the progressive failure of the material. The model is based on periodic boundary conditions for the calculations on the R.U.C. In his thesis [169] Crookston develops micromechanical models to predict the initial failure and the properties of unidirectional and woven fabric composites from the properties of the constituents and the C.L.T is used to study laminated structure. He considers also draping simulation to account for the reinforcement deformations during the manufacturing processes.

2.5.2.3 Notched textile composites

The influence of a hole on the strength and behavior of composites is also investigated to study the damage initiation and propagation in unidirectional or multidirectional laminates [170,171] and for textile composites [172]. Specimens with moulded-in hole exhibit a large failure strength and strain (up to 30%) but a lower initial stiffness than those with drilled hole under loading in the fiber direction. A load in shear does not allow to observe many significant differences between the two configurations [173–175]. In [176], the authors remark that the behavior of woven composites changes with the size of the holes. It is due to the fact, that a reorientation of the fibers occurs in the case of small diameter holes, whereas a stress-concentration effect is predominant for large diameter holes. In [177] they study the effect of the stacking sequence on the notched strength. The "undirectional" woven laminates present a higher unnotched strength than quasi-isotropic woven laminates but the phenomenon is inverted for the notched specimen. They remark also that the notch sensitivity of quasi-isotropic textile composite laminates can be reduced by placing the 45° plies near the mid-plane and dispersing the 0° plies with the 45° plies. In [178] the authors study numerically and experimentally the influence of moulded-in hole on a 2x2 twill-weave carbon epoxy material. The simulations are made with ANSYS and a streamline function is used to model the fiber configuration around the hole as in [179]. It is observed that a tensile matrix failure occurs initially at the edge of the hole. The damage propagates then across the cross-section of the laminate and a transfer of the load to the longitudinal yarns occurs. A tensile fiber failure is identified as the critical failure mode of the material. An increase of the notched strength is also highlighted with the increase of the hole size and an acceptable correlation between predictions and experiments is obtained (the proposed method lightly overestimates the notched strengths). Finally, the size and the creation of the hole (moulded-in or drilled) as well as the stacking sequence play an important role on the notched strength of textile laminates.

2.5.2.4 Focus on damage

Two types of damage can be distinguished: a pre-failure damage, where micro-cracks grows causing for example a nonlinear stress-strain behavior up to strength, and a post-failure damage, where a failed material is even able to carry loads before the catastrophic failure. Consequently, it is generally difficult to separate the mechanical behavior of a composite material and its damage evolution due to the presence of progressive failure linking intimately both phenomenons. The stability of the damage accumulation process is a very interesting feature of textile composites in particular for crash applications. Multiple

cracks can be accumulated without causing failure or a loss of structure integrity. Indeed, the damage accumulation mechanisms differ in textile composite from the U.D. laminates because the structure of the fabric plays a major role on the crack propagation and can stop or at least reduce it. Ivanov [64] classify the study of damage into different scales before combining them. On the micro-scale damage is characterized by fiber debonding and matrix inter-fiber crack formation. On the meso-scale damage is represented by a crack propagation, initiation and propagation of delamination and failure in matrix pockets. On the macro-scale damage appears in the form of fiber breakage or separation of the delaminated yarns.

Modeling damage is a considerable challenge due to the difficulty to correlate numerical and experimental results. In [180] a multilevel simulation approach based on finite elements calculations has been developed to calculate the elastic properties of a textile reinforced composite and to predict their damage behavior. Some micromechanical investigations use a continuum damage mechanics model (C.D.M) associated to thermodynamic forces to predict the progressive failure of woven composites, where damage is here considered as a pre-failure damage inducing a nonlinear behavior [181, 182]. In [183] a multiscale analysis is presented to study the macroscopic behavior of woven plies based on a microscopic damage state. Damage initiation is detected using the Hoffman's criterion and its propagation and distribution is studied on a mesoscopic level (R.U.C) leading to the prediction of the macroscopic stress-strain behavior. In [184], Thollon replaces a woven ply by two stacked unidirectional virtual plies. Based on the damage theories developed for unidirectional plies [185] he studies the loss of stiffness, inelastic strain and first failure of woven plies. Hochard *et al.* [186, 187] develop recently from [185] a non-local failure criterion based on the mean value of stress over a R.U.C called Fracture Characteristic Volume (FCV) and they implement it in ABAQUS. Considerable advantages of the model are its mesh-independence, its low computing costs and its independence to the adopted behavioral models (linear or nonlinear) and to the type of ply. Experimental studies on carbon/glass hybrid woven composites laminates show, that the tensile strength and ultimate strain are increased placing glass woven layers at the exterior and carbon fiber at the interior of the laminate [188]. It is due to the fact that the glass layers constrain the damage evolution process in the carbon layers. A hybridization effect is thus defined showing that experimental tensile and compressive ultimate strength and strain are higher than the predicted values obtained using the rule-of-mixture.

Key *et al.* [189] develop progressive failure models for fabric composites. They consider the woven composite as a combination of pure matrix pockets and separate but linked continua representing the warp and weft fiber bundles. Calculations are conducted using averaged constituents stress/strain fields. They noticed the multicontinuum theory better depicts the shear behavior (where large amounts of damage induce the nonlinearity) than an instantaneous degradation model. They show also that such modeling well predict intermediate failure under tensile loads due to matrix cracking in the fill bundles [190]. Consequently, a continuous degradation scheme seems to be more appropriate to depict the damage evolution in textile composites.

2.5.3 Discussion

Finally, due to the complex structure of a fabric composite the modeling of their mechanical behavior and failure is a non-trivial experimental or numerical study. Several analytic and numerical models have been developed, generally based on representative unit-cell to predict the effective stiffness and strength of a

woven composite. Then, several studies investigated experimentally the behavior of textile composites and their reported often a nonlinear behavior of the material. This macroscopic nonlinearity may be caused by micro-cracks in the material or be due to the properties of the constituents. Some models based on damage evolution laws have been developed to predict this nonlinear behavior up to failure. This irreversible damage should be correlated to plastic deformation because the material cannot recover its original state anymore. Finally, due to the complexity of the failure modes, the failure prediction of woven composite is a considerable challenge from the microscopic up to the macroscopic scale.

2.6 Impact behavior and strain rate-dependency of woven composites

2.6.1 Impact on woven composites

Several authors investigated the behavior of woven composites under impact loads considering the effects of the textile structure or of the stacking sequence [191–194], of the material thickness and of the impact energy [195]. In [196], the impact behavior of thermosetting and thermoplastic carbon woven composites is investigated. It has been shown that epoxy composites suffer from larger delamination than the thermoplastic materials. It has also been observed that the particular structure of textile composites tends to limit the delamination propagation. Due to the fiber crimping, a considerable level of fiber breakage is observed and the plastic behavior of the matrix in resin rich region has been identified as an important factor in the material behavior under impact.

In [197], the behavior of woven fabric laminated composite plates under low-velocity impact has been numerically investigated. It appears that multiple contacts occurred between the impactor and the plate during the impact event. Then, it has been observed, that woven fabric composites are more impact resistant than the common unidirectional or cross-ply non-crimp fabric laminates. Finally, it seems that in-plane failure initiates at the top layer for woven composites, whereas failure should initiate at the bottom layer for the non-crimp fabric laminates. The higher impact resistance and damage tolerance of woven composite has also been put in evidence in [198].

The damage process during the impact of glass fiber/epoxy woven composite has been investigated in [199]. It is reported that the damage evolution begins with matrix. Then, due to bending loads, fiber breakage appears at the non-impacted side of the plate, which represents the damage threshold of the material. Fiber breakage and matrix cracking increase until the beginning of perforation. These failure modes have been also reported in [200].

The investigation of the impact behavior of non-crimp fabric laminated structures is not reviewed here. From a general point of view, it seems that woven composites present a better impact resistance and damage tolerance than multidirectional non-crimp fabric, due to the particular textile structure contributing to the ductile behavior of the material and to the limitation of cracks and damage propagation.

2.6.2 Strain rate dependency

In fiber reinforced plastic, the dependence to the strain rate is mainly due to the viscoplastic behavior of the matrix material. Consequently, the strain-rate sensitivity of FRP materials is more significant under

matrix dominated loading like in shear. Due to the complex structure of the woven, transversal and shear stresses are almost always present regardless of the load patterns. Thus, miromechanical model have been developed to predict the strain-rate dependency of woven composites. Aminjikarai [201] proposed a 3D model for FEM simulations based on R.U.C using a viscoplastic behavior to model the resin and a set of strain-based criteria coupled with stiffness degradation to model the progressive failure. The model has been implemented in DYNA3D and good correlation with experiment has been reported. In [202] the strain rate sensitivity of a Prepreg carbon/epoxy plain weave composite has been investigated. The numerical predictions showed that the strength of woven composite increased with the strain rate. The in-plane longitudinal tension and compression load cases a law strain rate dependency of the material for law strain rate. Then, due to inertia effect, the strain rate dependency increased for strain rates higher than $100s^{-1}$. In shear, the strain rate dependency is mainly caused by the visco-plastic behavior of the resin. A numerical investigation based on two representative unit cells has been also conducted. The matrix is modeled by an elastic-plastic material model with strain rate sensitivity, and the yarns are modeled by means of an anisotropic plastic constitutive relation based on the Hill plasticity theory. A classical R.U.C of the plain weave composite structure and a single carbon fiber embedded in the resin have been modeled in ABAQUS. Failure of the material has been investigated by testing several failure scenarios.

In [203] the compressive behavior of glass fiber woven epoxy composites has been experimentally investigated using cylindrical specimen having a diameter about 8mm. An increase of the compressive strength with the strain rate has been observed, as well as an increase of the stiffness for high strain rate loading. An analytic model based on the $\sigma = A\varepsilon^m$ constitutive equation has been presented to predict the strain rate dependency of the material. A and m are strain rate depending nonlinear material parameters, that can be identified experimentally. In [204] the strain rate dependency of a glass fiber plain weave epoxy composite has been experimentally and numerically investigated. Smoothed tensile specimens have been used with a low width about 6mm in the middle of the specimen. Experiments show an increase of the tensile stiffness with the strain rate in the warp and weft directions. In shear, a viscoplastic behavior has been captured and the stiffness is here quite independent from the strain rate. An elastic-viscoplastic with anisotropic rate-dependent hardening has been developed and implemented in ABAQUS to conduct the numerical simulations of the experimental tests and a good correlation has been obtained. The experimental results published in [205] showed also an increase of both in-plane (warp and weft) and through the thickness tensile strengths with the strain rate for a common plain weave E-glass fiber/epoxy composite.

Constitutive models with post failure material degradation scheme [206], based on "viscous" elasto-plastic damageable models [207] or modeling the nonlinear strain rate dependent behavior using damage evolution laws [208] have been developed to predict the strain-rate dependency of woven composites. In [209], the rate-dependent behavior of unidirectional and woven glass fiber polymeric composite has been experimentally investigated. A three-parameter viscoplasticity model has been developed to predict numerically the nonlinear rate-dependent behavior of both materials and a single rate-dependent parameter failure criterion has been presented for the woven composite.

In [210] Zheng developed a nonlinear strain rate dependent model for FRP materials. It is based on the Goldberg's model adding a strain rate dependency for the initial elastic modulus and a damage

definition to improve the unloading behavior in the predictions. The model is implemented in the explicit formulation of LS-DYNA and a good correlation (mainly based on single shell element models) with experimental results on several kinds of composites is obtained.

2.7 Modeling of composite materials using the crash-solver LS-DYNA

2.7.1 Explicit time integration

The finite element solver LS-DYNA offers both explicit and implicit time integration schemes. Explicit schemes assess the equation of motion at the old time step t_n, whereas implicit methods use the equation of motion at the new time step t_{n+1}. For crash applications and for the simulations conducted and presented in this study, the explicit time integration has been used. The next sections give some details about the explicit formulation, the governing equations and the different steps of the resolution method used by the solver LS-DYNA.

2.7.1.1 Equation of motion

Considering the single degree of freedom system presented on Fig. 2.3, we can write [211–214]:

$$F^{\text{int}} + F_{\text{i}} + F_{\text{d}} = F^{\text{ext}}(t) \tag{2.4}$$

where

$$\begin{aligned} F^{\text{int}} &= ku \\ F_{\text{d}} &= c\dot{u} = c\frac{du}{dt} \\ F_{\text{i}} &= m\ddot{u} = m\frac{d^2u}{dt^2} \end{aligned} \tag{2.5}$$

u, k and c are respectively the displacement, the stiffness and the damping coefficients of the system. $\dot{u}$ and $\ddot{u}$ are respectively the velocity and the acceleration of the system. Consequently, the equation of motion of this single degree of freedom system is given by:

$$m\ddot{u} + c\dot{u} + ku = F^{\text{ext}}(t) \tag{2.6}$$

For an arbitrary degree of freedom system, the equation of motion written in a matrix form at the cycle number n and at time position t_n is expressed by:

$$M\left\{\ddot{u}\right\}_n + C\left\{\dot{u}\right\}_n + K\left\{u\right\}_n = \left\{F^{\text{ext}}\right\}_n \tag{2.7}$$

where M, C and K are the mass, damping and stiffness matrix respectively, and $\left\{F^{\text{ext}}\right\}_n$ is the vector of applied external forces. Finally, neglecting the material damping for short duration dynamic problem and replacing the $K\left\{u\right\}_n$ with the equivalent internal nodal force vector $\left\{F^{\text{int}}\right\}_n$, we obtain the following equation of motion:

$$M\left\{\ddot{u}\right\}_n = \left\{F^{\text{ext}}\right\}_n - \left\{F^{\text{int}}\right\}_n \tag{2.8}$$

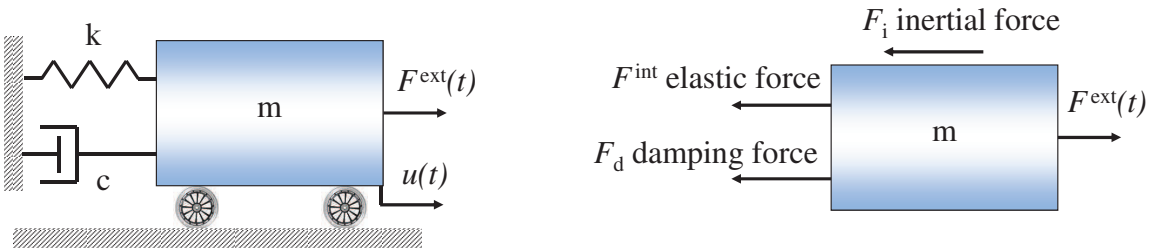

Figure 2.3: Single degree of freedom dynamic system

2.7.1.2 Central difference method

The central difference method is used in LS-DYNA to solve the equation of motion (see Eq. 2.8) at each time step. Referring to the left side of Fig. 2.4 [212,214], we can write:

$$\dot{u}_n = \frac{1}{2\Delta t}\left(u_{n+1} - u_{n-1}\right) \tag{2.9}$$

$$\ddot{u}_n = \frac{1}{\Delta t}\left(\dot{u}_{n+\frac{1}{2}} - \dot{u}_{n-\frac{1}{2}}\right) = \frac{1}{(\Delta t)^2}\left(u_{n+1} - 2u_n + u_{n-1}\right) \tag{2.10}$$

$$M\ddot{u}_n + C\dot{u}_n + Ku_n = F_n^{ext} \tag{2.11}$$

Using Eq. 2.9 and Eq. 2.10 in the Eq. 2.11 it leads to:

$$(M + \frac{1}{2}C\Delta t)u_{n+1} = \Delta t^2 F_n^{ext} - (\Delta t^2 K - 2M)u_n - (M - \frac{\Delta t}{2}C)u_{n-1} \tag{2.12}$$

where M, C, and K are respectively the mass, damping and stiffness. u_{n+1} is the unique unknown and is relatively easy to determine. In order to start the integration the following initialization is used:

$$u_{-1} = u_0 - \Delta t\dot{u}_0 + \frac{\Delta t^2}{2}\ddot{u}_0 \tag{2.13}$$

with u_0, $\dot{u}_0$ and $\ddot{u}_0$ being respectively the initial displacement, velocity and acceleration.

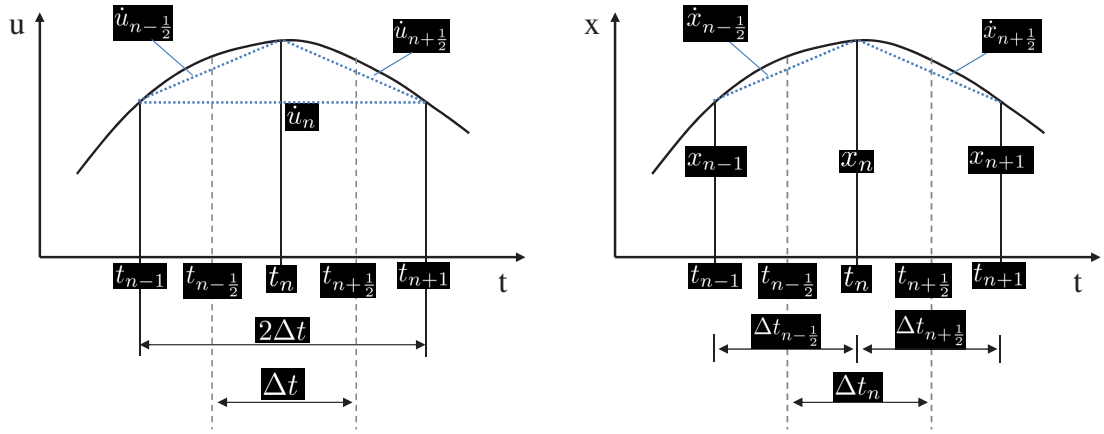

Figure 2.4: Central difference method (left) and time integration used in LS-DYNA (right)

2.7.1.3 Time integration in LS-DYNA

The time integration in LS-DYNA is based on the calculation of the accelerations and displacements at t_{n+1}, whereas the velocities are determined at $t_{n+\frac{1}{2}}$. To represent the discretization of the complete geometry the displacements u are replaced by the variable x. Referring to the right side of Fig. 2.4 [214], we can write:

$$\dot{x}_{n+\frac{1}{2}} = \frac{1}{\Delta t_{n+\frac{1}{2}}} \left(x_{n+1} - x_n\right) \tag{2.14}$$

$$\ddot{x}_n = \frac{1}{\Delta t_n} \left(\dot{x}_{n+\frac{1}{2}} - \dot{x}_{n-\frac{1}{2}}\right) \tag{2.15}$$

From Eq. 2.15 we obtain:

$$\dot{x}_{n+\frac{1}{2}} = \dot{x}_{n-\frac{1}{2}} + \Delta t_n \ddot{x}_n \tag{2.16}$$

It is assumed that the acceleration $\ddot{x}_n$ is given by (see Eq. 2.7):

$$\ddot{x}_n = M^{-1} \left(F_n^{ext} - F_n^{int} - C\dot{x}_{n-\frac{1}{2}}\right) \tag{2.17}$$

Finally, the new displacement is given by:

$$x_{n+1} = x_n + \Delta t_{n+\frac{1}{2}} \dot{x}_{n+\frac{1}{2}} \tag{2.18}$$

with

$$\Delta t_{n+\frac{1}{2}} = \frac{1}{2} \left(\Delta t_n + \Delta t_{n+1}\right) \tag{2.19}$$

The initial conditions are given by:

$$\begin{aligned} x_0 &= \bar{x_0} + u_{\text{stat}} \\ \dot{x_0} &= \tfrac{1}{2} \left(\dot{x}_{-\frac{1}{2}} + \dot{x}_{\frac{1}{2}}\right) \\ \ddot{x}_0 &= M^{-1} \left(F_0^{ext} + F_{\text{stat}}^{ext} - F_0^{int}\left(u_{\text{stat}}\right) - C\dot{x}_0\right) \\ \dot{x_{\frac{1}{2}}} &= \dot{x_0} + \tfrac{1}{2}\Delta t_0 \ddot{x}_0 \\ F_{\text{stat}}^{ext} &= F_0^{int}\left(u_{\text{stat}}\right) \end{aligned} \tag{2.20}$$

where $\bar{x_0}$ represents the initial geometry, u_{stat} the initial displacements from static loading, F_0^{int} the internal forces from initial strains, $F_{\text{stat}}^{\text{ext}}$ the external forces from static loading and F_0^{ext} the initial external forces on the system [214].

The mass matrix M is generally not diagonal. Consequently, its inversion is likely to be inefficient and a source of instability, whereas a diagonal matrix does not need to be inverted. The LS-DYNA formulation is based on lumped masses, which consists in adding the non-diagonal terms of a row to the corresponding diagonal terms of the mass matrix in order to obtain a diagonal mass matrix [210, 211].

2.7.1.4 Determination of the time step

A large time step can lead to unstable solutions, whereas a small time step makes the computation inefficient. Consequently, the time step has to be as large as possible but also as small as required. In this context, a critical time step is defined as the smallest time step such as for each time step, a stress wave does not go through more than one element. The critical time step $\Delta t_{\text{critical}}$ is based on the highest natural frequency ω_{max} of the system and it can be defined by (for non-damped equation of motion):

$$\Delta t \leqslant \frac{2}{\omega_{max}} = \Delta t_{\text{critical}} \tag{2.21}$$

It can be shown that ω_{max} depends on the wave or sound speed c_s and on the characteristic length of the element l_c, as expressed by:

$$\omega_{max} = 2\frac{c_s}{l_c} \tag{2.22}$$

Consequently the critical time step is given by (Courant-Friedrichs-Levy criterion):

$$\Delta t_{\text{critical}} = \frac{l_c}{c_s} \tag{2.23}$$

For a shell element, the characteristic length can be defined by ($\varphi = 0$ for 4-node shells, $\varphi = 1$ for 3-node shells and l_1, l_2, l_3, l_4 being the four side lengths of a square shell element):

$$l_c^{\text{shell}} = \frac{(1+\varphi)\,A}{\max\left(l_1, l_2, l_3, (1-\varphi)\,l_4\right)} \tag{2.24}$$

For solid element, the characteristic length is expressed by:

$$l_c^{\text{solid}} = \frac{Volume}{Maximal\ Area} \tag{2.25}$$

The wave speed in a shell c^{shell} and in a solid c^{solid} is defined by:

$$c^{\text{shell}} = \sqrt{\frac{E}{(1-\nu^2)\,\rho}} \tag{2.26}$$

$$c^{\text{solid}} = \sqrt{\frac{E\,(1-\nu)}{(1+\nu)\,(1-2\nu)\,\rho}} \tag{2.27}$$

where E, ν and ρ are respectively the Young's modulus, the Poisson' ratio and the density of the material. For stability reason, the time step is per default set to 90% of the critical time step, which is expressed by:

$$\Delta t = 0.9\Delta t_{\text{critical}} \tag{2.28}$$

This study is based on the following references [214, 215]

2.7.1.5 Governing equations

The following study is inspired from [210,211]. We are interested here by the time-dependent deformation of the 3D body having a volume V and a surface S, as presented on Fig. 2.5. A point B of this body initially at X_j ($j = 1, 2, 3$) in a fixed rectangular Cartesian coordinate system moves to the position x_i ($i = 1, 2, 3$). A Lagrangian formulation is used here and for the simulation using LS-DYNA. It means that the material is fixed to the finite element mesh and the mesh deforms and moves with the material. Consequently, the deformation of the body can be expressed in terms of the coordinates X_j and the time t:

$$x_i = x_i\left(X_j, t\right) \tag{2.29}$$

The initial conditions at time $t = 0$ are defined by:

$$x_i\left(X_j, 0\right) = X_j \tag{2.30}$$

Similar initial conditions can be defined for the velocity and the acceleration. The aim is to find a solution to the following momentum equation:

$$\sigma_{ij,j} + \rho f_i = \rho \ddot{x}_i \tag{2.31}$$

where σ_{ij} is the Cauchy' stress tensor, ρ the material density, f_i the body external force over the volume and $\ddot{x}_i$ the acceleration. Eq. 2.31 has to satisfy the traction boundary conditions on the surface S_t with n_j the normal direction to the surface

$$\sigma_{ij,j} n_j = t_i(t) \tag{2.32}$$

and the displacement boundary conditions over the surface S_d

$$x_i\left(X_j, t\right) = d_i(t) \tag{2.33}$$

where $t_i(t)$ are the traction forces on the surface S_t and $d_i(t)$ are the displacement prescribed over the surface S_d of the body.

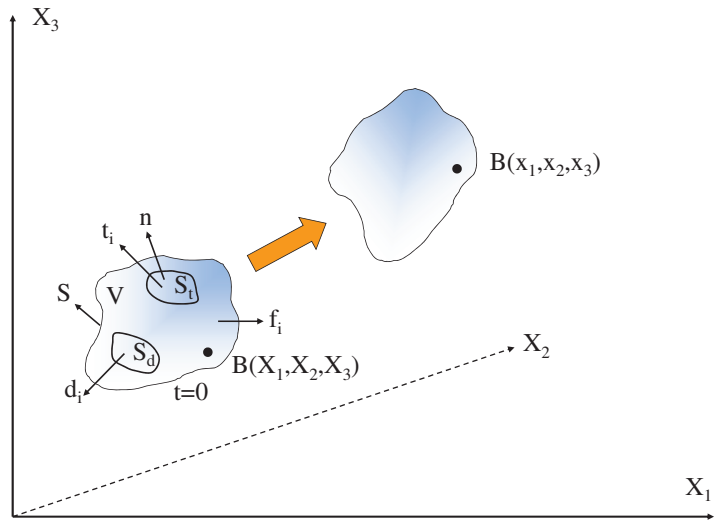

Figure 2.5: Time dependent deformation of a 3D body in a Cartesian space and the Lagrangian formulation.

These equations have to be satisfied at each point in the body or in its surface. Consequently, the equations have to be integrated on the volume V of the body. A virtual displacement δx_i satisfying the displacement boundary conditions on S_d is introduced. The integration of the Eq. 2.31 on the volume is expressed by:

$$\int_V \left(\rho \ddot{x}_i - \rho f_i - \sigma_{ij,j}\right) \delta x_i dV = 0 \tag{2.34}$$

Developing all the terms of the integral it leads to:

$$\int_V \rho \ddot{x}_i \delta x_i dV - \int_V \rho f_i \delta x_i dV - \int_V \sigma_{ij,j} \delta x_i dV = 0 \tag{2.35}$$

Noting that

$$\sigma_{ij,j} \delta x_i = \left(\sigma_{ij} \delta x_i\right)_{,j} - \sigma_{ij} \delta x_{i,j} \tag{2.36}$$

and replacing this expression in Eq. 2.35 it comes:

$$\int_V \rho \ddot{x}_i \delta x_i dV - \int_V \rho f_i \delta x_i dV - \int_V \left(\sigma_{ij} \delta x_i\right)_{,j} dV + \int_V \sigma_{ij} \delta x_{i,j} dV = 0 \tag{2.37}$$

Applying the theorem of divergence

$$\int_V \left(\sigma_{ij}\delta x_i\right)_{,j} dV = \int_{S_t} \sigma_{ij} n_j \delta x_i dS \tag{2.38}$$

and using Eq. 2.32

$$\int_{S_t} \sigma_{ij} n_j \delta x_i dS = \int_{S_t} t_i \delta x_i dS \tag{2.39}$$

Finally, it leads to the following equilibrium equation (statement of the principle of virtual work):

$$\boxed{\delta\Phi = \int_V \rho \ddot{x}_i \delta x_i dV - \int_V \rho f_i \delta x_i dV - \int_S t_i \delta x_i dS + \int_V \sigma_{ij} \delta x_{i,j} dV = 0} \tag{2.40}$$

2.7.1.6 Application to the spatial discretization

To conduct finite element simulations, the previous equilibrium equation has to be applied on a spatial discretization [210, 211]. To achieve that, we superimpose a mesh of finite elements interconnected at nodal points. Summing the Eq. 2.40 over the n elements constituting the mesh, $\delta\Phi$ is approximated with:

$$\delta\Phi = \sum_{m=1}^{n} \delta\Phi_m = 0 \tag{2.41}$$

The equilibrium equation can then be expressed by:

$$\sum_{m=1}^{n} \left[\int_{V_m} \rho \ddot{x}_i \delta x_i dV_m - \int_{V_m} \rho f_i \delta x_i dV_m - \int_{S_{tm}} t_i \delta x_i dS_m + \int_{V_m} \sigma_{ij} \delta x_{i,j} dV_m \right] = 0 \tag{2.42}$$

with V_m the volume of an element and S_{tm} the surface of an element, where act the traction forces.

Then, shape functions are introduced to link the displacements at inner points in the elements (points of integration) to the displacements at nodal points. It is expressed by:

$$\delta x_i = \sum_{k=1}^{q} N_k(\xi, \eta, \zeta) \delta x_{ki} \tag{2.43}$$

where δx_i are the displacements in the direction i at a point inside the element, q is the number of nodal points defining the element, N_k is the shape function at the node k in function of the (ξ, η, ζ) parametric coordinate of an element and δx_{ki} are the displacements at the kth node in the direction i. In a similar manner, the expression for the coordinates x_i, velocities, $\dot{x}_i$ and acceleration $\ddot{x}_i$ can be expressed by:

$$x_i = \sum_{k=1}^{q} N_k(\xi, \eta, \zeta) x_{ki} \tag{2.44}$$

$$\dot{x}_i = \sum_{k=1}^{q} N_k(\xi, \eta, \zeta) \dot{x}_{ki} \tag{2.45}$$

$$\ddot{x}_i = \sum_{k=1}^{q} N_k(\xi, \eta, \zeta) \ddot{x}_{ki} \tag{2.46}$$

Using Eq. 2.43 and Eq. 2.46 ind the Eq. 2.42 we obtain:

$$\sum_{m=1}^{n} \left[\int_{V_m} \rho \left(N_p^m \ddot{x}_{pi}\right) \left(N_k^m \delta x_{ki}^m\right) dV_m - \int_{V_m} \rho f_i \left(N_k^m \delta x_{ki}^m\right) dV_m \right] - \sum_{m=1}^{n} \left[\int_{S_{tm}} t_i \left(N_k^m \delta x_{ki}^m\right) dS_m + \int_{V_m} \sigma_{ij} \left(N_{k,j}^m \delta x_{ki}^m\right) dV_m \right] = 0 \tag{2.47}$$

where $N_k^m = (N_1, N_2, ..., N_k)^m$. Rearranging the previous equation and writing it in a matrix form, it leads to:

$$\sum_{m=1}^{n} \left[\int_{V_m} \rho N_p N_k \ddot{x}_{pi} dV_m \right] = \sum_{m=1}^{n} \int_{V_m} \rho f_i N_k dV_m + \sum_{m=1}^{n} \int_{S_{tm}} t_i N_k dS_m - \int_{V_m} \sigma_{ij} N_{k,j} dV_m \tag{2.48}$$

which corresponds to the equation of motion $M\{\ddot{x}\} = \{F\}$ where $\{\ddot{x}\}$ and $\{F\}$ are respectively the acceleration vector and the vector summation of the internal and external forces. $N_{k,j}$ refers commonly to the strain-displacement matrix allowing to obtain the strains from the displacements in each direction.

2.7.1.7 Milestone for the resolution

An overview of the resolution procedure used in the explicit formulation of LS-DYNA is proposed below [210].

Step 1: According to the different boundary conditions, a displacement increment is applied on each node.

Step 2: Based on the strain-displacement relationship (strain-displacement matrix), a strain increment is determined at each point of integration of each element.

Step 3: Based on the strain increment and on the material constitutive evolution law implemented in a material model, stresses are calculated at each point of integration. It leads then to the calculation of resultant forces and moments at each integration point.

Step 4: The internal forces are determined on each node of the finite element mesh.

Step 5: The current forces state is here injected in the governing equation, referring to the equation of motion presented previously (see equation 2.8).

Step 6: Finally, the nodal displacements are updated by solving the governing equation using the central difference method.

2.7.2 Elements available to model FRP-Materials

As described in [211,216] several types of elements are available to conduct simulations using the explicit finite element solver LS-DYNA. To model the fiber reinforced plastic and the structures investigated in this study, shell, thick shell and under-integrated solid elements have been used. These three element types are shortly described in the next sections.

2.7.2.1 Shell elements

The Belytschko-Lin-Tsay (ELFORM=2) and the full-integrated (ELFORM=16) shell elements are commonly used to model thin structures and for their computational efficiency. The complete stacking sequence of a composite laminate can be defined using several points of integration over the element

thickness. Each point of integration has thus a particular orientation and thickness. The Belytschko-Lin-Tsay shell element presents one point of integration in the middle of the element. This shell is based on a co-rotational and a velocity-strain formulation. An embedded coordinate system that deforms with the element is defined in terms of the nodal coordinates [211]. The shell element partitions any point in the shell in terms of mid-surface velocity, the angular velocity and the distance along the thickness of the element. Then, the co-rotational components of the rate of deformation are calculated. As they have to be evaluated at each quadrature point, standard bi-linear shape functions are applied to the mid-surface velocity, the angular velocity and the element's coordinates. The *PART_COMPOSITE keyword has been used to define the different points of integration over the element thickness. These transformations are then applied to the velocity-strain displacements relationships. The resulting stresses are then integrated over the thickness of the shell leading to the computation of local (element-centered) resultant forces and moments. They are then related to the local nodal forces and moments. Finally, they are transformed to the global coordinate system and summed over all nodes. The global equation of motion can then be solved.

The full-integrated shell elements offer four points in-plane of integration (instead of only one for the under-integrated Belytschko-Lin-Tsay shell). A similar local element coordinates system as for the Belytschko-Lin-Tsay shell is used. This formulation reduces the hourglass problems (see section 2.7.2.4) and should enhance the in-plane bending behavior.

2.7.2.2 Solid elements

Both under-integrated (ELFORM=1) fully-integrated (selective reduced) (ELFORM=2) brick elements have been considered in this study. Solid elements present some disadvantages for the modeling of composite materials. First, it is not possible to define several points of integration over the thickness in order to model the stacking sequence of the laminate. The use of one brick element per composite ply through the thickness could be a solution but it increases dramatically the number of elements and consequently the computing time. A second solution is to homogenize the material properties of a laminate. This sub-laminate approach is naturally not optimal to study the crash-behavior of composites, as it is necessary to identify the plies that failed during the simulation. Finally, under-integrated elements suffer from hourglass deformation modes. This element deficiency can be reduced using full-integrated elements but brick elements are from a general point of view not suitable for the modeling of composite materials and industrial applications. Consequently, these elements do not have been extensively investigated in this study. More information about brick elements can be found in [211].

2.7.2.3 Thick shell elements

Thick shell elements present the shape of a brick element but several points of integration can be defined through the thickness of the element, similarly to shells. This kind of elements is consequently suitable for the modeling of laminated composite. Several thick shell formulations are available in the element library of LS-DYNA. Only the formulation (ELFORM=5) offering a three-dimensional stress-state and a suitable efficiency has been investigated here. Thick shell elements are relatively sensitive to distortion and badly shaped elements should be avoided. A parabolic through-the-thickness transverse shear strain distribution is assumed per default, which is suitable for modeling involving a unique element layer, even it is likely to

be not sufficient for the modeling of composite materials. If several thick shell elements have to be stacked together, a flag allows to change the parabolic distribution into a constant one. The through-the-thickness points of integration have been defined using the recently implemented *PART_COMPOSITE_TSHELL keyword. As thick shell elements present a unique in-plane point of integration, they are likely to suffer from hourglass deformation (see section 2.7.2.4).

2.7.2.4 Hourglass control

Hourglass modes are nonphysical, zero-energy modes of deformation that produce zero strain energy and no stress. It occurs only in under-integrated elements (solid, shell or thick shell elements) and can be the cause of a calculation divergence. The phenomenon is identified by the fact that the element can shear without introducing any energy. To compensate it the finite element analysis takes this into account through a hourglass energy added in the energy balance, that have to be filled at every time step (see Eq. 2.49). It is evident that the hourglass energy must be as small as possible [217].

$$E_{\text{Total}} = E_{\text{K}} + E_{\text{S}} + E_{\text{I}} + E_{\text{H}} \tag{2.49}$$

where E_{Total}, E_{K}, E_{S}, E_{I}, and E_{H} are respectively the total energy, the kinetic energy, the sliding energy, the internal energy and the hourglass energy.

A refinement of the mesh and/or the use of full-integrated elements are two well-known methods used to reduce the hourglass phenomenon in numerical simulations. If none of these solutions can be applied, hourglass control formulations have to be used. The first hourglass control method is the stiffness-based hourglass control, which is more effective for structural parts. It aims at adding stiffness, which inhibits the hourglass modes but not the rigid body motions. The second hourglass control formulation is the viscous hourglass control, which is recommended for high velocity impacts. The principle is to damp velocities in the direction of hourglass modes.

2.7.3 Material models available to model FRP-Materials

This section presents an overview of the main orthotropic "composite material models" available in the library of LS-DYNA, that are commonly used for industrial applications or that will be investigated in the present study. Only the macroscopic behavior of the material models and some information about failure will be reported. More details about each material model can be found in the bibliographic references that will be mentioned. Fig. 2.6 presents an overview of the main four material models used for industrial applications and for laminated structures. The feature and the behavior of each material model will be discussed in the following corresponding sections.

2.7.3.1 *MAT_022

The material model *MAT_022 presents a linear elastic behavior until the strength following by a sudden failure with no softening in the post-failure regime. The Chang-Chang [218] failure criteria are used to predict failure. No failure criterion is defined for the longitudinal compressive failure mode. See [211,219] for more information about this material model.

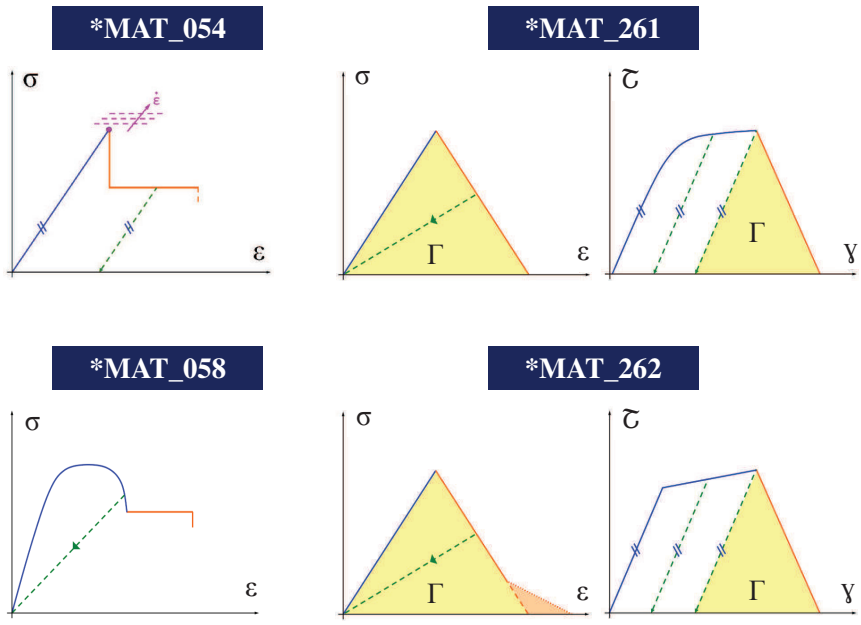

Figure 2.6: Overview of four composite material models regarding the macroscopic behavior

2.7.3.2 *MAT_054-055

Both models are enhanced versions of the composite material model *MAT_022 and they are implemented for thin shell elements only but thick shell elements can be used. *MAT_054 uses the Chang-Chang [218] matrix failure criterion, whereas *MAT_055 uses the Tsai-Wu [220] matrix failure criterion. The input data consists in the effective material properties: three Young's modulus, three Poisson's ratio, three shear modulus, the different strengths in various directions and strain at ultimate failure. An effective maximal strain parameter can also control failure, when it is defined. Some parameters should be soon implemented to predict the behavior of rate-sensitive composites. The strain at ultimate failure parameters (DFAILx) control the post-failure behavior of the material. They define the length of the post-failure constant stress level. The stress level in the post-failure behavior can be controlled for each direction using the corresponding $SLIMxx$ parameters. Without the set of these parameters the material present a linear-brittle elastic behavior, whereas their definition assures an ideal pseudo-plastic behavior until the ultimate failure after reaching the strength (see Fig. 2.6). A similar material behavior is considered in shear. More information about this material model can be found in [211, 219, 221].

2.7.3.3 *MAT_058

This material model is based on the work published by Matzenmiller, Lubliner and Taylor in [222]. This model is implemented for shell elements but it can be used with thick shell elements. It may be used to model composite laminates and woven fabrics stacked with unidirectional layers. A nonlinear elastic behavior can be defined using the strength and the strain at failure onset parameters. Internal variables are introduced to describe the evolution of the damage state and the degradation of the material stiffness, modeling thus the formation and evolution of microcracks and cavities in the material. These defects cause a stiffness softening and nonlinearity. After failure, the model uses stress limit factors ($SLIMxx$)

to impose a stress level until ultimate failure. The final failure is controlled by a maximum effective strain criterion working for tension, compression and shear loads ($ERODS$). Three damage and failure definitions are available based on the maximal stress or the Hashin failure criteria [211,219,221]. Finally, it is important to notice that no permanent deformation is accounted for, even if a nonlinear behavior caused by the evolution of damage and microcracks (irreversible phenomenon) is predicted. A nonlinear elastic behavior can be also defined in shear. Based on the formulation of *MAT_058, *MAT_158 allows to model rate sensitive composite materials.

In [223] a critical evaluation of the material model developed in [222] is proposed identifying its limits: coupling pre- and post-failure response, elastic unloading of the material following partial damage and mesh sensitivity caused by the localization of damage. More information about this material model can be also found in [211,219,221].

2.7.3.4 *MAT_059

The elastic-plastic material model *MAT_059 describes a linear elastic behavior until the strength followed by catastrophic failure or a smoothed post-failure behavior defining a minimum stress level in the post-failure regime. This material is implemented for shell and solid elements and two failure formulations are available. A first formulation presents a faceted failure surface due to the use of maximal stress failure criteria. The second formulation presents an ellipsoidal failure surface defined by a quadratic failure criterion [221].

2.7.3.5 *MAT_118

This material model is used to model only the elastic response of composites, as no failure criterion is implemented. Each term of the stiffness matrix (see Eq. 2.50) of the composite has to be given has an input. A pre-integration is then used to compute the extensional $[A]$, the bending $[D]$ and the coupling stiffness $[B]$ matrix (see Eq. 2.51). This model is implemented for the Belytschko-Tsay resultant shell formulation. Consequently, as the stresses are not computed in the resultant formulation, no stress is available in the output and no stress analysis can be made on a structural part.

$$\begin{Bmatrix} N_x \\ N_y \\ N_{xy} \\ M_x \\ M_x \\ M_{xy} \end{Bmatrix} = \begin{bmatrix} A_{11} & A_{12} & A_{16} & B_{11} & B_{12} & B_{16} \\ A_{21} & A_{22} & A_{26} & B_{21} & B_{22} & B_{26} \\ A_{16} & A_{26} & A_{66} & B_{16} & B_{26} & B_{66} \\ B_{11} & B_{12} & B_{16} & D_{11} & D_{12} & D_{16} \\ B_{21} & B_{22} & B_{26} & D_{21} & D_{22} & D_{26} \\ B_{16} & B_{26} & B_{66} & D_{16} & D_{26} & D_{66} \end{bmatrix} \begin{Bmatrix} \varepsilon_x \\ \varepsilon_y \\ \varepsilon_{xy} \\ \kappa_x \\ \kappa_x \\ \kappa_{xy} \end{Bmatrix} \tag{2.50}$$

$$\begin{Bmatrix} [N] \\ [M] \end{Bmatrix} = \begin{bmatrix} [A] & [B] \\ [B] & [D] \end{bmatrix} \begin{Bmatrix} [\varepsilon] \\ [\kappa] \end{Bmatrix} \tag{2.51}$$

The main advantage of this model is that the bending and extensional behavior can be controlled independently. Indeed, *MAT_116 is also based on a resultant formulation but the input data are based on the effective stiffness moduli. The coefficients of the stiffness matrix are internally computed but the bending behavior depends on the extensional behavior, as they are both linked to the same stiffness moduli.

2.7.3.6 *MAT_261

The *MAT_261 material model has been recently implemented and it relies on the work published by Pinho in [150, 151]. This model is able to predict a linear elastic behavior until failure onset. Failure is predicted using coupled physically-based failure criteria including a 3D kinking model in order to take into account the kinking phenomenon for the longitudinal compressive failure modes. In the transverse direction, failure is predicted in function of the orientation of the fracture plane. The post-failure behavior is characterized by a linear damage evolution, where the "undamaged" effective stresses are linearly degraded until ultimate failure. Fracture toughnesses have to be given as an input in each material direction. A smeared formulation ensures suitable localization and distribution of damage to this mesh-insensitive material model. The model is suitable for the modeling of non-crimp fabric laminated structures using shell, thick shell or solid elements. Finally, a nonlinear in-plane shear behavior coupled with a unidimensional plasticity theory accounting for permanent deformation is considered. A user-defined load curve is required as an input.

2.7.3.7 *MAT_262

The *MAT_262 material model has been recently implemented and it relies on the work published by Maimi, Camanho *et al.* in [224, 225]. This model is able to predict a linear elastic behavior until failure onset. Failure is predicted using coupled physically-based failure criteria (LaRC03 and LaRC04). A bi-linear post-failure material degradation scheme is implemented in the longitudinal direction based on two different fracture toughnesses. In the transverse direction, a linear damage evolution law degrades progressively the undamaged stresses until ultimate failure. This material model is suitable for the modeling of non-crimp fabric laminated structures using shell, thick shell or solid elements. Finally, a bi-linear in-plane shear behavior coupled with a unidimensional plasticity theory accounting for permanent deformation is considered.

2.7.3.8 *MAT_161-162

Both *MAT_161 and *MAT162 models may be used to model the progressive failure analysis for composite materials consisting of unidirectional and woven fabric layers. Failure is modeled based on the progressive layer failure criteria developed by Hashin [226] with a generalization to include the effect of highly constrained pressure on composite failure. Thus, fiber failure, matrix damage, and delamination behavior can be predicted by the model based on quadratic failure criteria.

For the unidirectional lamina mode in *MAT_161, fiber and shear tensile modes are coupled in the same failure criterion. Two other criteria account for compressive fiber mode and crush mode. Then, two criteria are implemented to predict the matrix failure mode perpendicularly to the plane of layering and another one to predict the in-plane matrix failure mode, which refers to delamination. These both matrix failure criteria are not coupled with the fiber failure criteria.

For the fabric lamina, similar quadratic failure criteria are developed for the shear and fiber tensile modes and they consider both warp and weft directions. The fiber compressive failure mode and the in-plane shear matrix mode are predicted using a maximum stress criterion. A similar criterion as for the unidirectional lamina model is used here for the crush mode.

The post-failure material degradation processes depending on the modes of failure are described in [211,219] but they are not reported here.

*MAT_162 is a generalization of the basic layer failure model of *MAT_161 by adopting the damage mechanics approach for characterizing the softening behavior after damage initiation [222,227].

2.7.4 Discretization and modeling of a woven ply

For industrial applications, non-crimp fabric laminates are generally modeled using one point of integration per elementary ply (see at the top of Fig. 2.7). Ideally, a woven ply should be also modeled by a unique integration point but due to its higher thickness and complexity, another discretization has to be considered, as presented at the bottom of Fig. 2.7. From a general point of view, two main modeling techniques can be used to model an elementary woven ply.

Modeling based on a unidirectional stack : In this case, each woven ply is modeled using one or several points of integration presenting the same orientation. The material properties of the woven ply should be there given as an input. The use of two or three points of integration per woven ply could be judicious to model thick structures or thick plies but they are not recommended for industrial applications.

Modeling based on a multidirectional stack : In this case, each woven ply is modeled using two or more points of integration presenting different orientations. Two kinds of input data can be considered here. First, the effective material properties are given as an input for each point of integration. In this case, the modeling of each woven ply based on a multidirectional stacking sequence does not have a physical meaning but it can reduce some numerical instability. Indeed, the modeling of a unidirectional stacking sequence is likely to induce numerical divergences, particularly regarding the post-failure behavior. The second way is to model a woven ply using a multidirectional stacking sequence but the material properties of a unidirectional ply, eventually accounting for fiber waviness, are given as an input for each point of integration. This modeling presents a higher physical meaning, but it represents also higher efforts to determine the different mechanical effective material properties (stiffness and strength) of a wavy unidirectional ply and to consider the different interactions induced by the textile structure. Moreover, the determination of the post-failure behavior and eventually fracture toughnesses of such unidirectional plies interacting together is not trivial.

Finally, the priority of this study is to model each woven ply using one point of integration. In the case where two points of integration should be preferred to model each woven ply, a bidirectional $[0°, 90°]$ stacking sequence will be used but the effective material properties of the woven ply are given as an input for each point of integration.

2.8 Discussion and synthesis of the literature review

Several analytic or numerical FEM micromechanical theories have been developed to predict the material properties of woven composite, from the determination of effective stiffness up to failure and damage of the material. These methods are sometimes very complex but they generally present a good correlation with experiments. Input data depend often on the material properties of the constituents and on the

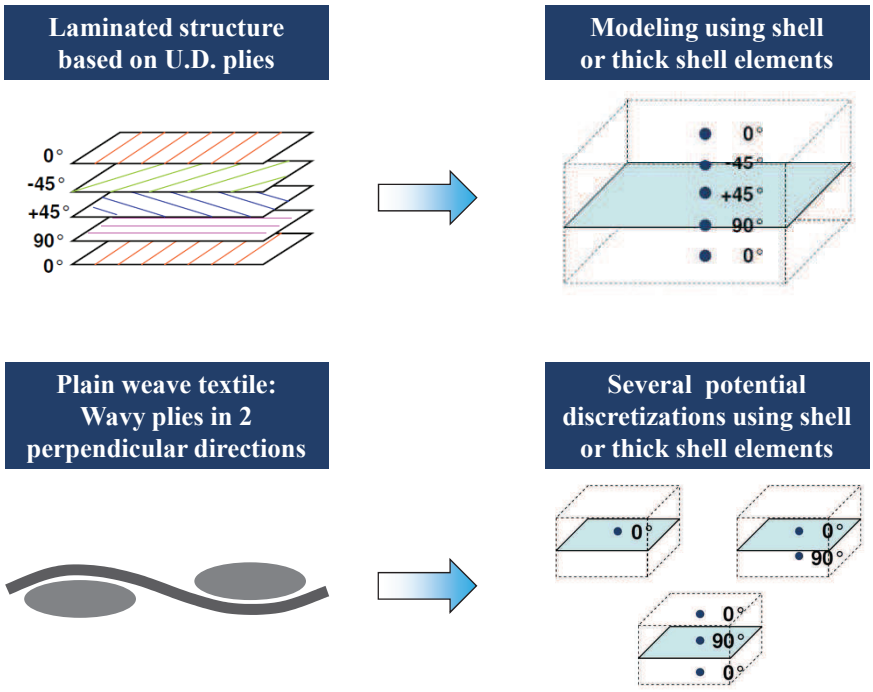

Figure 2.7: Comparison of the potential discretization of a non-crimp laminated structure and of a plain-weave textile structure

geometrical properties of the reinforcements. The main weaknesses of these theories rely on their computational costs, on the determination of the different material and geometrical parameters and on the assumption of periodicity of the R.U.C. Manufacturing processes bring imperfections in the materials and can modify the material structure shape, what can highly influence the predictions on a microscopic level. Lomov *et al.* [228] classified for example these possible sources of errors: they come from the yarn shapes, the nesting of the laminate layers, the fiber volume fraction and we can add the imprecision made in the experimental analysis. Micromechanical analyses are a promising way to homogenize the properties of woven reducing the experimental costs to obtain the stiffness and strength of the constituents. However, for industrial crash applications failure, fragmentation, permanent deformation and damage initiation and propagation have to be predicted. Considering the limitations on the elements size (about 3-5mm) micromechanical analysis cannot be here applied (damage and cracks can only propagate with steps having the size of the elements). Consequently a macromechanical study has to be conducted and requires a macromechanical numerical characterization of the material [229].

Woven composites have a complex progressive failure process. Damage and microcracks coupled with matrix nonlinear behavior lead to the macroscopic nonlinear behavior observed in experiments in different directions. These two sources of nonlinearity are difficult to separate on a macroscopic level. Industrial applications require to capture the macromechanical material behavior with an acceptable prediction of nonlinearity, permanent deformation, progressive failure and post-failure damage up to the ultimate failure. The modeling of delamination is a complex debate and requires additional modeling techniques that are likely to transgress the "cost" limitations imposed. That is why delamination will not be extensively study in this study while it is a preponderant failure mode of FRP-materials.

Structural composite parts, that are crash relevant for automotive applications present often a thick-

ness higher that 3mm. It means that for a modeling with shell elements, the thickness of the element is likely to be higher than its in-plane dimensions, which does not verify the assumptions of the plate theory. Consequently, to model such materials using a unique element layer a three-dimensional modeling has to be considered.

As described previously, most of orthotropic composite material models in LS-DYNA have been developed for the modeling of laminated non-crimp fabrics. They are able to predict a linear elastic behavior up to failure onset. Different failure criteria are applied to predict failure and they are mainly based on the effective material properties (stiffness and strength). Three material models (*MAT_054, *MAT_058 and *MAT_059) propose a post-failure constant stress level up to ultimate failure. Both recently implemented *MAT_261 and *MAT_262 define a linear (or bi-linear) post-failure material degradation based on a damage variable. Using a damage evolution referring to the evolution of microcracks in the material, the *MAT_058 model is able to predict the nonlinear behavior of composite. However, no permanent deformation is considered, as no plasticity definition has been implemented. Consequently, a large number of features are distributed over several material models but no model combines together nonlinearity, permanent deformation and post-failure material degradation, which should be required to model the behavior of textile composites.

Chapter 3

Experimental observations: quasi-static, impact and representative component tests on carbon woven reinforced plastics

This chapter presents the experimental results of quasi-static and low-velocity impact tests on a carbon plain weave RTM material and on a carbon twill-weave PREPREG composite. Quasi-static tensile, compressive and bending tests have been conducted on elementary specimens in order to determine the effective material properties of the material. Some preliminary tests have been conducted on a RTM carbon plain weave composite presenting two outer glass mat layers. Outer glass mat layers generally aim at protecting the carbon reinforced composite material against chemical attacks or mechanical contacts. For confidentiality reasons, all the quantitative results (for example stress vs. strain curves) have been normalized and they are presented using a scale expressed in percentage. The grey and black curves show the experimental results and the red bold curve is the physical reference used then for the comparison with numerical results. It corresponds to a representative curve of the experimental curves set. Then, the experimental results obtained from impact tests made on elementary plate and on hat-profiles will be presented. Impacts on elementary plates allow to assess the damage tolerance of the composite materials under impact load. Due to a modeling limited to a single-element layer, it is impossible to predict correctly the delamination phenomenon. Consequently, the delaminated area is assimilated to a damaged zone. The post-failure material behaviors implemented in some material models of LS-DYNA are used to predict the damage distribution. The impact test is currently one of the experimental tests used to fit the damage parameters. The hat-profiles are used as representative components tests and they are an important validation step of the composite modeling, as they represent the bridge between the elementary specimens and composite parts. They are also an additional experiments to investigate the damage localization and geometrical effects.

The scatter observed in the experiments is commonly assessed using statistical coefficients as the standard deviation. As no value of material properties can be reported here, this indicator was found to

be not representative enough of the deviation occurring in the results. The coefficient of variation allows to evaluate the percentage of variation in comparison to the average value. This indicator corresponds to the ratio between the standard deviation and the average and it is expressed in percentage. Moreover, it gives a striking assessment of the scatter observed in experiments. The coefficient of variation is calculated for the effective material properties obtained by the corresponding experimental tests and it has been used (when possible) to assess the scatter observed in the testing campaign.

Special thanks are addressed to Daniel Frede, Dr. Thomas Sommer-Dittrich and their colleagues at Daimler AG for the organization of the experimental tests.

3.1 Experimental tests on a RTM carbon plain weave presenting outer glass mat layers

The composite material considered here is a T700 carbon fiber plain weave textile embedded in an epoxy resin and manufactured via a RTM process. The dry textile presents a surface weight about $330g/m^2$. The material has a thickness about 2mm and a stacking sequence constituted by five woven plies. A fiber volume fraction about 47% has been experimentally estimated based on the standard ISO 14127. Quasi-static tensile, compressive, shear and bending tests have been conducted on elementary specimens and the results are reported in the next sections. Stress vs. strain curves and pictures illustrating failure are also presented. The stresses σ are calculated by the ratio between the force F measured by the traction machine over the cross section A of the specimen, that is assumed to be constant and equal to the initial one. For the in-plane traction and compression tests, the strain is determined either from the displacement of the traction machine or from a strain gauge glued on the specimen.

3.1.1 Longitudinal tensile tests

Quasi-static tensile tests have been conducted on 2mm thick $250mm \times 25mm$ specimens following the DIN ISO 527-4 standard. The stress vs. strain curves presented on Fig. 3.1 shows a linear behavior of the material up to failure, when it is loaded in a longitudinal direction. The longitudinal direction means here that the load direction is parallel to the warp or weft direction, since no distinction between the two in-plane yarn directions of the textile has been made. Only two specimens over three gave suitable experimental data. Considering the discontinuous behavior and the low number of repetition, no statistical assessment has been made here.

Fig. 3.2 presents several views of the failure location. One specimen failed in the middle of the coupon (see Fig. 3.2a), whereas failure happened closer to the end tabs for the two other specimens. Failure occurred suddenly but not so explosive, as it is generally observed for unidirectional laminated. The fracture surface is here normal to the load direction. Ultimate failure of the specimen is caused by the failure of the fibers and of the yarns (see Fig. 3.2 b, c and d). Fig. 3.3 presents a microscopic view of the failed material. On the left, the micrograph shows the brittle failure of the fibers and of the yarns. On the right, different kinds of cracks propagating away from the failure location are observed. Some cracks evolve along the longitudinal yarns whereas other cracks propagate through the transverse yarns. Different crack sizes can also be noticed. The largest cracks evolve quite following a line, whereas the smallest cracks find their way between the fibers changing often their direction.

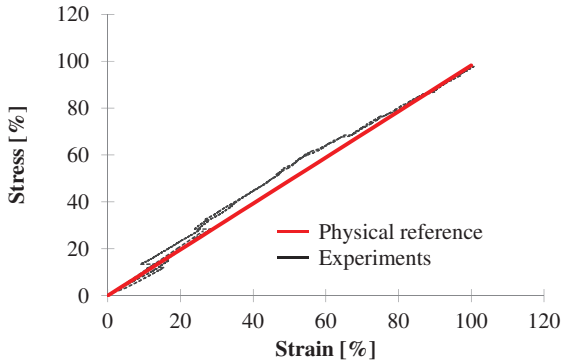

Figure 3.1: Experimental results for the quasi-static longitudinal tension

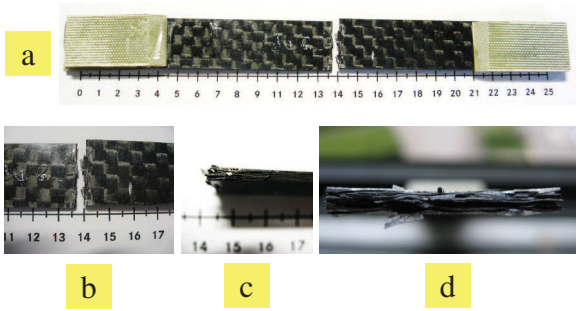

Figure 3.2: Analysis of the failure modes for the longitudinal tension: a) overview of the specimen, b) zoom on the failure location, c) view of the failure location from the left side, d) view of the failed cross-section

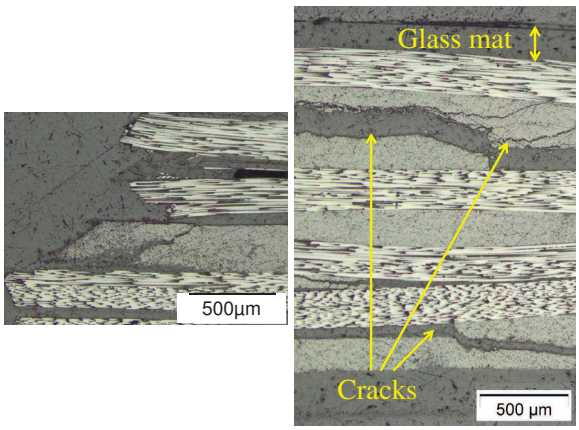

Figure 3.3: Analysis of the failure modes for the longitudinal tension: failure of the yarns (left) and view of some crack propagation away from the failure location (right)

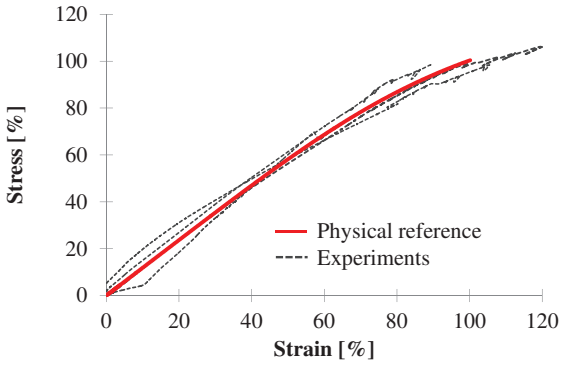

Figure 3.4: Experimental results for the quasi-static longitudinal compression

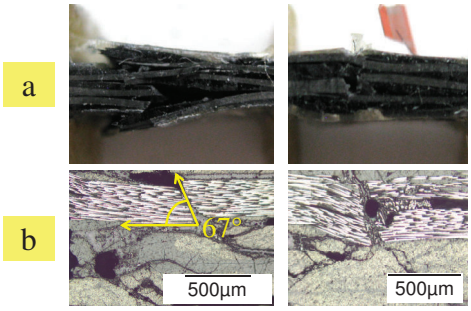

Figure 3.5: Analysis of the failure mode for the longitudinal compression: a) macroscopic failure of two specimens, b) micrographs of the failure location for two specimens

3.1.2 Longitudinal compressive tests

Quasi-static longitudinal compressive tests have been conducted on 2mm thick $100mm \times 10mm$ specimens following the DIN ISO 14126 standard and using type A specimen. As presented on Fig. 3.4, a nonlinear behavior of the stress vs. strain curves has been observed for the three tested coupons. Moreover, the initial stiffness in compression was found to be about 18% lower than the corresponding stiffness in tension. A coefficient of variation about 15.5% has been computed concerning the strength. This statistical coefficient is about 10% regarding the Young's modulus. Fig. 3.5 shows different views of the specimen failure. Fig. 3.5a presents a photography of the failure location for two different specimens. The picture on the left shows a quite-explosive failure, whereas the picture on the right presents a more brittle failure following the cross-section plane of the specimen. Fig. 3.5b shows micrographs of the failure location for two specimens. The failure of the yarns occurred following an angle about 67° with the load direction. The specimen type used to conduct these tests presents a very small free-zone (area without end tabs) about $10mm \times 10mm$, where the specimen failure can happen. For this plain weave textile, the average wavelength of the yarn undulation has been estimated about 4640μm with a lower bound about 3550μm and an upper bound about 6450μm. Consequently, the free-zone of the specimen is hardly able to represent a full-wave of the yarn. It can explain the different failure modes experimentally observed for the longitudinal compression load case. Moreover, the averaged amplitude of the yarn undulation has been estimated about 167μm with a lower bound about 110μm and an upper bound about 270μm.

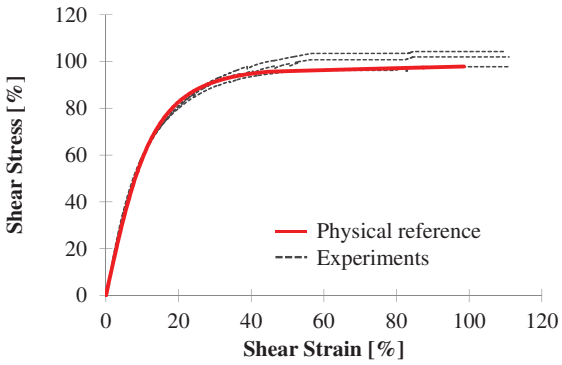

Figure 3.6: Experimental results for the quasi-static shear tension

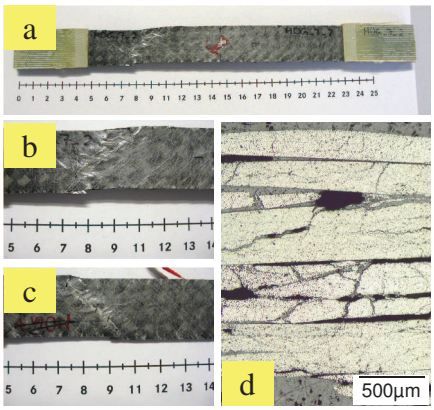

Figure 3.7: Analysis of the failure modes for the tensile shear: a) representative macroscopic failure, b) and c) zoom on the failure location, d) micrograph of the failure location

3.1.3 Shear tests

3.1.3.1 Tensile shear tests

Quasi-static shear tensile tests have been conducted on 2mm thick $250mm \times 25mm$ specimens following the ISO 527-4 standard. For these specimens, the two in-plane fiber directions of the textile depict a $\pm 45°$ angle with the direction of traction. The results are presented on Fig. 3.6. The shear stress vs. shear strain curves show a clear nonlinear behavior. Finally, a coefficient of variation about 3% and 11.5% have been respectively obtained concerning the shear modulus and the stress at 5% shear strain. Fig. 3.7 shows different views of the failure zone. Fig. 3.7a presents the macroscopic failure of a specimen under shear tensile loads. A failure with an angle about 45° to the load direction is observed. It is a common failure mode of composite laminates under such shear loading paths. Fig. 3.7b and Fig. 3.7c show a zoom on failure of the specimen. No large fiber breakage and no catastrophic failure of the specimen with complete fracture is observed. Finally, Fig. 3.7d presents a microscopic view of the failure location. Several cracks evolve through the yarns, some cracks evolve along the envelope of a yarn and other propagate through the thickness of the material. Failure in shear is thus characterized by the propagation of many cracks in the material leading to a progressive decrease of the stiffness contributing to the nonlinear behavior observed experimentally.

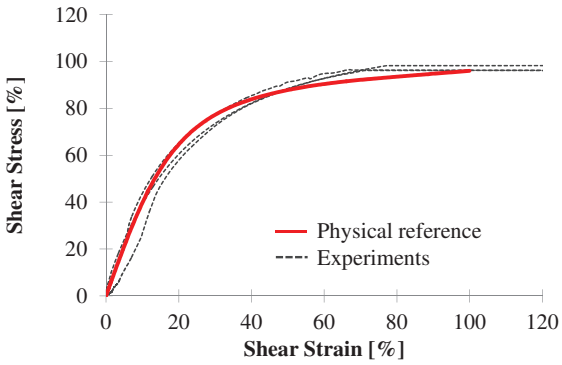

Figure 3.8: Experimental results for the quasi-static shear compression

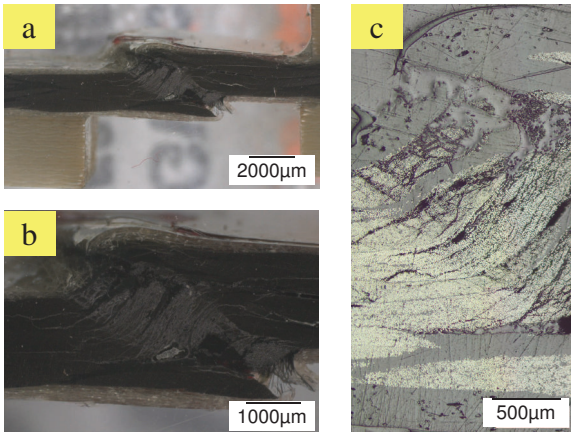

Figure 3.9: Analysis of the failure mode for the compressive shear: a) representative macroscopic failure, b) zoom on the representative failure location, c) micrograph of the failure location

3.1.3.2 Compressive shear tests

Quasi-static shear compressive tests have been conducted on $2mm$ thick $100mm \times 10mm$ specimens following the DIN ISO 14126 standard and the type A specimen. The two in-plane fiber directions of the textile depict a $\pm 45°$ angle with the load direction. As presented on Fig. 3.8, a nonlinear behavior (quite symmetrical to the corresponding shear tensile behavior presented above) of the shear stress vs. shear strain curves has been observed for the three tested specimens. A coefficient of variation about 4% is obtained regarding the stress at failure, whereas a relatively high deviation (more than 20% for the coefficient of variation) has been observed concerning the stiffness modulus Fig. 3.9a and Fig. 3.9b shows the representative failure modes of a specimen under a compression in shear. The specimen presents no explosive failure. Few fiber failures can be observed except on the outer side of the specimen. Failure location depicts a kind of wave and the yarn undulation is probably responsible for this particular failure mode. The failure surface makes an angle about 45° with the load direction, similarly as in tension. Fig. 3.9c presents a micrograph of the failure location. On this picture it is clear that many cracks and micro-cracks propagate in the material.

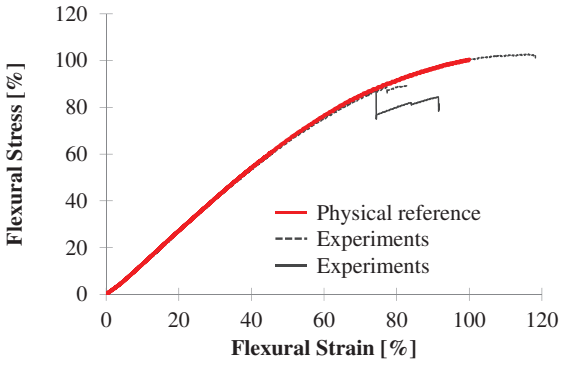

Figure 3.10: Experimental results for the quasi-static longitudinal three-point-bending

3.1.4 Three-point bending tests

Longitudinal and diagonal quasi-static three-point-bending tests have been conducted on 2mm thick $100mm \times 15mm$ specimens following the DIN ISO 14125 standard and the class IV specimens. A longitudinal bending means that the warp or the weft direction is parallel to the specimen length. A diagonal bending means that the warp and weft directions depict a $\pm 45°$ angle with the length of the specimen. The experimental flexural stress vs. outer surface strain (flexural strain) curves are presented in the next sections. These curves are obtained from the corresponding force vs. machine displacement curves captured during the tests and using the calculation method described in the ISO 14125 standard. It allows to reduce the scatter of the force vs. machine displacement curves due to the non-negligible variations in the width and thickness of the specimens coming from the process used for the specimen preparation.

3.1.4.1 Longitudinal three-point-bending

Fig. 3.10 presents the experimental flexural stress vs. strain of the outer surface for the longitudinal bending. A non-linear behavior is observed until failure. A non-negligible scatter for the failure stress and strain occurred. As only three specimens have been tested the physical reference defines the failure point as an average of the different stresses and strains at failure obtained experimentally. Finally, a coefficient of variation lower than 1% has been computed regarding the flexural modulus. Concerning the flexural stress at failure, this coefficient has a value close to 9%, which is still acceptable.

Fig. 3.11 presents two representative failure modes for the longitudinal bending load. Pictures on the left show a failure in compression, as only the upper side of the specimen presents a breakage. Pictures on the right show a complete failure of the coupon. This difference is due to the textile structure. The wavelength is relatively large compared to the specimen dimensions and the three-point-bending induces a localized failure in the middle of the specimen. Consequently, the failure mode is likely to depend on the internal material structure immediately under the loader. An abrupt failure of the yarns is observed in both cases.

3.1.4.2 Diagonal three-point-bending

Fig. 3.12 presents the experimental flexural stress vs. flexural strain for the diagonal bending. A non-linear behavior is observed until failure and an acceptable scatter is observed. The physical reference is also here represented by the average of the three material responses obtained experimentally. Fig.

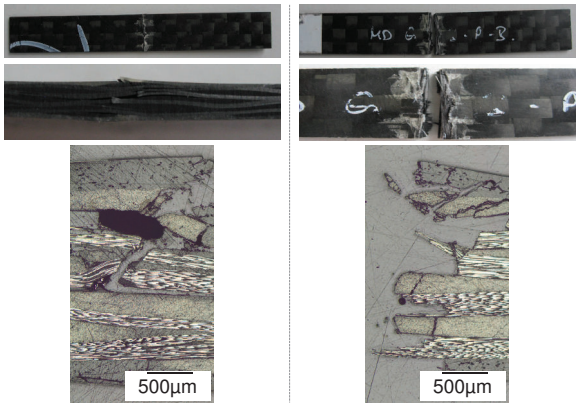

Figure 3.11: Analysis of the failure modes for the longitudinal three-point bending: photography of the compressive fracture of the specimen (top left), micrograph of the compressive fracture (bottom left), photography of the full-fracture of the specimen (top right) and micrograph of the full-fracture (bottom right)

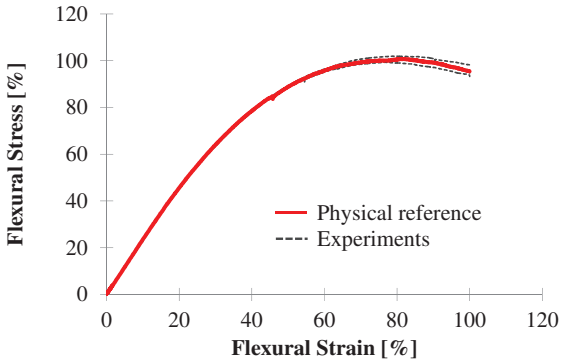

Figure 3.12: Experimental results for the quasi-static diagonal three-point bending

Figure 3.13: Failure analysis for the diagonal bending

3.13 presents two pictures of a specimen under diagonal bending. No failure occurred and a permanent deformation is clearly visible. Due to the large deformation, the tests had to be stopped before any potential failure of the specimen. A coefficient of variation about 5.4% is observed for the flexural modulus. This coefficient has a value of 1.25% regarding the flexural stress at the end of the test.

3.2 Experimental tests on a RTM carbon plain weave without glass mat

In this part, the experimental tests conducted on a RTM carbon plain weave composite are presented. The material is here similar as the one described in the section 3.1 but without the glass mat as outer layers. The experimental results used to determine the effective properties of the material will be presented first. Then, impact tests on small coupon plates and representative component tests (impact on hat-profiles) will be reported.

3.2.1 Experimental determination of the effective material properties

In this section, the quasi-static tensile, compressive and four-point bending tests conducted on 2.4mm thick elementary specimens are presented. The laminated material is constituted by six carbon plain weave layers. For each load case, the figures show a representative picture of the failure mode and the stress vs. strain graphs. For each load case, six repetitions have been conducted. A testing speed about $2mm/min$ has been used for all these quasi-static tests. Tensile tests have been conducted following the DIN ISO 527-4 standard. Compressive tests are based on the DIN ISO 14126 standard and type B2 specimens ($125mm \times 25mm$) have been used. Finally, four-point bending tests refer to the DIN ISO 14125 standard and class IV specimens have been considered.

3.2.1.1 Longitudinal tensile tests

Fig. 3.14 presents the results for the quasi-static longitudinal tensile tests. Both warp and weft directions have been investigated and similar results for both directions have been observed. The continuous lines show the results for the warp direction and the dashed lines represent the results for the weft direction. A linear behavior up to the strength is obtained for this material, when loaded in tension parallel to a yarn direction. The photography shows a failure of the specimen at two locations away enough from the end tabs. A fracture surface orthogonal to the load direction is observed without explosive failure.

Table 3.1 presents the coefficients of variation concerning the stiffness, the strength and the strain at failure for the longitudinal tension. A distinction between the warp and weft directions has been made. A

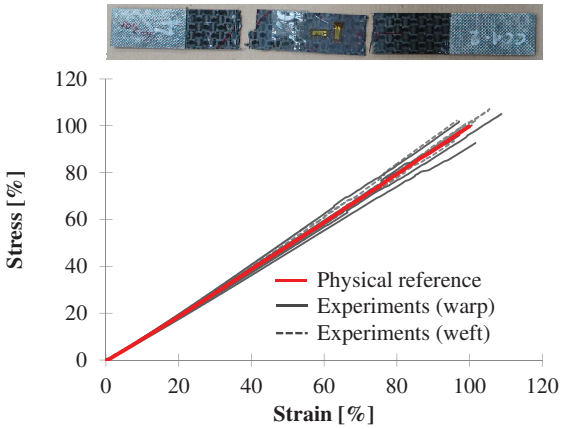

Figure 3.14: Experimental results for the longitudinal tension: representative failure (top) and stress vs. strain material response (bottom)

Table 3.1: Coefficients of variation (in %) for the effective material properties in longitudinal tension

Load case	Stiffness	Strength	Strain at failure
Tension in warp direction	2.26	4.91	4.35
Tension in weft direction	4.75	4.48	4.20

coefficient of variation lower than 5% is obtained for these effective material properties in both directions of traction. Consequently, the scatter observed in the experimental results is acceptable.

3.2.1.2 Longitudinal compressive tests

Fig. 3.15 presents the results for the quasi-static longitudinal compressive tests. Both warp and weft directions have been investigated and similar results for both directions have been observed. The continuous lines show the results for the warp direction and the dashed lines represent the results for the weft direction. A clear nonlinear behavior up to the strength is obtained for this material, when loaded in compression parallel to a yarn direction. The photography shows a failure of the specimen unfortunately relatively close to the tabs, which propagates through the thickness of the specimen.

Table 3.2 presents the coefficients of variation concerning the stiffness, the strength and the strain at failure for the longitudinal compression. A distinction between the warp and weft directions has been made. A coefficient of variation lower than 5% is obtained for all effective material properties in the weft direction. A low dispersion is observed concerning the stiffness for both directions. However, a larger scatter appears concerning the strength and the strain at failure for the warp direction. Consequently, it shows that this kind of compressive tests is likely to be more sensitive to different factors than the tensile tests described above. Fiber undulation in the free-zone of the specimen, fiber alignment to the load direction, defects inherent to the material or experimental set up can be identified as potential sensitivity factors being likely to cause a scatter in the experimental results.

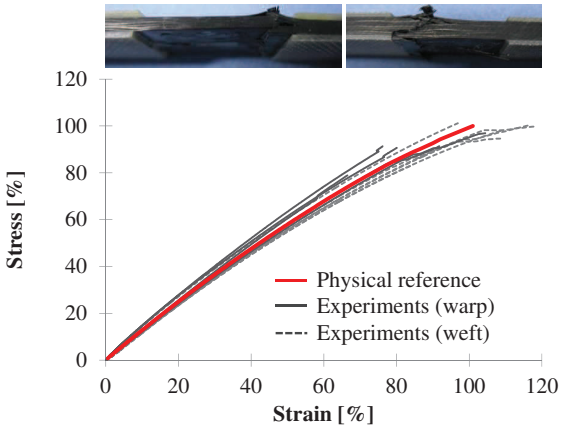

Figure 3.15: Experimental results for the longitudinal compression: representative failure (top) and stress vs. strain material response (bottom)

Table 3.2: Coefficients of variation (in %) for the effective material properties in longitudinal compression

Load case	Stiffness	Strength	Strain at failure
Compression in warp direction	1.41	7.19	10.2
Compression in weft direction	0.77	2.20	3.55

3.2.1.3 Tensile shear tests

Fig. 3.16 presents the results for the quasi-static shear tensile tests. The textile yarns depict here an angle about 45° with the direction of traction. No distinction between warp and weft direction has been made. A common nonlinear behavior up to the strength is obtained for this material when loaded in shear. The photography shows a representative failure of the specimen away enough from the end tabs. A common matrix failure is responsible for the large deformation observed experimentally and interpreted as the specimen failure. The coefficient of variation is about 1.66% concerning the shear stiffness modulus. An acceptable dispersion about 2.5% for the shear strength is observed at 5% shear strain.

3.2.1.4 Compressive shear tests

Fig. 3.17 presents the results for the quasi-static shear compressive tests. The textile yarns depict here an angle about 45° with the direction of compression. No distinction between warp and weft direction has been made. A common nonlinear behavior up to the strength is obtained for this material when loaded in shear. The photography shows a representative failure of the specimen. A common matrix failure is responsible for the specimen failure. No large fracture can be observed, but only large local deformation and resin failure. The coefficient of variation is about 8.6% concerning the shear stiffness modulus. This relatively high value of the dispersion indicator confirms that compressive tests are likely to be more sensitive to the experimental set-up or to the material structure than tensile tests. An acceptable dispersion about 1.9% for the shear strength is observed at 5% shear strain.

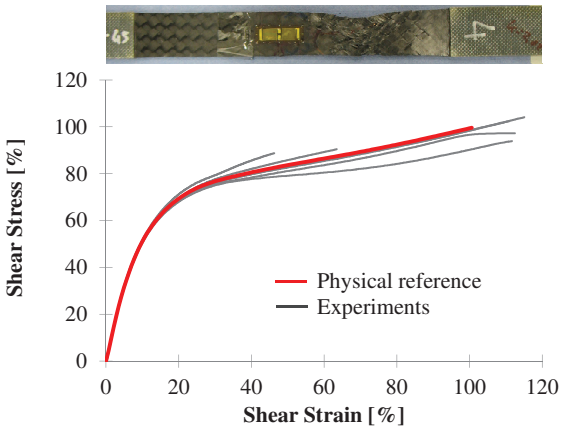

Figure 3.16: Experimental results for the shear tensile tests: representative failure (top) and shear stress vs. shear strain material response (bottom)

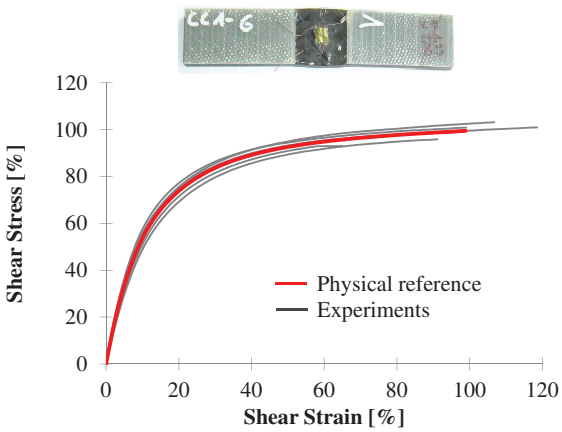

Figure 3.17: Experimental results for the shear compressive tests: representative failure (top) and shear stress vs. shear strain material response (bottom)

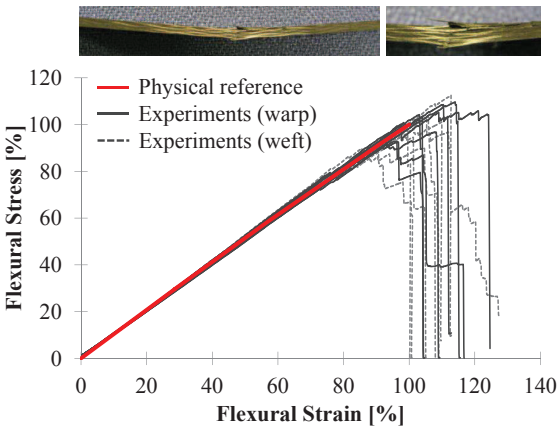

Figure 3.18: Experimental results for the longitudinal bending: representative failure (top) and flexural stress vs. flexural strain material response (bottom)

Table 3.3: Coefficients of variation (in %) for the flexural stiffness, strength and strain at failure for the longitudinal four-point bending tests

Load case	Bending modulus	Flexural strength	Flexural strain at failure
Bending in warp direction	1.21	5.38	9.99
Bending in weft direction	1.80	4.86	7.65

3.2.1.5 Longitudinal four-point bending tests

Bending pre-tests have been conducted using the three-point bending method. This kind of bending tests induces relatively high compressive contact stresses and a localized load distribution under the single loading piston. The four-point bending tests offer a constant bending moment and a uniform load distribution between the two central loaders. Considering the structure of the textile, the material behavior (particularly failure) is likely to depend on the position of the loader on the wavy yarn if too localized loading conditions are applied. Consequently, quasi-static four-point bending tests have been conducted now to investigate the bending properties of the woven composites. Fig. 3.18 presents the results for the quasi-static longitudinal four-point bending tests on class IV specimens. Both warp and weft directions have been investigated and similar results for both directions have been observed but with a non-negligible scatter, regarding the strain at failure. The continuous lines show the results for the warp direction and the dotted lines represent the results for the weft direction. The flexural stresses and strains have been here computed following the equations developed for large deformations, as described in the ISO 14125 standard. A quasi-linear behavior up to the strength has been captured. The photography shows a representative compressive failure of the specimen occurring in the inner span or below the loaders. Few specimens present a failure in tension or a full specimen fracture.

Table 3.3 presents the coefficients of variation concerning the bending stiffness, the flexural strength and the flexural strain at failure (flexural strain at the maximal force peak) for the longitudinal four-point bending. A distinction between the warp and weft directions has been made. Acceptable values of the coefficient of variation are obtained concerning the bending modulus and the flexural strength. Higher values are observed concerning the flexural strain at failure.

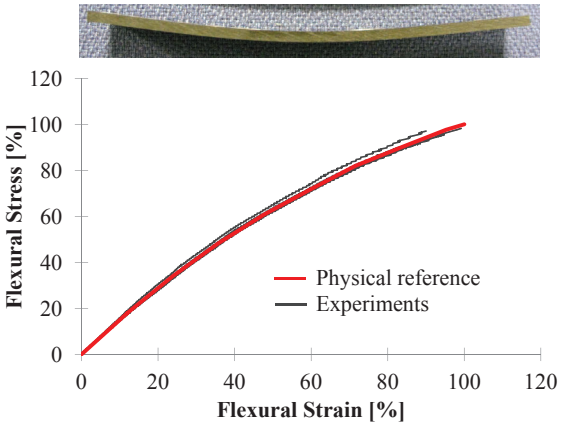

Figure 3.19: Experimental results for the diagonal bending: representative failure (top) and flexural stress vs. flexural strain material response (bottom)

Table 3.4: Coefficients of variation (in %) concerning the bending stiffness, maximal flexural stress and maximal flexural strain for the diagonal four-point bending tests

Load case	Bending modulus	Max. flexural stress	Max. flexural strain
Diagonal bending	2.90	2.41	5.60

3.2.1.6 Diagonal four-point bending tests

Fig. 3.19 presents the results for the quasi-static diagonal four-point bending tests on class *IV* specimens. The flexural stresses and strains have been computed following the equations developed for large deformations as described in the ISO 14125 standard. A nonlinear behavior up to the strength has been captured. The photography shows that a permanent deformation is observed but no failure happens. The coefficients of variation for the bending stiffness, the maximal flexural stress and the maximal flexural strain are presented in the Table 3.4. The values of the dispersion indicator are acceptable and they confirm the low scatter observed for the material response.

3.2.2 Impact tests and representative component tests

3.2.2.1 Impact tests on elementary plates

In this section, the experimental impact tests made on elementary plates are presented. These impact tests are based on the well-known compression after impact (C.A.I.) experiments referring to the DIN EN 6038 standard. The experimental set-up is described in Fig. 3.20. The test specimen relies on a fixture base. The position of the sample is maintained using rubber-tipped clamps. The compression after impact used to investigate the remaining compressive strength is not presented here. The test specimen is a 4mm thick $150mm \times 100mm$ composite plate. A $[0°/45°/0°/45°/0°]_s$ multidirectional stacking sequence is considered and two orientations (0° and 45°) have been investigated. To simplify the manufacturing of the composite plates, a unique stacking sequence has been firstly produced and the cutting direction of the plates defines the two considered orientations as described in Fig. 3.20. The impacting mass has a diameter about 16mm. The mass of the impactor has been modified in function of the wished impact energy. Three impact energies have been considered: 5J, 25J and 50J. For each

Table 3.5: Overview of the impact energies and the corresponding impacting mass and impact velocity

Impact energies [J]	Impacting Mass [kg]	Impact velocity [m/s]
5	2	2.24
25	5	3.16
50	7	3.78

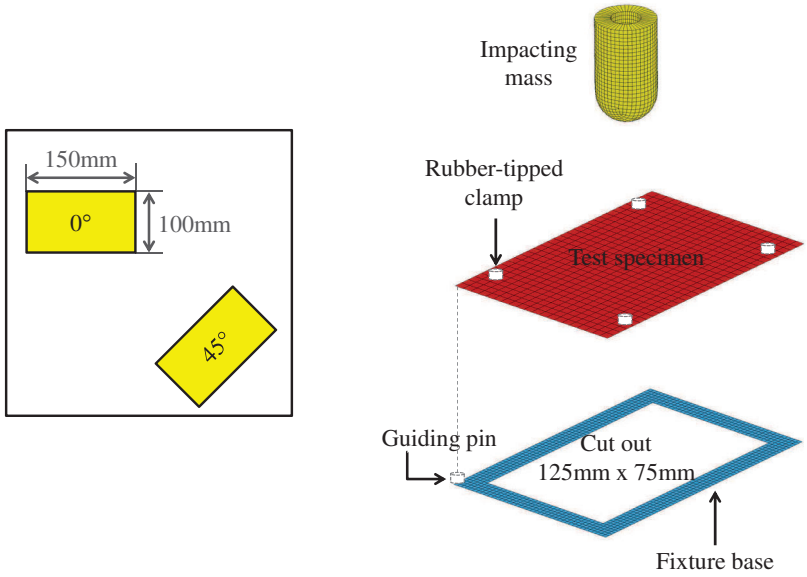

Figure 3.20: Cutting plan of the test specimen (left) and experimental set up (right)

energy and specimen cutting direction, four samples have been impacted. An overview of the impact energies and the corresponding impacting mass and impact velocity is presented in the Table 3.5. After the impact, an ultra-sound (C-SCAN) analysis allowed to determine the maximal projected damaged and/or delaminated area of the test specimen. For each impacting energy and cutting orientation, the following curves are considered: displacement of the impactor vs. time, resultant force vs. time and resultant force vs. displacement of the impactor. It represents the quantitative analysis of the impact test. A representative picture of the front and back sides of the plates and a representative result of the ultra-sound analysis are also reported, which corresponds to the qualitative analysis of the impact test. The tests have been conducted at the university of Girona AMADE.

Fig. 3.21 presents the experimental results for a 5J impact. The curves show a similar material response for both orientations. No clearly visible damage is observed on the test specimens. The C-SCAN analysis shows an averaged damaged zone about $89mm^2$ for the 0° orientation and about $119mm^2$ for the 45° orientation. For both cutting directions, a low dispersion appears in the experimental curves whereas a higher scatter has been observed for the evaluation of the damaged surface.

Fig. 3.22 presents the experimental results for a 25J impact. The curves show a similar material response for both orientations. A small visible damage is observed on the test specimens, particularly on the back side of the sample. The C-SCAN analysis shows an averaged damaged zone about $734mm^2$ for the 0° orientation and about $863mm^2$ for the 45° orientation. For both cutting directions, a similar

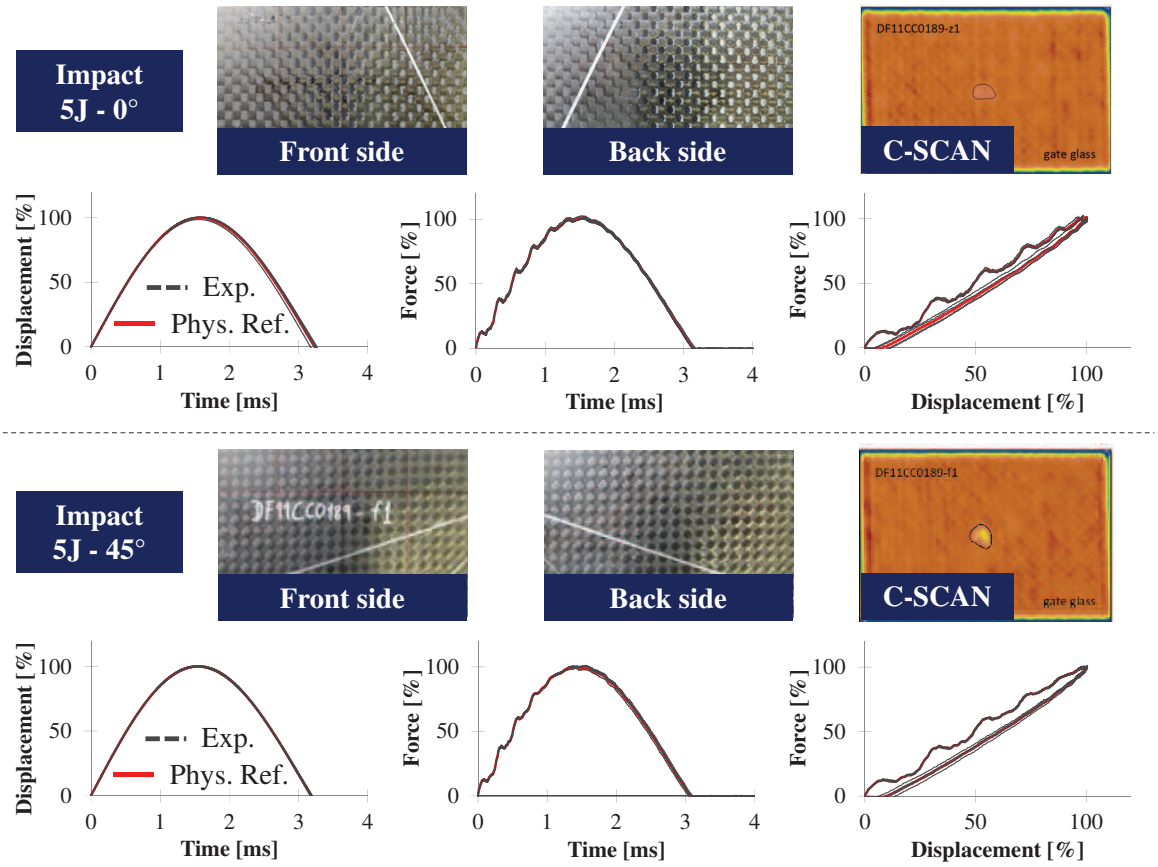

Figure 3.21: Experimental results of the 5J impact tests for the 0° and 45° orientations

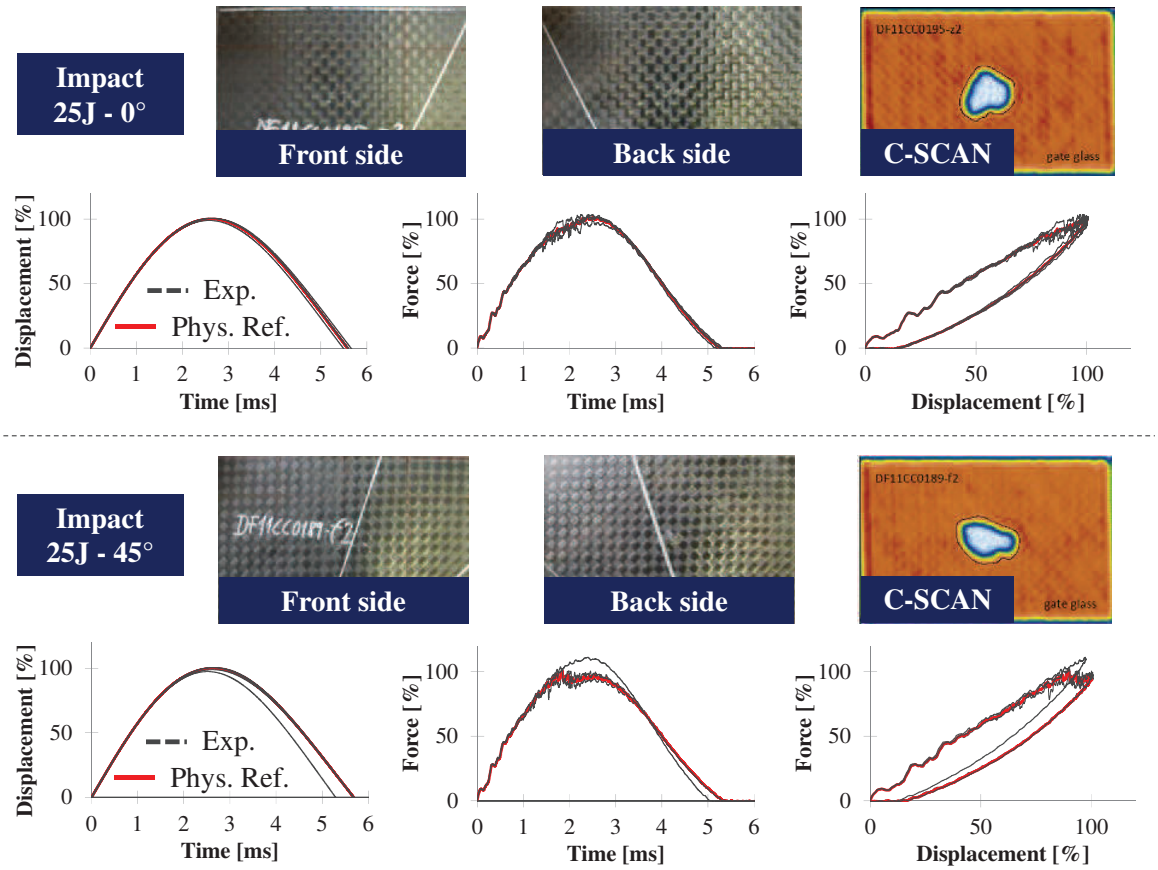

Figure 3.22: Experimental results of the 25J impact tests for the 0° and 45° orientations

dispersion appears in the experimental curves and in the evaluation of the damaged surfaces except for one test in the 45° direction.

Fig. 3.23 presents the experimental results for a 50J impact. The curves show a similar material response for both orientations. A visible damage is observed on the test specimens. A compressive fracture occurred on the front side and a tensile collapse appeared on the back side of the sample. The C-SCAN analysis shows an averaged damaged zone about $1078mm^2$ for the 0° orientation and about $1097mm^2$ for the 45° orientation. A similar dispersion appears in the experimental curves and in the evaluation of the damaged surfaces for both orientations. Due to the quite perforation and the high damage level in the plate, the curve of the reaction force presents a clear decrease after the force peak. A quite constant force level follows until the unload of the plate. This decrease of the force shows a considerable intralaminar and interlaminar failure of the material.

Fig. 3.24 presents a comparison of the experimental results for the three impact energies. A similar material response is obtained for both orientations. Similar force levels are reached for the 50J and the 25J impact energies, whereas the maximal impactor displacement for 25J reached only 65% of the maximal impactor displacement at 50J. The comparison of the representative damaged surfaces uses the same color code than in the curves. The damaged area increases logically, when the impact energy increases. The shape of the damaged areas comes from a representative C-SCAN giving a delaminated zone close to the averaged one.

The Tables 3.6 and 3.7 present respectively for the 0° and the 45° orientations the coefficients of

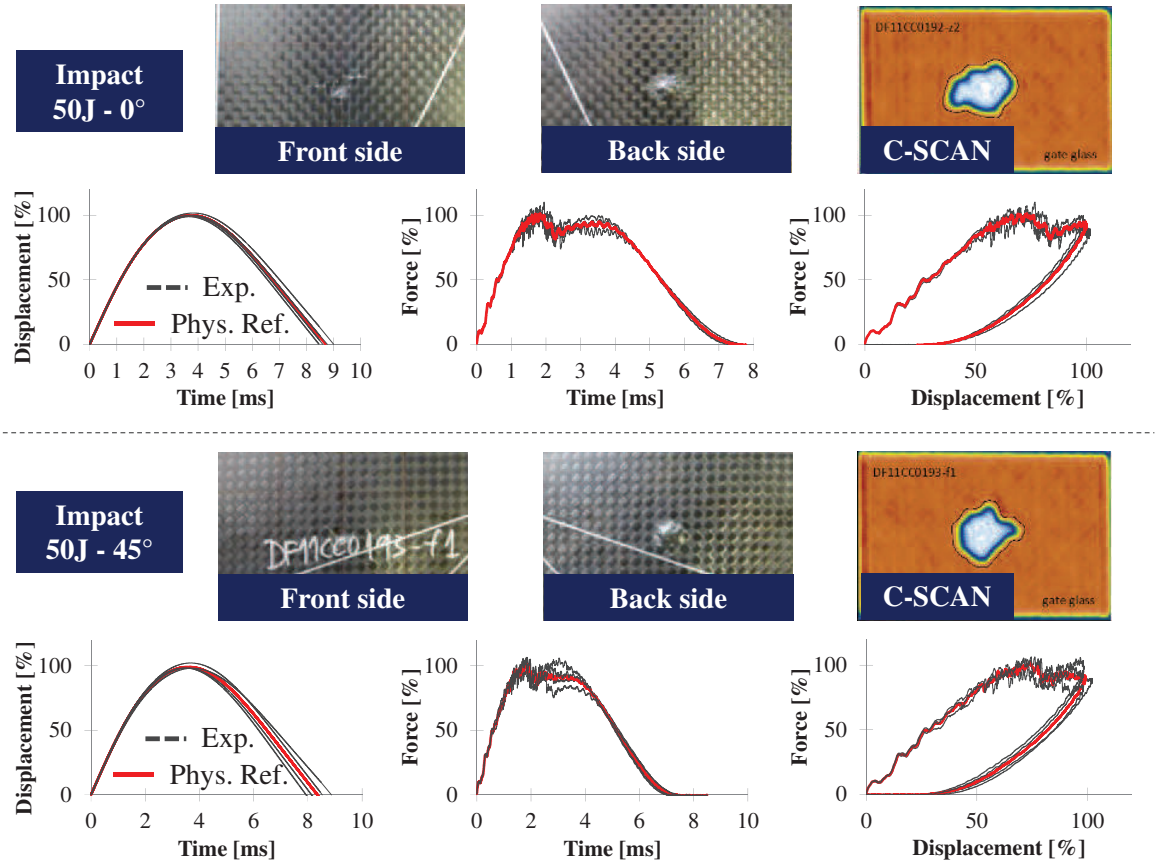

Figure 3.23: Experimental results of the 50J impact tests for the 0° and 45° orientations

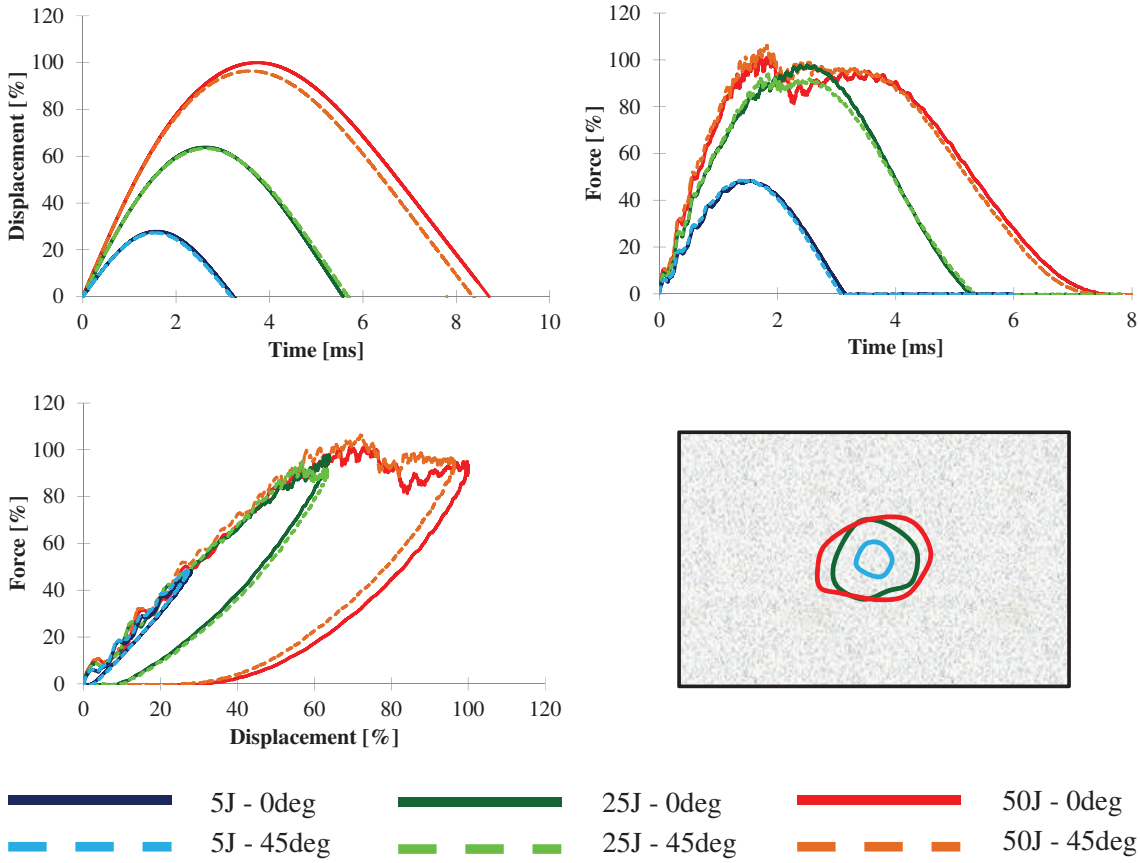

Figure 3.24: Comparison of the experimental results (material response and damaged surfaces) for the three impact energies and for both 0° and 45° orientations

Table 3.6: Coefficients of variation (in %) concerning the maximal impactor's displacement, the maximal force peak and the damaged surfaces for the impact tests on the RTM material and the 0° orientation

RTM - 0°	5J	25J	50J
Maximal displacement	0.9	0.8	1.1
Maximal force peak	1.0	1.8	2.8
Damaged surfaces	66.3	9.99	10.9

Table 3.7: Coefficients of variation (in %) concerning the maximal impactor's displacement, the maximal force peak and the damaged surfaces for the impact tests on the RTM material and the 45° orientation

RTM - 45°	5J	25J	50J
Maximal displacement	0.5	1.5	2.2
Maximal force peak	0.4	4.7	1.9
Damaged surfaces	59.0	17.4	7.1

variation concerning the maximal impactor's displacement, the maximal force peak and the damaged surfaces for the impact tests on the RTM specimens. For both orientations, a low dispersion is observed for each impact energy regarding the displacement of the impactor and the maximal force peak. It is also in agreement with the low scatter observed on the curves. A large dispersion can be remarked for the determination of the damaged areas induced by a 5J impact. An acceptable dispersion is reported for both 25J and 50J energies of impact regarding the damaged zones.

3.2.2.2 Representative component tests: drop tower tests on hat-profiles

In this section, the experimental results of drop tower tests made on 2mm thick hat-profiles are presented. The hat-profiles offer a more complex geometry than the flat elementary coupons and they are used as representative components. They constitute the last validation step on standard coupons before the simulation of real automotive composite parts or of full-size car models. Hat-profiles represent a very important step for the validation of the material parameters determined using elementary coupons, of the modeling techniques (element type, mesh size, numerical material model) and of the methodology of the material characterization (building block approach described in 1.2). Additionally to the different validations, these representative components tests allow to assess the effects induced by a more complex geometry on the material behavior. In these tests, the specimen is made up with five carbon plain weave composite plies and it presents the $[45°/0°/45°/0°/45°]$ multidirectional stacking sequence. As only two repetitions of this test have been conducted, no statistical analysis is presented.

Fig. 3.25 presents the dimensions of the hat-profile and the experimental set-up for 200J impacts on hat-profiles. A 2mm thick steel plate is riveted on the specimen to avoid its flattening during the impact phase. The position of the rivets and the experimental set-up are detailed on the picture on the right. The tests are assimilated to three-point bending impact tests, where the span is about 400mm. The supports and the impacting mass have a diameter of 50mm. The impactor's mass is about 214kg and the impact speed is about $1.37m/s$.

Fig. 3.26 presents the experimental results for a 200J impact on a RTM hat-profile. Two repetitions

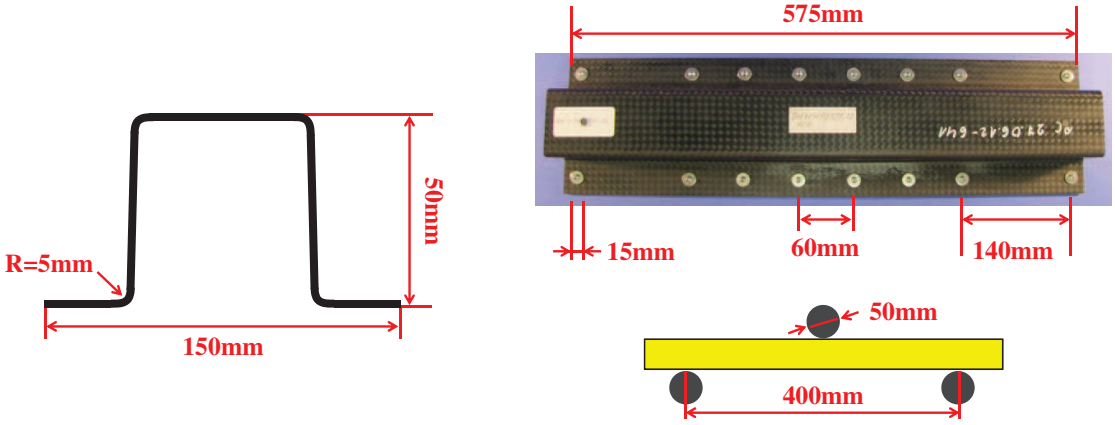

Figure 3.25: Experimental set-up for the 200J drop tower tests on hat-profiles: dimensions of the specimen (left), experimental set-up and specimen preparation (right)

have been conducted and the results are similar for both impacts. Fig. 3.26a) shows a side-view of the complete hat-profile after the impact. Failure is localized in the middle of the specimen below the impactor. Fig. 3.26b) and c) show respectively a side view and a top view of failure. A clear fracture surface is observed on the top, left and right flat sides of the specimen. The parts of the hat-profile, where the rivets are fastened underwent no clear failure, but a large bending deformation. A fragmentation of the material and a kind of explosive failure are observed in the corners. The progressive failure of the hat-profile begins with a first collapse in the corners and of the top side. Then, buckling can be observed on the vertical sides before ultimate failure. The constant force level is mainly due to the friction at the fracture plane and to the deformation of the steel plate.

3.3 Experimental tests on a PREPREG carbon twill weave

The composite material considered here is a T700SC 60E carbon fiber twill-weave textile embedded in an epoxy resin with 12K filaments. The dry textile presents a surface weight about $660g/m^2$. Each woven composite ply presents a thickness about 0.67mm. The fiber volume fraction is estimated by the manufacturer about 56%. The laminate is manufactured in an autoclave using pre-impregnated (PREPREG) twill-weave tapes. Quasi-static tensile, compressive, shear and bending tests have been conducted on elementary specimens and the results are reported in the next sections. Stress vs. strain curves and pictures illustrating failure are presented. The stresses σ are calculated by the ratio between the force F measured by the traction machine over the cross section A of the specimen, assumed to be constant and equal to the initial one. For the in-plane traction and compression tests, the strain is determined either from the displacement of the traction machine or from a strain gauge glued on the specimen.

3.3.1 Experimental determination of effective material properties

In this section, the quasi-static tensile, compressive and four-point bending tests conducted on elementary specimens are presented. For each load case, the figures show a representative picture of the failure mode and the normalized stress vs. strain material response. The coefficient of variation, calculated for the

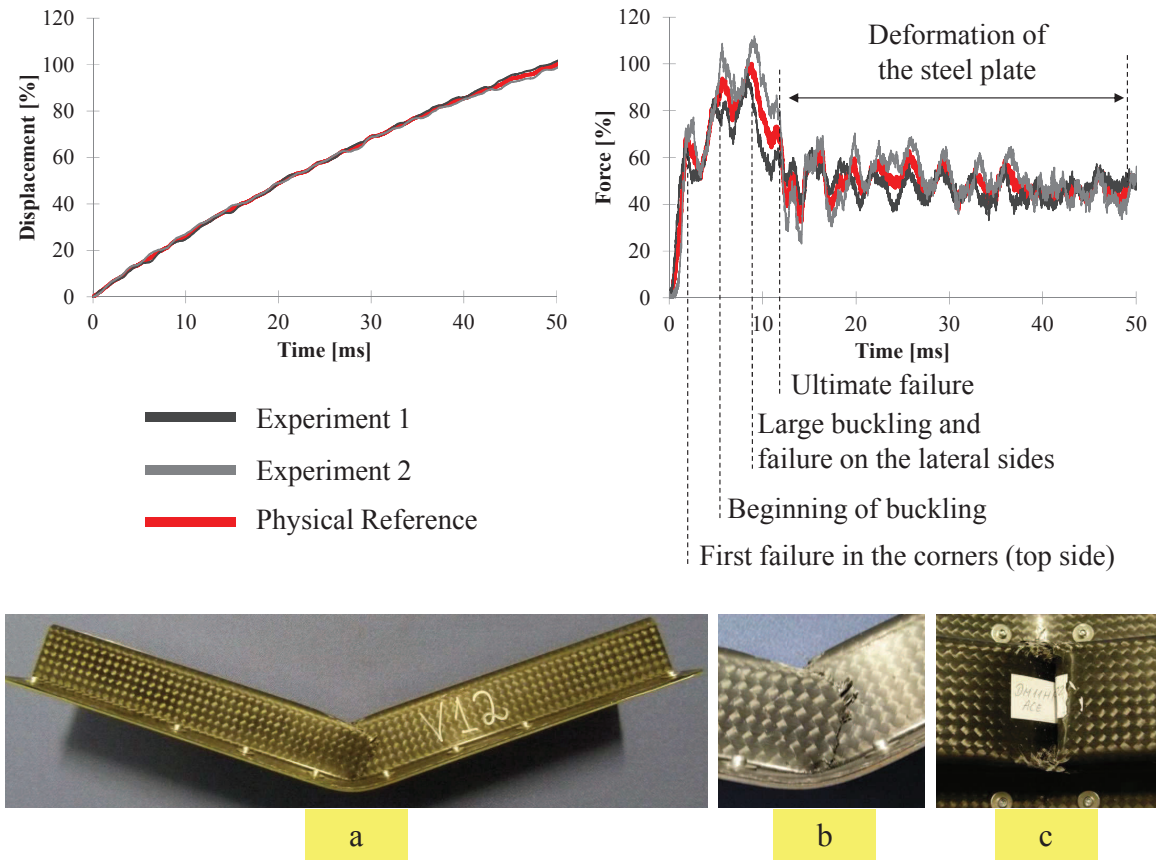

Figure 3.26: Experimental results for the 200J drop tower tests on hat-profiles: displacement vs. time and force vs. time (top), a) side view of the hat-profile after impact - b) side view and zoom on failure - c) top view and zoom on failure

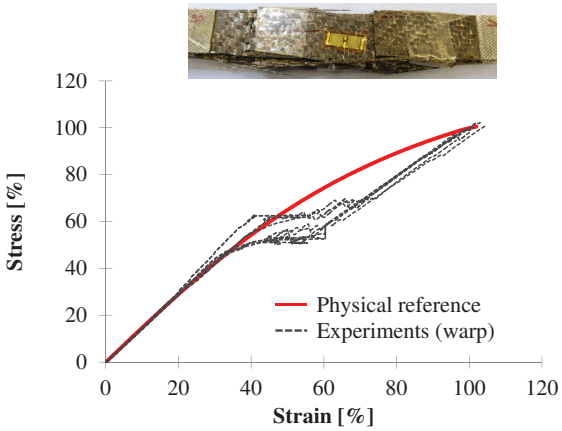

Figure 3.27: Experimental results for the longitudinal tension: representative failure (top) and stress vs. strain material response (bottom)

effective material properties obtained by the corresponding experimental tests, has been used to assess the scatter observed in the experimental test series. Tensile tests have been conducted on $\pm 45°$ specimens to characterize the behavior in shear. The shear stress vs. shear strain material response captured during the tests will be directly used as a load curve to predict numerically the shear behavior of the material.

3.3.1.1 Unidirectional tensile tests

Fig. 3.27 presents the experimental results for the longitudinal tensile tests. These experiments are based on the DIN ISO 527-4 standard. Considering the thickness of a unique ply and 2mm thick specimens, the woven laminate is constituted by only three elementary woven plies, defining a unidirectional (U.D.) stacking sequence (all the plies have the same orientation). Six repetitions of this test have been conducted and they lead to similar results. The material depicts first a linear behavior until a delamination of the specimen leading to a separation of each composite layer and to a yarn-resin debonding. Continuing the traction, the material is always able to carry tensile loads until the ultimate fiber failure. The delamination phenomenon occurred at about the half of the final strength. It is important to notice that the initial cross-section of the specimen is used for the computation of the stress even after the first debonding. After reaching the half of the strength value, the strain is computed using the displacement of the traction machine, since the delamination broke the strain gauge glued on the specimen. The strength of this composite material could be taken, when delamination occurred. However, as the material can still carry tensile load, the "crash strength" has be chosen as the last one at ultimate failure of the specimen (at ultimate fiber/yarn failure). In order to keep a physical consistency and to take into account the loss of stiffness of the material due to debonding and delamination, the nonlinear behavior represented by the red line on Fig. 3.27 is used as a physical reference for the behavior of this carbon twill-weave PREPREG composite, when loaded in longitudinal tension. Some light differences have been observed regarding the ultimate strength between a tension in the warp or in the weft direction, but due to the delamination phenomenon occurring at a low stress level, we choose to neglect them. The extrapolation of the strain has been successfully correlated to additional experimental measurements made using extensiometers. Finally, suitable coefficients of variation about 3.5% have been computed regarding the Young's modulus and the ultimate stress at failure.

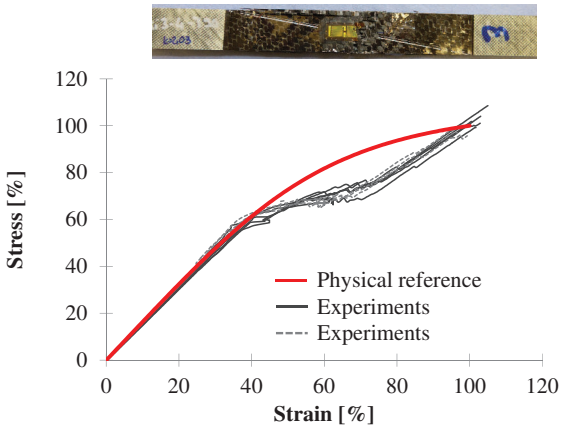

Figure 3.28: Experimental results for the longitudinal tension on a multidirectional stacking sequence: representative failure (top) and stress vs. strain material response (bottom)

3.3.1.2 Multidirectional tensile tests

Similar tests as those described in 3.3.1.1 have been conducted on 4mm thick specimens presenting a multidirectional [0°/45°/0°/0°/45°/0°] stacking sequence. A tension in the 0° or longitudinal direction means here that the outer and middle layers have a 0° orientation with the direction of traction. Similarly, a tension in the 45° or diagonal direction means that both outer and middle layers have a 45° orientation with the direction of traction. Fig. 3.28 presents the results for the quasi-static longitudinal tension on the multidirectional (M.D.) stacking sequence. Eight repetitions have been conducted. The two different grey colors for the curves are only used in order to separate them into two packages of four curves and to make the observations easier. A similar delamination phenomenon occurred as in the unidirectional tension. However, ultimate failure occurred at a 20% lower strength and a constraining effect of the 45° layers has been observed, since no kind of explosive failure happened. In order to keep a physical consistency and to take into account the loss of stiffness of the material due to debonding and delamination, the nonlinear behavior represented by the red line is used as a physical reference. Finally, suitable coefficients of variation about 3.5% have been computed regarding the stiffness and the ultimate stress at failure.

Fig. 3.29 presents the results for the quasi-static 45° tension on the multidirectional stacking sequence. Eight repetitions have been conducted. Ultimate failure occurred at a stress approximately equal to the half of the strength observed in the 0° tension. A delamination phenomenon occurred that led to the failure of the specimen. A constraining effects of the 45° layers has been observed, since no kind of explosive failure happened. Finally, suitable coefficients of variation about 2% regarding the ultimate stress at failure and about 3.3% concerning the stiffness have been obtained.

3.3.1.3 Shear tensile tests

Fig. 3.30 presents the experimental results for the characterization of the tensile shear behavior. These experiments are based on the DIN ISO 527-4 standard. Considering the thickness of a unique ply and 2mm thick specimens, the woven laminate is constituted by only three elementary woven plies, defining a ±45° stacking sequence. Six repetitions of this test have been conducted and a low scatter is observed.

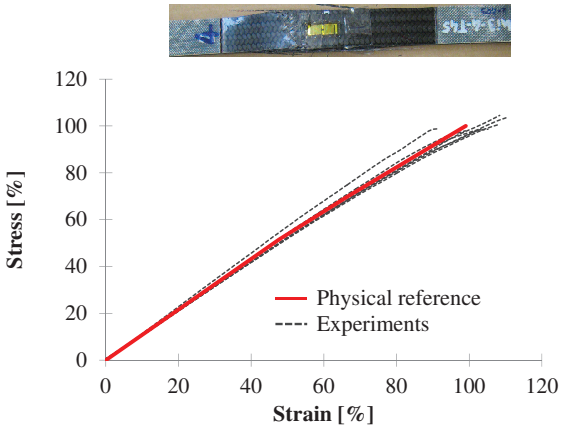

Figure 3.29: Experimental results for the diagonal tension on a multidirectional stacking sequence: representative failure (top) and stress vs. strain material response (bottom)

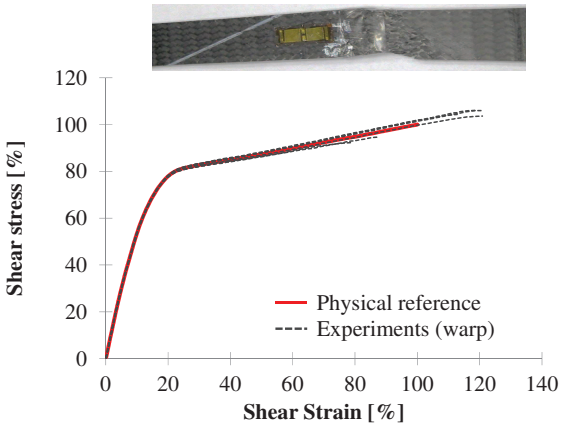

Figure 3.30: Experimental results for the shear tensile tests: representative failure (top) and shear stress vs. shear strain material response (bottom)

A common nonlinear behavior has been captured as well as a common matrix failure with a diagonal failure surface. Finally, suitable coefficients of variation about 1% have been computed regarding the shear module and the stress at 5% shear strain.

3.3.1.4 Unidirectional compressive tests

Fig. 3.31 presents the experimental results for the quasi-static longitudinal compressive tests. These experiments are based on the DIN ISO 14126 standard and 4mm thick type B2 specimens. Considering the thickness of a unique ply, the woven laminate is constituted by six elementary woven plies, defining a unidirectional stacking sequence (all the plies have the same orientation). Four repetitions of this test are presented. An acceptable coefficient of variation about 3.5% is obtained concerning the stiffness. However, this coefficient is about 17% regarding the strength. Consequently, the ultimate strength of the material is chosen equal to the averaged one neglecting the specimens that failed too prematurely, as shown by the red curve representing the physical reference of the experimental tests. As presented on Fig. 3.31, failure is caused by delamination, crack propagation and yarn failure. A particular failure

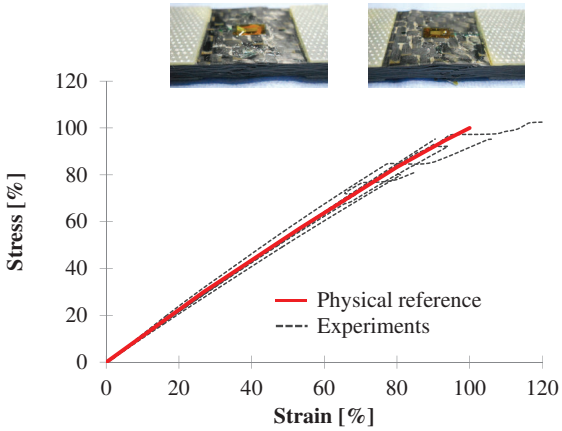

Figure 3.31: Experimental results for the longitudinal compression: representative failure (top) and stress vs. strain material response (bottom)

angle commonly referring to a kinking angle has been observed but not measured. The relative high ply thickness combined to the material complexity induced by the textile structure and the fiber waviness could explain the large scatter obtained for the longitudinal compressive strength. It could be interesting to conduct for example such compressive tests on 2mm thick specimen. Finally, it is important to notice that a light nonlinear behavior has been captured for the longitudinal compression of this carbon twill-weave PREPREG composite.

3.3.1.5 Multidirectional compressive tests

Similar tests as those described in 3.3.1.4 have been conducted on 4mm thick type B1 specimens presenting a multidirectional [0°/45°/0°/0°/45°/0°] stacking sequence. A compression in the 0° or longitudinal direction means here that both outer and middle layers have a 0° orientation with the direction of compression. Similarly, a compression in the 45° or diagonal direction means that both outer and middle layers have a 45° orientation with the direction of compression. Fig. 3.32 presents the results for the quasi-static longitudinal compression on the multidirectional stacking sequence. Eight representative repetitions are presented. A nonlinear behavior is captured and the stress at ultimate failure is about 20% lower than the compressive strength observed for a unidirectional stacking sequence. An acceptable scatter is observed regarding the stress at failure with a coefficient of variation about 7%. Concerning the stiffness, a non-negligible dispersion has been remarked with a coefficient of variation about 20%. A zoom on the failure location shows that delamination, crack propagation and fiber/yarn failure are responsible for the specimen failure.

Fig. 3.33 presents the results for the quasi-static 45° compression on the multidirectional stacking sequence. Six representative repetitions are presented on the graph. Ultimate failure occurred at a stress approximately equal to the one observed for the 0° compression on the M.D. stacking sequence. A low scatter is observed concerning the stress at failure, which is confirmed by a low value of the coefficient of variation about 3%. A low dispersion of 5% is also observed for the stiffness. Regarding the failure mode of the specimens, it seems that crack propagation and delamination are responsible for failure, since no clear fiber/yarn failure is observed. Consequently, both outer layer having a 45° orientation with the compression direction could have a constraining effect, "stabilizing" thus the specimen's behavior under

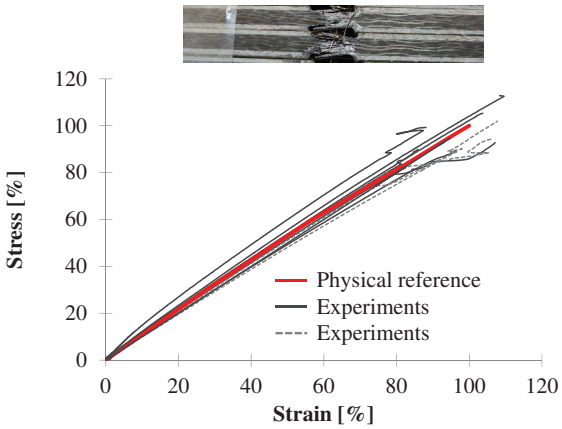

Figure 3.32: Experimental results for the longitudinal compression on a multidirectional stacking sequence: representative failure (top) and stress vs. strain material response (bottom)

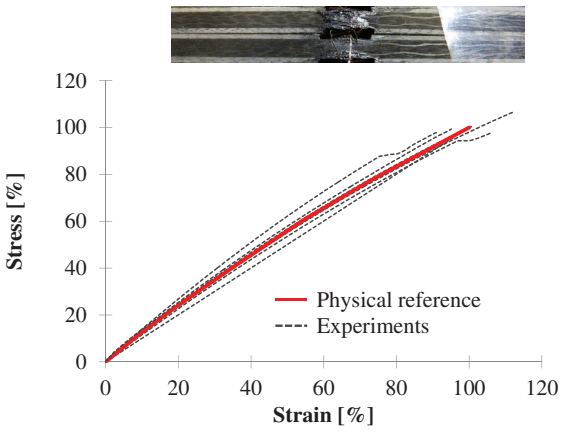

Figure 3.33: Experimental results for the diagonal compression on a multidirectional stacking sequence: representative failure (top) and stress vs. strain material response (bottom)

uniaxial compressive loads.

3.3.1.6 Unidirectional bending tests

Fig. 3.34 presents the results of quasi-static longitudinal four-point bending tests on 2mm thick and class *IV* specimens based on the DIN ISO 14125 standard. Considering the thickness of a unique ply, the woven laminate is constituted by only three elementary woven plies, defining a unidirectional stacking sequence (all the plies have the same orientation). The curves show the six repetitions for each bending in the warp and weft directions. A bending in the warp direction means that the warp direction of the textile is aligned with the length of the specimen. A non-negligible dispersion regarding the bending stiffness (about 19%) and the bending strength (about 11%) is observed. The physical reference is taken as an average of experimental results and no difference will be made between the warp and weft directions for the comparison with numerical results. Finally, the specimens failed in compression, as failure occurred on the top side of the specimen.

Fig. 3.35 presents the results of quasi-static diagonal four-point bending tests on 2mm thick and class

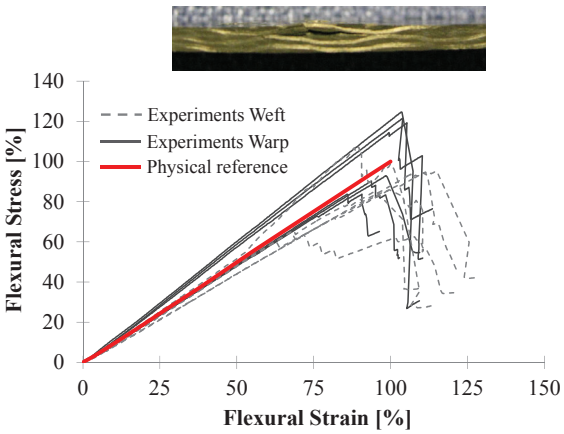

Figure 3.34: Experimental results for the longitudinal bending: representative failure (top) and flexural stress vs. flexural strain material response (bottom)

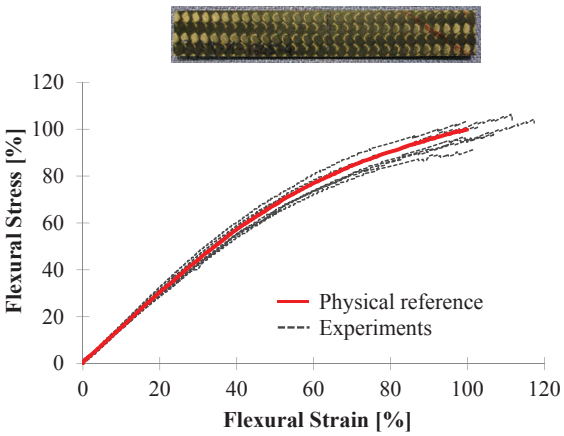

Figure 3.35: Experimental results for the diagonal bending: representative failure (top) and flexural stress vs. flexural strain material response (bottom)

IV specimens based on the DIN ISO 14125 standard. All the three plies have a 45° orientation with the length of the specimen. Eight repetitions of this test have been conducted giving a coefficient of variation of 6% regarding the bending stiffness and of 4% concerning the maximal strength. No clear failure of the specimen has been reported but a considerable permanent deformation has been observed.

3.3.1.7 Multidirectional bending tests

Four-point bending tests, based on the DIN ISO 14125 standard, have been conducted on 4mm thick specimens presenting a multidirectional [0°/45°/0°/0°/45°/0°] stacking sequence. The length of the specimen is 200mm and the width is 15mm. The outer span of the four-point bending is about 157.5mm and the inner span is about 52.5mm. A bending in the 0° or longitudinal direction means here that both outer and middle layers have a 0° orientation with the length of the specimen. Similarly, a bending in the 45° or diagonal direction means that both outer and middle layers have a 45° orientation with the length of the specimen.

Fig. 3.36 presents the results of quasi-static longitudinal four-point bending tests. Six repetitions of this test representing a bending in the weft direction are presented. A coefficient of variation about 3% is

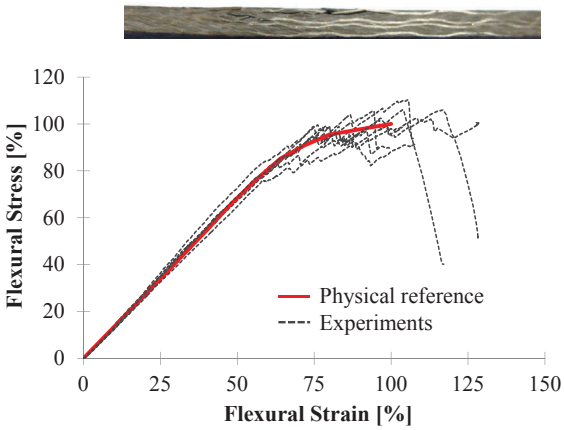

Figure 3.36: Experimental results for the longitudinal bending on a M.D. stacking sequence: representative failure (top) and flexural stress vs. flexural strain material response (bottom)

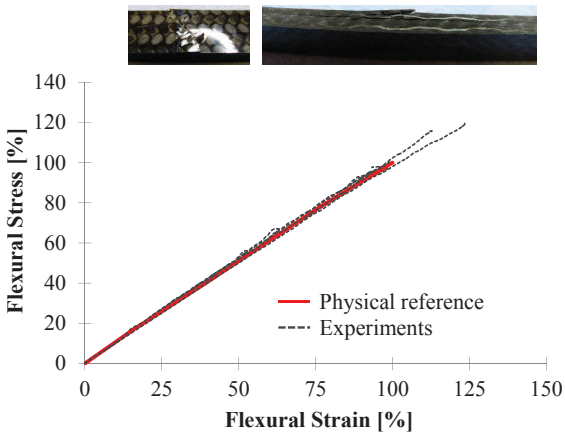

Figure 3.37: Experimental results for the diagonal bending on a M.D. stacking sequence: representative failure (top) and flexural stress vs. flexural strain material response (bottom)

obtained concerning the stiffness, whereas this coefficient is about 4% regarding the stress at failure. A progressive failure of the material is observed, beginning at approximately 80% of the ultimate flexural strength. Similar tests have been conducted on specimens, where the warp direction is aligned with the specimen's length. Similar coefficients of variation have been reported and failure occurred at a similar stress level. However, no progressive failure has been captured and a linear behavior until ultimate failure has been observed. We chose to have a focus only on the results for the weft direction as they present a higher interest induced by the progressive failure. Failure occurred on the top side of the specimens, which means that this M.D. longitudinal bending failed in compression.

Fig. 3.37 presents the results of quasi-static diagonal four-point bending tests. A linear behavior is observed until ultimate failure occurring on the upper side of the specimen loaded in compression. The stress at failure is here quite 20% lower than the one observed for the longitudinal bending reported above. Eight repetitions have been made but only four representative results are presented. Finally, the low dispersion is confirmed by suitable coefficients of variation about 3% for the stiffness.

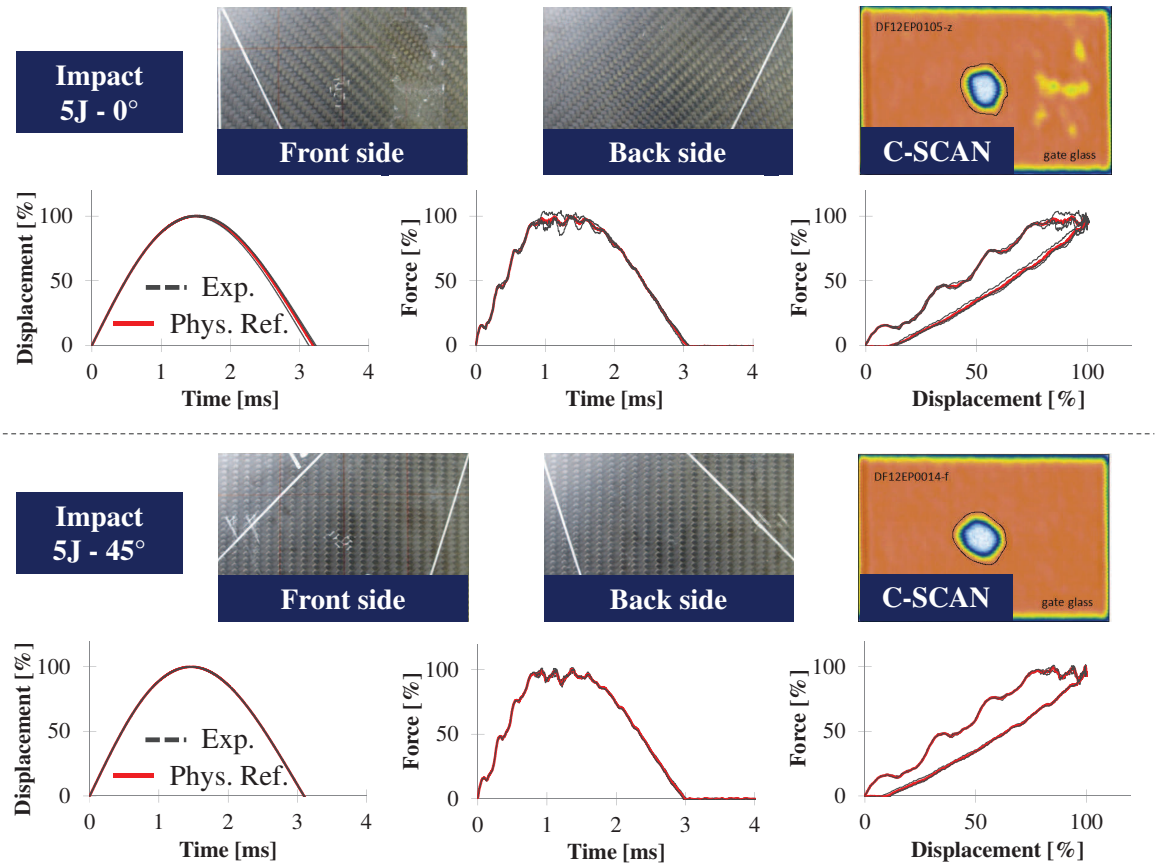

Figure 3.38: Experimental results of the 5J impact tests for the 0° and 45° orientations

3.3.2 Impact tests on elementary plates

The impact tests on elementary plates conducted on the PREPREG material have a similar experimental set-up and impact energies as those described in the section 3.2.2.1. A $[0°/45°/0°]_s$ multidirectional stacking sequence is considered here.

Fig. 3.38 presents the experimental results for a 5J impact. The curves show a similar behavior for both 0° and 45° orientations. A clearly visible damage is observed on the front side of the test specimens, where the impactor hit the plate. The C-SCAN analysis shows an average damage zone about $685mm^2$ for the 0° orientation and about $716mm^2$ for the 45° orientation. For both cutting directions, a low dispersion appears in the experimental curves. A higher scatter has been observed for the evaluation of the damaged surfaces. Finally, the damaged surface is more than six times higher for the PREPREG material than for the RTM composite. The maximal displacement of the impactor and the maximal force peaks are lightly higher for the RTM material than for the PREPREG composite.

Fig. 3.39 presents the experimental results for a 25J impact. The curves show a similar behavior for both orientations. A clearly visible damage is observed on the test specimens, particularly on the front side, where the impactor hit the plate. A lower damage is visible on the back side of the plate. The C-SCAN analysis shows an average damage zone about $2295mm^2$ for the 0° orientation and about $2316mm^2$ for the 45° orientation. For both cutting directions, a low dispersion appears in the experimental curves, whereas a higher scatter has been observed for the evaluation of the damaged surface. Finally, the damaged surface is about three times higher for the PREPREG material than for the RTM composite.

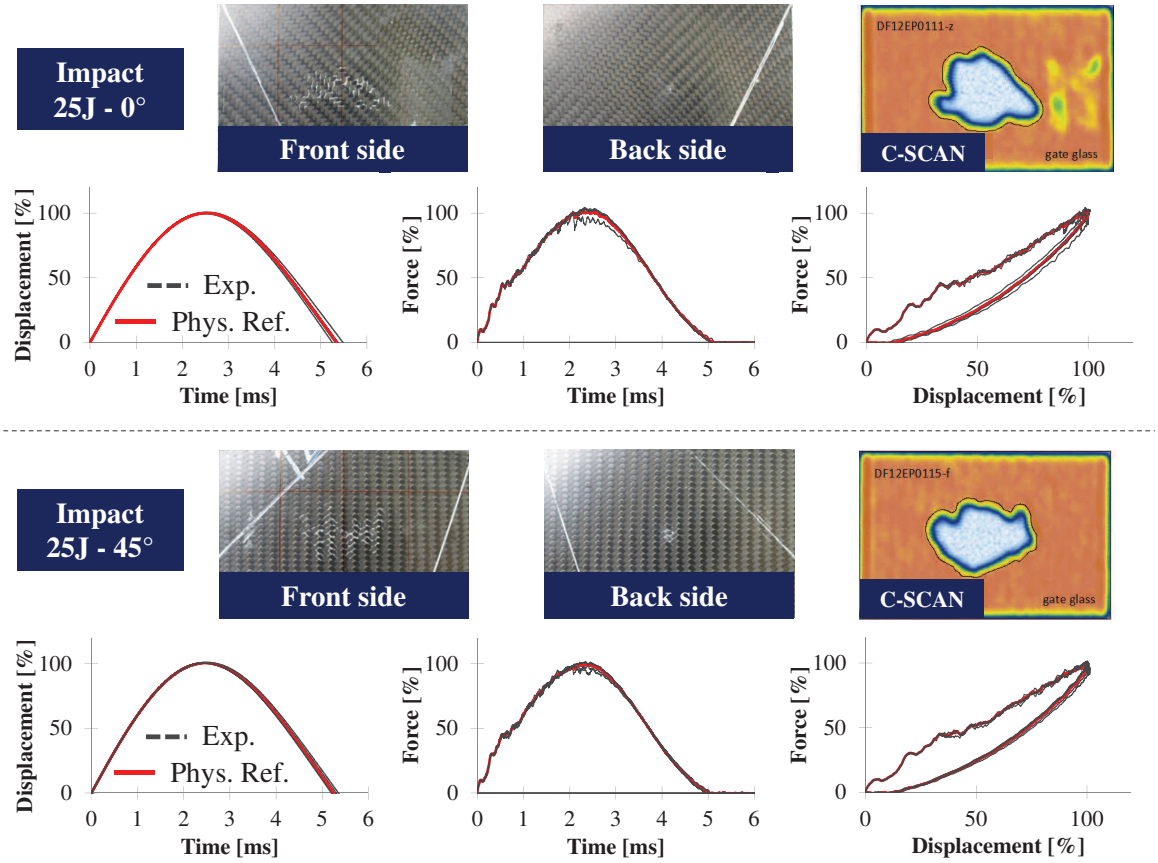

Figure 3.39: Experimental results of the 25J impact tests for the 0° and 45° orientations

The maximal displacement of the impactor and the maximal force peak are similar as or lightly higher for the RTM material than for the PREPREG composite. A change of the slope in the curve of the force occurring about 50% of the force peak represents a sudden delamination propagation in the laminate, resulting in a loss of stiffness.

Fig. 3.40 describes the experimental results for a 50J impact. The curves show a similar behavior for both orientations. A clearly visible damage is observed on both sides of the test specimens. For the 45° orientation, the outer layer presents a yarn orientation of 45° with the length and width of the specimen. On the front side, the shape of the damage propagation illustrates this orientation defining a kind of cross around the impacted zone. This phenomenon has not been observed for the lower impact energies. The C-SCAN analysis shows an average damage zone about $2872mm^2$ for the 0° orientation and about $2903mm^2$ for the 45° orientation. For both cutting directions, a low dispersion appears in the experimental curves, whereas a higher scatter has been observed for the evaluation of the damaged surface. Finally, the damaged surface is quite about three times higher for the PREPREG material than for the RTM composite. A higher maximal force peak has been captured for the PREPREG material, whereas the maximal displacement is observed for the RTM composite. Similarly to the RTM material, due to the quite perforation and the high damage level in the plate, the curve of the reaction force presents a clear decrease after the force peak. A quite constant force level follows until the unload of the plate. This decrease of the force shows a considerable intralaminar and interlaminar failure of the material.

Fig. 3.41 presents a comparison of the experimental results for the three impact energies. A similar

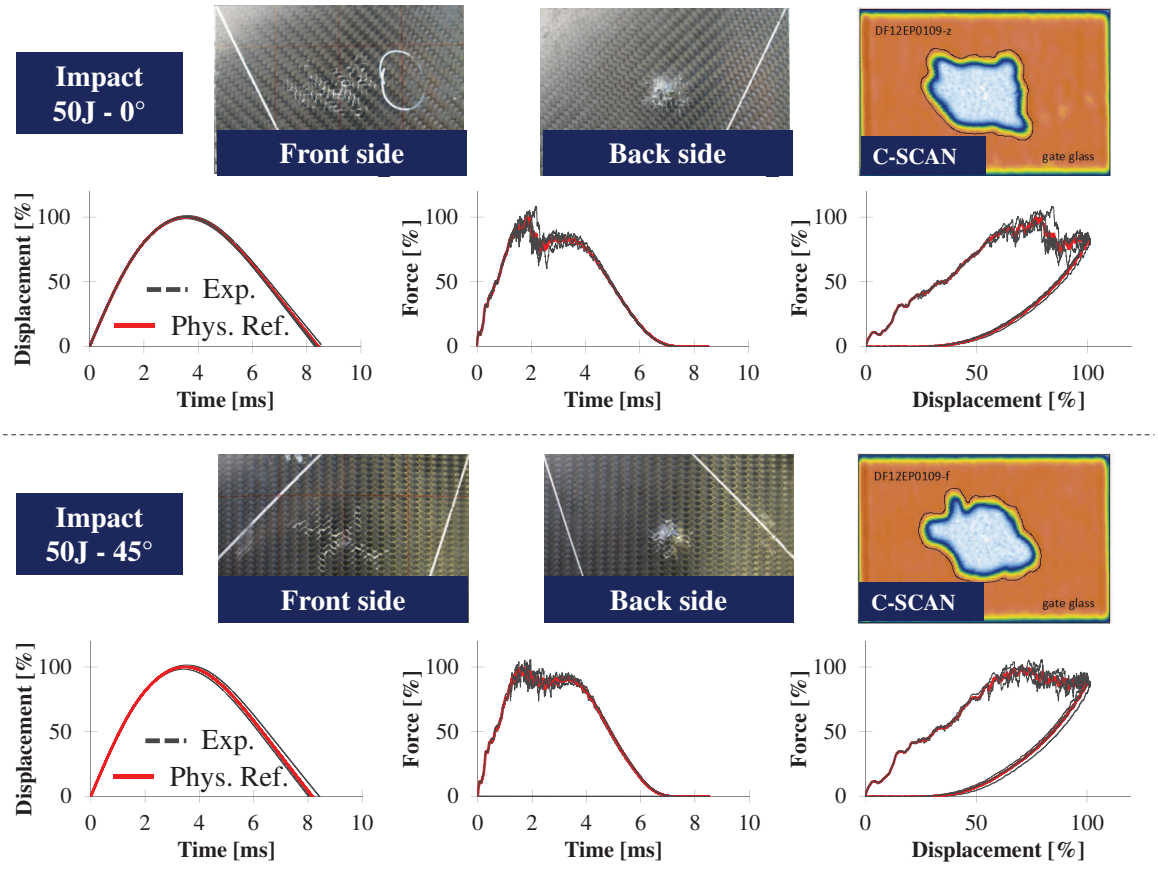

Figure 3.40: Experimental results of the 50J impact tests for the 0° and 45° orientations

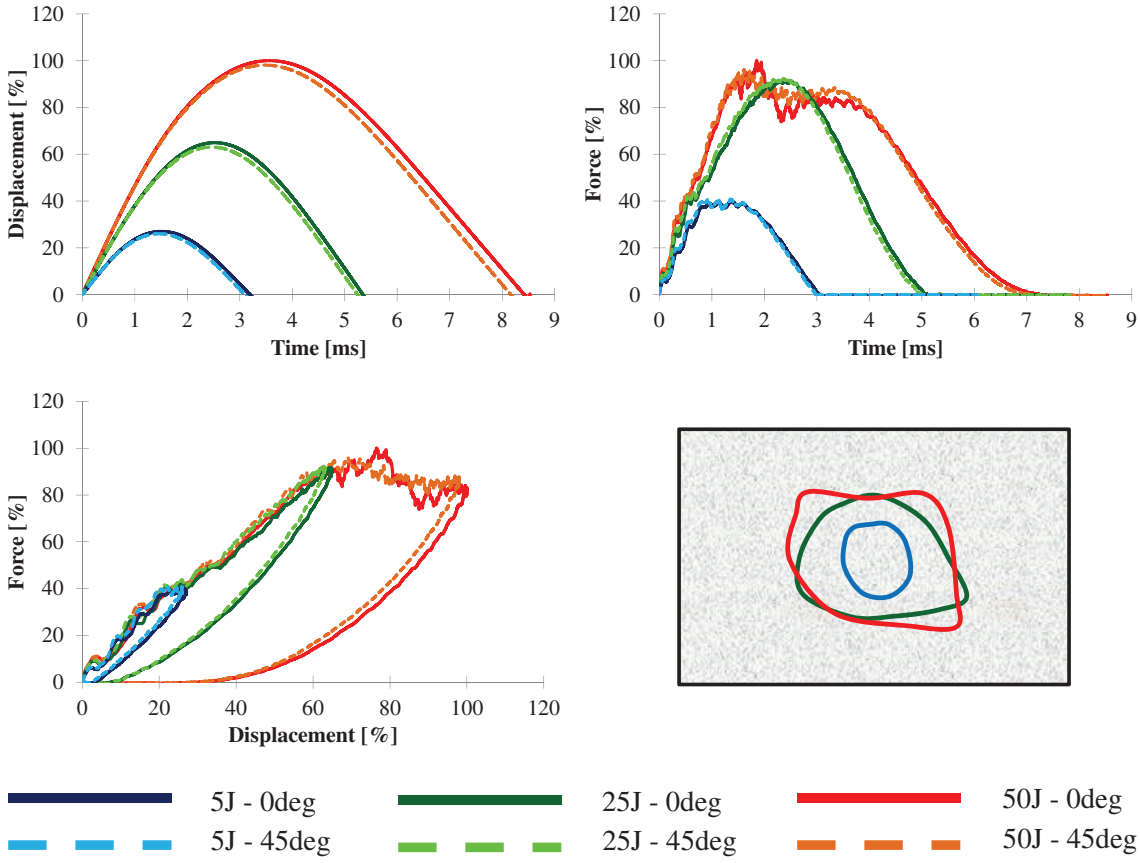

Figure 3.41: Comparison of the experimental results (material response and damaged surfaces) for the three impact energies and for both 0° and 45° orientations

material response is obtained for both orientations. Similar force levels are reached for the 50J and the 25J impact energies, whereas the maximal impactor displacement for 25J reached only 65% of the maximal impactor displacement for a 50J impact. The comparison of the damaged surfaces uses the same color code as in the curves. The damaged area increases logically, when the impact energy increases. The shape of the damaged areas comes from a representative C-SCAN giving a delaminated zone close to the averaged one.

The Tables 3.8 and 3.9 present respectively for the 0° and the 45° orientations the coefficients of variation concerning the maximal impactor's displacement, the maximal force peak and the damaged surfaces for the impact tests on the PREPREG specimens. For both orientations, a low dispersion is observed for each impact energy regarding the displacement of the impactor and the maximal force peak. It is also in agreement with the low scatter observed on the curves. For this PREPREG material, an acceptable dispersion is observed for all impact energies regarding the damaged surfaces.

3.3.3 Representative component tests: drop tower tests on hat-profiles

As described in the section 3.2.2.2, drop tower tests have been also conducted on 2mm and 4mm thick PREPREG hat-profiles. The hat-profiles present a similar cross-section than the RTM hat-profiles but their length is about 500mm. Consequently, the position of the rivets changes but the span and the diameter of the impactor and of the support are not modified, as described on Fig. 3.42.

Table 3.8: Coefficients of variation (in %) concerning the maximal impactor's displacement, the maximal force peak and the damaged surfaces for the impact tests on the PREPREG material and the 0° orientation

PREPREG - 0°	5J	25J	50J
Maximal displacement	0.7	0.7	1.0
Maximal force peak	2.3	1.2	4.2
Damaged surfaces	9.9	16.4	15.2

Table 3.9: Coefficients of variation (in %) concerning the maximal impactor's displacement, the maximal force peak and the damaged surfaces for the impact tests on the PREPREG material and the 45° orientation

PREPREG - 45°	5J	25J	50J
Maximal displacement	0.1	0.4	1.3
Maximal force peak	1.3	1.4	2.5
Damaged surfaces	5.5	10.1	10.2

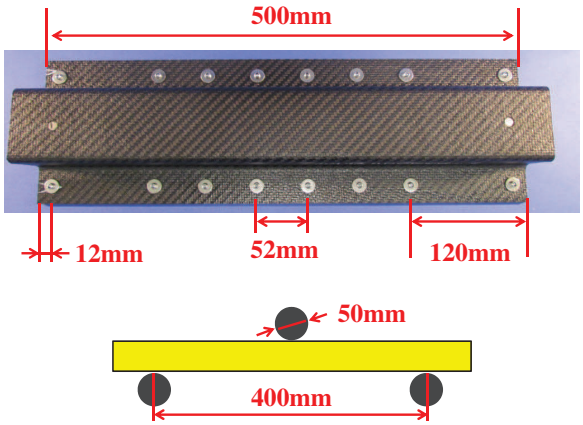

Figure 3.42: Experimental set-up for the drop tower tests on PREPREG hat-profiles: dimensions of the specimen (top) and experimental set-up (bottom)

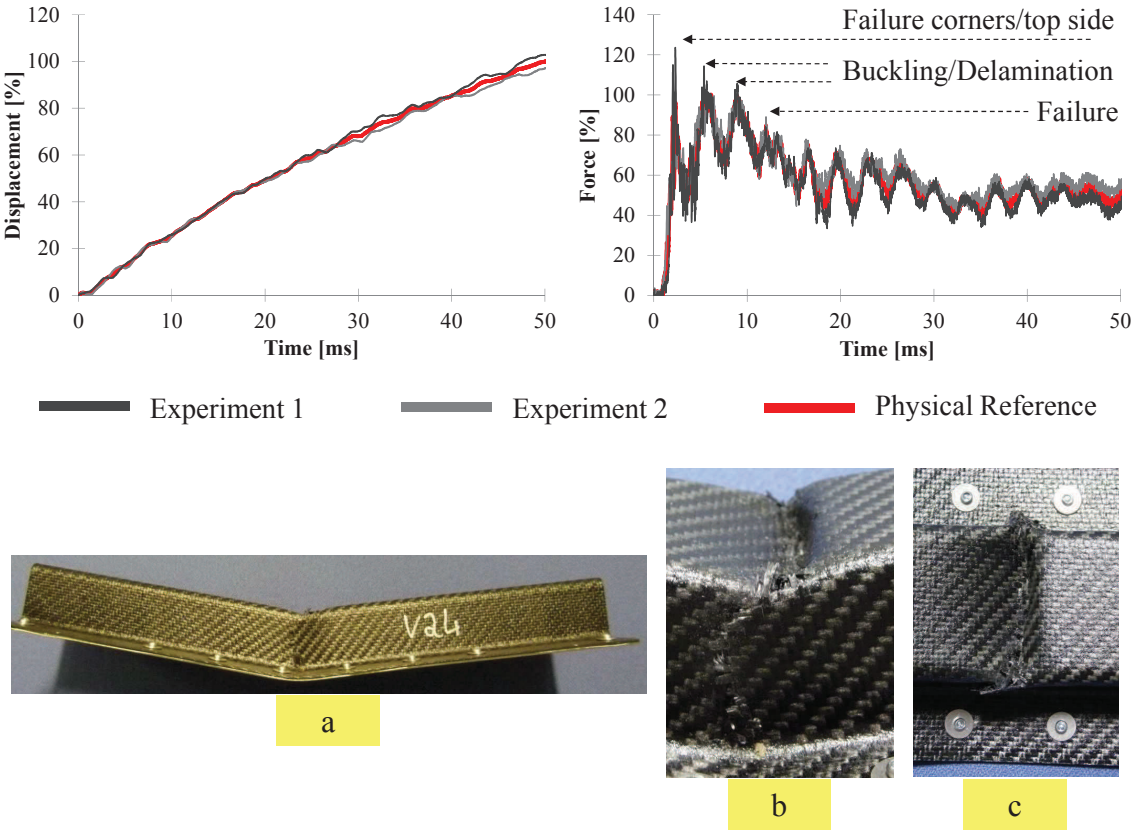

Figure 3.43: Experimental results for the 100J drop tower tests on 2mm thick PREPREG hat-profiles: displacement vs. time and force vs. time (top), a) side view of the hat-profile after impact - b) side view and zoom on failure - c) top view and zoom on failure

3.3.3.1 Impact on 2mm thick hat-profiles

Fig. 3.43 presents the experimental results for a 100J impact on a 2mm thick PREPREG hat-profile having a unidirectional $[0°]_3$ stacking sequence. Two repetitions of the tests have been conducted and a low dispersion has been observed. Fig. 3.43a) shows a side-view of the complete hat-profile after the impact. A progressive failure process beginning with a material collapse in the corners and on the top side, followed by buckling and delamination leads to the ultimate failure of the hat-profile. Failure is localized in the middle of the specimen below the impactor. Fig. 3.43b) and c) show respectively a side view and a top view of failure. A clear fracture surface is observed on the top, left and right flat sides of the specimen. The parts of the hat-profile, where the rivets are fastened, underwent no clear failure, but a large bending deformation. A fragmentation of the material and a kind of explosive failure are observed in the corners. As only two repetitions of this test have been conducted, no statistical analysis is presented.

3.3.3.2 Impact on 4mm thick hat-profiles

Fig. 3.44 presents the experimental results for a 350J impact on a 4mm thick hat-profile having a unidirectional $[0°]_6$ stacking sequence. Two repetitions of the tests have been conducted and a low dispersion has been observed. Fig. 3.44a) shows a side-view of the complete hat-profile after the impact.

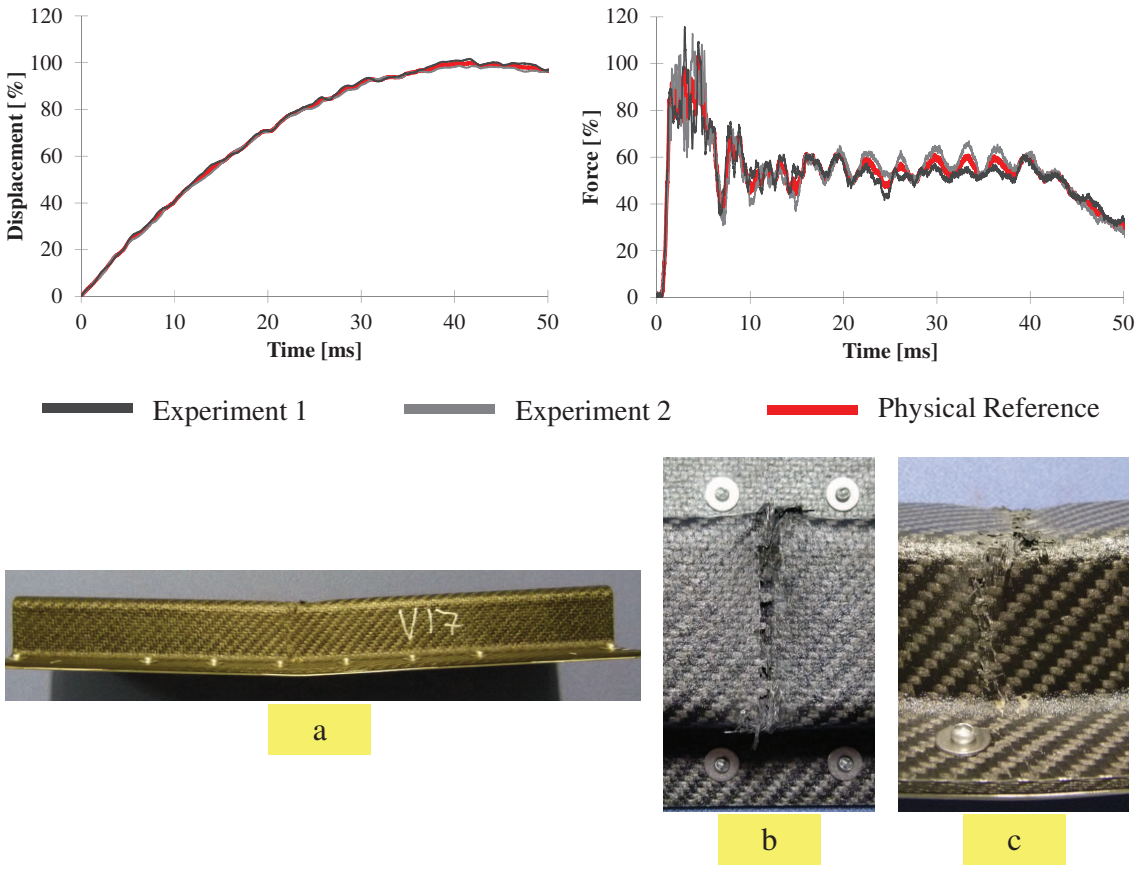

Figure 3.44: Experimental results for the 350J drop tower tests on 4mm thick PREPREG hat-profiles: displacement vs. time and force vs. time (top), a) side view of the hat-profile after impact - b) side view and zoom on failure - c) top view and zoom on failure

Failure is localized in the middle of the specimen below the impactor. Fig. 3.44b) and c) show respectively a side view and a top view of failure. A localized fracture surface is observed on the top, left and right flat sides of the specimen. The parts of the hat-profile, where the rivets are fastened, underwent no clear failure. A fragmentation of the material is observed over the complete fracture surface of the hat-profile. As only two repetitions of this test have been conducted, no statistical analysis is presented. Due to the high impact velocity it is difficult to identify a clear progressive material failure.

Fig. 3.45 presents the experimental results for a 500J impact on a 4mm thick hat-profile having a multidirectional $[0°/45°/0°]_s$ stacking sequence. Three repetitions of the tests have been conducted and a low dispersion has been observed. Fig. 3.45a) shows a side-view of the complete hat-profile after the impact. Failure is localized in the middle of the specimen below the impactor and a larger damaged area is observed by comparison with a 350J impact. Fig. 3.45b) and c) show respectively a side view and a top view of failure. A localized fracture surface is observed on the top flat sides of the specimen. On the vertical left and right flat sides of the specimen, a damaged zone with a width about 50mm is observed. The parts of the hat-profile, where the rivets are fastened, underwent no clear failure but a large bending deformation. A fragmentation of the material is observed over the complete fracture surface of the hat-profile. Due to the higher impact velocity it is difficult to identify a clear progressive material failure. Finally, a suitable coefficient of variation about 3.8% has been computed regarding the maximal force

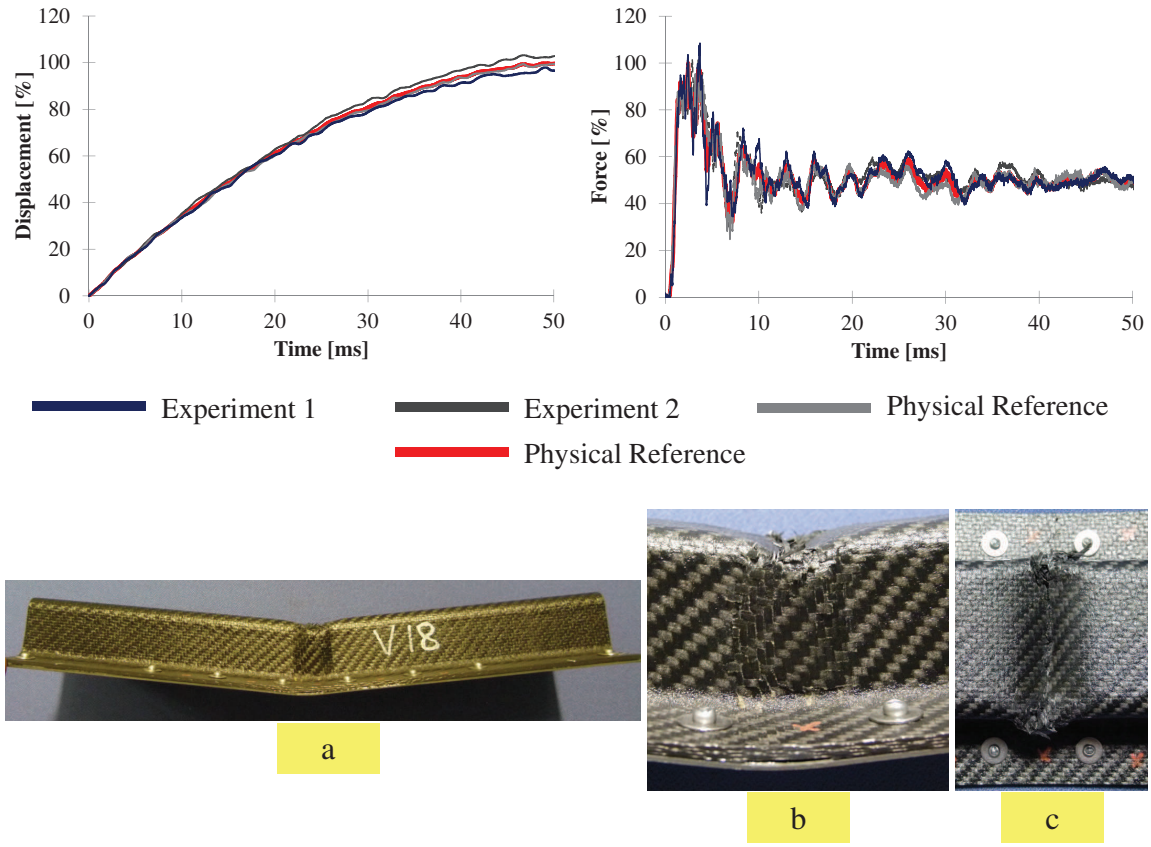

Figure 3.45: Experimental results for the 500J drop tower tests on 4mm thick PREPREG hat-profiles: displacement vs. time and force vs. time (top), a) side view of the hat-profile after impact - b) side view and zoom on failure - c) top view and zoom on failure

peak.

3.4 Partial conclusions

The effective mechanical properties of the carbon plain-weave RTM composite have been obtained using the quasi-static material characterization tests on elementary coupons. A linear behavior has been observed for a tension parallel to a yarn direction. A compression in this longitudinal direction showed a nonlinear behavior with a reduced stiffness (about 6%) in comparison to the corresponding tensile load case. A common nonlinear behavior has been captured in shear tension and compression. The longitudinal four-point bending tests showed a linear behavior until failure. A common and expected nonlinear behavior has been obtained for the diagonal four-point bending tests. For this carbon twill-weave PREPREG composite, delamination and yarn debonding occurred for the longitudinal tension load case. However, the material is still to carry load until the ultimate failure of the specimen. A nonlinear behavior has been defined to take into account the loss of stiffness and of material integrity. A similar behavior has been also captured for a longitudinal tension on a multidirectional stacking sequence. However, when both outer layers present a $\pm 45°$ orientation with the direction of traction, delamination and yarn debonding induced catastrophic failure. Compressive tests on a multidirectional stacking sequence

showed a constraining and stabilizing effect of the $\pm 45^{\circ}$ outer layers. Four-point bending tests on a multidirectional stacking sequence showed a linear behavior and a progressive failure for the longitudinal direction, whereas a linear behavior and a brittle failure have been observed for the diagonal orientation.

The impact tests on the RTM elementary plates showed a low dispersion regarding the quantitative analysis of the material response for the three impact energies. The damaged and delaminated surfaces have been assessed using a non-destructive ultra-sound technique. A high dispersion has been remarked concerning the determination of the damaged zones for the 5J impacts and for both orientations. For both 25J and 50J impacts and both orientations, acceptable values of the coefficients of variation have been computed for the evaluation of the damaged surfaces. A large damage with intralaminar failure has been quantitatively and qualitatively observed for the highest energy of impact. The impact tests on the PREPREG elementary plates showed also a low dispersion regarding the quantitative analysis of the material response for the three impact energies. Low values of the coefficient of variation have been reported concerning the assessment of the damaged surfaces too. For this composite material, the highest dispersion regarding the damaged zones is obtained for both 25J and 50J energies of impact.

For both RTM and PREPREG composites, drop tower tests on hat-profiles have been conducted and they are used as representative component tests for the validation of the modeling techniques. The reaction force increases until a maximal peak referring to failure. Then, a quite-constant post-failure force level is observed, mainly influenced by the deformation of the steel plate and the fragmentation of the composite. As no ultra-sound investigation has been made for these experiments, no assessment of the damaged zones can be made. Finally, a low scatter has been observed regarding the material responses and the failure modes for all impact energies of the drop tower tests on hat-profiles.

Chapter 4

Development of a user-defined material model: theory and implementation

4.1 Introduction

This section presents the theory and the implementation of a user-defined material model (UMAT) for the explicit FE-solver LS-DYNA. It is necessary to keep in mind the industrial requirements regarding a suitable compromise between accuracy and efficiency. In this context, not only the computational costs but also the required efforts to collect the parameters of the model have to be kept as low as possible. Thus, the input data of the UMAT are based on homogenized material properties of a composite ply, such as the effective stiffnesses and strengths.

According to the experimental results presented in the chapter 3, the material model has to be able to predict the linear and the nonlinear macroscopic behavior of a composite for each in-plane material direction in tension and in compression. The nonlinear behavior of a material can be described by two different approaches. Firstly, the Continuum Damage Mechanics (CDM) approach uses generally a damage parameter characterizing the damage evolution responsible for the loss of stiffness of the materials caused by the evolution of microcracks. A second way is to consider the nonlinearity as a macroscopic behavior of the material independently from a damage evolution. Due to its pragmatic aspect and to the limited number of input data, the latter approach has been chosen in order to predict a nonlinear behavior. The Ramberg-Osgood model has been applied here to compute the stresses in the material corresponding to a given strain state. This method has been compared to a more pragmatic one, which consists in providing directly the stress vs. strain behavior of the material using a load curve as input data. For both models, a unidimensional plasticity theory is applied to account for plastic strain as soon as a nonlinear behavior is predicted. A failure criterion based on the effective mechanical properties of a composite ply has to be used in order to predict failure. The simple and well-known maximal stress criterion has been implemented to detect material failure. As the automotive composite structural parts present generally a multidirectional stacking sequence, the quadratic 2D Tsai-Wu failure criterion has also been implemented. The results given by both failure criteria will be then compared and discussed.

Post-failure material degradation models have been implemented in order to reduce progressively the bearing-load capability of the material after failure. It allows also to investigate the damage tolerance

of the studied composite under crash or impact loads. Two continuous post-failure damage evolution laws have been implemented. A linear one is based on the work published by Pinho in [150, 151] and a nonlinear one has been developed in the present study. Two other discontinuous post-failure material degradation models have been investigated. One model describes a post-failure constant stress level and the other one proposes a step-based progressive material degradation. More details about the required parameters and the shape of the post-failure behavior are presented in the next sections.

Finally, it is important notice that the following material evolution laws and equations are applied to each point of integration defined in each shell or thick shell element.

4.2 Behavior before failure

Fig. 4.1 describes the material coordinate system used in this study. The direction 1 refers to the longitudinal or fiber direction and the direction 2 refers to the transverse direction. The in-plane shear direction is represented by the subscript 4. A linear behavior is assumed per default for all material directions. Nonlinearity is considered in shear and for both longitudinal and transverse directions. A linear elastic behavior is always assumed in the through-the-thickness direction 3.

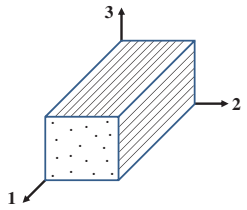

Figure 4.1: Material coordinate system for a unidirectional composite ply

4.2.1 Linear behavior and incremental implementation

The numerical model is based on the prediction of the linear elastic behavior of an orthotropic material. It relies on the calculation of each term of the stiffness matrix C_{ij} $(i, j = 1, ..., 6)$ and on an incremental implementation. The stress-strain relations of an orthotropic linear elastic material are given by:

$$\begin{bmatrix} \sigma_1 \\ \sigma_2 \\ \sigma_3 \\ \sigma_4 \\ \sigma_5 \\ \sigma_6 \end{bmatrix} = \begin{bmatrix} C_{11} & C_{12} & C_{13} & 0 & 0 & 0 \\ C_{12} & C_{22} & C_{23} & 0 & 0 & 0 \\ C_{13} & C_{23} & C_{33} & 0 & 0 & 0 \\ 0 & 0 & 0 & C_{44} & 0 & 0 \\ 0 & 0 & 0 & 0 & C_{55} & 0 \\ 0 & 0 & 0 & 0 & 0 & C_{66} \end{bmatrix} \begin{bmatrix} \varepsilon_1 \\ \varepsilon_2 \\ \varepsilon_3 \\ \varepsilon_4 \\ \varepsilon_5 \\ \varepsilon_6 \end{bmatrix} \tag{4.1}$$

where the different components of the stiffness matrix are expressed by:

$$\begin{aligned}
C_{11} &= \frac{(1-\nu_{23}\times\nu_{32})\times E_1}{S} \\
C_{12} &= \frac{(\nu_{21}+\nu_{31}\times\nu_{23})\times E_1}{S} \\
C_{13} &= \frac{(\nu_{31}+\nu_{21}\times\nu_{32})\times E_1}{S} \\
C_{22} &= \frac{(1-\nu_{31}\times\nu_{13})\times E_2}{S} \\
C_{23} &= \frac{(\nu_{32}+\nu_{31}\times\nu_{12})\times E_2}{S} \\
C_{33} &= \frac{(1-\nu_{12}\times\nu_{21})\times E_3}{S} \\
C_{44} &= G_{12} \\
C_{55} &= G_{23} \\
C_{66} &= G_{31}
\end{aligned} \tag{4.2}$$

and the parameter S is defined by:

$$S = 1-\nu_{12}\nu_{21}-\nu_{23}\nu_{32}-\nu_{31}\nu_{13}-2\times\nu_{21}\nu_{32}\nu_{13} \tag{4.3}$$

In the previous equations, E_1 is the longitudinal Young's modulus, E_2 is the transverse Young's modulus and E_3 is the through-the-thickness Young's modulus. G_{12} is the in-plane shear modulus and G_{23} and G_{31} are the transverse shear moduli. The different Poisson's ratios are expressed by ν_{ij} $(i \neq j, i, j = 1, ..., 6)$. The stresses in each direction are then determined from the current strain state. Considering the relations defined by Eq. (4.1) the current stress state $\sigma_i^{t_n}$ $(i = 1, ..., 6)$ is expressed in function of the stresses at the last time step $\sigma_i^{t_{n-1}}$ $(i = 1, ..., 6)$, of the strain increments $d\varepsilon_i$ $(i = 1, ..., 6)$ and of the stiffness matrix components C_{ij} $(i, j = 1, ..., 6)$:

$$\begin{aligned}
\sigma_1^{t_n} &= \sigma_1^{t_{n-1}} + C_{11}d\varepsilon_1 + C_{12}d\varepsilon_2 + C_{13}d\varepsilon_3 \\
\sigma_2^{t_n} &= \sigma_2^{t_{n-1}} + C_{12}d\varepsilon_1 + C_{22}d\varepsilon_2 + C_{23}d\varepsilon_3 \\
\sigma_3^{t_n} &= \sigma_3^{t_{n-1}} + C_{13}d\varepsilon_1 + C_{23}d\varepsilon_2 + C_{33}d\varepsilon_3 \\
\sigma_4^{t_n} &= \sigma_4^{t_{n-1}} + C_{44}d\varepsilon_4 \\
\sigma_5^{t_n} &= \sigma_5^{t_{n-1}} + C_{55}d\varepsilon_5 \\
\sigma_6^{t_n} &= \sigma_6^{t_{n-1}} + C_{66}d\varepsilon_6
\end{aligned} \tag{4.4}$$

For plane stress conditions we have:

$$\sigma_3^{t_n} = 0 \; and \; d\varepsilon_3 = -\frac{C_{13}d\varepsilon_1 + C_{23}d\varepsilon_2}{C_{33}} \tag{4.5}$$

The current strain state $\varepsilon_i^{t_n}$ is defined by the sum of the strain increments up to the current step (corresponding to the strain at the last time steps $\varepsilon_i^{t_{n-1}}$) as given by the following equation (ε_3=0 for shells) and for i=1,...,6:

$$\varepsilon_i^{t_n} = \varepsilon_i^{t_{n-1}} + d\varepsilon_i \tag{4.6}$$

4.2.2 The Ramberg-Osgood model

The previous section described the incremental implementation that is used to predict the linear elastic behavior of an orthotropic material. In [230, 231], Bogetti *et. al* predict the macroscopic nonlinear behavior of a composite using the Ramberg-Osgood model [232]. It is based on the estimation of an equivalent stress σ_i corresponding to a strain state ε_i for each material direction i=1,2,4 (the shear modulus is written G_{12} instead of E_4):

$$\sigma_i = \frac{E_i \varepsilon_i}{\left(1 + \left(\frac{E_i \varepsilon_i}{\sigma_i^a}\right)^{n_i}\right)^{\frac{1}{n_i}}} \tag{4.7}$$

where E_i is the initial elastic modulus, σ_i^a the asymptotic stress level, and n_i is the shape parameter. As σ_i^a is an asymptotic value, the stress will never reach or exceed it. This fact is likely to cause some difficulties in the prediction of failure using failure criteria based on particular strength values. To solve this problem, the asymptotic value is automatically computed knowing the material stress and strain at failure onset. Defining the strength of the material by σ_i^o and its corresponding strain ε_i^o the value of σ_i^a is given by:

$$\sigma_i^a = \frac{E_i \sigma_i^o \varepsilon_i^o}{\sqrt[n_i]{(E_i \varepsilon_i^o)^{n_i} - (\sigma_i^o)^{n_i}}} \tag{4.8}$$

Fig. 4.2 shows the failure point, commonly referred to the failure onset $(\varepsilon_i^o, \sigma_i^o)$. The influence of the shape parameter n_i on the nonlinear behavior is also presented and compared to the linear behavior represented by the black curve. It is clear that high values of the exponent n_i lead to a quasi-linear behavior until the strength value (set to $1GPa$ here), whereas lower exponent values control the nonlinearity. It is recommended to let the value for the exponent n_i blank to depict a linear behavior (the standard linear behavior of orthotropic material implemented in LS-DYNA is here automatically summoned) instead of setting high exponent values, bound to bring numerical instabilities within the model. In this case, the model used only the initial elastic modulus E_i and the strength σ_i^o. The material model has now four parameters as input data for each material direction i=1,2,4: the effective stiffness E_i or G_{12}, the strain at failure onset ε_i^o and the strength σ_i^o that are easily determined by simple experiments on coupons and the shape parameter n_i to fit the material behavior with the experiments. To keep the incremental aspect of the implementation, the stresses are computed following the procedure described in Eqs. (4.2),(4.3) and (4.4), where the stiffness parameters E_i $(i = 1, 2)$ and G_{12} are replaced by the instantaneous tangential stiffnesses E_i^t depending on the current strain state, being expressed by:

$$E_i^t = \frac{E_i}{\left(1 + \left(\frac{E_i \varepsilon_i}{\sigma_i^a}\right)^{n_i}\right)^{1+\frac{1}{n_i}}} \tag{4.9}$$

The material nonlinearity is characterized by an instantaneous stiffness decreasing with the deformation and lower than the initial stiffness. This generally implies some change in the values of the Poisson's ratio. However, the Poisson' ratio values are considered constant in the present material model.

4.2.3 User-defined load curve

If the experimental stress-strain curves describing the behavior of a material are available, the user can supply them as input data in the model instead of the parameters of the Ramberg-Osgood model. Based on the curve, the UMAT determines the local stiffness corresponding to the current strain state and this

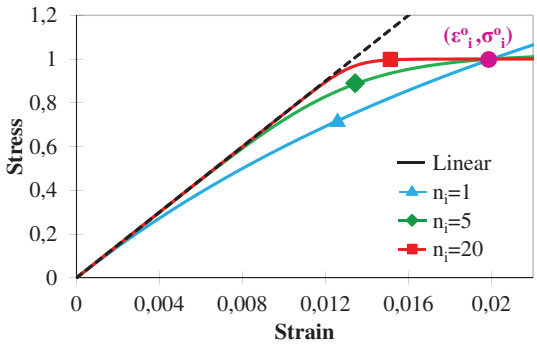

Figure 4.2: Illustration of the influence of the shape parameter n_i on the nonlinear behavior until the failure onset

stiffness parameter is then used in the stress computational procedure as described by the Eqs. (4.2), (4.3) and (4.4). The user has to define the curves in tension and compression for both main in-plane directions. Only one curve is defined for the shear, as no distinction between tension and compression is made. As mentioned previously, the Poisson' ratio values are considered constant in the present material model.

4.2.4 Stiffness in compression

Different initial stiffnesses can be experimentally observed in tension and compression for a same material direction, as reported in the chapter 3. In the present model, the user can define a compression stiffness modulus different from the corresponding tensile modulus. When a compressive load is detected, the new compressive modulus is automatically involved in the calculation procedures of the stiffness matrix components and in the stress computations. If the parameter is let blank in the input, the compressive modulus is assumed to be equal to the tensile one. As previously mentioned, the Poisson's ratio values are not updated even if different stiffness modules are defined in tension and compression.

4.2.5 Unidimensional plasticity formulation

In order to account for permanent deformation, a unidimensional plasticity model has been associated to the nonlinear behavior in each in-plane material direction. As soon as the instantaneous stiffness is lower than the initial one defined as input data, the model begins to accumulate plastic strain. It is important to notice that this plasticity formulation is a separate subroutine only aiming at accounting for permanent deformation. It has no influence on the material behavior or on the computation of the stress state. Without calling this unidimensional plasticity subroutine, the model is able to predict a nonlinear elastic behavior from a load curve or by using the Ramberg-Osgood model.

As the nonlinear behavior of the material is predicted independently from the unidimensional plasticity, a linear hardening is considered in the plastic model. Fig. 4.3 illustrates the principle of the unidimensional plasticity formulation with a linear hardening. The implementation has been made for a combined isotropic/kinematic hardening. However, to simplify the equation and because in the first instance the isotropic hardening has been used in the simulations, the algorithm presented below describes the case of a linear isotropic hardening only. The unidimensional rate-independent plasticity theory with

linear isotropic hardening presented hereby is based on the notes of Yaw [233] and on the works published by Simo and Hugues in [234].

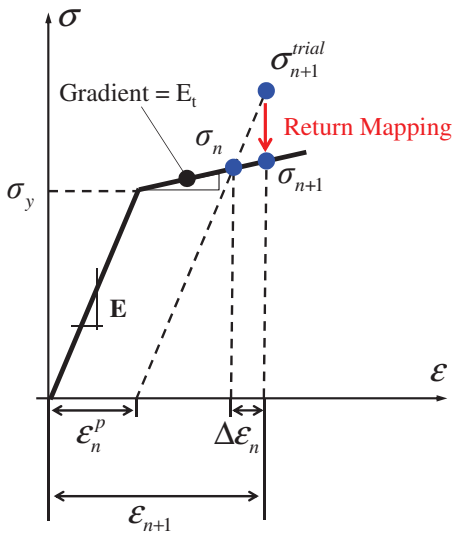

Figure 4.3: Schematic representation of the 1D plasticity formulation with linear hardening

The following two standard equations are assumed and they represent the starting point of the theory. The total strain rate $\dot{\varepsilon}$ can be divided into an elastic part $\dot{\varepsilon}^e$ and a plastic part $\dot{\varepsilon}^p$ as defined by the following equation:

$$\dot{\varepsilon} = \dot{\varepsilon}^e + \dot{\varepsilon}^p \tag{4.10}$$

The elastic stress-strain relationship, where $\dot{\sigma}$ represents the stress rate and E the stiffness of the system, is then expressed by:

$$\dot{\sigma} = E\left(\dot{\varepsilon} - \dot{\varepsilon}^p\right) \tag{4.11}$$

The flow rule and the isotropic hardening law are respectively defined by:

$$\dot{\varepsilon}^p = \lambda \text{sign}\left(\sigma\right) \tag{4.12}$$

$$\dot{\alpha} = \lambda \tag{4.13}$$

where α is a non-negative function considered as an internal hardening variable. It allows to keep track of the accumulated hardening and it represents the equivalent plastic strain for isotropic hardening. The *sign* function returns the value -1 if the variable is negative and 1 if the variable is positive. λ can be seen as the absolute value of the slip rate, which can be mathematically described by:

$$\begin{cases} \dot{\varepsilon}^p = \lambda \geqslant 0 & (\sigma = \sigma_y > 0) \\ \dot{\varepsilon}^p = -\lambda \leqslant 0 & (\sigma = -\sigma_y < 0) \end{cases} \tag{4.14}$$

A yield criterion is then introduced to identify the elastic and plastic regime. In the case of a linear hardening, this condition is expressed by:

$$f\left(\sigma, \alpha\right) = |\sigma| - \left(\sigma_y + K\alpha\right) \tag{4.15}$$

where f is called the yield function and it has to be negative to remain within the elastic regime. A positive value of f is not admissible. σ_y is the yield stress and K is generally called the plastic modulus.

Finally, the modeling of the plastic flow is based on the Kuhn-Tucker conditions Eq. (4.16) and on a consistency condition Eq. (4.17) defined by:

$$\lambda \geqslant 0,\ f(\sigma,\alpha) \leqslant 0,\ \lambda f(\sigma,\alpha) = 0 \tag{4.16}$$

$$\lambda \dot{f}(\sigma,\alpha) = 0,\ \text{if } f(\sigma,\alpha) = 0 \tag{4.17}$$

Assuming now a smooth function f defined over $\mathbb{R}$ as:

$$\begin{cases} \dot{x}(t) = f(x(t)) \\ x(0) = x_n \end{cases} \tag{4.18}$$

The incremental integration algorithm defined by the Eq. (4.19) is based on the backward-Euler methods and it allows to approximate the value of x at time $t_{n+1} = t_n + \Delta t$.

$$x_{n+1} = x_n + \Delta t\,(f(x_{n+1})) \tag{4.19}$$

The aim is now to integrate the previous equations to be used on a finite time step Δt. Using the Eqs. (4.12) and (4.13), we obtain the incremental formulation of the flow rule and of the hardening law expressed by:

$$\varepsilon^p_{n+1} = \varepsilon^p_n + \Delta\lambda \text{sign}(\sigma_{n+1}) \tag{4.20}$$

$$\alpha_{n+1} = \alpha_n + \Delta\lambda \tag{4.21}$$

The discrete stress-strain relationship is then defined by:

$$\begin{cases} \sigma_{n+1} = E\left(\varepsilon_{n+1} - \varepsilon^p_{n+1}\right) \\ \varepsilon_{n+1} := \varepsilon_n + \Delta\varepsilon_n \end{cases} \tag{4.22}$$

In this case the mathematical operator $:=$ means that we affect the value $\varepsilon_n + \Delta\varepsilon_n$ to the variable ε_{n+1}, $\Delta\varepsilon_n$ being known. Finally the discrete Kuhn-Tucker conditions can be expressed by:

$$\begin{cases} f_{n+1} := |\sigma_{n+1}| - (\sigma_y + K\alpha_{n+1}) \leqslant 0 \\ \Delta\lambda \geqslant 0 \\ \Delta\lambda f_{n+1} = 0 \end{cases} \tag{4.23}$$

The process begins with the trial of an elastic state as defined by:

$$\begin{aligned} \sigma^{trial}_{n+1} &:= E\left(\varepsilon_{n+1} - \varepsilon^{p^{trial}}_{n+1}\right) = E\left(\varepsilon_{n+1} - \varepsilon^p_n\right) \\ \varepsilon^{p^{trial}}_{n+1} &:= \varepsilon^p_n \\ f^{trial}_{n+1} &:= \left|\sigma^{trial}_{n+1}\right| - (\sigma_y + K\alpha_n) \\ \alpha^{trial}_{n+1} &:= \alpha_n \end{aligned} \tag{4.24}$$

where the value of $(\sigma_y + K\alpha_n)$ is known because it is given either by the Ramberg-Osgood model or by the algorithm finding the stress of the corresponding strain in the user-defined load curve. Then, the statement that for a given incremental strain $\Delta\varepsilon_n$ the process leads to an elastic or a plastic state, is made based on the trial elastic state and according the criterion expressed by:

$$f^{trial}_{n+1} \begin{cases} \leqslant 0 \text{ elastic state} & \Delta\lambda = 0 \\ > 0 \text{ plastic state} & \Delta\lambda > 0 \end{cases} \tag{4.25}$$

The objective is to determine the solutions $\Delta\lambda$, ε^p_{n+1}, α_{n+1} and σ_{n+1} to the Eqs. (4.20), (4.21) and (4.23). It is clear that all the solutions rely on the determination of $\Delta\lambda$. Applying the Eqs. (4.21) and (4.22) in the expression of f_{n+1} (Eq. (4.23)) it leads to:

$$\begin{aligned} f_{n+1} &= \left|E\left(\varepsilon_{n+1} - \varepsilon^p_{n+1}\right)\right| - (\sigma_y + K\alpha_n + K\Delta\lambda) \\ &= \left|E\left(\varepsilon_{n+1} - \varepsilon^p_n\right) - E\left(\varepsilon^p_{n+1} - \varepsilon^p_n\right)\right| - (\sigma_y + K\alpha_n + K\Delta\lambda) \end{aligned} \tag{4.26}$$

Then, by application of the Eqs. (4.24) and (4.20) it leads to:

$$\begin{aligned} f_{n+1} &= \left|\sigma^{trial}_{n+1}\right| - (\sigma_y + K\alpha_n) - \left|E\left(\varepsilon^p_{n+1} - \varepsilon^p_n\right)\right| - K\Delta\lambda \\ f_{n+1} &= f^{trial}_{n+1} - \Delta\lambda\left(E + K\right) \end{aligned} \tag{4.27}$$

Hence, making $f_{n+1} = 0$ we obtain

$$\boxed{\Delta\lambda = \frac{f^{trial}_{n+1}}{E+K} > 0} \tag{4.28}$$

Transforming the expression of σ_{n+1} in terms of σ^{trial}_{n+1} and $\Delta\lambda$ we obtain:

$$\begin{aligned} \sigma_{n+1} &= E\left(\varepsilon_{n+1} - \varepsilon^p_n\right) - E\left(\varepsilon^p_{n+1} - \varepsilon^p_n\right) \\ &= \sigma^{trial}_{n+1} - E\,\Delta\lambda\,\mathrm{sign}\left(\sigma_{n+1}\right) \end{aligned} \tag{4.29}$$

Finally, the last three solutions of the problem are expressed by (the demonstration of $\mathrm{sign}\left(\sigma^{trial}_{n+1}\right) = \mathrm{sign}\left(\sigma_{n+1}\right)$ can be found in [234]):

$$\boxed{\begin{aligned} \sigma_{n+1} &= \sigma^{trial}_{n+1} - E\,\Delta\lambda\,\mathrm{sign}\left(\sigma^{trial}_{n+1}\right) \\ \varepsilon^p_{n+1} &= \varepsilon^p_n + \Delta\lambda\,\mathrm{sign}\left(\sigma^{trial}_{n+1}\right) \\ \alpha_{n+1} &= \alpha_n + \Delta\lambda \end{aligned}} \tag{4.30}$$

The numerical solution of Eq. 4.30 requires the knowledge of the plastic module K. Considering a linear isotropic hardening function we can write that the increment in plastic strain $d\varepsilon^p$ and in elastic strain $d\varepsilon^e$ are expressed by [235]:

$$\begin{aligned} \mathrm{d}\varepsilon^p &= \frac{\mathrm{d}\sigma}{K} \\ \mathrm{d}\varepsilon^e &= \frac{\mathrm{d}\sigma}{E} \end{aligned} \tag{4.31}$$

From the Eq. 4.10, the total strain is then defined by:

$$\begin{aligned} \mathrm{d}\varepsilon &= \mathrm{d}\varepsilon^e + \mathrm{d}\varepsilon^p \\ &= \frac{\mathrm{d}\sigma}{E} + \frac{\mathrm{d}\sigma}{K} \\ &= \mathrm{d}\sigma\left(\frac{E+K}{EK}\right) \end{aligned} \tag{4.32}$$

The incremental stress $\mathrm{d}\sigma$ expressed in function of the tangent module E_t (see Fig. 4.3), which is determined by the algorithms of the Ramberg-Osgood model or of the load curve and which is consequently known, is:

$$\mathrm{d}\sigma = \left(\frac{EK}{E+K}\right)\mathrm{d}\varepsilon = E_t\mathrm{d}\varepsilon \tag{4.33}$$

The expression of K is finally given by:

$$\boxed{K = \frac{E_t E}{E - E_t}} \tag{4.34}$$

4.3 Failure criterion

Several failure criteria have been developed and investigated in the World Wide Failure Exercise [72]. They are generally suitable for laminated composites based on unidirectional lamina. However, due to the waviness of the yarns and the particular fabric structure, textile composites are likely to fail in different modes than non-crimp fabrics involving also different phenomena. Moreover, for efficiency reasons, failure criteria based on the effective strengths of a lamina are preferred. Finally, as no trivial failure criterion have been developed for woven composites, we chose to investigate first the very simple maximum stress criterion. In order to improve the failure prediction of multidirectional stacking sequences, the quadratic Tsai-Wu failure criterion [236] has been also implemented.

4.3.1 Maximal stress failure criterion

The maximum stress criterion compares the current stress state in the lamina to the strength of the material in each direction. Consequently, if the ratio between the stress σ_i and its corresponding strength X_i is greater than or equal to 1, failure is detected. It can be expressed by:

$$\frac{\sigma_i}{X_i} = 1 \ \ (i = 1, 2, 3, 4) \tag{4.35}$$

The resulting failure surface is a square bounded by the different strengths of the material as presented on Fig. 4.4.

4.3.2 The 2D Tsai-Wu failure criterion

The 2D Tsai-Wu failure criterion [236] is a quadratic failure criterion based on the in-plane effective strengths of a material. Its advantage in comparison with the maximum stress criterion is that it offers a smooth continuous ellipsoidal failure surface (see Fig. 4.4) without involving specific and complex failure modes. The three-dimensional formulation of the Tsai-Wu failure criterion [27, 237] will be considered in a future work particularly for a modeling involving thick-shell elements featuring a three-dimensional stress state. However, as complex experimental tests are required to determine some transverse strengths and some parameters of the three-dimensional Tsai-Wu failure criterion, only the in-plane Tsai-Wu failure criterion is considered in the present study. It is expressed by:

$$\frac{\sigma_1^2}{X_\mathrm{t} X_\mathrm{c}} + \frac{\sigma_2^2}{Y_\mathrm{t} Y_\mathrm{c}} + \frac{\sigma_4^2}{S_{12}^2} + \left[\frac{1}{X_\mathrm{t}} - \frac{1}{X_\mathrm{c}}\right]\sigma_1 + \left[\frac{1}{Y_\mathrm{t}} - \frac{1}{Y_\mathrm{c}}\right]\sigma_2 + \frac{2F_{xy}^*\sigma_1\sigma_2}{\sqrt{X_\mathrm{t} X_\mathrm{c} Y_\mathrm{t} Y_\mathrm{c}}} = 1 \tag{4.36}$$

where X_t and X_c are respectively the longitudinal tensile and compressive strengths. Y_t and Y_c are respectively the transverse tensile and compressive strengths. S_{12} is the shear strength and F_{xy}^* is defined as a bounded ($-1 \leqslant F_{xy}^* \leqslant 1$) normalized interaction term closing the failure surface. Fig. 4.4 compares the failure surfaces of the maximum stress and Tsai-Wu ($F_{xy}^* = -0,5$) criteria. Both tensile strengths have a value of $1GPa$ whereas both compressive strengths have a value of $0.5GPa$. The shear strength is set to $0.07GPa$. The graph on the left represents the failure surface in the (σ_1, σ_2) space and the graph on the right represents the failure surface on the frame (σ_1, σ_4). A similar failure surface is obtained in the frame (σ_2, σ_4) considering the value of the strengths in this case.

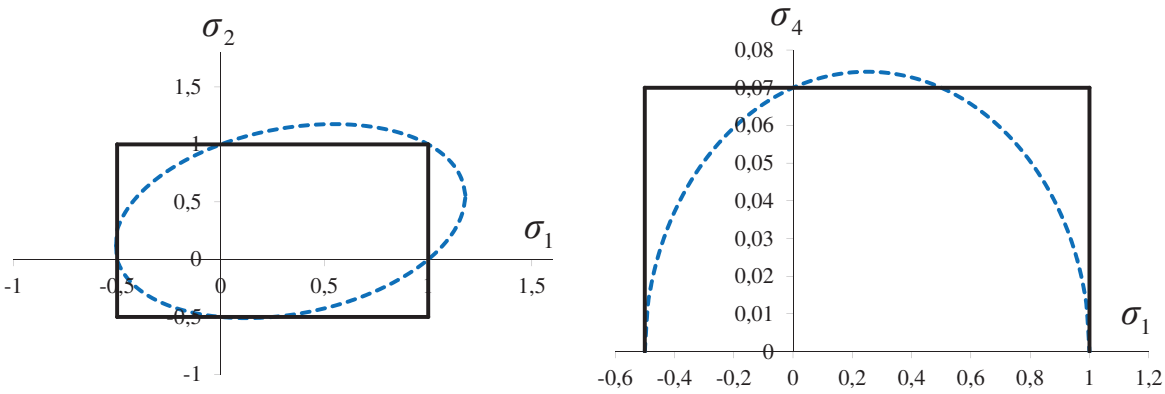

Figure 4.4: Failure surfaces of the maximum stress (black curve) and Tsai-Wu (dotted blue curve) failure criteria

4.4 Post-failure behavior and damage

The damage processes described in the next sections are applied to each ply of composite generally represented by one point of integration in elements based on a reduced integration (shell and thick shell elements). The complete stacking sequence of the composite material is then modeled by the definition of several points of integration through the thickness of the element. To simplify the equations, no subscript representing the different material and load directions is used. However, each fracture energy, stress, strain and damage variable depends on the material and load direction of each point of integration. For the in-plane shear a linear damage evolution law is always defined independently from the damage evolution law of the other in-plane material directions.

4.4.1 Smeared formulation

A smeared formulation involving damage variables has been used to avoid undesirable localization phenomena [151, 238]. As laminated structures are generally modeled by a unique shell or thick shell element layer over the thickness (industrial limitations), the post-failure behavior quantifies the damage accumulation in the material and also its damage tolerance. The basic principle of the smeared formulation is the introduction of a length parameter in the damage constitutive law in order to achieve a constant energy released per unit area of crack generated independently from the element dimensions. The total energy U absorbed by one element after failure can be expressed by:

$$U = VU_{vol} = L_1 L_2 L_3 \left(\Gamma_1 + \Gamma_2\right) \tag{4.37}$$

where V is the volume of the element and U_{vol} is the total energy absorbed per unit volume. The fracture plane and the element lengths are defined on Fig. 4.5a. Γ_1 and Γ_2 are respectively the areas under the stress-strain curve before and after the strain at failure onset ε^o, as schematically represented in Fig. 4.5b. The aim is to define an energy per unit area Γ being a constant material property. It can be expressed by:

$$U = A\Gamma = L_1 L_3 \Gamma \tag{4.38}$$

and consequently we obtain:

$$\Gamma = U_{\text{vol}} \frac{V}{A} = (\Gamma_1 + \Gamma_2) \frac{V}{A} \tag{4.39}$$

where A is the area of the fracture plane assumed to be orthogonal to the load direction. As Γ is a constant value referring to a fracture toughness, the mesh independent behavior relies on the update of the Γ_1 and Γ_2. For an imposed material strength σ^o and a strain at failure onset ε^o, this update clearly depends on the value of the final strain ε^f. This parameter is given as input data and the energies are calculated for a particular mesh size. Then, for other sizes of elements, this value is updated to obtain the adequate corresponding fracture energy as described in the next sections. The computation of both energies and the update of the final strain ε^f are presented below.

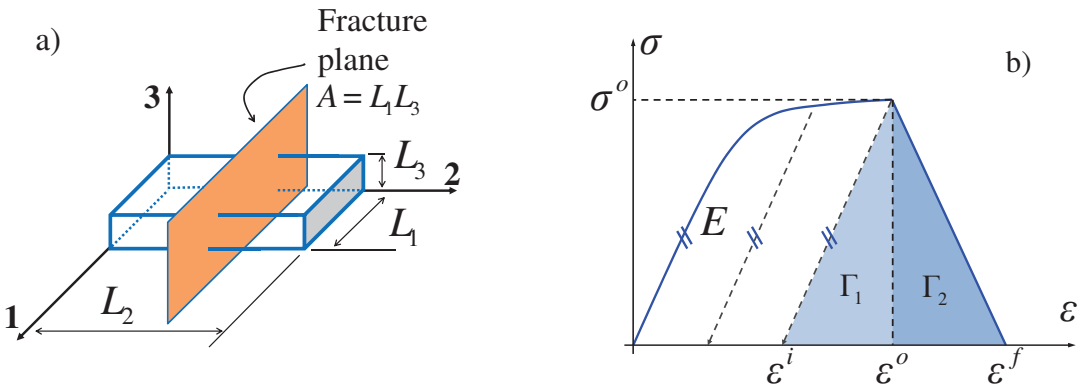

Figure 4.5: a) Fracture plane for a load in the direction 2 - b) Example of a material law with a linear post-failure material degradation

The energy dissipated per unit volume $U_{\text{vol}} = \Gamma_1 + \Gamma_2$ is equal to the ratio between the fracture toughness Γ and the element characteristic length l^* as expressed by:

$$U_{\text{vol}} = \frac{\Gamma}{l^*} \tag{4.40}$$

As the direction of crack propagation may feature a random aspect in crash, the average of the element characteristic length is used. For square elements (aspect ratio close to one) it is expressed by [225, 238]:

$$l^* = 1,12\sqrt{A_{\text{IP}}} \tag{4.41}$$

where A_{IP} is the area associated with each integration point. As the shape of an automotive part is likely to be relatively complex, triangular elements will appear in the mesh. For these elements, the characteristic element length can be approximated by [225]:

$$l^* = 2\sqrt{\frac{A_{IP}}{\sqrt{3}}} \simeq 1,52\sqrt{A_{\text{IP}}} \tag{4.42}$$

The different final strains defining the fracture energies (see the next sections) are generally validated for a particular mesh size. A reference fracture toughness Γ^{ref} depending on a reference characteristic length l^*_{ref} corresponding to this element size can thus be calculated:

$$\Gamma^{\text{ref}} = U_{\text{vol}} l^*_{\text{ref}} \tag{4.43}$$

Finally, after failure onset, damage variables d can be used to drive the degradation process and to evaluate the level of damage of the material. A damage variable is defined in tension and in compression for the in-plane longitudinal, transverse and shear directions. No damage variable through the thickness is defined for the modeling with bricks or thick shell elements. In the present UMAT, the quantity $(1-d)$ is multiplied to the undamaged stress σ^{ud} corresponding to the current strain state as defined by the following equation:

$$\sigma = (1-d)\,\sigma^{\mathrm{ud}} \tag{4.44}$$

The damage variables take the value 0 at the failure onset and value 1 at the ultimate failure (stress also reduced to 0). They are always positive and the irreversibility of the process is expressed by:

$$d(t) = \max_{t' \leqslant t} \{d(t')\} \tag{4.45}$$

4.4.2 Determination of the energy before failure onset Γ_1

In the case of a linear elastic behavior up to failure onset $(\varepsilon^o, \sigma^o)$, the calculation of Γ_1^{L} is relatively trivial since it is represented by the area of a square triangle and expressed by:

$$\Gamma_1^{\mathrm{L}} = \frac{\varepsilon^o \sigma^o}{2} = \frac{(\sigma^o)^2}{2E} \tag{4.46}$$

In the case of a nonlinear plastic behavior up to failure onset, two kinds of energies have to be distinguished: the energy absorbed by the nonlinear process (irreversible microcracks and plasticity) and the energy absorbed due to the formation of a localized failure surface at failure onset. Only the elastic internal energy in the element is involved in the fracture process at the failure onset and only this energy has to be considered in the determination of the fracture toughness, as depicted by Fig. 4.5b. The absorbed energy up to failure onset in the case of a nonlinear plastic material behavior Γ_1^{NLP} can be expressed by:

$$\Gamma_1^{\mathrm{NLP}} = \frac{\left(\varepsilon^o - \varepsilon^i\right)\sigma^o}{2} = \frac{(\sigma^o)^2}{2E} \tag{4.47}$$

As no stiffness degradation is defined for the unload of the material and the accumulation of permanent deformation, the quantity $\varepsilon^o - \varepsilon^i$ is equivalent to the ratio σ^o/E. Finally, in the case of a pure nonlinear elastic behavior, a numerical integration method based on the trapezoid rule is used to approximate the area under the curve until the failure onset. The following sections deal with the determination of energy after failure Γ_2 for four post-failure material degradation models.

4.4.3 Post-failure material degradation models

Four different post-failure material degradation models have been developed and implemented. Fig. 4.6 shows an overview and a schematic representation of these models, in the case of a nonlinear plastic pre-failure material behavior.

4.4.3.1 Linear damage

A linear damage evolution law similar as the one developed by Pinho [150, 151] has been implemented. The instantaneous damage is expressed by:

$$d_{\mathrm{L}}^{\mathrm{inst}} = \max\left\{0, \min\left\{1, \varepsilon^f \frac{\varepsilon - \varepsilon^o}{\varepsilon\left(\varepsilon^f - \varepsilon^o\right)}\right\}\right\} \tag{4.48}$$

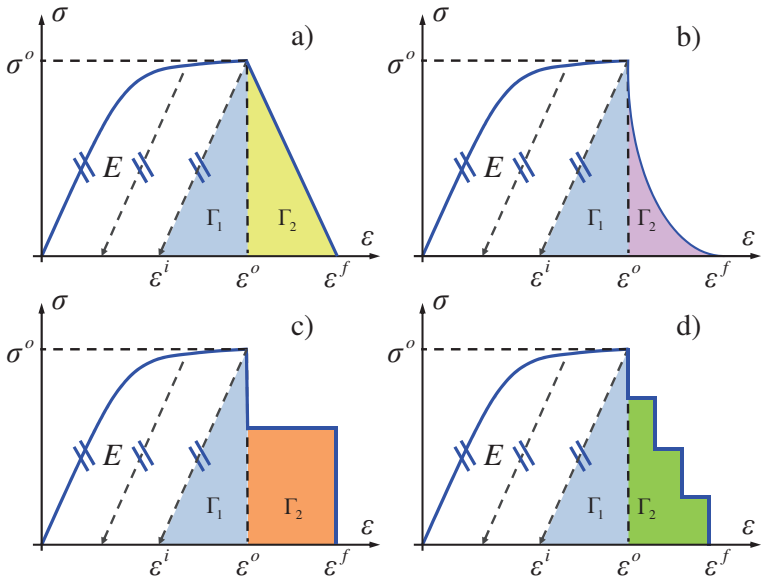

Figure 4.6: Overview and schematic representation of the four post-failure material degradation models: a) linear damage - b) nonlinear damage - c) constant stress level post-failure material degradation - d) steps-based post-failure material degradation

The calculation of the second part of the fracture toughness Γ_2^{L} from the failure onset until the ultimate failure is here relatively trivial and it is defined by:

$$\Gamma_2^{\mathrm{L}} = \frac{\left(\varepsilon^f - \varepsilon^o\right)\sigma^o}{2} \tag{4.49}$$

The final strain $\varepsilon^f_{\mathrm{new}}$ is then calculated and eventually updated for the new mesh size. The new final strain is expressed by:

$$\varepsilon^f_{\mathrm{new}} = \frac{2\Gamma^{\mathrm{ref}}}{\sigma^o l^*} \tag{4.50}$$

For the nonlinear plastic behavior until the failure onset the updated final strain is defined by:

$$\varepsilon^f_{\mathrm{new}} = \frac{2\Gamma^{\mathrm{ref}}}{\sigma^o l^*} + \varepsilon^{\mathrm{i}} \tag{4.51}$$

where ε^{i} is defined in the Fig. 4.5b and it represents the plastic strain from which the final strain has to be calculated. ε^{i} can be expressed by:

$$\varepsilon^{\mathrm{i}} = \varepsilon^o - \frac{\sigma^o}{E} \tag{4.52}$$

4.4.3.2 Step-based material degradation

In addition to the linear evolution law, a step-based degradation scheme has been implemented as post-failure behavior. A number between 1 and 4 steps can be defined between the failure onset and the ultimate failure. Here, no damage variable pilots the degradation. Mathematical operations show that the area under the curve Γ_2 is the same as in the case of a linear damage independently from the number of steps. The aim is here to depict the progressive and non-homogeneous degradation process in the structural behavior of the laminate. To evaluate the damage state of the material after failure onset, the linear damage variable defined previously is used here only as a damage indicator. The final strain and fracture toughness determinations are similar as those of the linear case.

4.4.3.3 Constant stress level material degradation

In this case a constant stress level is defined as post failure behavior, similarly to the *MAT_054 and *MAT_058. The second fracture energy Γ_2^{level} is expressed by:

$$\Gamma_2^{\text{level}} = \left(\varepsilon^f - \varepsilon^o\right) \sigma^o \times coef_{xx} \tag{4.53}$$

where $coef_{xx}$ is a factor ranging from 0 to 1. Being multiplied by the strength value, it defines the level of the constant post-failure stress. Subscript xx indicates the strength in each direction as defined for Eq. (4.36). The basic equation to determine the updated final strain is given by:

$$\frac{\Gamma^{\text{ref}}}{l^*} = \frac{\left(\sigma^o\right)^2}{2E} + \left(\varepsilon^f_{\text{new}} - \varepsilon^o\right) \sigma^o \times coef_{xx} \tag{4.54}$$

For the linear elastic case, the updated final strain is expressed by:

$$\varepsilon^f_{\text{new}} = \varepsilon^o + \left(\frac{\Gamma^{\text{ref}}}{l^*} + \frac{\left(\sigma^o\right)^2}{2E}\right) \times \frac{1}{\sigma^o \times coef_{xx}} \tag{4.55}$$

and for the nonlinear plastic case it is defined by:

$$\varepsilon^f_{\text{new}} = \varepsilon^o + \left(\frac{\Gamma^{\text{ref}}}{l^*} + \frac{\left(\sigma^o\right)^2}{2E}\right) \times \frac{1}{\sigma^o \times coef_{xx}} + \varepsilon^i \tag{4.56}$$

The linear damage variable is also used here as a damage indicator.

4.4.3.4 Nonlinear damage

In this section, the formulation of a damage variable defining a nonlinear post-failure material degradation is investigated. A first formulation d^1_{NL} based on the nth root of the linear damage variable is expressed by:

$$\boxed{d^1_{\text{NL}} = \sqrt[n]{\varepsilon^f \frac{\varepsilon - \varepsilon^o}{\varepsilon\left(\varepsilon^f - \varepsilon^o\right)}}} \tag{4.57}$$

The irreversibility condition mentioned in Eq. (4.45) and the formulation for the instantaneous value of the damage used in Eq. (4.48) are also here valid. The parameter n is an input data value to control the shape of the degradation between the failure onset and the ultimate failure. Due to some numerical instability after reaching the failure onset, a second nonlinear damage formulation has been developed based on an exponential model. This new formulation offers a softer degradation of the material immediately after failure onset. We assume that in the post failure domain the stress can be expressed by:

$$\sigma = \exp\left(-A\varepsilon + B\right) \tag{4.58}$$

where A and B are constants that have to be determined using the boundary conditions of the damage variable. Combining Eqs. (4.44) and (4.58) and considering σ^{ud} as an increasing function of the strain state ε in each material direction such as $\sigma^{\text{ud}} = \sigma^{\text{ud}}(\varepsilon)$ we can write:

$$d_{\text{NL}} = 1 - \frac{\exp\left(-A\varepsilon + B\right)}{\sigma^{\text{ud}}\left(\varepsilon\right)} \tag{4.59}$$

As mentioned above, the values of the damage variable range from 0 at failure onset ε^o to 1 at ultimate failure ε^f. These boundary conditions are applied to Eq. (4.59) and it leads to the following system

involving two unknown variables A, B to be calculated:

$$\begin{aligned} 1 - \frac{\exp\left(-A\varepsilon^f + B\right)}{\sigma^{\mathrm{ud}}\left(\varepsilon^f\right)} &= 1 - \beta \\ 1 - \frac{\exp\left(-A\varepsilon^0 + B\right)}{\sigma^{\mathrm{ud}}\left(\varepsilon^0\right)} &= 0 \end{aligned} \tag{4.60}$$

The term $\exp\left(-A\varepsilon^f + B\right)$ cannot be equal to zero. The exponential function presents only an asymptotic behavior to the value 0. A parameter β is introduced in the equation and represents a very small value close to 0. This parameter is given as input data because it allows to control the shape of the post-failure nonlinear damage. After some mathematical operations we obtain the expression of the nonlinear damage variable d_{NL} given by:

$$\boxed{d_{\mathrm{NL}} = 1 - \frac{\exp\left[-\left(\frac{\ln\left(\frac{\sigma^{\mathrm{ud}}\left(\varepsilon^0\right)}{\beta\sigma^{\mathrm{ud}}\left(\varepsilon^f\right)}\right)}{\varepsilon^f - \varepsilon^0}\right)\varepsilon + \left(\ln\left(\sigma^{\mathrm{ud}}\left(\varepsilon^0\right)\right) + \varepsilon^0 \frac{\ln\left(\frac{\sigma^{\mathrm{ud}}\left(\varepsilon^0\right)}{\beta\sigma^{\mathrm{ud}}\left(\varepsilon^f\right)}\right)}{\varepsilon^f - \varepsilon^0}\right)\right]}{\sigma^{\mathrm{ud}}\left(\varepsilon\right)}} \tag{4.61}$$

The irreversibility condition mentioned in Eq. (4.45) and the formulation for the instantaneous value of the damage used in Eq. (4.48) are valid again. As no trivial equation can be found to determine the updated final strain at ultimate failure ε^f, a trial-and-error FORTRAN routine has been implemented to look for the adequate value of the final strain.

4.4.4 Mesh dependency

To avoid mesh dependency, a non-local approach has been developed and implemented in LS-DYNA [239]. In the present UMAT, the mesh independence is provided by the smeared formulation, which automatically adapts the strain at ultimate failure in function of the mesh size. Fig. 4.7 presents a longitudinal tensile test on different mesh sizes for a given $12mm \times 12mm$ initial area. Both graphs illustrate the mesh-independence of the regularized linear (see Fig. 4.7a) and nonlinear (see Fig. 4.7b) damage formulations. A light numerical dispersion can be observed on the linear formulation. For the nonlinear damage, a larger dispersion occurred due to the presence of the β parameter. In the case of the nonlinear damage, the sudden force level reduction after failure onset is caused by a sudden increase in the damaged element deformation, the damage variable being based on the strain evolution. A light dispersion has also been observed for the constant stress level and step-based post-failure behavior. Fig. 4.8 illustrates the update of the final strain in function of the mesh size for the constant stress level Fig. (4.8a) and for the step-based (4.8b) post-failure material degradation schemes. The last vertical line at the ultimate failure point is not inherent to the material model. Here it allows only to identify the value of the final strain more easily. We can observe that the regularization formulation logically doubles the value of the final strain whenever the mesh size becomes twice as fine. Indeed, using Eq. (4.50) when the characteristic length l^* is twice as low, the final strain $\varepsilon^f_{\mathrm{new}}$ has to become twice as great.

4.4.5 Critical element length

As described before, the strain at ultimate failure $\varepsilon^f_{\mathrm{new}}$ is automatically adapted to each mesh size in function of a reference element size, for which the parameter has been calibrated. In the case of a linear elastic behavior followed by a linear post-failure damage, the new strain at ultimate failure is given by the

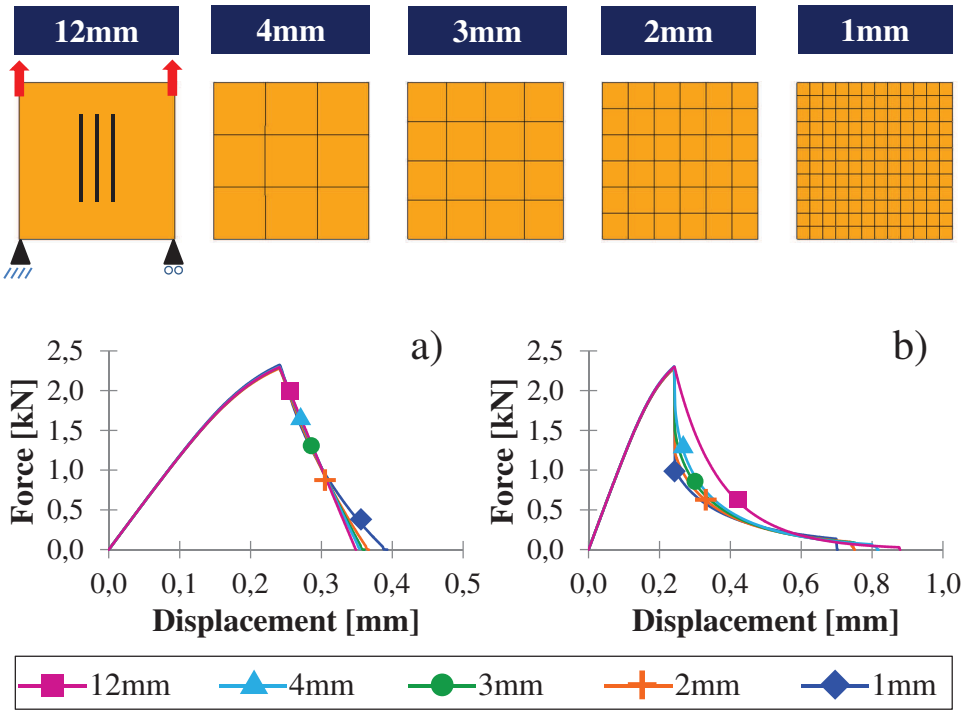

Figure 4.7: Mesh-size independence of the regularized linear a) and nonlinear b) damage

Eq. 4.50. A coarser mesh than the reference element size (corresponding to higher values of l^*) implies a decrease of the strain at ultimate failure. If the element characteristic length tends to the infinite, the updated strain at failure tends to zero. This shows that a new strain at ultimate failure lower than the strain at failure onset ε^o is likely to be computed. In this case, the element has more energy at the failure onset than the energy required for the formation of a crack across it [151]. Consequently, the element size must be kept smaller than a maximal critical element size. It can be shown that the critical element size (for a linear behavior and a linear damage) can be expressed by [225, 238]:

$$l^{\text{crit}} \leqslant \frac{2E\Gamma}{(\sigma^o)^2} \tag{4.62}$$

where E, Γ and σ^o are respectively the Young's modulus, the fracture energy (see Eq. 4.39) and the strength of the material in the considered direction. If the model involves elements larger than the critical element size, a mesh refinement is recommended to avoid the snap-back in the stress-strain relation. If a mesh refinement is impossible, another solution could be to reduce the strength of the material according to the Eq. 4.62 and as expressed by the following equation:

$$\sigma^o \leqslant \sqrt{\frac{2E\Gamma}{l^{\text{crit}}}} \tag{4.63}$$

However, the modification of the strength is not wished. Moreover, no trivial equation allows to link the critical element length to the fracture energy or strain at ultimate failure in the case of the nonlinear post-failure damage evolution law. Consequently, if a higher element size than the critical one is used in the numerical model, a minimal strain at ultimate failure has been defined in the actual implementation. Thus, as soon as an updated strain at failure lower than the strain at failure onset is detected, the updated strain at failure is given by:

$$\varepsilon^f_{\text{new}} = 1.01\varepsilon^o \tag{4.64}$$

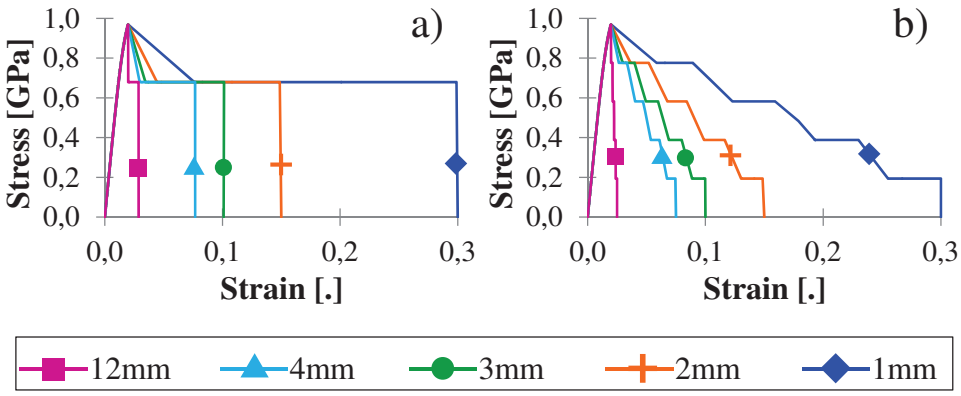

Figure 4.8: Final strain update for the regularized constant stress level a) and step-based b) post-failure material degradation

A quite vertical and very quickly post-failure material degradation is thus defined and the elements will absorb in this case more energy than they should during failure. The user has to be aware of this phenomenon and he has to consider it in the analysis of the numerical results. In the case of industrial applications, the strain at ultimate failure parameters will be generally already calibrated and set for relatively coarse meshes. The risk to be confronted to the problem of the critical length is thus reduced.

4.5 Input data of the model

This section presents an overview of the parameters required as an input for the numerical material model developed in this study. First, the three "tensile" Young's modules (E_1, E_2, E_3) and the three shear modules (G_{12}, G_{23}, G_{31}) have to be given. Both in-plane longitudinal and transverse "compressive" Young's modules can be defined if different stiffnesses in tension and in compression have to be considered. The in-plane stiffness modules are easily obtained using quasi-static tests on elementary coupons. The out-of-plane modules have been determined using the work presented in [51]. The three Poisson's ratio $(\nu_{21}, \nu_{31}, \nu_{32})$ have to be given as an input and they can also been obtained using the results reported in [51]. The model requires then the five material strengths $(X_t, X_c, Y_t, Y_c, S_{12})$ to predict failure. Both strengths through the thickness (Z_t, Z_c) must be defined, as a maximal stress failure criterion has been implemented for a failure in the out-of-plane direction. This applies to the modeling with thick shell or brick elements. An additional parameter allows to choose between the maximal stress and the Tsai-Wu criteria to predict failure. The previous parameters are the basic material parameters required for the modeling of the elastic response and the prediction of failure of an orthotropic composite.

To model the nonlinear behavior using the Ramberg-Osgood equation, the five strains at failure onset and the five exponents n have to be given as an input. If the macroscopic nonlinear behavior is predicted using a load curve, its identification number and the five strains at failure onset have to be given. A separate parameter allows to choose between both models to predict nonlinearity. It permits also to activate or not the 1D plasticity theory and the consideration of a post-failure material degradation.

Regarding the definition of a post-failure material degradation, the five strains at ultimate failure are required. For the linear damage, no additional parameter is needed. For the nonlinear damage the value of the parameter β is required to control the shape of the nonlinear material degradation. Concerning

the step-based degradation, the number of steps has to be defined (between 1 and 4). For the constant stress level, the five $coef_{xx}$ coefficients are required in order to define the level of the post-failure stress. An additional parameter allows to choose one of the four post-failure degradation models. Finally, a parameter controls the number of integration points (per element) that have to fail before the deletion of the element.

The strain at ultimate failure defines the intralaminar fracture toughness of the material. They are currently set to obtain acceptable results for the impact tests on elementary plates or on representative components like the hat-profiles. These energy release rate of intralaminar fracture are relatively difficult to obtain experimentally. The common experimental tests used to determine them are the Compact Tension (CT) often referring to the ASTM-E399 standard for metallic materials [240–244], Compact Compression (CC) [245, 246], three-point bending [240, 247], centrally cracked four-point bending tests [241, 248], double edge notch [241] and double cantilever beam (DCB) [249]. Such kind of experimental tests are generally made on unidirectional non-crimp fabric laminate. It could be interesting to investigate the validity of such tests on woven composites. Moreover, bearing tests should also contribute in the determination and the calibration of the post-failure damage parameters [250], particularly for the compressive failure modes. Indeed, this kind of tests, based on the ASTM 5961 standard allows to investigate the progressive post-failure degradation and fragmentation of a composite material. Finally, a consistent method is still to develop for the characterization of the different fracture toughnesses and their direct application in numerical models adapted for industrial applications.

4.6 Analysis of the results

This section presents the different indicators available to facilitate the analysis of the results. They are saved as history variables during the simulations. Macroscopic strains and their corresponding plastic strains are also saved for each point of integration and for each in-plane material direction. The values of each fracture energy and each updated strain at ultimate failure are also saved to help the user in his work.

4.6.1 Failure indicators

Failure indicators are used to assess the state of failure of each integration point. A value of 0 means that the material is unloaded, whereas a value of 1 means that failure is detected using the failure criterion.

For the maximum stress criterion, the failure indicator is trivial and it is expressed by the ratio between the current stress and the strength of the material (see Eq. 4.35). An irreversibility condition has been implemented to save the maximal failure level reached during the simulation. A failure indicator is used for each in-plane material directions, which corresponds to a total of five failure indicators.

The failure index referring to the Tsai-Wu criterion is inspired for the method detailed in [236]. The failure index is defined as the inverse of the strength ratio R expressed by:

$$R = \frac{-b}{2a} + \sqrt{\frac{b^2}{4a^2} + \frac{1}{a}} \tag{4.65}$$

where the parameters a and b are respectively given by:

$$a = \frac{\sigma_1^2}{X_\mathrm{t} X_\mathrm{c}} + \frac{2F_{12}^* \sigma_1 \sigma_2}{\sqrt{X_\mathrm{t} X_\mathrm{c} Y_\mathrm{t} Y_\mathrm{c}}} + \frac{\sigma_2^2}{Y_\mathrm{t} Y_\mathrm{c}} + \frac{\sigma_4^2}{S_{12}^2} + \iota \tag{4.66}$$

$$b = \left(\frac{1}{X_\mathrm{t}} - \frac{1}{X_\mathrm{c}}\right)\sigma_1 + \left(\frac{1}{Y_\mathrm{t}} - \frac{1}{Y_\mathrm{c}}\right)\sigma_2 \tag{4.67}$$

The ι parameter used in the expression of a takes a very small value close to zero. Thus, the value of the strength ratio is defined at the places undergoing no deformation and no load, which corresponds to $a = 0$. The Tsai-Wu failure criterion involves only one failure indicator.

4.6.2 Damage indicators

Once failure is detected, the failure indicators take the value 1 and a post-failure material degradation begins. To assess the level of damage in the material, damage indicators similar as the failure indicators are used. In the case of the linear and nonlinear damage, the damage indicator is equal to the value of the damage variable. In the case of the step-based and constant stress level post-failure material degradation models, no damage variable pilots the material degradation process. In order to assess the level of post-failure damage in these both configurations, the linear damage variable is internally computed and used as a damage indicator. For each material degradation models, five damage indicators corresponding to the five in-plane material directions are used. A value of 0 means that no damage evolves and a value of 1 represents a full damaged state.

For industrial applications, it is important to know in first instance if the material underwent any damage or not. Consequently, the analysis of each damage indicators is likely to cost much time. Another damage indicator, referred to an averaged damage indicator, has been implemented in order to identify the areas of a large composite part being "in damage". For each of the four (not in shear) in-plane material directions and for each point of integration, a value of 2 is attributed to an extra history variable if no damage (i. e. no failure) has been detected. When the point of integration is identified as "in damage", a value of 1 is given to the history variable. Finally, if the ultimate failure is reached, it takes the value 0. Consequently, four history variables are thus defined, giving a qualitative state of the material. For each integration point, the averaged value of these four history variables is computed. Then, in each element, if at least one point of integration undergoes post-failure damage, the average is no more equal to 2 but it takes a value between 1 and 2. Finally, the minimal value of the averaged damage indicator has to be considered over the thickness of an element in order to identify the maximal damaged surface. Some fringe plots of this averaged damage indicator will be presented for the analysis of the numerical results concerning the impact tests on elementary plates (see the sections 5.3.5 and 6.3).

The work presented in this chapter resulted in the following publications [251–253] [1].

4.7 Partial conclusions

This section described the development of a mesh-insensitive user-defined material model being able to predict the linear and nonlinear behaviors of orthotropic composite materials and accounting for permanent deformation. A post-failure material degradation coupled to a smeared formulation in order to avoid unsuitable localization phenomena has been also implemented. Finally, in order to respect the limitations imposed by the industrial and engineering fields, the theory and the implementation have

[1] These publications include work from other chapters of this thesis and therefore feature again in the corresponding chapters

been kept as simple as possible and the main input parameters of the model are based on the effective mechanical properties of an elementary ply.

Chapter 5

Numerical results and validation on carbon plain-weave RTM specimens

5.1 Introduction

This chapter presents the numerical results obtained for the simulation of the experimental characterization tests made on the RTM plain-weave composite. Based on the experimental data coming from pre-tests on a material presenting outer glass mat layers, a comparison of the four main composite material models used for industrial applications and available in the LS-DYNA material models library will be presented. It will put in evidence the merits and limits of each model and it will allow to identify the missing features for more reliable predictions. The correlation will be also made for the numerical results obtained with the material model developed in this work (UMAT), highlighting its advantages over the current modeling techniques. Then, the numerical predictions obtained with the UMAT will be discussed and compared to the experimental results obtained on the RTM without glass mat. It will concern the quasi-static tests on elementary coupons, the impact tests on CAI-plates and the drop tower tests on hat-profiles.

The numerical models used for the simulation of the tensile (top) and compressive (bottom) tests are presented on Fig. 5.1. The load distribution provided by the end tabs in the real specimens is modeled by the use of interpolation constraints referring to the *CONSTRAINED_INTERPOLATION keyword. For both sides of the specimen, the nodes being in the zone of the end tabs constitute a set of independent nodes linked to a single dependent node. This single node belongs to a beam element. On one specimen's side, a traction load is applied on the second node of the beam by controlling its displacement. On the other side, the second node of the beam is locked. In order to avoid undesirable rotations, the corresponding degrees of freedom of some nodes in the area of tabs are locked. These nodes are not linked by interpolation constraints in order to avoid double constraints on a unique node, which can lead to numerical problems. Finally, an infinitesimal mass is attributed to some nodes in the middle of the specimen (*ELEMENT_MASS keyword) in order to facilitate the strain analysis. These elements play the role of a strain gauge and the evolution of their relative displacement leads to the determination of the longitudinal and transversal strain. The bottom side of Fig. 5.1 presents the numerical model used for the simulation of the experimental compressive tests. A similar modeling than for the tensile tests

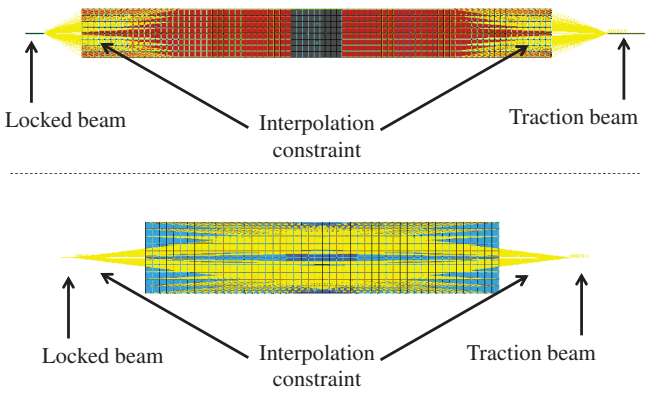

Figure 5.1: Description of the numerical models for the tensile (top) and compressive tests (bottom)

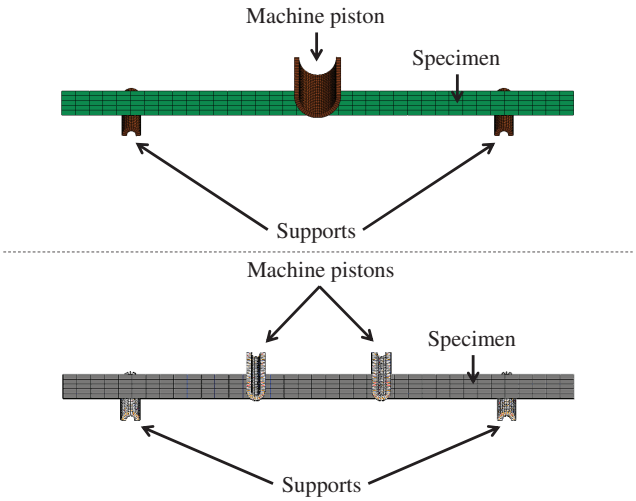

Figure 5.2: Description of the numerical models for the three-point bending (top) and four-point bending (bottom) tests

is used. However, we can remark that the traction is defined on the beam at the right of the specimen, which transmits a traction through the interpolation constraint to the left side of the specimen. The beam on the left is locked and linked to the right side of the specimen. The reason of this modeling is that it was found more stable to work with interpolation constraints loaded in tension than in compression. For both models, a mesh size about 3mm has been presented here. Considering the low number of elements, the full specimen is modeled without using any symmetry condition.

Fig. 5.2 presents the numerical models for the three-point bending (top) and the four-point bending (bottom) tests. The supports and the machine pistons are modeled with under-integrated brick elements. A simple contact is defined between the specimen and the supports (resp. the pistons). The supports are locked, the specimen is completely free and the machine pistons have only one degree of freedom corresponding to their vertical displacement. For both models, a mesh size about 3mm is presented. Considering the low number of elements, the full specimen is also here modeled without using any symmetry condition.

For the in-plane test, the vertical lines presented on the next graphs have been added manually. They permit to better identify the failure point in the case where the curves are superimposed. They do not represent a particular material behavior and they have no physical meaning. Without any specification, each woven ply is always modeled using one point of integration. The use of more points of integration did not significantly improve the results. The effective material properties of a woven ply are given in input and are applied to each point of integration. It means that the longitudinal and transversal Young's moduli and strengths are generally similar (differentiating tension and compression) in the case of a well-balanced textile like here. Under-integrated shell elements (element type 2) and thick shell elements with assumed strain reduced integration (element type 5) are used per default in the numerical models.

Finally, for confidentiality reasons, all the quantitative results (for example stress vs. strain curves) have been normalized and they are presented using a scale expressed in percentage.

5.2 RTM carbon plain-weave with outer glass mat layers

The aim of the pre-tests on this carbon plain-weave composite with outer glass mat layers was to conduct a first investigation of the macroscopical material behavior under different load cases. A mesh size about 3mm has been used in the models and the comparison between experimental and numerical results is presented in the next sections. The effective material properties captured experimentally are given as input data in the numerical models. A longitudinal tension means that a yarn direction is parallel to the load direction. Without any specification, no distinction between the warp and weft directions is made.

5.2.1 Simulations with four current composite material models

Fig. 5.3 presents the correlation for the in-plane tests on elementary coupons using the four *MAT_054, *MAT_058, *MAT_261 and *MAT_262 composite material models. As shown on Fig. 5.3a, the four material models depict very well the linear behavior and failure of longitudinal tensile loads. Fig. 5.3b presents the results for the longitudinal compression. As expected only the *MAT_058 model is able to predict a nonlinear behavior, the other three material models being restricted to a linear evolution law. As described in the section 3.1.2, a lower compressive stiffness has been experimentally observed in comparison with the tensile stiffness. Consequently, as the material models investigated here do not differentiate these both stiffnesses, the predictions show too stiff results. However, a good correlation is observed regarding the stress level at failure. On Fig. 5.3c, the results for the tensile shear (tension where the yarns define an angle of 45° with the direction of traction) are presented. As expected, a good correlation is obtained for both *MAT_058 and *MAT_261 material models, since they present a nonlinear behavior in shear. Both *MAT_054 and *MAT_262 models gave acceptable results considering their limitation to a bi-linear behavior in shear. Finally, Fig. 5.3d show the results for the compressive shear. Regarding the prediction of nonlinearity, similar remarks as for the tensile shear can be made. The *MAT_054 model led to inadequate results, that have not been reported. Moreover, the numerical results show a light too stiff compressive shear behavior. This difference could come from the effects of the transverse deformation, that are not negligible for the shear compression. In the numerical model,

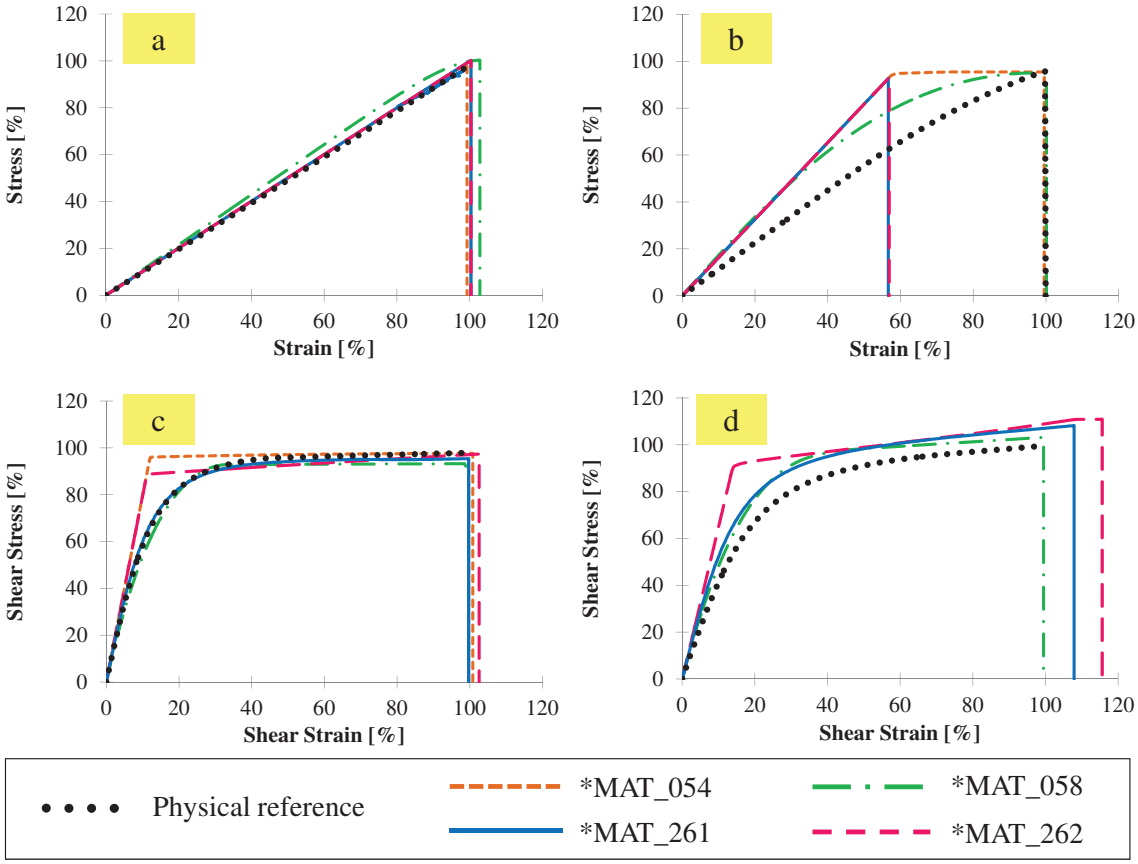

Figure 5.3: Comparison of the numerical results obtained for four composite material models: a) longitudinal tension - b) longitudinal compression - c) shear tension - d) shear compression

a mesh size of 3mm allows to have only three elements over the width (10mm) of the specimen. It has been found (but not reported) that a mesh refinement allowed to obtain a better correlation. Finally, the stress vs. strain curves measured in each element respects perfectly the shear stress vs. shear strain curve given as input data. It confirms the influence of the transverse effects on the compressive shear behavior. That is why, the use of bigger test specimens could be require to facilitate their numerical modeling using mesh sizes larger than 3mm.

Fig. 5.4 presents the correlation for the three-point bending tests on elementary coupons using the four *MAT_054, *MAT_058, *MAT_261 and *MAT_262 composite material models. A too stiff bending stiffness is predicted for the longitudinal bending, as shown on Fig. 5.4a. The premature failure predicted by *MAT_261 and *MAT_262 is due to the collapse of the specimen, as soon as failure has been detected in one point of integration (first-ply failure). Further developments of these models allowed to control the number of integration points that have to fail before deleting the elements. The stress level at failure predicted by the *MAT_054 and *MAT_058 models are acceptable regarding the experimental data. The next sections will propose a deeper investigation of the bending stiffness. Fig. 5.4b presents the results for the diagonal three-point bending tests. The *MAT_058 and *MAT_261 material models offering a nonlinear shear behavior predict an acceptable bending behavior in shear. On the contrary, the two other material models presenting a bi-linear shear behavior predict too stiff results and too high stress levels.

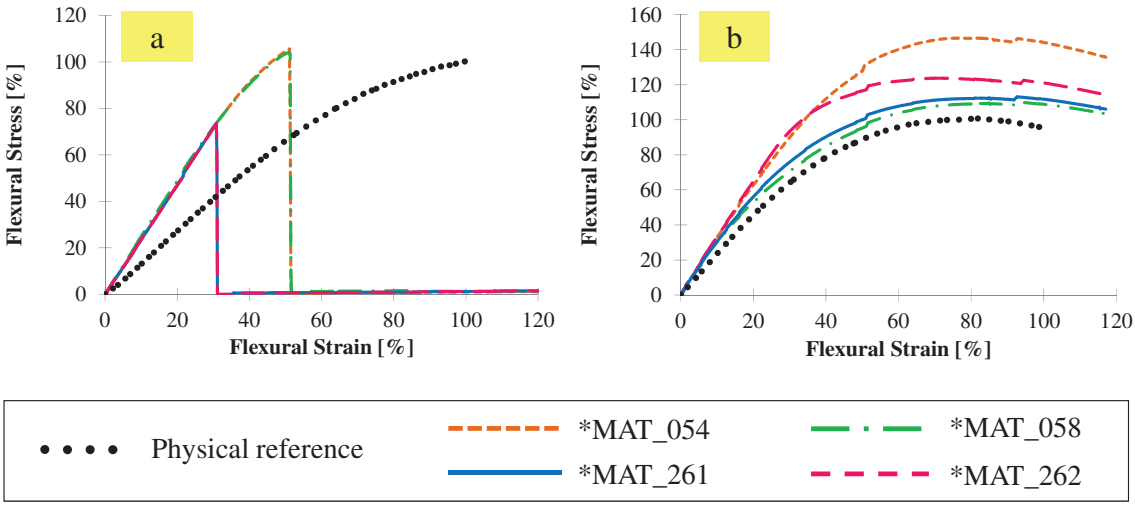

Figure 5.4: Comparison of the numerical results obtained for four composite material models: a) longitudinal bending - b) diagonal (shear) bending

The results presented previously showed some deficiencies for four of the current composite material models of the LS-DYNA explicit solver. The *MAT_058 model seems to give the best compromise here but no permanent deformation is taken into account. In order to investigate the behavior of structures and materials under impact or crash loads, it is necessary to consider plastic deformation. Moreover, the nonlinear behavior of 2D woven composite materials comes generally either from the macroscopic nonlinear behavior of the material's constituents, or from the initiation and propagation of microcracks leading to a stiffness softening. This irreversible damage has to be considered by the progressive accumulation of permanent deformation using a plasticity model coupled to the nonlinearity for each in-plane material direction.

5.2.2 Numerical results obtained with the UMAT

Fig. 5.5 presents the numerical results obtained for the in-plane tests using the material model developed in this study. Both shell and thick shell elements have been investigated. The Ramberg-Osgood model has been used to predict the macroscopic behavior of the material under the different load cases, except in shear where a user-defined load curve defines the shear behavior of the material. Similar results have been obtained using user-defined load curves for each material direction but they are not reported here. Failure is predicted by the maximal stress criterion. As it was expected, the tested material presenting here a "unidirectional" stacking sequence, similar results are obtained using the Tsai-Wu failure criterion but they are not reported here. Finally, the results obtained with the UMAT are compared to those coming from simulations with the *MAT_054 material model, that is commonly used for industrial applications. Fig. 5.5a shows similar good results for both material models and both element types concerning the longitudinal tensile loads. Fig. 5.5b presents the results for the longitudinal compression. The nonlinear behavior is well predicted by the Ramberg-Osgood model. A light stiffer behavior is observed for a modeling with thick shells caused by the influence of a tri-dimensional stress state in the elements, and the presence of a material stiffness in the out-of-plane direction. Failure is also in good agreement with the experimental observations. The results concerning the tensile shear behavior are presented on Fig.

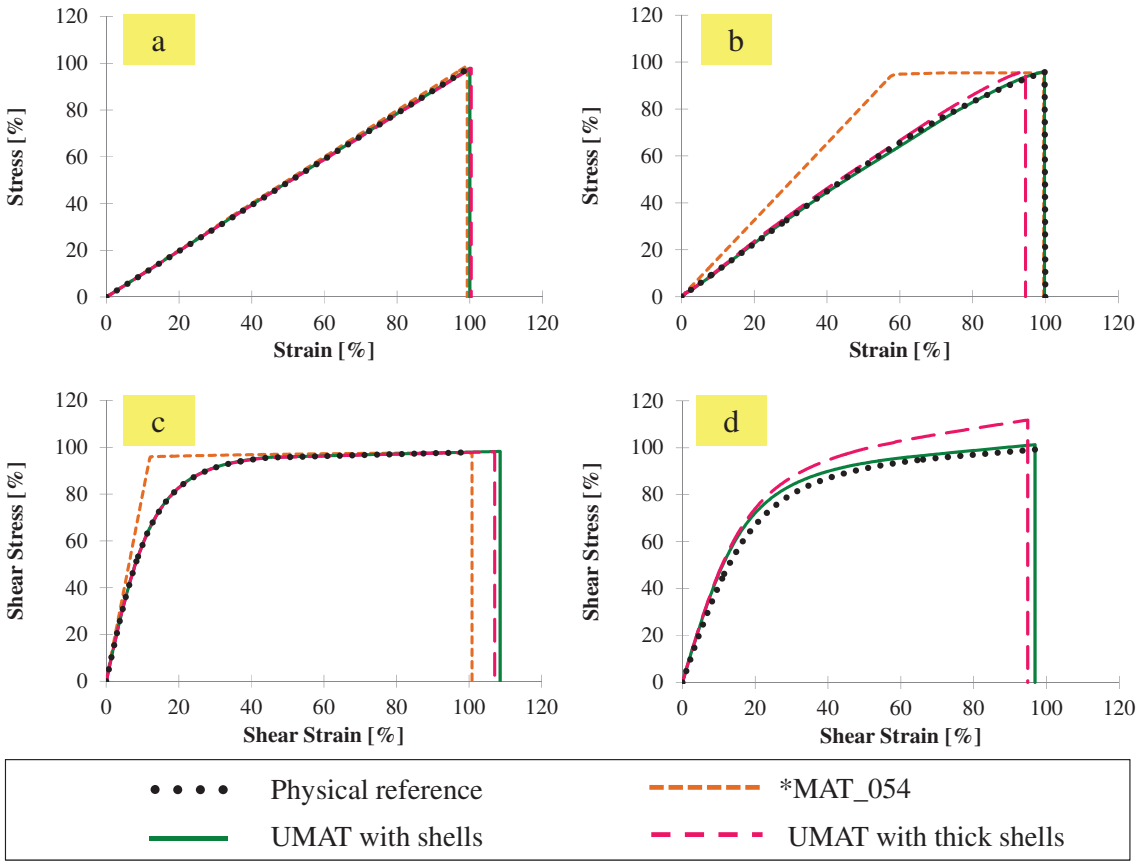

Figure 5.5: Numerical results obtained with the UMAT and a modeling with shell and thick shell elements: a) longitudinal tension - b) longitudinal compression - c) shear tension - d) shear compression

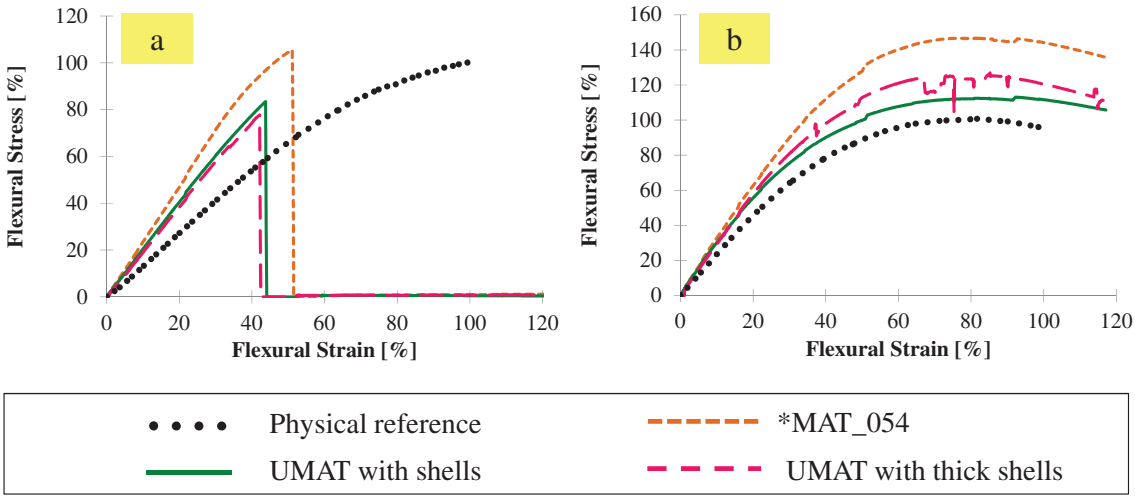

Figure 5.6: Numerical results obtained with the UMAT and a modeling with shell and thick shell elements: a) longitudinal bending - b) diagonal (shear) bending

5.5c. Shell and thick shell elements give similar results and a good correlation. Failure being predicted using a maximum stress criterion in the UMAT, it is difficult to match accurately a particular strain at failure, which explains the low dispersion observed on the curves regarding failure. The UMAT gives a very good prediction of the compressive shear behavior as presented in Fig. 5.5d. The modeling with thick shell elements led to a lightly too stiff compressive shear behavior, as it has already been noticed for the longitudinal compression.

Fig. 5.6a and Fig. 5.6b present respectively the results for the longitudinal and diagonal bending. The UMAT predicts a lower bending stiffness than the *MAT_054 model, which is in a better agreement with the experiments. This is mainly due to the better prediction of the nonlinear macroscopic longitudinal compressive behavior. Failure stress is about 20% under-predicted, due to the failure of the first point of integration loaded in compression, which leads to the collapse of the specimen. It seems that this RTM plain weave composite has a weaker bending behavior as expected and some effects probably induced by the curved deformation could delay the first ply failure. The prediction of a premature failure could be also caused by a too low longitudinal compressive strength. Finally, the bending behavior predicted for the diagonal bending is acceptable for a modeling with shell elements, whereas too stiff and relatively unstable results are obtained for a modeling with thick shell elements.

Regarding the longitudinal compression, Fig. 5.7a compares the evolution over the time of the maximal macroscopic longitudinal compressive strain and of the maximal longitudinal plastic strain in an element close to failure location. The plastic strain increases with the degree of nonlinearity corresponding to the progressive stiffness reduction of the material. As expected, when failure occurred, the macroscopic strain in one element has the same value than the maximal accumulated plastic strain. A similar analysis has been conducted regarding the tensile shear test, comparing the macroscopic shear strain and the plastic shear strain evolutions, as presented on Fig. 5.7b. In shear, the nonlinearity and stiffness reduction are higher than for the longitudinal compressive case, which explains the quite parallel evolution of both investigated strains. Finally, Fig. 5.7c shows the maximal tensile shear strain distribution over the complete specimen just before and just after failure. The color scale in percentage corresponds also to

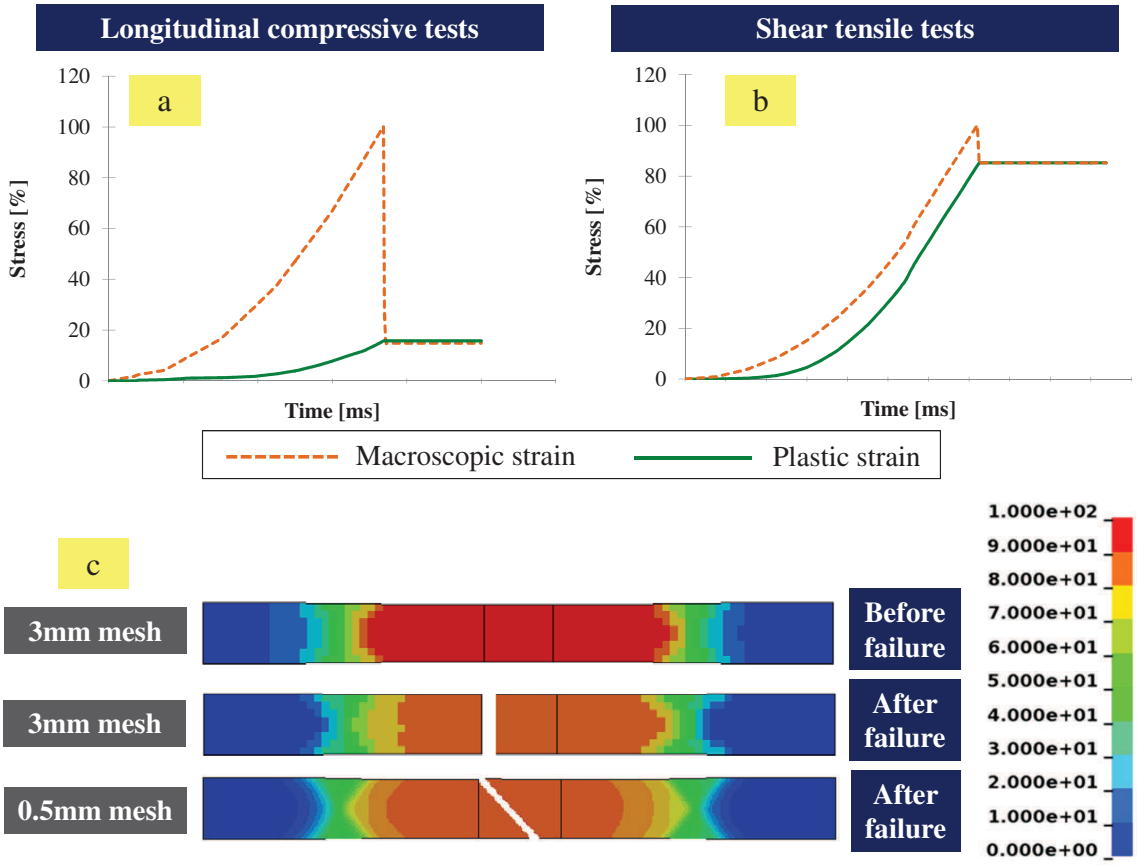

Figure 5.7: Comparison between the evolution of the macroscopic and plastic strains: a) Longitudinal compressive tests - b) Shear tensile tests - c) Maximal shear strain distribution over the specimen for the shear tensile test

the ordinate axis of the graph. The mesh size about 3mm does not allow to obtain a suitable diagonal failure surface but similar simulations have been conducted with finer element sizes and a diagonal failure surface has been predicted, as reported for the 0.5mm mesh size.

5.2.3 Investigation of the bending stiffness

The previous numerical results showed a too high stiffness for the longitudinal bending, whereas a good agreement with experiments has been obtained for the in-plane tensile and compressive tests. Consequently, some investigations have been conducted regarding the mesh size, the use of other material models and the modeling of the outer glass mat layers. The corresponding results are presented in the following sections.

5.2.3.1 Influence of the mesh size on the bending behavior

The effect of the element size and of the type of element on the bending behavior has been investigated and the results are reported on Fig. 5.8. The simulations have been made using the *MAT_054 model but similar observations could be reported for the other models and the UMAT. Fig. 5.8a presents the results for a modeling with under-integrated shell elements (element type 2) and Fig. 5.8b shows the results for a modeling with full-integrated shell elements (element type 16). First, the use of full-

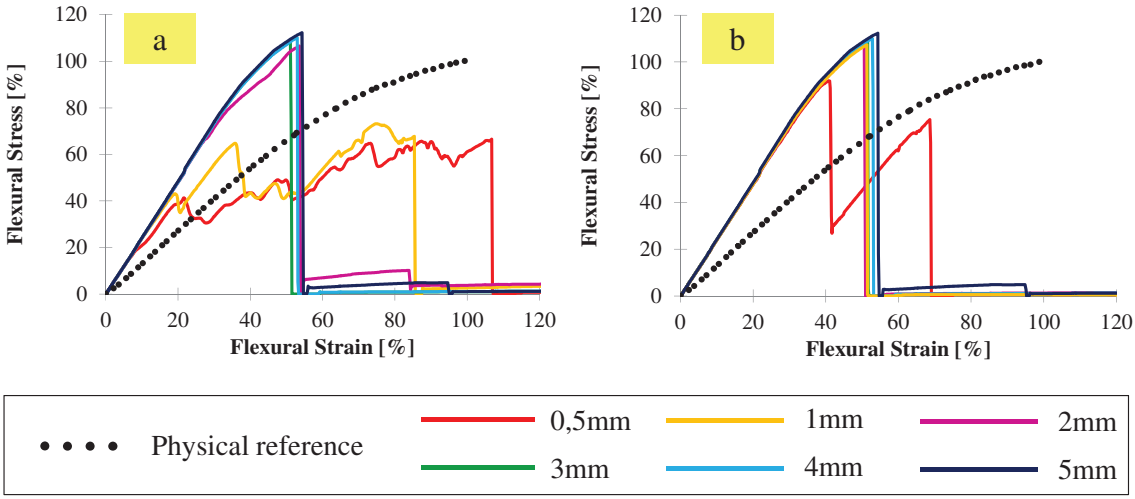

Figure 5.8: Influence of the mesh size on the longitudinal bending behavior for the *MAT_054 model: a) Using under-integrated shell elements - b) Using full-integrated shell elements

integrated shell elements does not improve directly the bending stiffness. Then, a mesh finer than 2mm does not give acceptable results using under-integrated shells but the use of full-integrated shells improved the results for the 1mm and 2mm element sizes. Consequently, for this bending test, it seems that the in-plane dimension of an element should be greater than or at least equal to the thickness in order to obtain usable results. Finally, a similar investigation has been conducted with thick shell elements. No improvement of the bending stiffness has been observed but all mesh sizes gave similar results. It confirms that shell elements present a physical limit regarding their aspect ratio (in-plane length over their thickness) and they are not suitable for the modeling of relatively small and thick structures.

5.2.3.2 Numerical results using the *MAT_118 model

The constitutive laws of the material models used until now cannot control the bending behavior independently from the in-plane material properties. The *MAT_118 material model (see 2.7.3.5) requires each term of the laminate's stiffness matrix as input data, which means that the extensional and bending sub-matrix have to be here explicitly defined. The stiffness matrix links the forces and moments to the membrane strains and curvatures. Analytic computations based on the C.L.T. have been set up to determine the coefficients of the stiffness matrix. Giving the appropriate effective material properties as input of the analytic computations, the simulations lead to the results depicted by the red dashed curves on Fig. 5.9a concerning the longitudinal tension and on Fig. 5.9b regarding the longitudinal bending. The results correspond exactly to those obtained with the common composite material models and that have been presented in the precedent sections. However, using the *MAT_118 model, the bending behavior can be adapted independently of the extensional behavior. As a symmetric unidirectional stacking sequence has been defined, the terms of the coupling $[B]$-matrix are equal to zero. The $[D_{11}]$ and $[D_{22}]$ coefficient of the $[D]$ bending stiffness matrix have to be fitted to match the bending stiffness observed experimentally. The numerically predicted bending stiffness is about twice higher than the real bending stiffness. Both $[D_{11}]$ and $[D_{22}]$ coefficients have been divided by two and the corresponding results are represented by the continuous green curves on Fig. 5.9. As expected, a similar material response is obtained for the

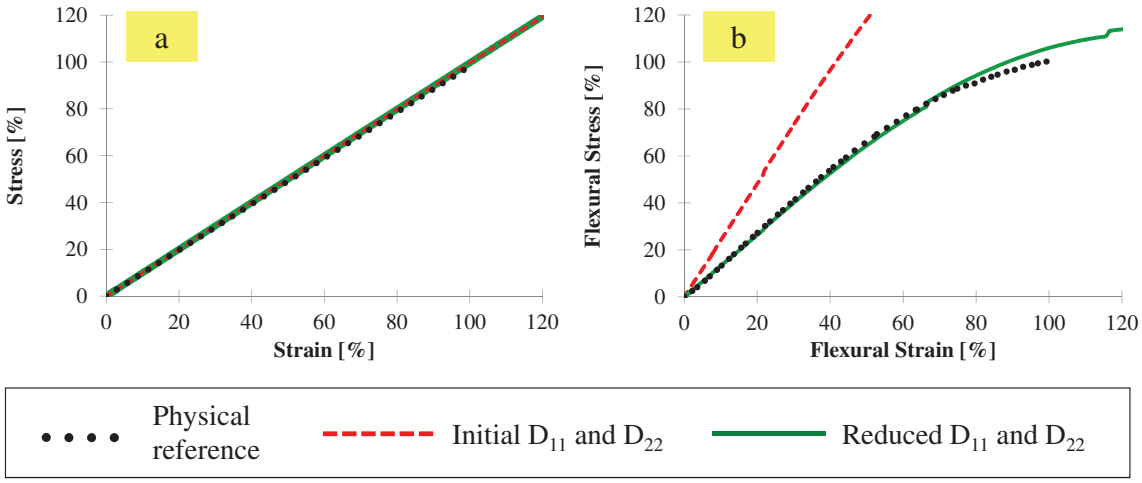

Figure 5.9: Numerical results obtained with the *MAT_118 model and under-integrated shell elements: a) Longitudinal tension - b) Longitudinal bending

longitudinal tension but the bending stiffness is now in good agreement with the experimental data.

As this material model is based on a resultant formulation, the stresses in the output are equal to zero, which obviates any stress analysis in the material. Moreover, no failure can be correctly predicted as the *MAT_118 model offers no suitable failure criterion. Finally, neither nonlinearity nor plasticity definition is available for this model. Consequently, even if this material model offers a better agreement with experiments in term of bending stiffness, it is not well-adapted to industrial applications for the reasons mentioned previously. The *MAT_118 material model has to be used to predict the elastic response of composite materials without consideration of failure or stress analysis.

5.2.3.3 Consideration of the fiber waviness

In this section, the modeling using the effective material properties of the woven composite for each integration point is replaced by a modeling based on a bidirectional stacking sequence and the material properties of non-crimp fabric composite plies taking in consideration the effects of the fiber waviness. Each woven layer has been modeled by two points of integration presenting the [0°] and [90°] orientations. It means that a woven ply is assimilated to two unidirectional homogeneous wavy plies. The effect of the fiber waviness has been analytically investigated based on the works published by Hsiao in [77, 254, 255]. Fig. 5.10 presents the variation of the compressive Young's modulus in function of the wavelength and of the wave amplitude of the fibers.

A longitudinal Young's modulus of a unidirectional non-crimp fabric about 110GPa and a transverse Young's modulus about 10GPa have been taken for the analytic analysis. These values have been determined using the rule of mixture, the fiber volume fraction and the stiffness properties of the constituents. Based on micrographs, an averaged wavelength of this RTM material has been found about $4640\mu m$. An averaged amplitude of the waviness has been assessed about $167\mu m$. Using these input data, new longitudinal and transverse Young's moduli accounting for the effect of fiber waviness have been analytically determined. Considering these new stiffnesses in the *MAT_054 model, it leads to the results presented on Fig. 5.11a for the longitudinal tension and compression. Fig. 5.11b shows the results for the longi-

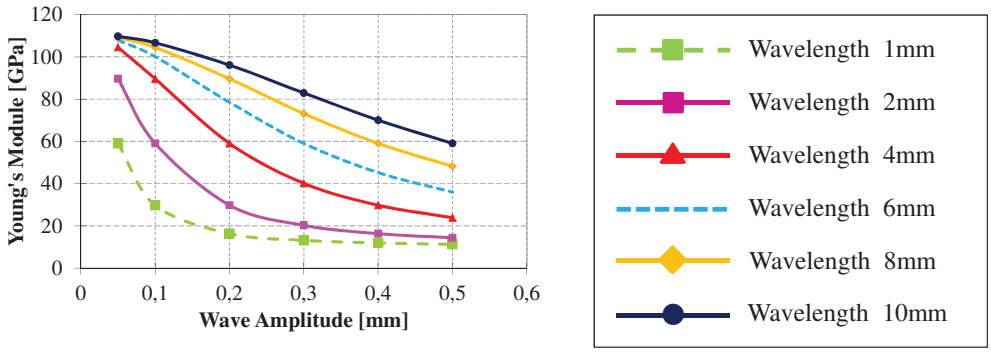

Figure 5.10: Analytic evaluation of the effect of fiber waviness on the compressive longitudinal Young's modulus of a wavy ply

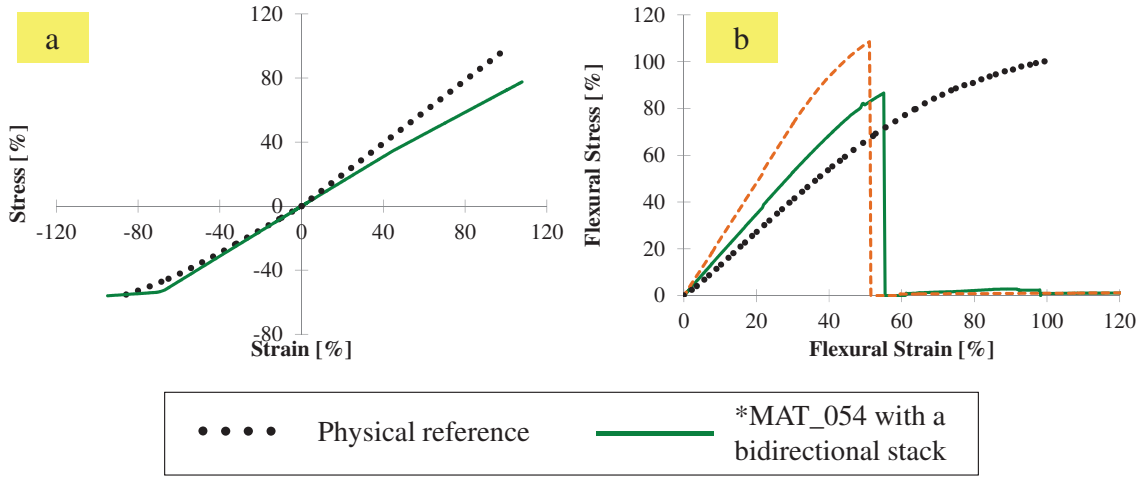

Figure 5.11: Numerical results obtained with the *MAT_054 model, a bidirectional stacking sequence and material properties accounting for fiber waviness: a) longitudinal tension and compression - b) longitudinal three-point bending

tudinal bending. In term of stiffness, the new Young's moduli offer a good agreement with experiments for the compression. A better prediction of the bending stiffness is the naturally observed on Fig. 5.11b (the orange dashed line refers to the previous results obtained with the unidirectional stack). On the contrary, the predicted tensile stiffness is not suitable (see Fig. 5.11a).

To conclude this study, the analytic method aiming at considering the effect of fiber waviness on the compressive Young's modulus showed acceptable results for the longitudinal compression, while no influence of the interaction between the yarns due to the textile structures has been taken into account. It naturally improved the bending stiffness but the predicted tensile stiffness is no more in agreement with experiments. It confirms that different Young's moduli should be defined in tension and in compression for such woven composites.

5.2.3.4 Modeling of the outer glass mat layers

As described in the section 3.1 and on Fig. 3.2, the carbon plain weave RTM composite considered here presents two outer glass mat layers. Using micrographs, the thickness of each glass mat layer has been estimated about $150\mu m$. Under bending loads, both outer layers of a laminate play a preponderant role in the bending response of the material, as they undergo the highest strains. Moreover, in the case of a heterogeneous stiffness distribution over the thickness of the specimen like here, the low stiffness of these outer layers should have a relative high effect on the bending stiffness. It means that the glass mat layers should be modeled to assess their potential effects on the bending stiffness.

The main difficulty for the modeling of the glass mat is the lack of information about this material regarding the stiffness, the strength and the fiber volume fraction. Some authors investigated glass mat composites [256–263] generally based on thermoplastic resins. Low fiber volume fraction are often reported for glass mat composites which leads to tensile Young's moduli between 3GPa and 7GPa. Tensile tests on pure epoxy resin specimens were available at Daimler AG. A nonlinear behavior has been captured with an initial stiffness being in the same domain of values than the one mentioned previously. Due to the lack of accurate information about the glass mat layers, we assume that the behavior of a glass mat layer is close enough to the behavior of the resin. Consequently, the material properties obtained with the tensile test on pure epoxy resin specimens are taken as reference for the glass mat layers. The *MAT_054 model and the UMAT have been used to model the glass mat layers. The coupling of two different material models in the same stacking sequence is likely to bring some instability particularly in term of failure. For this reason it is preferable to use the same material model for all integration points of the stacking sequence, using different material properties in input if it is necessary. Both glass mat layers have been modeled by one point of integration having a thickness of $150\mu m$. The thickness of the carbon woven layers has been adapted to obtain a total thickness of 2mm for the specimen. The effective longitudinal Young's moduli of the woven plies have also to be adapted to this new modeling. They have been set, such as the macroscopic tensile and compressive stiffnesses of the laminate including the glass mat layers match the effective stiffness obtained in the corresponding experimental tests.

Fig. 5.12a presents the results for the longitudinal three-point bending and for a modeling using the UMAT and the *MAT_054 models. Both shell and thick shell elements have been investigated for the modeling with the UMAT. The graphs show that a good agreement is obtained for the UMAT and for both element types regarding the bending stiffness. Failure occurred prematurely due to a specimen collapse caused by the element deletion at a first-ply failure. The modeling with the *MAT_054 model gives a stiffer behavior due to the longitudinal compressive stiffness, that is not ideally predicted (see Fig. 5.13b). Fig. 5.12b presents the results for the diagonal bending. As mentioned previously, the *MAT_054 model does not predict acceptable results caused by a unsuitable compressive shear behavior. Regarding the results given by the UMAT, a good agreement is obtained for a modeling with shell elements, whereas thick shell elements show a too stiff behavior. As the stiffness of the glass mat is close to the one of a woven ply under shear loads, few differences are observed for this load case compared to a modeling without glass mat.

Fig. 5.13a presents the results for the longitudinal tension and a good agreement with experiments is obtained. The results of the longitudinal compression are reported on Fig. 5.13b. Suitable results are obtained for the UMAT but, as expected, a too stiff behavior is obtained for a modeling with the

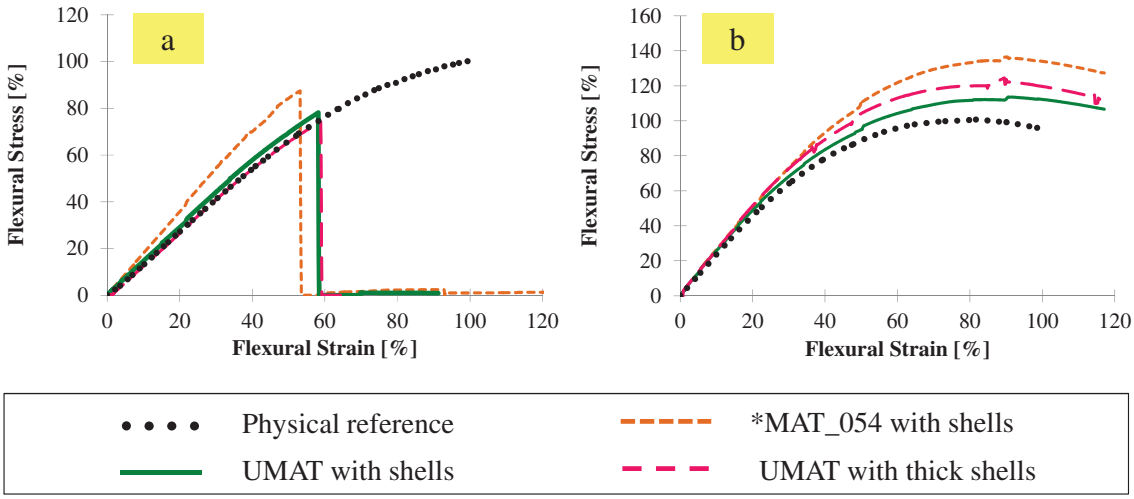

Figure 5.12: Numerical results obtained with the *MAT_054 and the UMAT models with shell and thick shell elements and the modeling of the outer glass mat layers: a) longitudinal bending - b) diagonal bending

*MAT_054 model. At the largest strains, thick shell elements gave a light weaker behavior than shell elements, which lightly delays failure. Fig. 5.13c presents the results for the shear tension and a good agreement with experimental results is obtained for a modeling using the UMAT material model. An expected bi-linear behavior is obtained for a modeling with the *MAT_054 model. Failure has been set to occur at a 5% shear strain, which explains the behavior of the curves. The results for the compressive shear are reported on Fig. 5.13d for a modeling with the UMAT only. An acceptable agreement with experiments is obtained. Finally, as mentioned above, the stiffness of the glass mat being close to the one of a woven ply loaded in shear, few differences are observed for this load case compared to a modeling without glass mat.

5.2.4 Partial conclusions

For the in-plane tensile and compressive loads, a good correlation can be obtained using the user-defined material model (UMAT). Acceptable results are reported for the four other composite material models of LS-DYNA investigated in this study. Regarding bending loads, too stiff results have been obtained in a first instance. The study of the effect of the mesh size does not allow to improve the bending stiffness. However, it put in evidence a certain limit concerning the element size of shell elements in order to obtain adaquate results. Indeed, for the modeling presented here, the in-plane dimensions of the shell elements should be higher than the thickness of the material. Then, the effect of the fiber waviness has been investigated based on analytic computations. It improved the compressive stiffness and the bending behavior but the longitudinal tensile stiffness is then no more acceptable. Experimental tests on a wavy composite loaded in longitudinal tension could help to study the influence of the yarn waviness on the tensile properties. Finally, the modeling of the outer glass mat layers allowed to obtain an acceptable compromise between all load cases. However, experimental results on a real glass mat composite have to be conducted to obtain the mechanical properties of such a material.

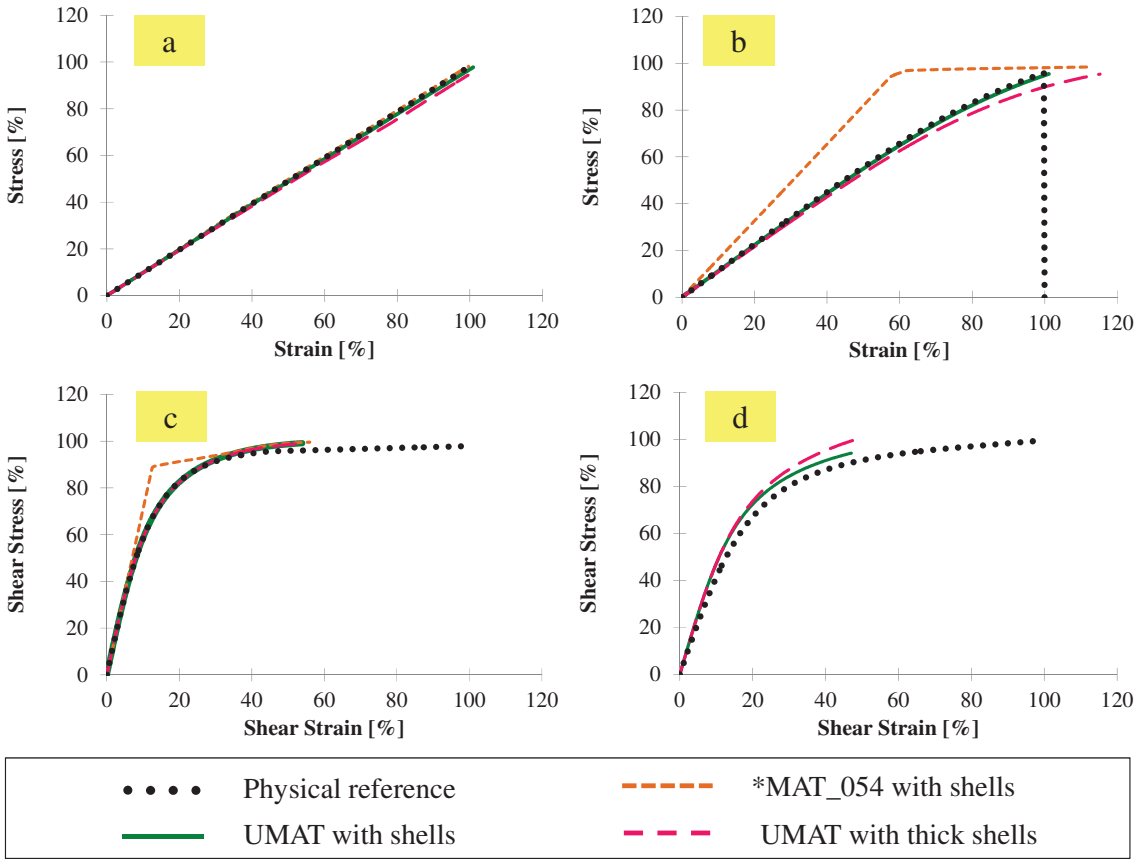

Figure 5.13: Numerical results obtained with the *MAT_054 and the UMAT model with shell and thick shell elements and the modeling of the outer glass mat layers: a) longitudinal tension - b) longitudinal compression - c) shear tension - d) shear compression

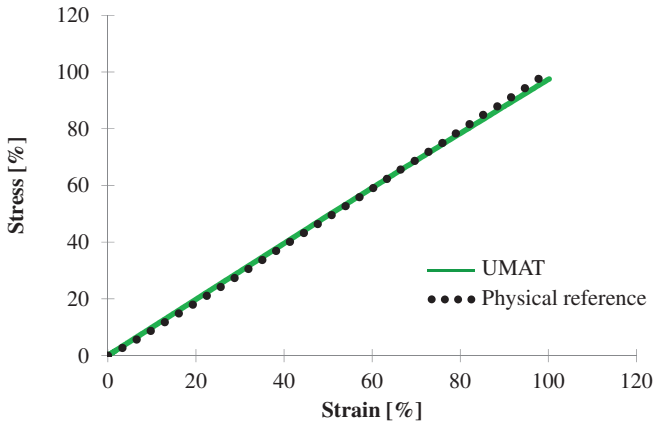

Figure 5.14: Correlation for the carbon plain-weave RTM composite: longitudinal tension

5.3 RTM carbon plain-weave without glass mat

In the present section, simulations have been conducted only using the UMAT material model. The numerical results corresponding to the different experimental tests described in the section 3.2 are reported and discussed. Only one representative curve is generally presented to depict the numerical predictions of the UMAT. However, for each in-plane and bending load case, both pre-failure models (user-defined load curve and Ramberg-Osgood model) and both failure criteria (2D Tsai-Wu and maximal stress criteria) have been investigated. A mesh size about 3mm has been used in the simulations.

5.3.1 Longitudinal tensile tests

As shown on Fig. 5.14, the macroscopic linear behavior observed experimentally for a longitudinal tensile load is well predicted by the UMAT. The light stiffness increase due to the textile straightening is not considered in the simulation. Both Tsai-Wu and maximal stress failure criteria predict an acceptable stress at failure. The implementation of a linear behavior provided in the UMAT objects is invocated here but similar results are obtained using a linear user-defined load curve as input data of the model.

5.3.2 Longitudinal compressive tests

Fig. 5.15 presents the correlation for the longitudinal compression. The red dashed curve shows the numerical results obtained using a linear behavior and a similar stiffness as in tension. As expected, too stiff and unsuitable results are obtained, since a nonlinear behavior and a lower stiffness than in tension have been experimentally observed. The blue dashed curve presents the numerical prediction based on a linear behavior but a compressive stiffness adapted to the one captured in the experiments. More suitable results are obtained but a nonlinear behavior is required to better correspond to the experimental observations. Finally, the green continuous curve shows a very good correlation. Similar results are obtained using a user-defined load curve or the Ramberg-Osgood model. Failure is also numerically well-predicted and both failure criteria give suitable results.

Fig. 5.16a and Fig. 5.16b present respectively the predicted strain distribution over the elementary coupon just before and just after failure. Fig. 5.16c compares both strains on a graph. The red dotted curve represents the maximal macroscopical longitudinal compressive strain in one element close to the

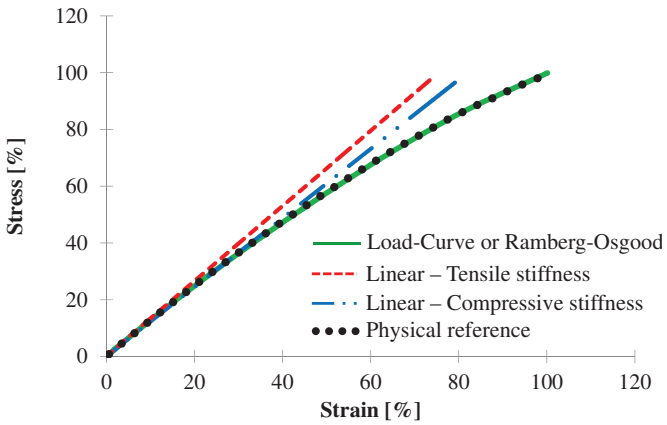

Figure 5.15: Correlation for the carbon plain-weave RTM composite: longitudinal compression

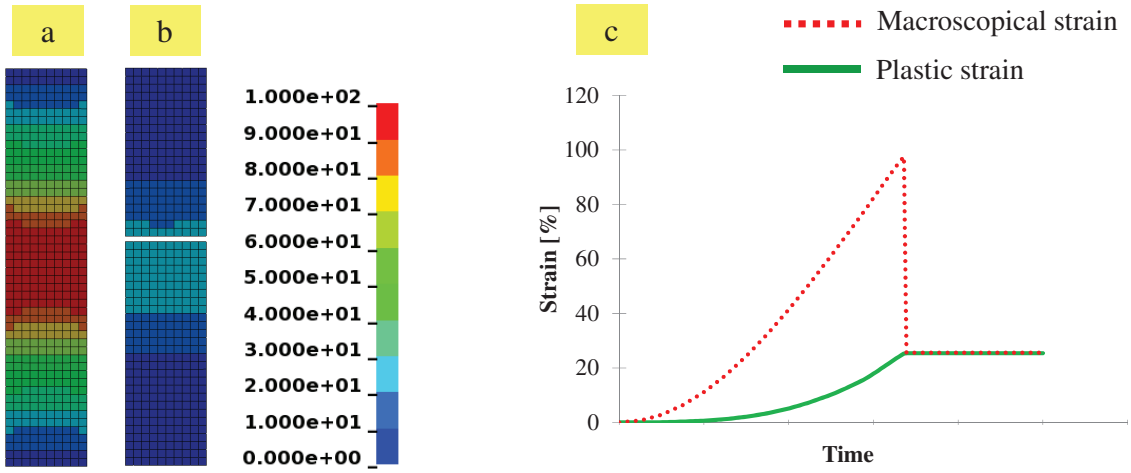

Figure 5.16: Distribution of the maximal macroscopical compressive strain and its corresponding plastic strain

failure location. The green continuous line represents the corresponding accumulated plastic strain in the same element. The values observed on the graph are in agreement with the fringe plots. As expected the accumulation of plastic strains increases with the degree of nonlinearity. However, a permanent deformation about 25% of the total deformation seems to be too high and a degradation of the stiffness for the plastic behavior (unload) should be implemented.

5.3.3 Tensile and compressive shear

Fig. 5.17 shows the results for both tensile and compressive shear tests. A very good agreement is obtained using a load curve as input data. The numerical results are symmetric, as no distinction is made between the tensile and compressive shear behaviors. It confirms also the importance to use a specimen presenting a sufficient width in order to take appropriately into account the transverse deformation and to obtain acceptable results. However, at relatively large shear strain, the experimental results are not perfectly symmetric. A constant stress level is observed in compression, whereas a constant stress increase is observed in tension.

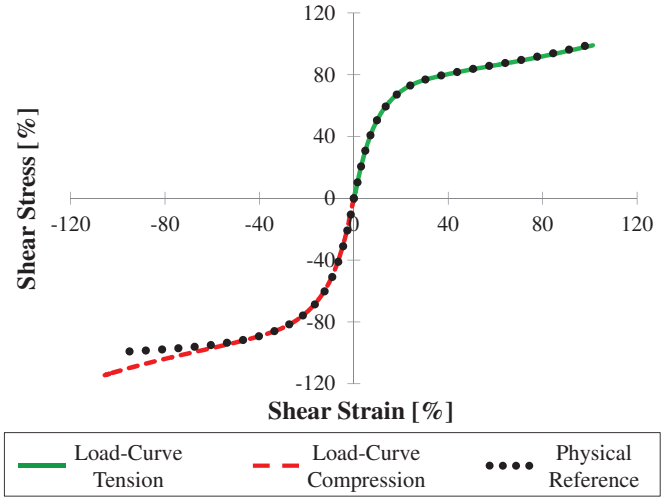

Figure 5.17: Correlation for the carbon plain-weave RTM composite: tensile and compressive shear

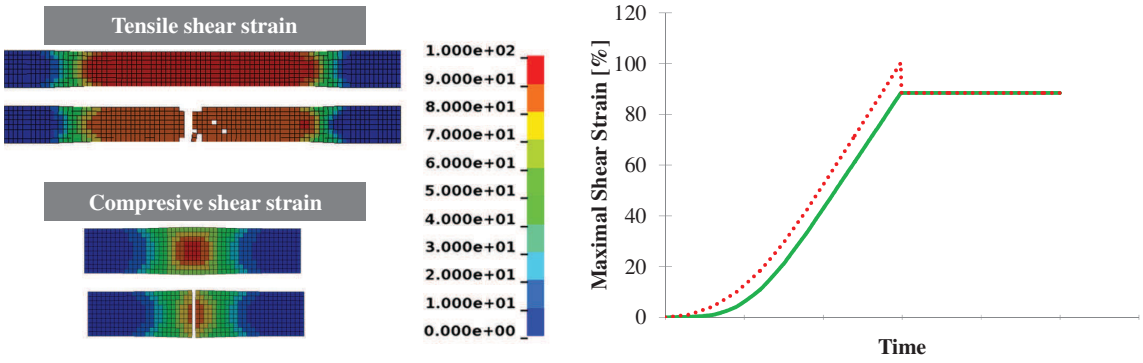

Figure 5.18: Distribution of the maximal macroscopical tensile shear strain and its corresponding shear plastic strain

Fig. 5.18 presents the evolution of the maximal shear strain and its corresponding plastic shear strain in an element close to the failure location. The graph shows a close evolution between both strains. It is in correlation with the high nonlinearity level for the shear behavior of the investigated RTM plain-weave material. The fringe plots show the distributions of the macroscopic shear strain and the plastic shear strain before and after failure for the compressive and tensile shear. A high accumulation of plastic strains resulting in a large permanent deformation is predicted. An adapted degradation of the stiffness in the unload state of the material will give more realistic predictions of the remaining permanent deformation. However, such a model would require additional tests with unload and cyclic paths to validate it.

5.3.4 Four-point Bending tests

5.3.4.1 Longitudinal four-point bending tests

Fig. 5.19 presents the comparison between numerical and experimental results in the case of a longitudinal four-point bending load. A modeling with under-integrated shell elements and the UMAT predicts a too stiff bending behavior, as shown by the continuous green curve on the graph. Similarly to the

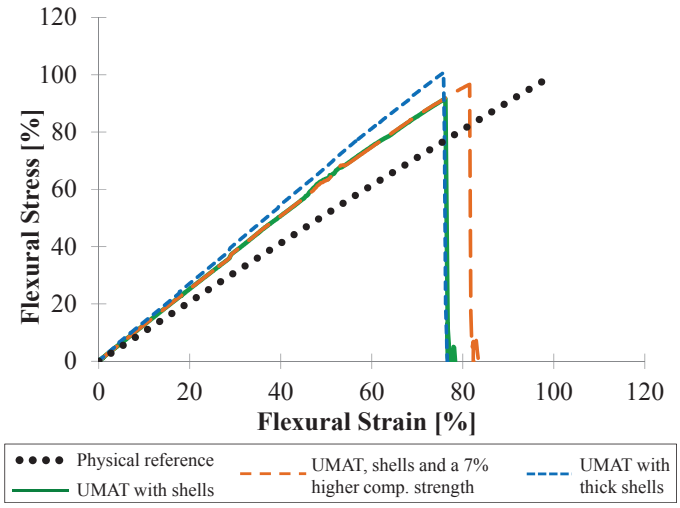

Figure 5.19: Correlation for the carbon plain-weave RTM composite: longitudinal four-point bending

experiments, a failure in compression is responsible for the collapse of the specimen in the simulations. Due to a collapse at first ply failure, a too low flexural stress at failure is obtained. A 7% increase of the longitudinal compressive strength leads to better results, as shown by the orange dashed line. This increase is acceptable and leads to suitable results regarding the simulation of the in-plane longitudinal compressive load. The 7% increased compressive strength corresponds to the upper bound of stress at failure observed experimentally. Finally, simulations with thick shells show acceptable results regarding the flexural stress at failure but a too high bending stiffness is predicted. This difference of bending stiffness is due to the use of damping in the simulations (*DAMPING_PART_MASS keyword) to prevent the numerical instabilities appearing for a modeling with thick shell elements. Indeed, it can be shown that the bending stiffness rises by increasing the level of damping.

Several mesh sizes have been also investigated and similar observations as those presented in the section 5.2.3.1 have been obtained. Using thick shells, between one and five layers of elements have been investigated in order to improve the stability of the model or the bending stiffness. No interface between the layers is considered and the nodes between two layers are coincident. No effect of the number of layers using this modeling has been noticed, that is why the results are not reported here.

5.3.4.2 Diagonal four-point bending tests

Fig. 5.20 presents the correlation for the diagonal four-point bending. A modeling with shell elements and the UMAT predicts a good agreement with experiments. Due to the low stiffness in shear, high damping values were required for a modeling with thick shell elements but it led to an unsuitable material response, that is why the corresponding results are not presented here.

5.3.5 Impact tests on elementary plates

5.3.5.1 Introduction

These impact tests are used to study the damage tolerance and the delamination propagation in composite laminates. As a modeling based on a unique element layer has to be used, delamination cannot be directly predicted using the definition of an interface. Consequently, the post-failure damage definitions are used to

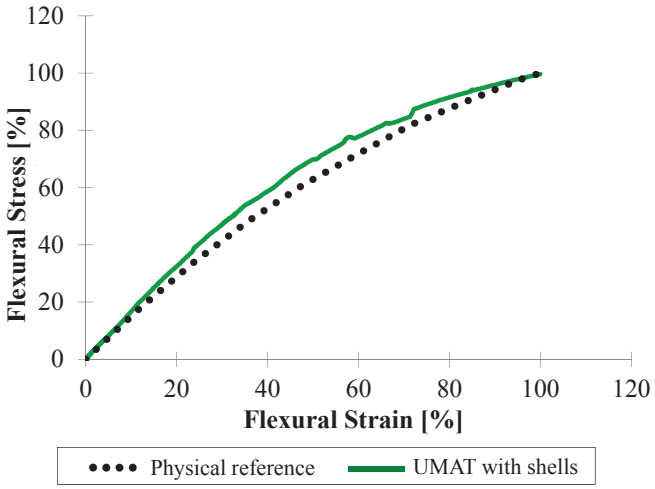

Figure 5.20: Correlation for the carbon plain-weave RTM composite: diagonal four-point bending

model the damage and delamination propagation in the material. This damage is a post-failure behavior, which consists in a progressive reduction of the load-bearing capability of each composite ply before the ultimate collapse of the material. The areas, where the material is identified in a "in damage" state, will be compared to the delaminated and damaged surfaces observed experimentally using the ultra-sound technique. The four damage formulations implemented in the UMAT and both shell and thick shell elements have been investigated. The comparison between experimental and numerical results is presented in the following sections. The analysis of the numerical results consists in a quantitative analysis based on the correlation of the material response and a qualitative analysis that compares the numerical damaged area to those observed experimentally. The maximal values of the failure and damage indicators over the thickness are used to assess the damage propagation in the material. Moreover, it corresponds very well to the experimental data obtained using a C-SCAN analysis, as it determines the maximal delaminated area in the composite sample. The white line on the pictures shows the representative damaged area observed experimentally. The numerical model used to conduct the simulations has been presented on Fig. 3.20.

Some numerical instability is likely to appear using load curves to predict the pre-failure macroscopical material behavior. Moreover, the Tsai-Wu failure criterion is not able to clearly identify the mode or the direction of failure and it induced some difficulties in the prediction of the post-failure material degradation process. Thus, the Ramberg-Osgood model has been used to predict the material behavior before failure and the maximal stress failure criterion is applied to detect failure and the beginning of the post-failure damage evolution. The material parameters used in the simulations of impact tests come from the numerical validation of the quasi-static tests on elementary coupons reported previously in the section 5.3. Each woven ply is modeled here by one point of integration points. The UMAT is based on an orthotropic material model. We can so distinguish a longitudinal direction (referring often to a fiber direction) and a transverse direction, which is orthogonal in the plane to the fiber direction. To calibrate the post-failure final strain parameters, the final strains at ultimate failure corresponding to the longitudinal direction (in tension and compression) are set first to match the maximal force peak and the force level just after the force peak. Then, the final strains at failure corresponding to the transverse direction are set to obtain a good agreement concerning the damaged surfaces and the

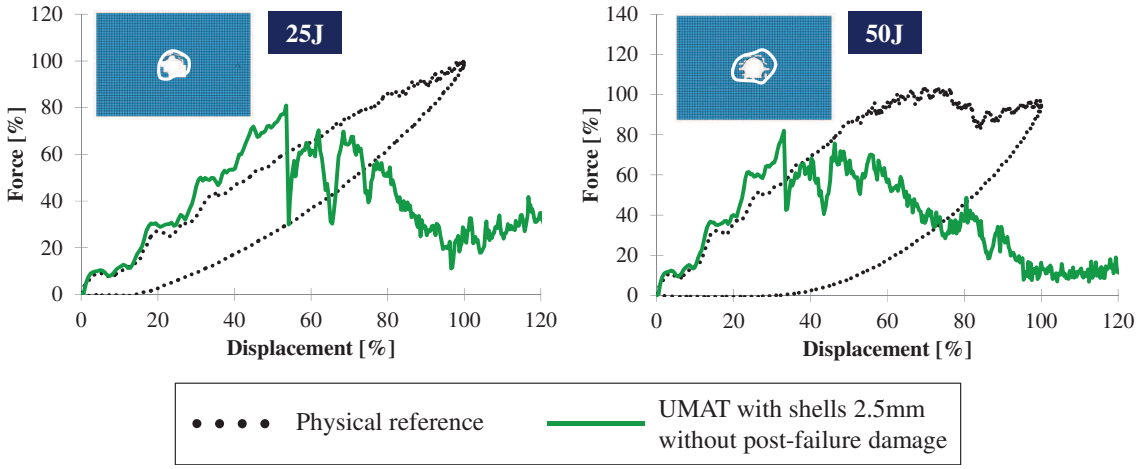

Figure 5.21: Correlation for the carbon plain-weave RTM composite: 25J and 50J impact and modeling with shell elements but without post-failure material degradation

rebound of the impactor. This methodology is naturally in first instance based on a curve fitting for the material response and on a qualitative analysis regarding the damaged and the delaminated areas. An ideal way is to determine these post-failure damage parameters experimentally. Such experiments aiming at determining the fracture toughness of a material are unfortunately very complex and it is highly difficult to obtain reliable results. Finally, it is important to notice that no strain-rate dependency of the composite material is considered here. Moreover, a last-ply failure is considered, which consists in deleting an element only when all its points of integration detected the ultimate failure.

If no post-failure material degradation is defined, once failure is detected in the ply the properties are reduced to zero and the material cannot bear load anymore. Moreover, once all points of integration of the element failed, the element is deleted from the simulation. Fig. 5.21 presents the force vs. displacement material responses predicted by the UMAT, for a mesh with shells and an element size about 2.5mm. The curves show that there is no rebound but a premature failure of the plate and the pictures show a perforation of the plate for both energies. All elements are deleted below the impactor and it follows its way without any rebound. Consequently, the definition of a post-failure material degradation will allow to avoid this brittle failure under impact load. A damage evolution starting at failure will progressively degrade the material properties, allowing to predict and to model the damage propagation in the material and to assess its damage tolerance.

5.3.5.2 Modeling with shell elements

In this section, the numerical results obtained using a modeling with under-integrated shell elements and the UMAT are presented. Mesh sizes of 2.5mm and 5mm have been investigated. Without a clear indication, the results presented concern the 0° orientation of the plates (see Fig. 3.20).

Linear damage Fig. 5.22 presents the numerical results for a 5J impact. Both mesh sizes predict similar results. Regarding the material response, the maximal displacement of the impactor is about 10% under-estimated and the maximal reaction force peak is about 15% over-estimated. The damaged area is assessed here using failure indicators. The maximal value over the thickness of the failure indicator

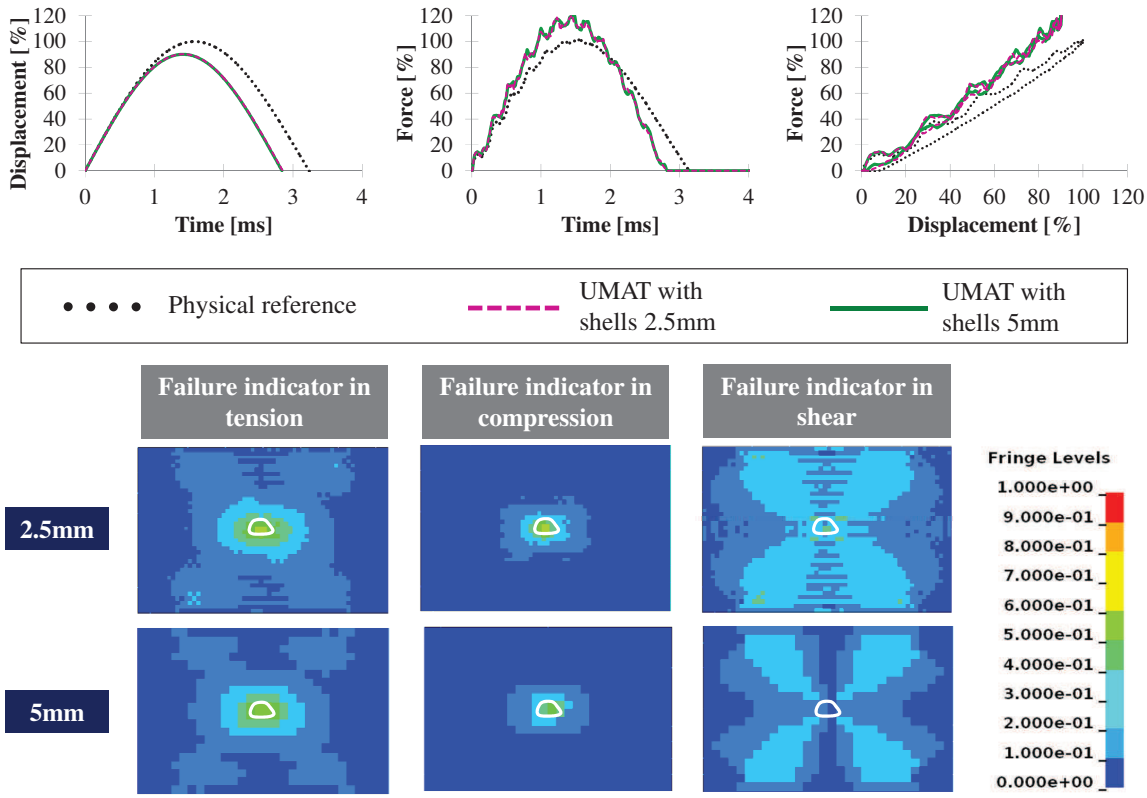

Figure 5.22: Correlation for the carbon plain-weave RTM composite: 5J impact, linear damage and a modeling with shell elements

is represented by the fringe plots. A value of 1 (red color) means that failure is detected by the failure criterion. A value about 0 (blue color) means that the material undergoes negligible deformation. Due to the relative intuitive aspect of the color meanings, the fringe level color scale will not be presented on figures anymore. A larger stress distribution is clearly observed in tension, which corresponds to the reality. A cross-shape shear stress distribution is observed, which seems to be acceptable. The localization of the maximal failure indicators values is in a good agreement with the small damaged surface observed experimentally. Finally, these low impact energies induced very localized deformation. With such a 4mm thick composite plates, the through-the-thickness strains and transverse effects could be non-negligible but a 2D modeling with a unique shell element layer is not able to take them into account.

Fig. 5.23 presents the numerical results for a 25J impact. Both mesh sizes predict similar results. The maximal displacement of the impactor is here about 12% under-estimated, whereas the maximal force peak is about 20% over-estimated. As failure has been detected, post-failure damage indicators are used to assess the damage propagation and the damaged surfaces. A value of 1 (red color) means that ultimate collapse of a ply occurred. A value about 0 (blue color) means that no damage propagates. A higher damage in tension than in compression is observed, which is in agreement with experimental observations. Finally, an acceptable correlation is obtained regarding the area of the damaged surfaces.

Fig. 5.24 presents the numerical results for a 50J impact and a 0° orientation. Both mesh sizes show similar results. The maximal displacement of the impactor is about 15% under-estimated, whereas the maximal force peak is about 30% over-estimated. The shape of the force vs. time curves is in

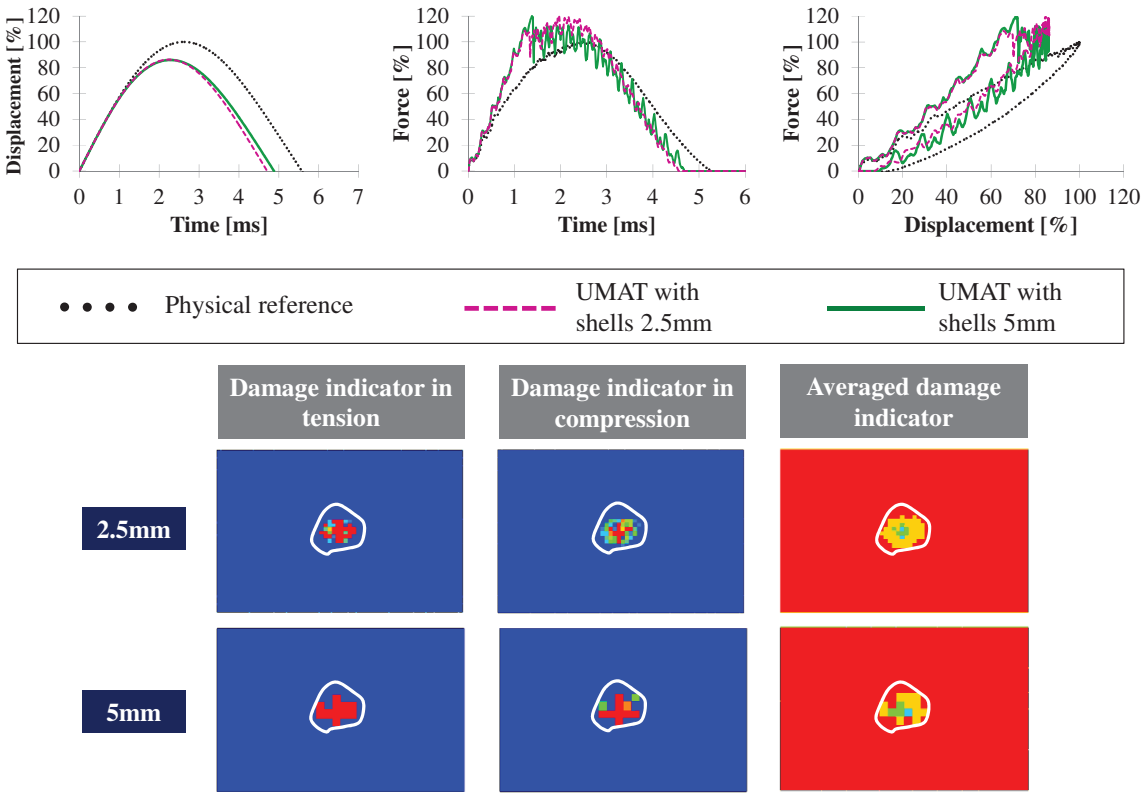

Figure 5.23: Correlation for the carbon plain-weave RTM composite: 25J impact, linear damage and a modeling with shell elements

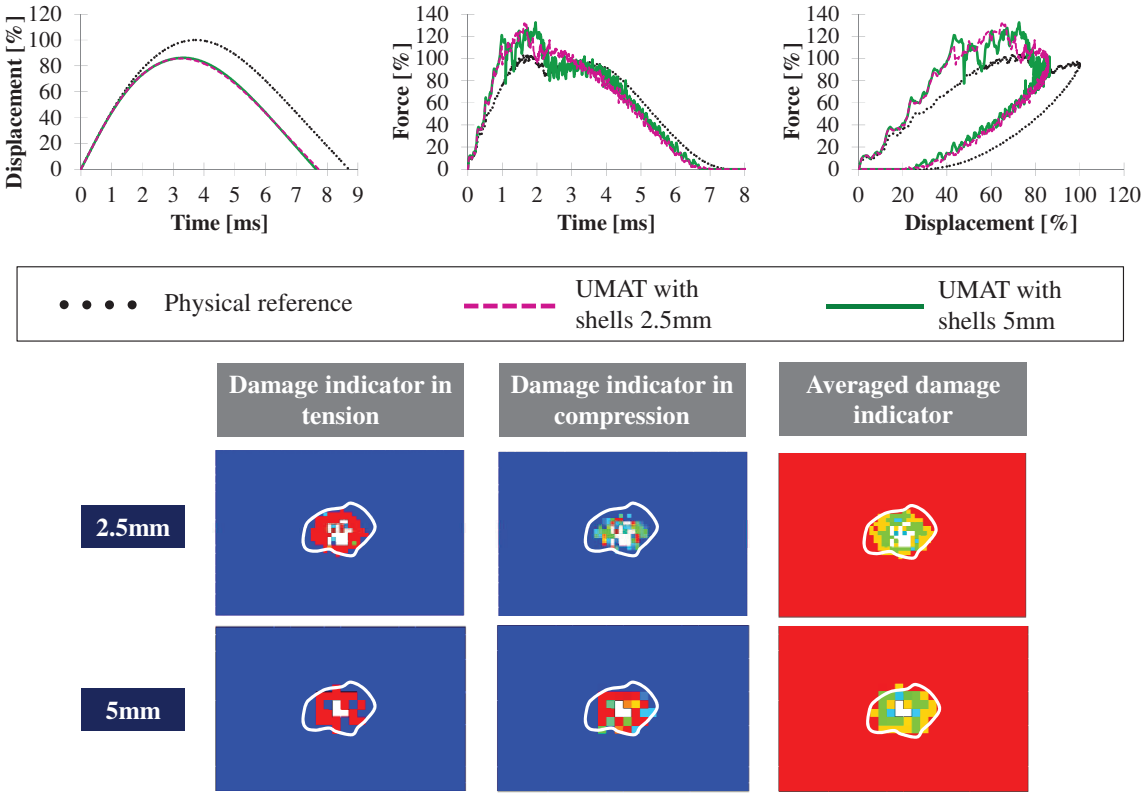

Figure 5.24: Correlation for the carbon plain-weave RTM composite: 50J impact, linear damage and a modeling with shell elements

accordance with the experimental curve. The use of a more suitable failure criterion for multidirectional stacking sequence and multidirectional load, as for example the Tsai-Wu failure criterion, could improve the prediction of the material response. A higher damage in tension than in compression is observed, which is in agreement with the experimental observations. Finally, an acceptable correlation is obtained regarding the area of the damaged surfaces. Some elements are deleted, which is acceptable regarding the large damage and the quite perforation of the plate observed experimentally.

Fig. 5.25 presents the force vs. displacement curves for the three impact energies and the 45° orientation. Regarding the material response similar conclusions as for the 0° direction can be made. Acceptable damaged surfaces are predicted (see the fringe plot of the averaged damage) compared to experimental observations. No fringe plot for the 5J impact is presented as no failure is detected and no damage evolves in the material. Finally, comparing the results obtained for the 0° and 45° orientations, similar remarks and conclusions can be made for both directions.

As neither failure nor damage are involved for a 5J impact, the numerical results for this impact energy are always the same for a given orientation and a given modeling. Consequently, the results for this energy of impact will no more be presented for a modeling with shell elements.

Step-based material degradation Fig. 5.26 presents the force vs. displacement curves for the 25J and 50J impact energies, the 0° orientation and a modeling based on a four-step post-failure material degradation. Few differences are observed in comparison with the modeling using a linear damage. A

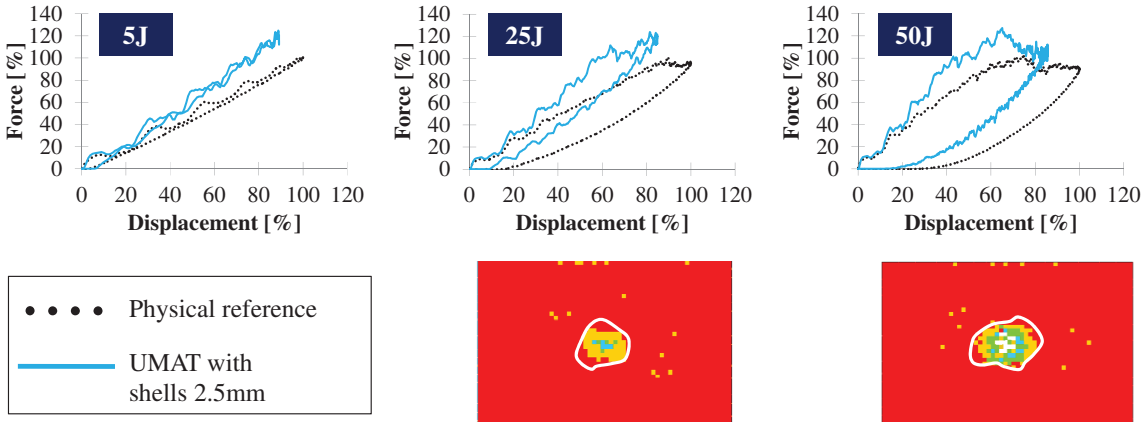

Figure 5.25: Correlation for the carbon plain-weave RTM composite: 5J, 25J, 50J impact energies, a 2.5mm mesh size, a linear damage, a modeling with shell elements and the 45° orientation

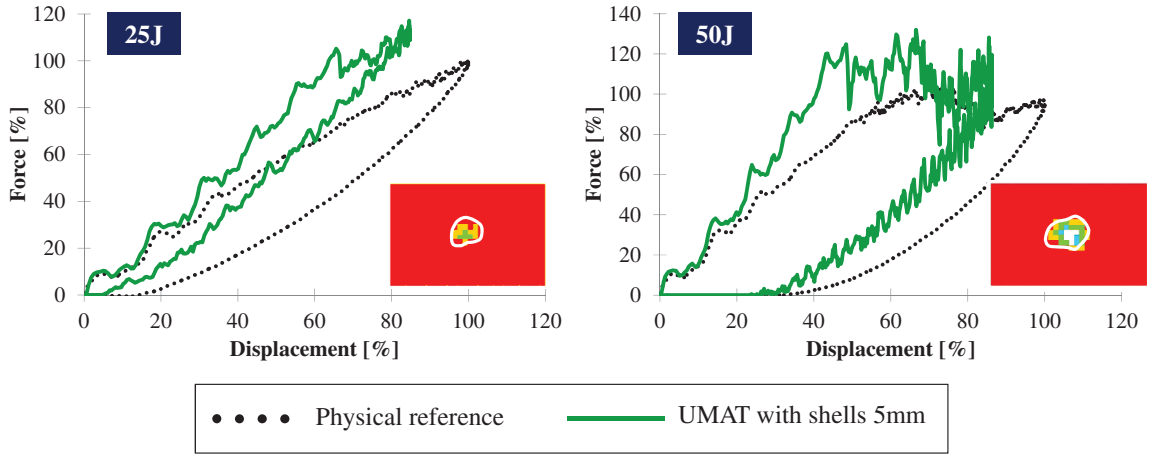

Figure 5.26: Correlation for the carbon plain-weave RTM composite: 25J, 50J impact energies, a 5mm mesh size, a step-based post-failure material degradation and a modeling with shell elements

too stiff material response is still predicted, whereas acceptable damaged areas are captured. It has been observed that the decrease of the number of levels does not highly influence the material response but it is likely to bring more oscillations in the curves (see Fig. 5.37).

Constant stress level material degradation Fig. 5.27 presents the force vs. displacement curves for the 25J and 50J impact energies, the 0° orientation and a modeling based on a step-based post-failure material degradation. A post-failure stress level about 50% of the strength is set for each material direction. A too stiff material response is still predicted, whereas acceptable damaged areas are captured. It has been observed that the decrease of the stress level tends to delay the rebound of the impact but it is likely to bring more oscillations in the curves (see Fig. 5.39).

Nonlinear damage Fig. 5.28 presents the numerical results for a 25J impact and a 0° orientation using a nonlinear post-failure material degradation. Both mesh sizes predict similar results in terms of material response and damaged surfaces. The maximal displacement of the impactor is about 12%

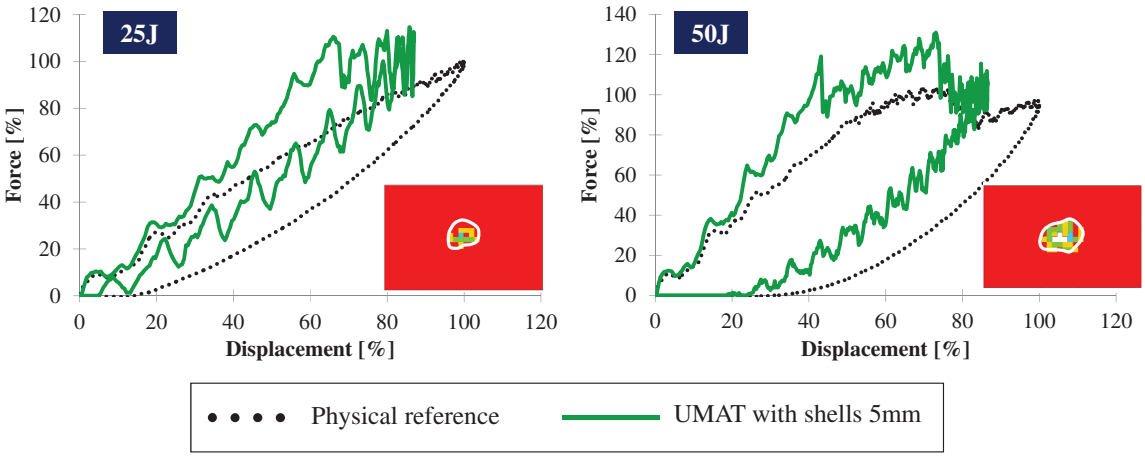

Figure 5.27: Correlation for the carbon plain-weave RTM composite: 25J, 50J impact energies, a 5mm mesh size, a constant-stress level post-failure material degradation and a modeling with shell elements

under-estimated, whereas the maximal force peak is about 15% over-estimated. A higher damage in tension than in compression is observed, which is in agreement with experimental observations. Finally, an acceptable correlation is obtained regarding the area of the damaged surface.

Fig. 5.29 presents the numerical results for a 50J impact and a 0° orientation using a nonlinear post-failure material degradation. Both mesh sizes predict similar results in terms of material response and damaged surfaces. The maximal displacement of the impactor is about 18% under-estimated, whereas the maximal force peak is about 30% over-estimated. The shape of the force vs. time curves is in accordance with the experimental curve. A higher damage in tension than in compression is observed, which is in agreement with experimental observations. Finally, an acceptable correlation is obtained regarding the area of the damaged surface, considering also the deletion of some elements.

Comparison of the four post-failure material degradation models Fig. 5.30 presents the numerical results for the four post-failure material degradation models, a mesh size of 2.5mm and for a 25J impact in the 0° orientation. The four models give similar results in terms of averaged damaged areas and regarding the curves of the material response. In a similar manner, Fig. 5.31 presents the numerical results for the four post-failure material degradation models, a mesh size of 2.5mm and for a 50J impact in the 0° orientation. However, it can be noticed that a lightly higher damage level and a larger element erosion are observed for both discontinuous material degradation. Moreover, the continuous post-failure damage evolution laws tend to reduce oscillations in the material response curves. Finally, the values of the final strain given in the input play the major role on the numerical predictions. The shape of the post-failure material degradation has a lower effect but it is recommended to use a continuous post-failure material degradation.

5.3.5.3 Modeling with thick shell elements

This section presents the numerical results obtained using the UMAT and a modeling with thick shell elements. The simulations are conducted with the R5 LS-DYNA release and a mesh size about 5mm. A unique element layer represents the composite laminate and two points of integration with a [0°/90°]

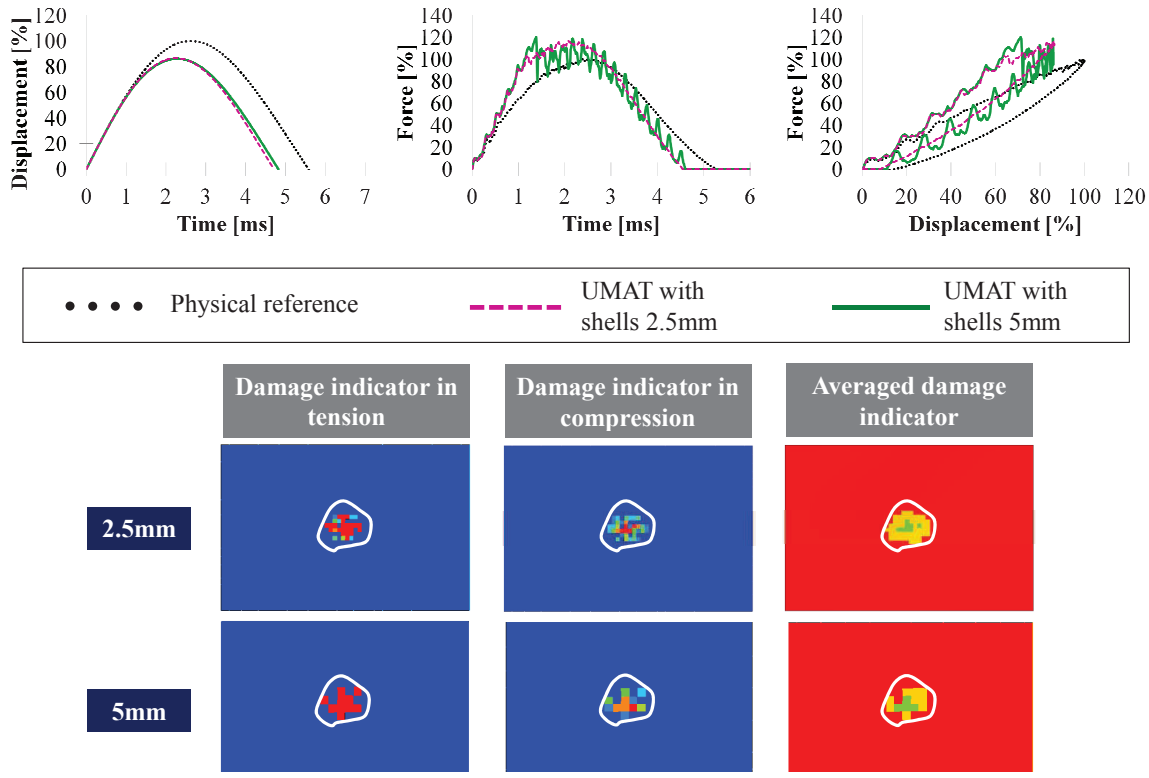

Figure 5.28: Correlation for the carbon plain-weave RTM composite: 25J impact, nonlinear damage and a modeling with shell elements

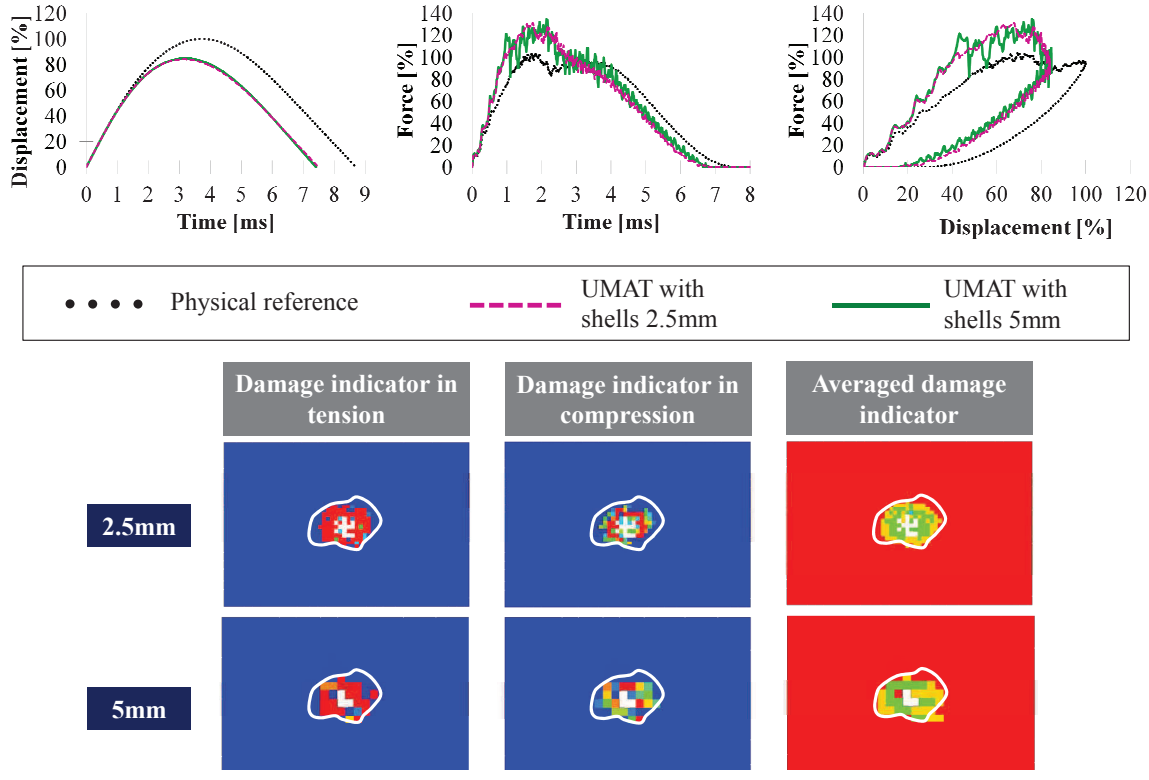

Figure 5.29: Correlation for the carbon plain-weave RTM composite: 50J impact, nonlinear damage and a modeling with shell elements

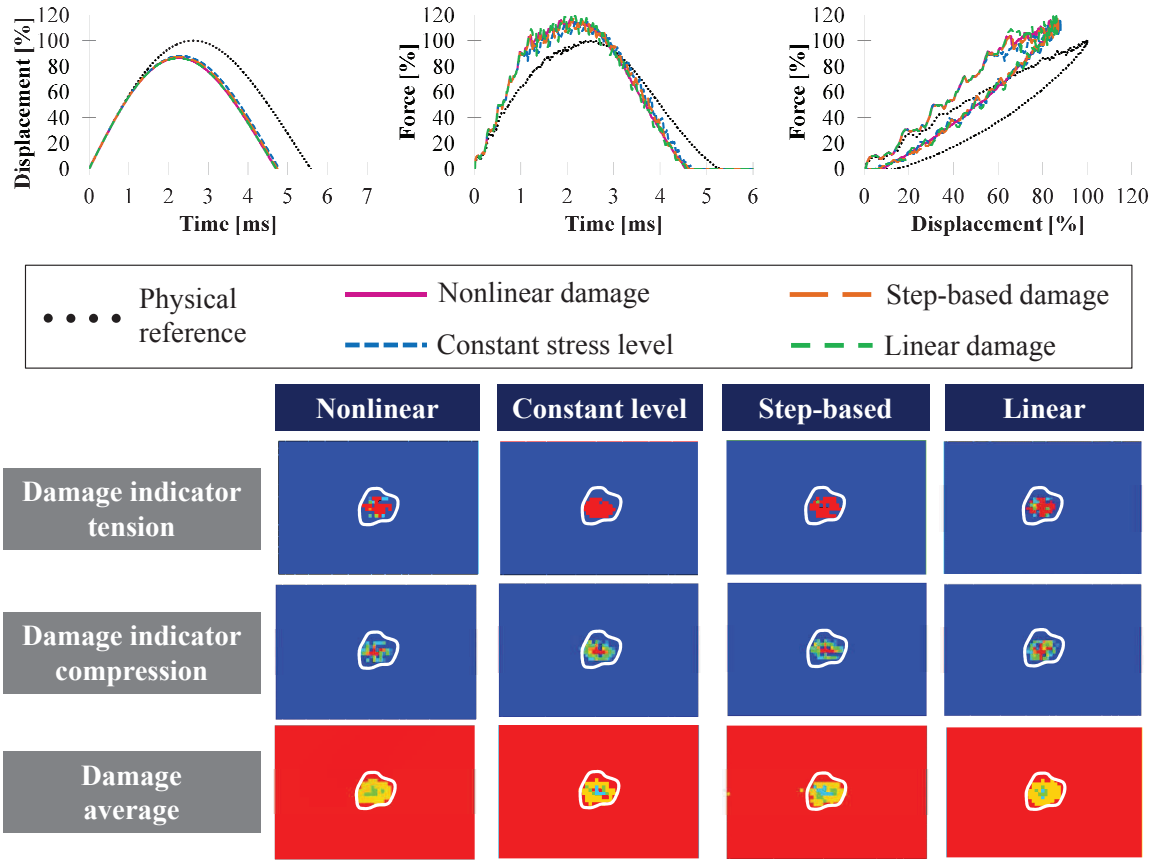

Figure 5.30: Comparison of the numerical results for the four post-failure material degradation models for a 25J impact and a modeling with shell elements

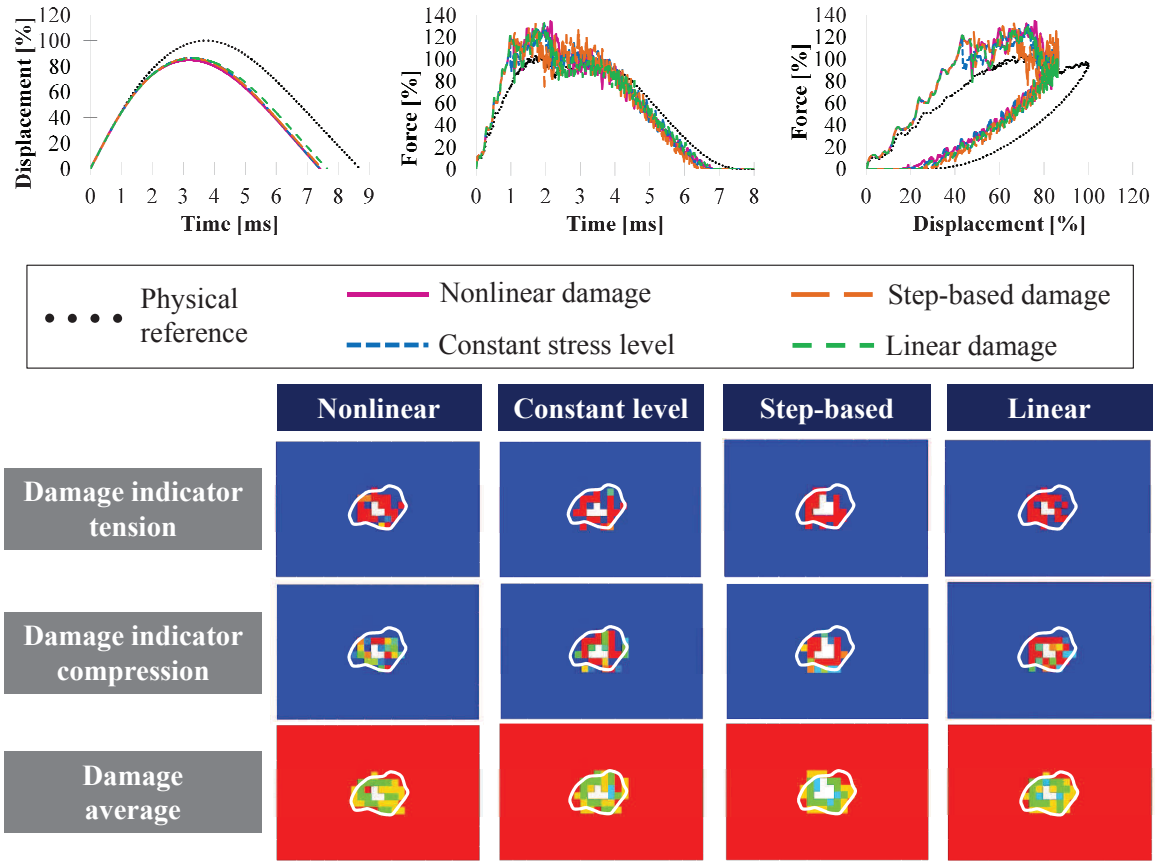

Figure 5.31: Comparison of the numerical results for the four post-failure material degradation models for a 50J impact and a modeling with shell elements

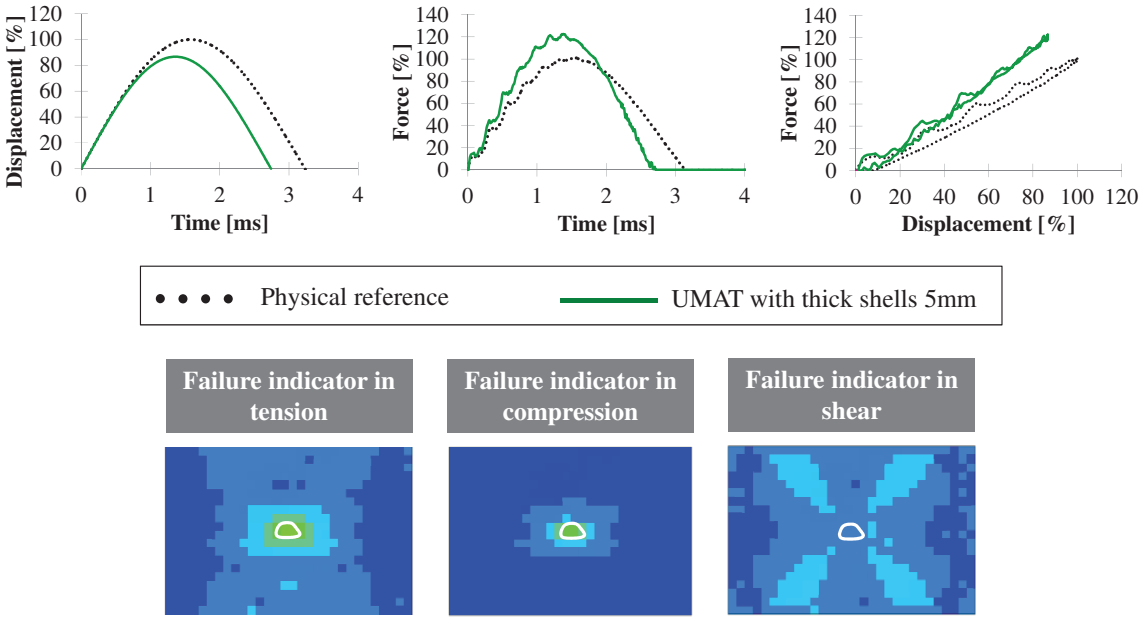

Figure 5.32: Correlation for the carbon plain-weave RTM composite: 5J impact, linear damage and a modeling with thick shells

orientation will numerically model each woven layer.

Linear damage Fig. 5.32 presents the numerical results for a 5J impact, a linear post-failure material degradation and a modeling with thick shell elements. Similarly to the modeling with shell elements, a too stiff material response is obtained compared to experimental observations. The maximal displacement of the impactor is 15% under-estimated and the maximal force peak is about 20% over-estimated. Thick shell elements offers a 3D stress state, so it is possible to take some transverse effect and through-the-thickness deformations in account but the high localized damage cannot be well predicted using a unique element layer and a 5mm mesh size. The failure indicator shows a load distribution over the composite plate similar as the modeling with shell elements.

Fig. 5.33 presents the numerical results for a 25J impact, a linear post-failure material degradation and a modeling with thick shell elements. A very good agreement is obtained regarding the predicted displacement of the impactor over the time. The force vs. time as well as the force vs. displacement curves offer an acceptable correlation. However, the analysis of the damaged shows inadequate cross-shape damage distributions. As investigated thereafter, this unsuitable distribution of the material degradation should rely on the element formulation and not in the UMAT implementation, as the damage distribution seems to be acceptable for a modeling with common under-integrated brick elements (see Fig. 5.35).

Fig. 5.34 presents the numerical results for a 50J impact, a linear post-failure material degradation and a modeling with thick shell elements. A very good agreement is obtained regarding the material response. However, similarly to the 25J impact, the analysis of the damaged zones presents inadequate cross-shape damage distributions. As mentioned previously, the problem should come from the thick shell element implementation but it needs still further investigation, beginning by the test of the UMAT on the updated R6 or R7 LS-DYNA release.

In order to identify the potential cause of the unsuitable damage distribution in thick shell elements,

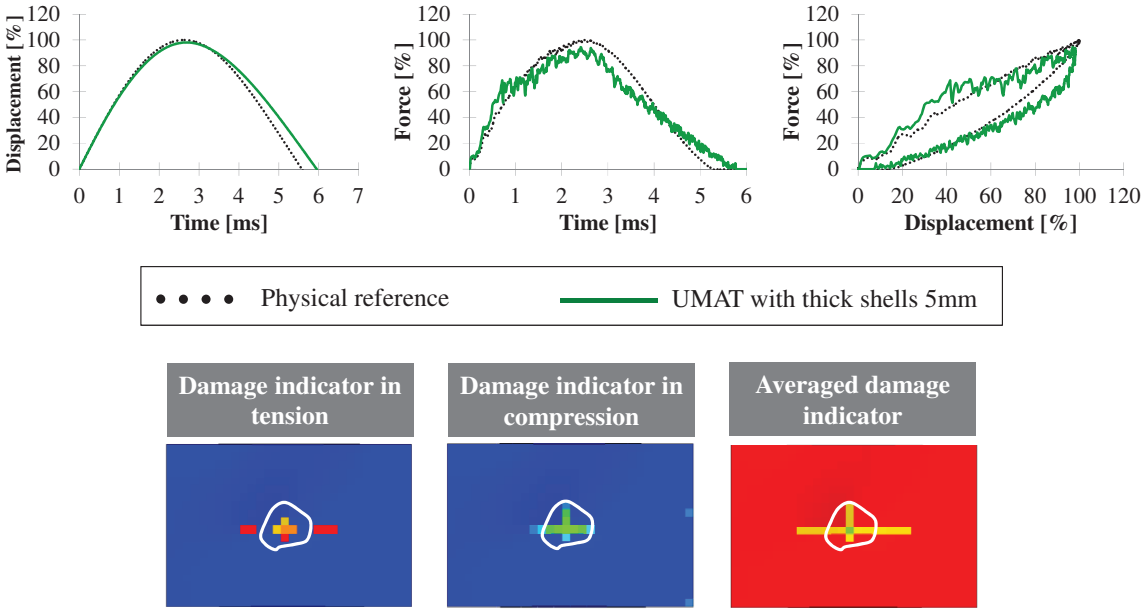

Figure 5.33: Correlation for the carbon plain-weave RTM composite: 25J impact, linear damage and a modeling with thick shells

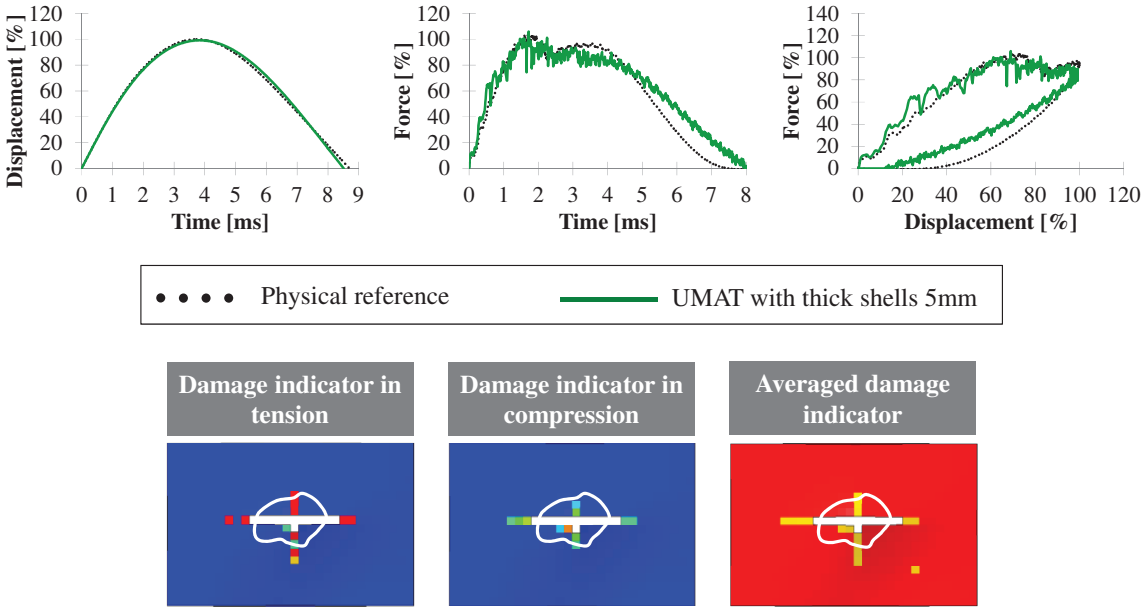

Figure 5.34: Correlation for the carbon plain-weave RTM composite: 50J impact, linear damage and a modeling with thick shells

simulations have been conducted using models constituted by ten element layers. The deletion of elements during the simulation has been not permitted. A comparison between a modeling with ten thick shell layers and a modeling with ten under-integrated common brick elements (element type one in the LS-DYNA element library) has been made. Under-integrated brick element presents a unique point of integration in the center of the element. This configuration has also been used for the thick shells defining only one point of integration per element. This point of integration presents the material properties of a woven ply and the correct orientation. The same hourglass control and material parameters have been used for both types of elements. The numerical results are presented on Fig. 5.35. Both elements show a good agreement regarding the force over the time. Concerning the displacement of the impactor, brick elements offer a better correlation than thick shell elements. The failure and damage indicators present respectively the pre-failure loads and post-failure damage distributions. The failure indicators in tension and compression show clearly a cross-shape load distribution around the impacted zone for the modeling with thick shell elements. The modeling with brick elements shows a localized load distribution around the impacted zone, which seems to be more realistic. Regarding the damage indicators, a similar effect is observed with a better localization of the damage around the impacted zone for the modeling with brick elements. Thick shell elements predict a cross-shape damage distribution over the thickness of the laminate. Finally, it seems that the unsuitable cross distribution of load and damage relies on the thick shell formulation, as a modeling with common under-integrated brick elements gives more realistic predictions. Despite these discrepancies, both elements depict some acceptable results, such as the diagonal cross load distribution in shear, the upper layers loaded in compression and the bottom layers loaded in tension.

To conclude this part, an acceptable agreement regarding the material response is obtained for the 25J and 50J impact energies, a linear post-failure damage evolution law and a modeling with thick shell elements. The unsuitable cross-shape of the damage area seems to be caused by some deficiencies in the implementation of the thick shell elements. The next paragraphs present the correlation for the three others post-failure material degradations. As the 5J impact energy does not involve the post-failure material behavior, the results obtained for this impact energy will not be reported.

Step-based material degradation Fig. 5.36 presents the force vs. displacement curves for the 25J and 50J impact energies, the 0° orientation and a modeling based on a four-step post-failure material degradation. Few differences are observed in comparison with the modeling using a linear damage. An acceptable agreement is obtained for both energies but the cross-shape of the damage distribution is not suitable.

Fig. 5.37 shows the effect of the number of steps on the force vs. displacement material response of a 50J impact. It is clear that the number of steps presents a quite negligible effect but it can be noticed, that the reduction of the number of steps tends to increase the oscillations in the curves. A low effect has also been observed on the damage distribution.

Constant stress level material degradation Fig. 5.38 presents the force vs. displacement curves for the 25J and 50J impact energies, the 0° orientation and a modeling based on a constant stress level post-failure material degradation. A post-failure stress level about 50% of the strength is set for each material direction. An acceptable agreement is obtained for the highest impact energy. For the 25J impact, the

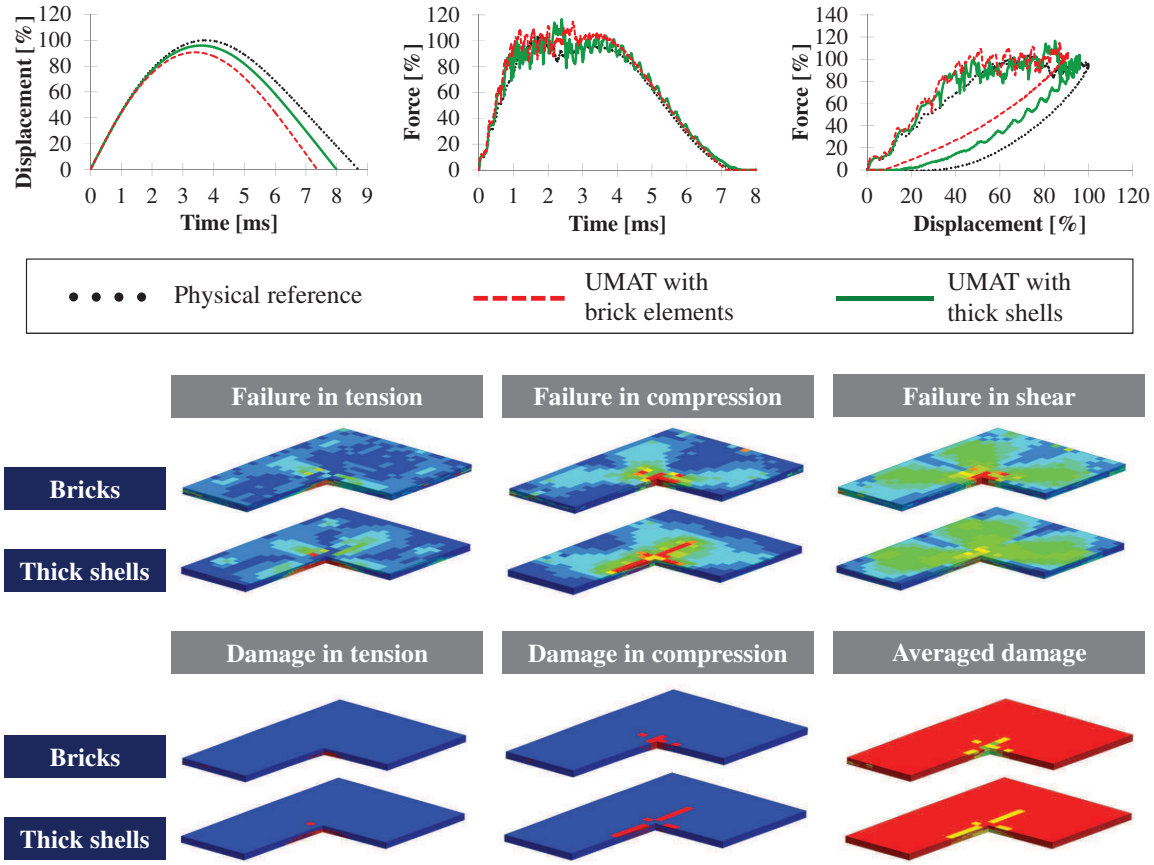

Figure 5.35: Comparison between a modeling with ten layers of thick shell and ten layers of under-integrated brick elements: 50J impact and linear damage

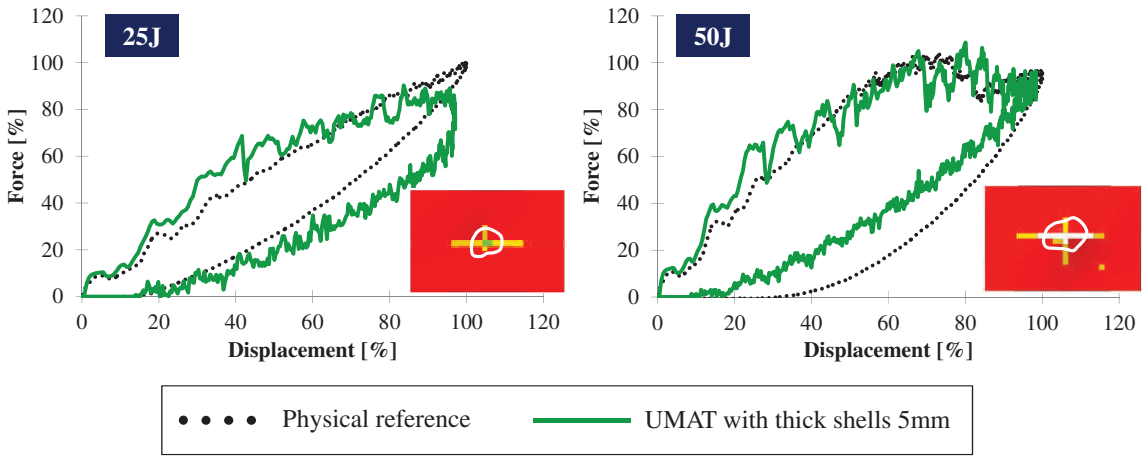

Figure 5.36: Correlation for the carbon plain-weave RTM composite: 25J, 50J impact energies, a 5mm mesh size, a step-based post-failure material degradation and a modeling with thick shell elements

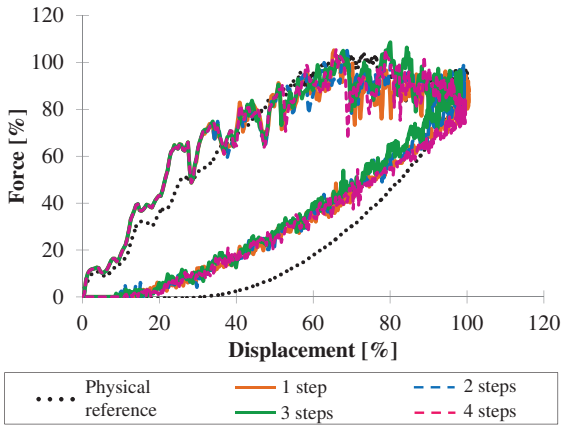

Figure 5.37: Effect of the post-failure number of steps on the material response: 50J impact and a modeling with thick shells

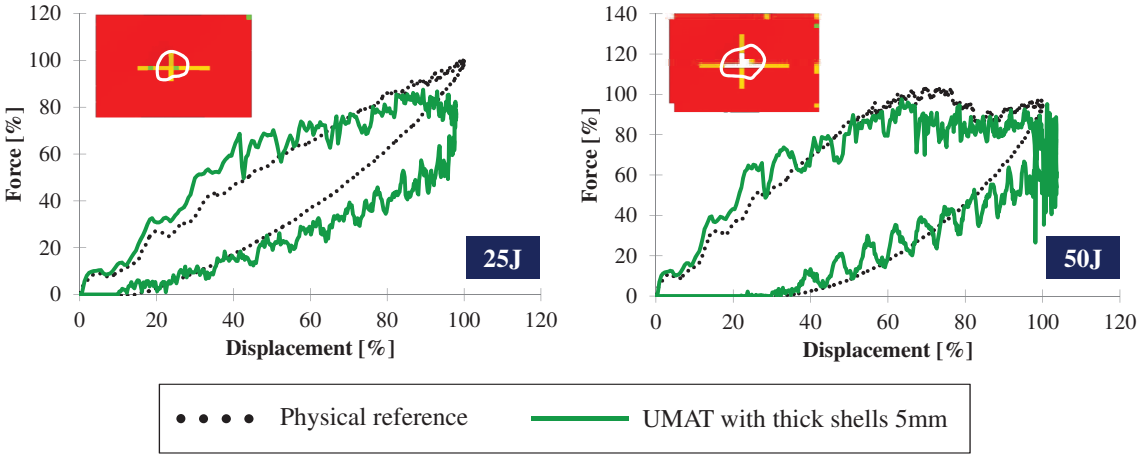

Figure 5.38: Correlation for the carbon plain-weave RTM composite: 25J, 50J impact energies, a 5mm mesh size, a constant stress level post-failure material degradation and a modeling with thick shell elements

maximal force peak is about 18% under-predicted. The cross-shape of the damage distribution is not suitable for both energies.

Fig. 5.39 shows effect of the stress level on the force vs. displacement material response for a 50J impact. A decrease of the stress level allows to delay the rebound and to keep the contact between the plate and the impactor longer. However, it tends to bring more oscillations in the curves due to the sudden reduction of the load bearing capability. Consequently, the step based degradation or a continuous post-failure damage evolution law are recommended, in particular to reduce the potential numerical instabilities.

Nonlinear damage Fig. 5.40 presents the force vs. displacement curves for the 25J and 50J impact energies, the 0° orientation and a modeling based on a nonlinear post-failure material degradation. A very good agreement is obtained concerning the material response for the 50J impact. Regarding the 25J impact, the maximal force peak is about 15% under-estimated but an acceptable material response

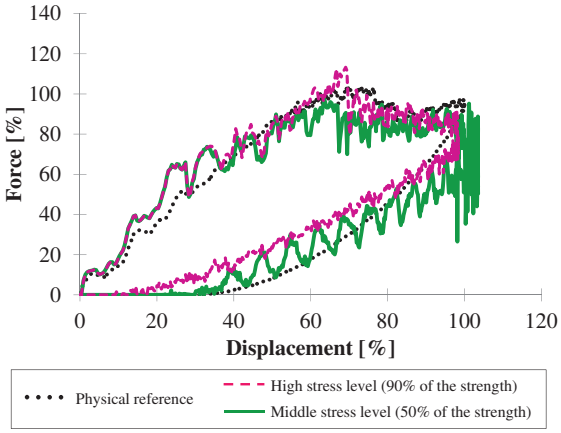

Figure 5.39: Effect of the post-failure stress level on the material response: 50J impact and a modeling with thick shells

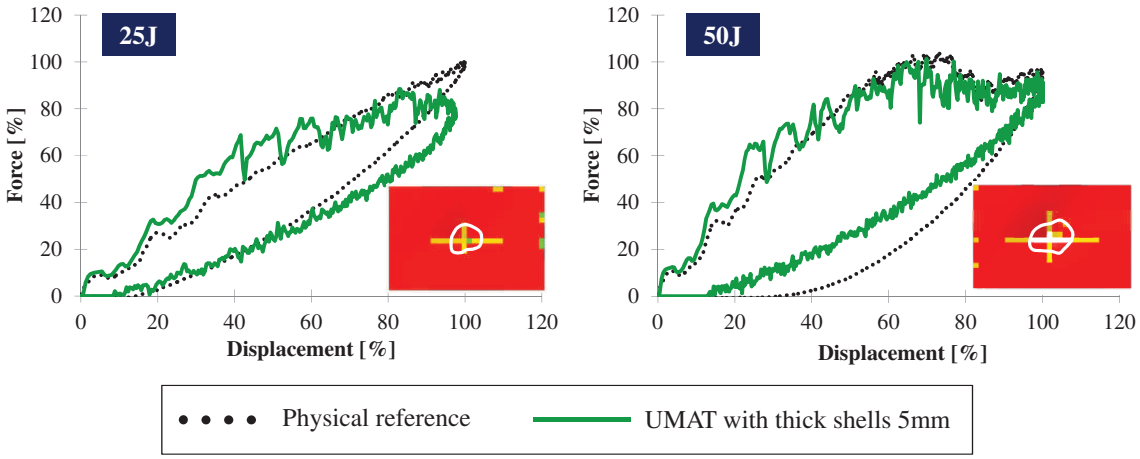

Figure 5.40: Correlation for the carbon plain-weave RTM composite: 25J, 50J impact energies, a 5mm mesh size, a nonlinear post-failure damage and a modeling with thick shell elements

is obtained considering the discretization of the model. The predicted damaged areas present still an unsuitable cross-shape.

Comparison of the four post-failure material degradation models Fig. 5.41 presents the numerical results for the four post-failure material degradation models, a mesh size of 5mm and both 25J and 50J impact energies. The four models give similar results regarding the curves of the material response. Continuous post-failure material degradation models tend to avoid the oscillations in the curves and the instabilities that are likely to appear using a too low post-failure constant stress level or too few levels in the step-based material degradation. The predicted damaged areas are similar for the four damage models but they are not presented.

Simulations have been also conducted for the 45° orientation. Similar results and correlation as for the 0° orientation have been observed, that is why the results are not reported here.

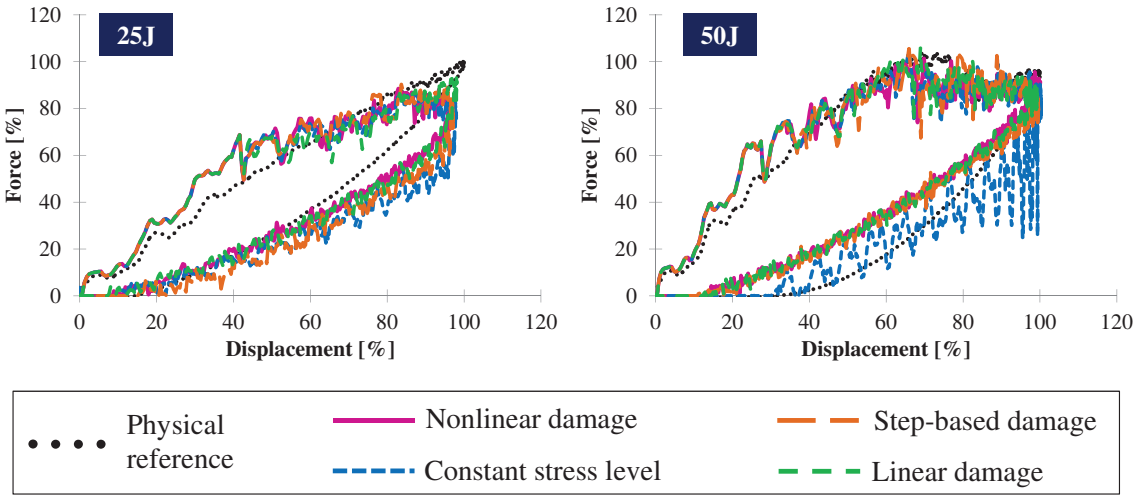

Figure 5.41: Comparison of the numerical results for the four post-failure material degradation models for both 25J and 50J impact energies and a modeling with thick shell elements

5.3.6 Drop tower tests on hat-profiles

As presented in the section 3.2.2.2, experimental drop tower tests have been conducted on 2mm thick hat-profiles and a 200J impact energy. In the numerical model, under-integrated shell elements and a mesh size about 5mm have been used. The modeling techniques and the material parameters obtained from the previous validations on quasi-static and impact tests are used here for the simulations of drop tower tests on hat-profiles. Both continuous post-failure damage evolution laws have been only investigated. Finally, due to high numerical instabilities leading to the crash of the simulations, the results for a modeling with thick shell elements will not be reported. Once the hat-profile failed, a quite constant force level is experimentally observed corresponding in a large part to the material response of the steel plate and to the friction at the fracture plane. For this reason, all simulations have been stopped after 25ms.

Linear damage Fig. 5.42 presents the numerical results for the 200J drop tower test on a hat-profile. A very good agreement is observed for the displacement of the impactor over the time. However, the results concerning the reaction force does not present a good correlation, despite an acceptable prediction about 90% of the first force peak. Then, a sudden failure occurred, which explains the abrupt fall of the force. The repetition of failure and sudden force collapse is due to the difficulty to model accurately the local fragmentation of the material observed experimentally. Indeed, the collapse of the hat-profile is followed by a kind of crushing and fragmentation of the material, inducing a high level of friction and a progressive material degradation, which contributes to the quite constant force level after failure. In the simulation, failure leads to the deletion of the elements. This implies a sudden loss of contact between the impactor and the hat-profile, which is responsible for the oscillations in the force vs. time curve. Moreover, using 2D elements, a edge to edge contact is quite impossible and the crushing and fragmentation phenomenon occurring at the failure location is very difficult to model numerically. The fringe plots presented on Fig. 5.42 illustrates the brittle failure of the hat-profile. A line of deleted elements appears transversely to the hat-profile. In comparison with experimental observations (see Fig. 3.26) an adequate mode of collapse is numerically predicted. The failure indicators in tension and compression show a localized failure of the

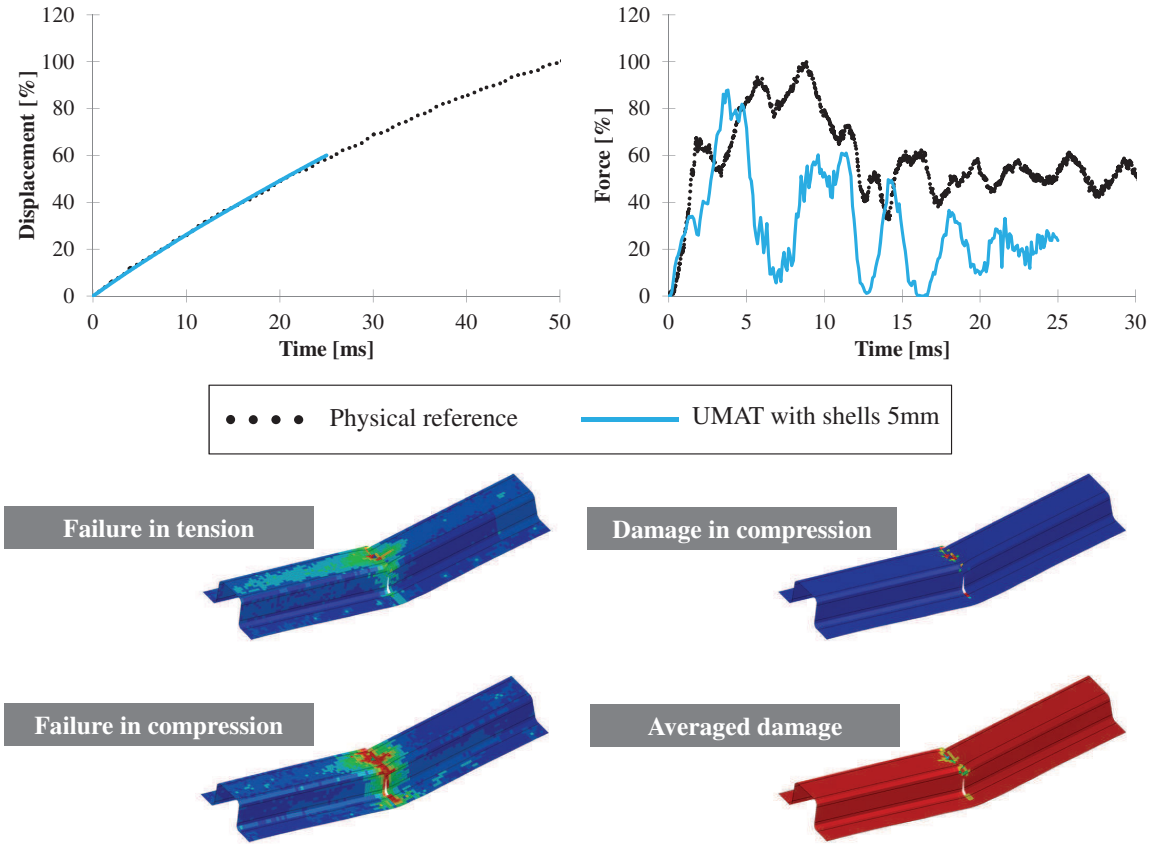

Figure 5.42: Correlation for the carbon plain-weave RTM hat-profile: 200J impact energy, a 5mm mesh size, a linear post-failure damage, a modeling with shell elements and the previous validated material parameters

hat-profile, at the place where the impactor hits the specimen. A more important failure in compression is observed, which is acceptable. As some elements have been quickly deleted, a limited damage distribution is observed around the collapsed area. Finally, the flat sides of the hat-profile supporting the rivets do not fail but they undergo large deformations, considerable loads and some damage, which is in good agreement with experimental observations.

The previous results based on the material parameters obtained from coupons tests showed an acceptable qualitative prediction of the behavior of hat-profile under impact but the quantitative material response does not present a good agreement with experimental observations. An update of the strain at failure has been investigated in order to obtain a better correlation. All the effective strengths and stiffnesses are not modified. The best compromise is presented on Fig. 5.43. To obtain these results, the previous validated material parameters are kept in the corners of the hat-profile. On the flat sides of the specimen, the strains at failure material parameters ε_f are set to high values about 200%. Consequently, the material presents there a long post-failure material degradation. Large deformation can be thus undergone by the material before the final collapse, which delays the deletion of elements. However, in order to avoid nonphysical huge element deformations, which increases dramatically the computing time, an effective strain failure criterion is set using the *MAT_ADD_EROSION keyword. The deletion of element occurred, when an effective strain about 25% is detected in the element. An acceptable correlation is

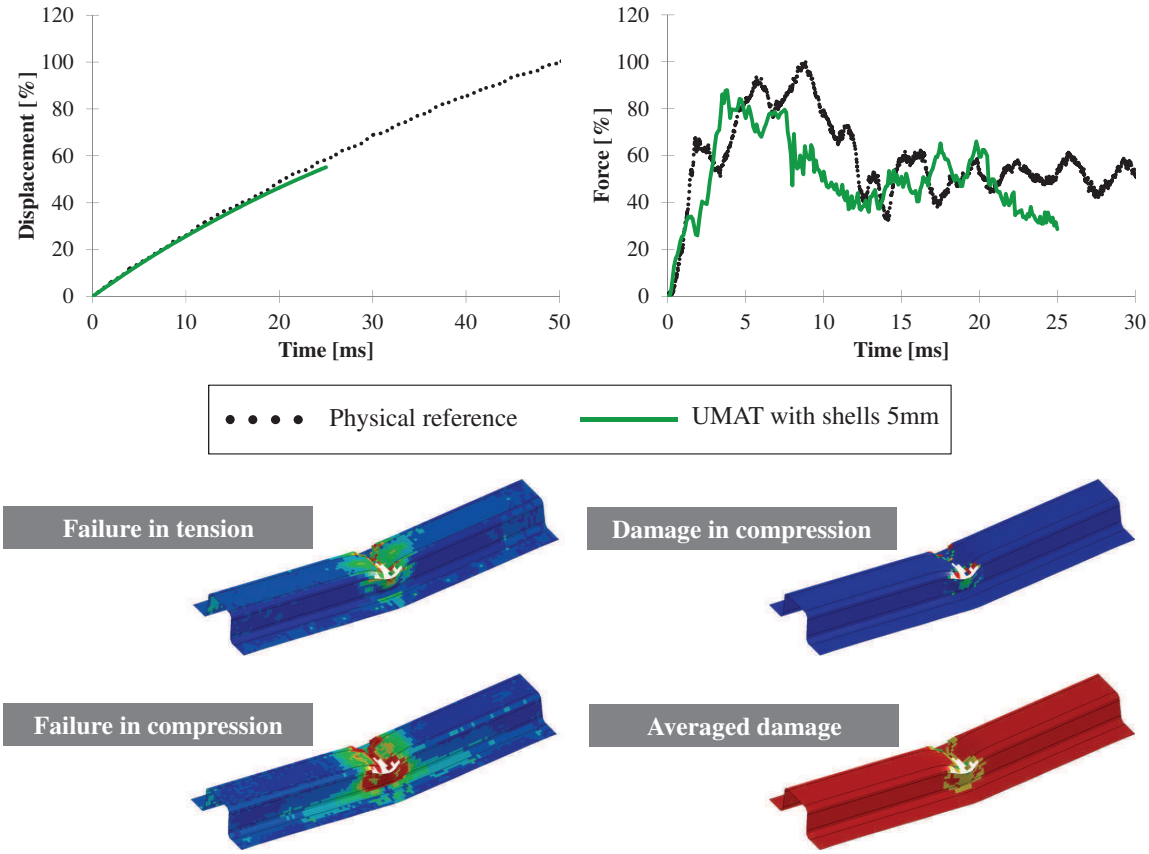

Figure 5.43: Correlation for the carbon plain-weave RTM hat-profile: 200J impact energy, a 5mm mesh size, a linear post-failure damage, a modeling with shell elements and updated material parameters

obtained regarding the curves of the material response. Failure indicators show a larger load distribution around the impacted zone than previously. Element have been deleted only on the upper flat side and in the corners, which induced the force decrease at 8ms. As no element is deleted on the vertical flat sides of the hat-profile, it contributes to the modeling of the progressive crushing and fragmentation of the material. The material underwent some damage there, which is acceptable regarding the experiments.

The material parameters used to obtain the results presented on Fig. 5.43 gave naturally unacceptable results for the impact tests on elementary plates. It confirms the difficulty to predict delamination and post-failure damage using a similar evolution law and a modeling based on a unique element layer. The prediction of delamination initiation and propagation seems to require a particular modeling based on an interface definition between at least to element layers. The post-failure damage parameters should be then validated on particular experiments like the bearing tests, which involve crushing, fragmentation and progressive damage of the material.

Nonlinear damage Similarly to the linear damage, the nonlinear post-failure material degradation has been investigated for the simulation of drop tower tests on hat-profiles. The results obtained using the material parameters validated on the coupon tests are presented on Fig. 5.44. Similar observations and conclusions as for the linear damage can be also made here. A brittle failure and element deletion occurred at the impacted zone inducing large oscillations in the curve of the reaction force. An acceptable

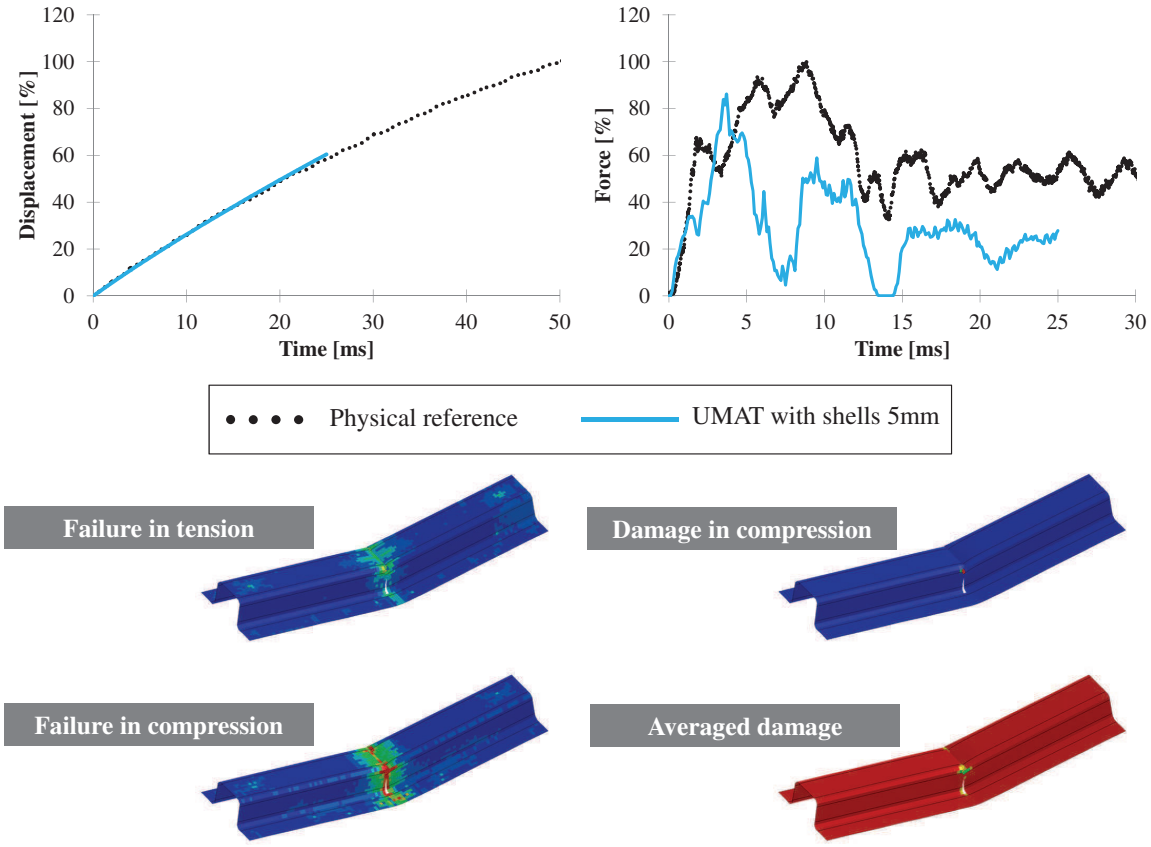

Figure 5.44: Correlation for the carbon plain-weave RTM hat-profile: 200J impact energy, a 5mm mesh size, a nonlinear post-failure damage, a modeling with shell elements and the previous validated material parameters

correlation is obtained regarding the displacement of the impactor over the time. The fringe plots illustrate very well the very localized failure of the material around the impacted zone, with very limited load and damage distributions.

Fig. 5.45 presents the results of a simulation with the same "updated" material parameters, as described previously for the linear damage. An acceptable correlation is obtained regarding the material response. However, the linear damage offered a longer force peak level than the nonlinear damage. It is probably due to the fact, that for a given strain at ultimate collapse, the nonlinear damage degrades the material faster just after failure than the linear damage. Failure and damage indicators show acceptable load and damage distributions, which are also similar as those obtained for the linear damage.

5.3.7 Partial conclusions

The previous sections presented the comparison between numerical and experimental results for a T700 plain-weave RTM composite. Models built up with shell and thick shell elements have been used in association with the developed UMAT to conduct the simulations of the different experimental tests. A very good correlation is obtained regarding the in-plane quasi-static tensile and compressive load cases. The longitudinal bending loads showed generally a too stiff behavior, whereas the predictions for the diagonal bending are acceptable. For thick shell elements, the use of damping in order to stabilize the

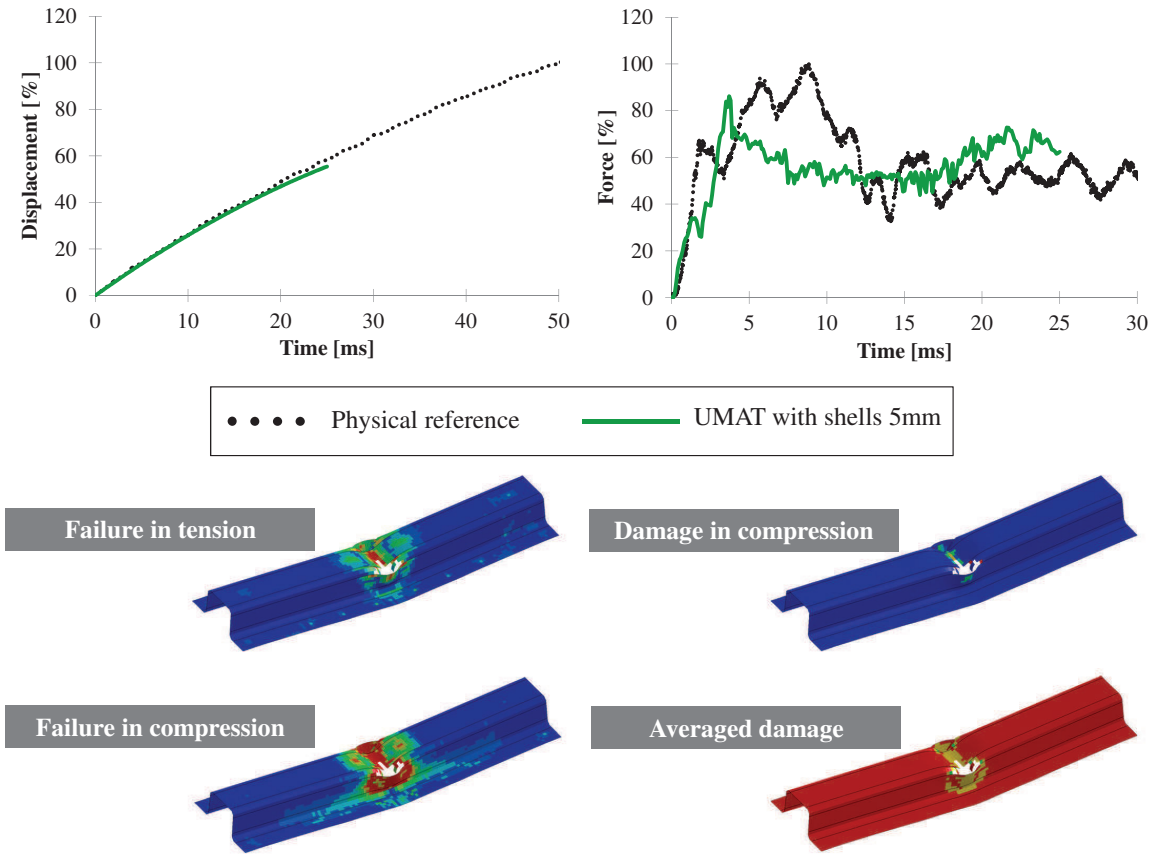

Figure 5.45: Correlation for the carbon plain-weave RTM hat-profile: 200J impact energy, a 5mm mesh size, a nonlinear post-failure damage, a modeling with shell elements and updated material parameters

simulations led to an unsuitable bending stiffness. This effect seems to increase when the stiffness of the specimen decreases. No considerable influence of the mesh size and of the number of thick shell layers (without modeling of any interface between each element layer) has been observed. The modeling of the outer glass mat layers allowed to obtain acceptable predictions of the bending behavior. However, due to the lack of information concerning the outer glass mat layers, this modeling has to be further investigated, beginning by the characterization of the effective properties and of the behavior of the glass mat material.

Impact tests on a 4mm thick composite plate have been modeled for three impact energies and compared to experimental results. The single-layer model did not allow to predict accurately the delamination propagation, as the post-failure material degradation models the progressive damage occurring in the material after failure and not the behavior of an interface. A modeling with shell elements showed a too stiff material response probably due to the fact that the 2D stress state is not able to take into account the deformation in the thickness direction and their associated transverse effects. Consequently, the maximal displacement of the impactor was about 12% under-estimated and the maximal reaction force peak was between 15% and 30% over-estimated. However, the prediction of the damaged areas was in very good agreement with the experimental observations. Both 2.5mm and 5mm mesh sizes gave similar results for the quantitative and the qualitative analysis of the impact tests. The four post-failure material degradation models gave similar results but it has been observed that a continuous damage evolution law limits the oscillations in the curves and the instabilities in the simulations. A modeling with thick shell elements improved the correlation of the material responses for the 25J and 50J impact energies. A very good agreement is obtained regarding the displacement of the impactor and the reaction force. However, an unsuitable cross-shape of the damage distribution and of the element deletion is observed for each damage definition and for each impact energy. It has been shown that it should come from the formulation of the thick shell elements in the R5 LS-DYNA release. Similarly to the modeling with shell elements, a continuous post-failure damage model is recommended to limit the numerical instabilities. For both element types, the numerical predictions for the 0° and the 45° orientations are similar, which is in agreement with the experimental results. Finally, the results concerning the 5J impact showed a unsatisfactory agreement with experimental observations. As the numerical model presents a finest mesh about 2.5mm it is very difficult to capture the high localized effects and damages induced by such a low energy of impact.

The simulations of the drop tower tests made on hat-profiles showed the difficulty to calibrate the post-failure damage evolution in a composite material. The post-failure damage parameters validated for the impact tests on elementary plates gave a too brittle failure of the hat-profile. A better correlation has been obtained by setting high strain at failure corresponding to a large post-failure material behavior and by triggering the element deletion using an effective strain criterion. Due to a modeling with a unique element layer, post-failure material degradation and delamination propagation have to be modeled by the same damage evolution law. Delamination is so assimilated to a damage propagation in the material. This assumption showed some limits here, which means that these two kinds of material damage should be considered separately. A particular modeling of the interface between two composite layers should predict delamination and the post-failure material degradation should account for the modeling of the post-failure fragmentation of the composite in order to assess the damage tolerance of the material independently from delamination. These remarks consider naturally a modeling based on a sublaminate approach and

a mesh size about 5mm.

The work presented in this chapter resulted in the following publications [251–253][2].

[2]These publications include work from other chapters of this thesis and therefore feature again in the corresponding chapters

Chapter 6

Numerical results and validation on carbon twill-weave PREPREG specimens

This chapter presents the numerical results obtained for the simulation of the quasi-static, impact and drop tower tests made on the PREPREG twill-weave composite, using the UMAT material model and the models presented in the section 5.1. The experimental results have been described in the section 3.3 and they are represented by the physical reference for the comparison with the numerical results. Only one representative curve is generally reported to depict the numerical predictions of the UMAT. However, for each in-plane and bending load case, both pre-failure models (user-defined load curve and Ramberg-Osgood model) and both failure criteria (2D Tsai-Wu and maximal stress criteria) have been investigated. A mesh size about 3mm has been used in the simulations. As each woven ply presents a thickness about 0.66mm, a modeling with two points of integration per woven ply is used.

Concerning the quasi-static in-plane tests on elementary coupons, the numerical results presented here are obtained using the Ramberg-Osgood model but similar results have been obtained using a user-defined load curve. Without any particular indication, failure has been predicted by the maximal stress criterion and similar results have been obtained with the Tsai-Wu failure criterion. Finally, the numerical results reported for the quasi-static coupon tests have been obtained using shell elements but a modeling with thick shell elements has been investigated. Without any specific indication, similar results have been obtained using the thick shells.

Finally, for confidentiality reasons, all the quantitative results (for example stress vs. strain curves) have been normalized and they are presented using a scale expressed in percentage.

6.1 Quasi-static tests on a unidirectional stacking sequence

This section presents the results concerning the quasi-static tensile, compressive and bending tests on coupons having a "unidirectional" stacking sequence. All the elementary woven plies of the laminate have the same orientation.

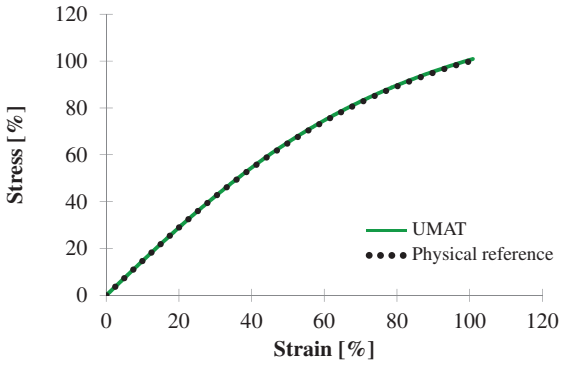

Figure 6.1: Correlation for the carbon twill-weave PREPREG composite: longitudinal unidirectional tension

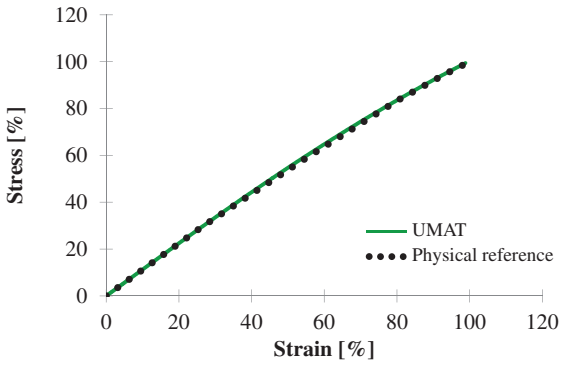

Figure 6.2: Correlation for the carbon twill-weave PREPREG composite: longitudinal unidirectional compression

6.1.1 Tensile tests

Fig. 6.1 presents the results for the longitudinal tension. A delamination of the specimen about the half of the strength has been experimentally captured, which leads to a discontinuous tensile behavior. A continuous nonlinear behavior has been chosen to account for the pre-failure damage and the loss of stiffness of the material. This macroscopic nonlinear behavior is well-predicted by the UMAT using both Ramberg-Osgood and user-defined load curve models. Both maximal stress and Tsai-Wu failure criteria give also similar predictions. Due to the nonlinearity, plastic strain has been accumulated but its distribution is not represented here, as it has no physical meaning to compare it with the permanent deformation caused by delamination and yarn debonding.

6.1.2 Compressive tests

As shown on Fig. 6.2 the macroscopic nonlinear compressive behavior and failure are well-predicted for the longitudinal compression. Both nonlinear models and both failure criteria give here also similar results. A low quantity of plastic strain has been accumulated due to the low level of nonlinearity but it is not reported here.

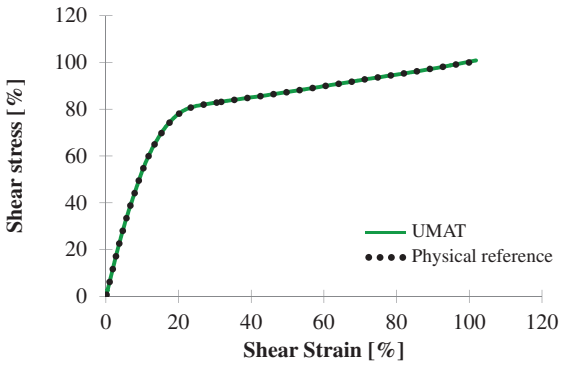

Figure 6.3: Correlation for the carbon twill-weave PREPREG composite: shear tension

6.1.3 Shear tests

As shown on Fig. 6.3, a good agreement between the numerical and experimental results is obtained for the shear tensile behavior. The nonlinear behavior is predicted here only based on a user-defined load curve. Similar results have been noticed for both failure criterion but only the failure prediction made by the maximal stress criterion is reported here. Similar shear strain and plastic shear strain distributions as those presented on Fig. 5.18 are observed.

6.1.4 Longitudinal four-point bending tests

Fig 6.4 presents the results for the longitudinal four-point bending tests. The stiffest bending behavior captured experimentally has been added to the physical reference on the graphs. Indeed, a considerable scatter in the bending stiffness has been experimentally captured, as shown on Fig. 3.34. The predicted bending stiffness is not in agreement with the physical reference, but an acceptable correlation is observed regarding the stiffest experimental results. Without using post-failure damage, failure occurred at 70% of the bending strength observed experimentally. The collapse of the numerical specimen is caused by the failure in compression of the first ply below the loaders. The in-plane longitudinal compressive strength captured experimentally was relatively low and it could explain the premature failure observed here. However, in order to keep unchanged the compressive strength determined experimentally, we choose to use the post-failure material degradation laws implemented in the UMAT to delay the collapse of the specimen and to better match the bending strength given by the physical reference. The three investigated post-failure damage models show similar and acceptable results. The strains at ultimate failure have been set here only in compression in order to obtain the best agreement with experimental results. The use of thick shell elements led to a lightly stiffer material response and a lightly over-estimation of the stress at failure.

6.1.5 Diagonal four-point bending tests

The shear bending behavior predicted by the UMAT model is presented on Fig. 6.5. A very good agreement is obtained in terms of stiffness, nonlinearity and failure. Consequently, the modeling based on a load curve in order to predict the in-plane and bending shear behaviors offers a good correlation for the carbon twill-weave PREPREG composite investigated here.

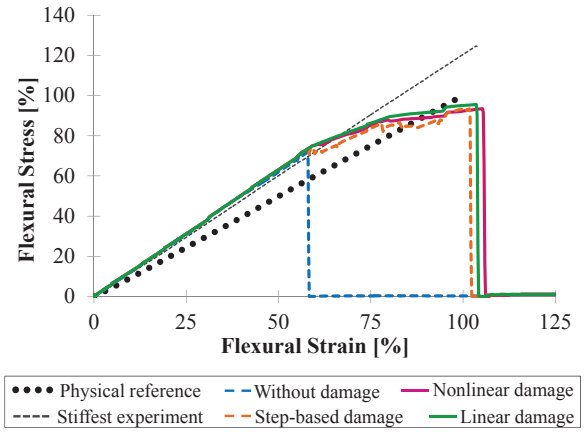

Figure 6.4: Correlation for the carbon twill-weave PREPREG composite: longitudinal unidirectional four-point bending

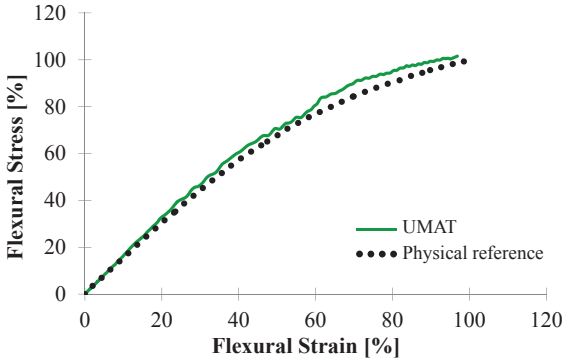

Figure 6.5: Correlation for the carbon twill-weave PREPREG composite: diagonal unidirectional four-point bending

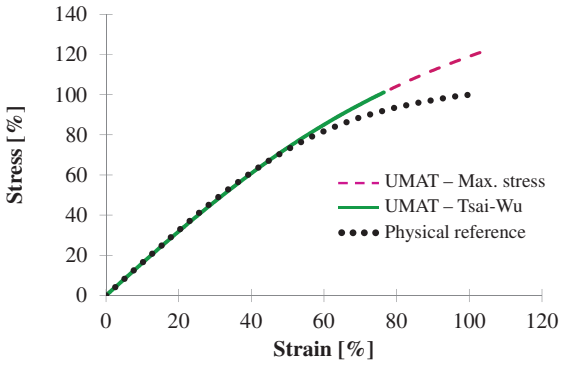

Figure 6.6: Correlation for the carbon twill-weave PREPREG composite: longitudinal multidirectional tension

6.2 Quasi-static tests on a multidirectional stacking sequence

This section presents the results concerning the quasi-static tensile, compressive and bending tests on coupons having a "multidirectional" $[0°/45°/0°]_s$ stacking sequence, which corresponds to a 4mm thick laminate. The longitudinal direction means here that the 0° plies are aligned with the loading direction (the warp or weft direction is parallel to the loading direction). The diagonal direction means here that most of plies of the laminate present a $\pm 45°$ angle with the loading direction. For the four-point bending tests, the loading direction corresponds to the longest dimension of the specimen.

6.2.1 Tensile tests on a multidirectional stacking sequence

6.2.1.1 Longitudinal tensile tests on a multidirectional stacking sequence

Fig. 6.6 presents the results given by the UMAT model and both implemented failure criteria for the longitudinal tension on a multidirectional (M.D.) stacking sequence. A good agreement is observed in term of stiffness but due to the particular delamination phenomenon occurring for this PREPREG composite in tension, the predicted nonlinear behavior is not acceptable regarding the physical reference. However, due to the low precision in the measurement of the strain after that delamination occurred, it is difficult to give a definitive and reliable conclusion about the prediction of the nonlinear behavior here. Concerning the maximal stress at failure, the Tsai-Wu failure criterion shows more acceptable results than the maximal stress criterion. This conclusion seems to be logical, as the equations of the Tsai-Wu criterion involves the stresses in all the main in-plane material directions. Moreover, with such a M.D. stacking sequence, each ply undergoes simultaneously longitudinal and shear deformation, which is also accounted for in the LS-DYNA solver.

6.2.1.2 Diagonal tensile tests on a multidirectional stacking sequence

The material response predicted by the UMAT model for a diagonal tension on a multidirectional stacking sequence is presented on Fig. 6.7. A very good agreement is obtained in term of stiffness and the light nonlinear behavior is numerically well-predicted. Similarly to the longitudinal tension, the Tsai-Wu failure criterion gives a better prediction of failure than the maximal stress criterion.

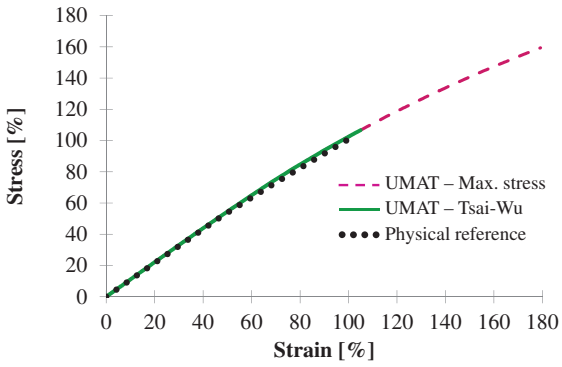

Figure 6.7: Correlation for the carbon twill-weave PREPREG composite: diagonal multidirectional tension

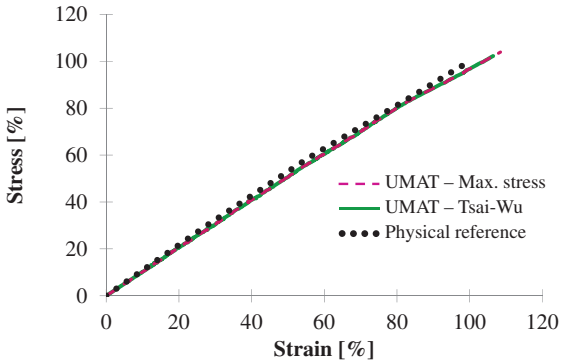

Figure 6.8: Correlation for the carbon twill-weave PREPREG composite: longitudinal multidirectional compression

6.2.2 Compressive tests on a multidirectional stacking sequence

6.2.2.1 Longitudinal compressive tests on a multidirectional stacking sequence

Fig. 6.8 shows the results for the longitudinal compression. A very good agreement is observed in terms of stiffness and nonlinearity. Both failure criteria predict a similar failure, which is also acceptable in comparison to the experimental measurements.

6.2.2.2 Diagonal compressive tests on a multidirectional stacking sequence

The results obtained for the diagonal compression are reported on Fig. 6.9. A very good agreement is obtained in terms of stiffness and nonlinearity. However, both failure criteria predict a similar but too pessimistic failure. The compressive failure of the plies having a 0° orientation is responsible for the collapse of the specimen in the simulation. The difference observed on the graph could come from the constraining effect induced by the weak and more ductile outer ±45° plies. In compression, they would tend to stabilize the specimen delaying thus the final collapse. Naturally, this assumption should be the subject of future works and investigations.

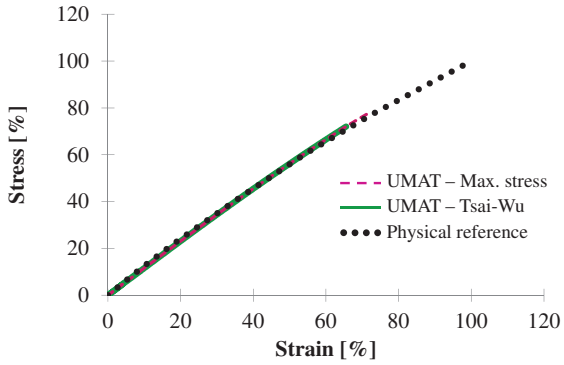

Figure 6.9: Correlation for the carbon twill-weave PREPREG composite: diagonal multidirectional compression

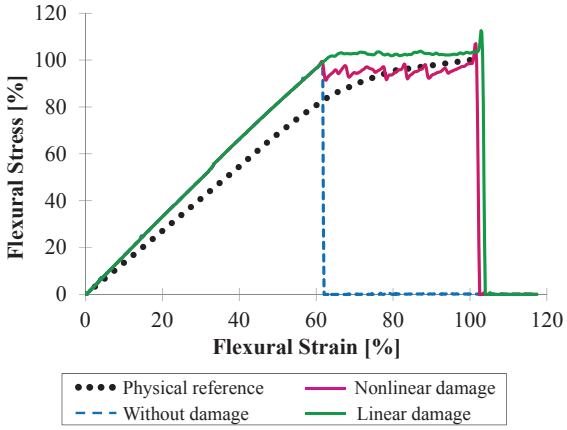

Figure 6.10: Correlation for the carbon twill-weave PREPREG composite: longitudinal multidirectional four-point bending

6.2.3 Four-point bending tests on a multidirectional stacking sequence

6.2.3.1 Longitudinal four-point bending tests on a multidirectional stacking sequence

Fig. 6.10 presents the results for the longitudinal bending on a multidirectional stacking sequence. Without using any post-failure material degradation, the progressive failure of the material cannot be predicted but the flexural stress at failure is relatively acceptable. Using similar strain at ultimate failure (in compression) as those set in the section 6.1.4, it is possible to delay the collapse of the specimen allowing to match the flexural strain at failure observed experimentally. Only both continuous post-failure material degradation models have been investigated here and they give suitable results. Finally, an acceptable but too stiff bending stiffness is predicted compared to experiments, as it has already been noticed in the section 6.1.4. The maximum stress criterion has been used here to predict failure.

6.2.3.2 Diagonal four-point bending tests on a multidirectional stacking sequence

Fig. 6.11 shows the results for the diagonal bending. Similar results are obtained using a post-failure material degradation or not, as the collapse of the specimen is here induced by delamination and failure of both upper $\pm 45°$ and $0°$ plies loaded in compression. As remarked previously, the Tsai-Wu failure criterion

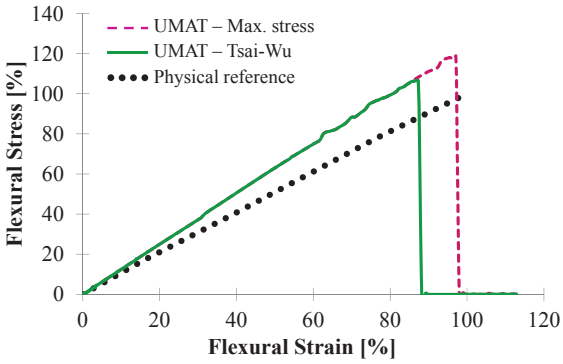

Figure 6.11: Correlation for the carbon twill-weave PREPREG composite: diagonal multidirectional four-point bending

predicts a more suitable stress at failure than the maximal stress criterion. A too stiff bending stiffness is here also predicted compared to the one captured experimentally. Except for pure diagonal bending, where all the plies have the same $\pm 45°$ orientation, the numerical model predicts a too high bending stiffness, whereas a very good agreement is obtained for the in-plane load cases. This is probably due to the particular structure of a twill-weave textile composite, leading too a unexpected weaker behavior in bending.

6.3 Impact tests on elementary plates

The basic context of such a study is similar as the one described in the section 5.3.5.1. Similar numerical models and methodologies for the identification of each damage parameters are here also used. The post-failure damage parameters set for the four-point bending tests (see the sections 6.1.4 and 6.2.3) represent the start point of the present investigation. It was necessary to lightly adapt the values of the parameters to better fit with the material responses captured by the impact tests. No deeper investigation concerning the effect of these modifications on the results for the four-point bending has been conducted. Finally, only both linear and nonlinear continuous post-failure damage models have been studied here for a mesh size of 5mm. Both shell and thick shell elements, as well as both $0°$ and $45°$ orientations have been investigated and without particular indication the $0°$ orientation is considered per default. The white line on the fringe plots represents the maximal damaged surface observed experimentally.

6.3.1 Modeling with shell elements

Fig. 6.12 presents the results for the 5J impact, a modeling with shell elements and a nonlinear post-failure damage model. A quite acceptable agreement is obtained regarding the curve of the impactor's displacement. However, the reaction force peak is about 30% over-predicted. In comparison with the RTM material, a better correlation is obtained here for the PREPREG material. The curves obtained numerically correspond very well to experimental one until the maximal displacement and force peak. At this point, a localized delamination evolves around the impacted zone and this can be hardly modeled using a unique element layer and a mesh size about 5mm. This should explain the differences observed in the quantitative analysis of the impact tests.

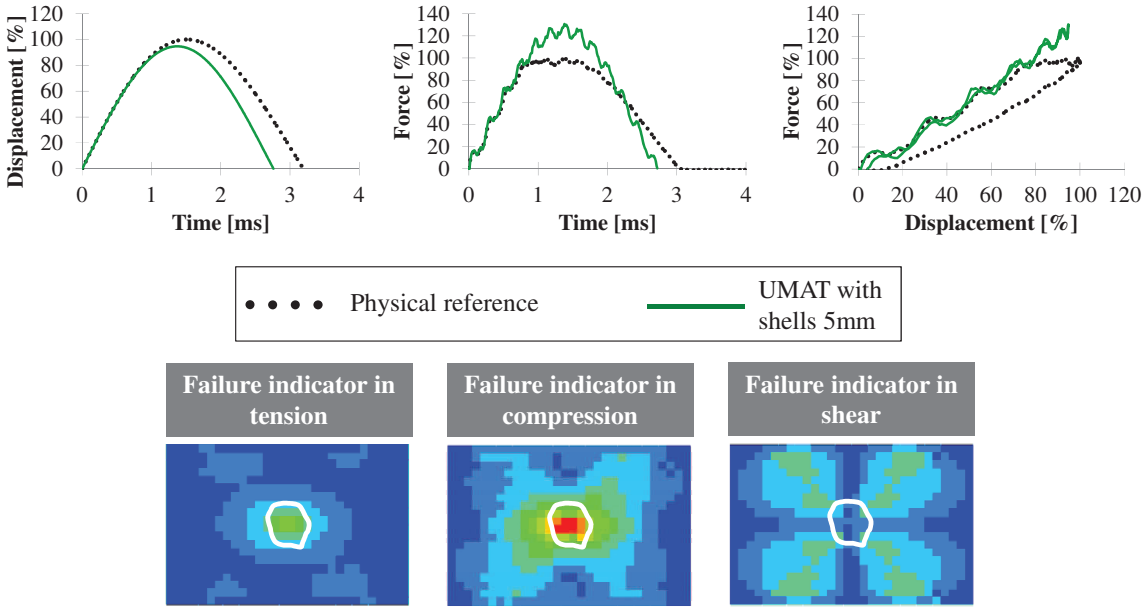

Figure 6.12: Correlation for the carbon twill-weave PREPREG composite: 5J impact and a modeling with shell elements

Regarding the predicted damaged surfaces, a larger load distribution and higher values of the failure indicators are observed compared to the RTM material. It is in good agreement with experiments, as larger damaged surfaces have been captured for the PREPREG composite. A higher compressive than tensile load distribution is observed, which is agreement with the experimental observations. As no failure and consequently no damage occurred, both linear and nonlinear post-failure damage models give similar results. A delaminated surface has been experimentally observed but no post-failure damage is predicted in the simulations. It shows the difficulty to model both damage and delamination phenomenons using a unique post-failure material degradation model. Delamination should be considered independently using a particular interface modeling between sublaminates.

Fig. 6.13 presents the results for the 25J impact and a modeling with shell elements. A comparison between both linear and nonlinear continuous post-failure damage models is also proposed. Regarding the curves of the material response and the damaged surfaces, it is clear that both damage models give similar results. An acceptable correlation is obtained for the displacement of the impactor, as the maximal value is about 10% under-estimated. The reaction force is very well predicted until 50% of the force peak. Then, the laminate underwent damage, which clearly changes the slope of the experimental curve. This damage is a sudden delamination propagation and the numerical model used here is not able to capture it. The predicted damaged surfaces show a higher but more localized damage distribution in tension than in compression. This tendency corresponds very well to the experimental observations presented on Fig. 3.39, where a diffuse damage of the material is visible on the impacted side of the plate whereas a localized damage appears on the back side. The contrary has been observed for the RTM material, where a larger damage appeared on the back side than on the impacted side of the coupon. Finally, the predicted maximal damaged surface showed by the averaged damage indicator is in good agreement with the experimental observations.

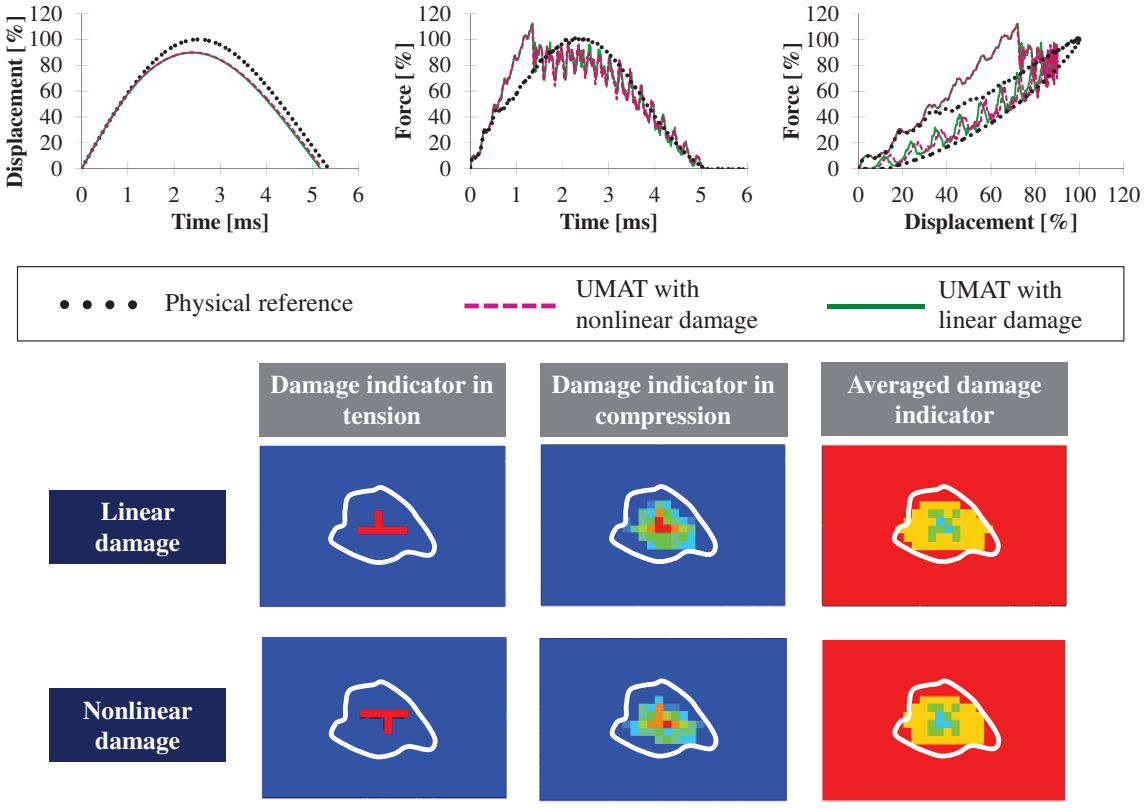

Figure 6.13: Correlation for the carbon twill-weave PREPREG composite: 25J impact and a modeling with shell elements

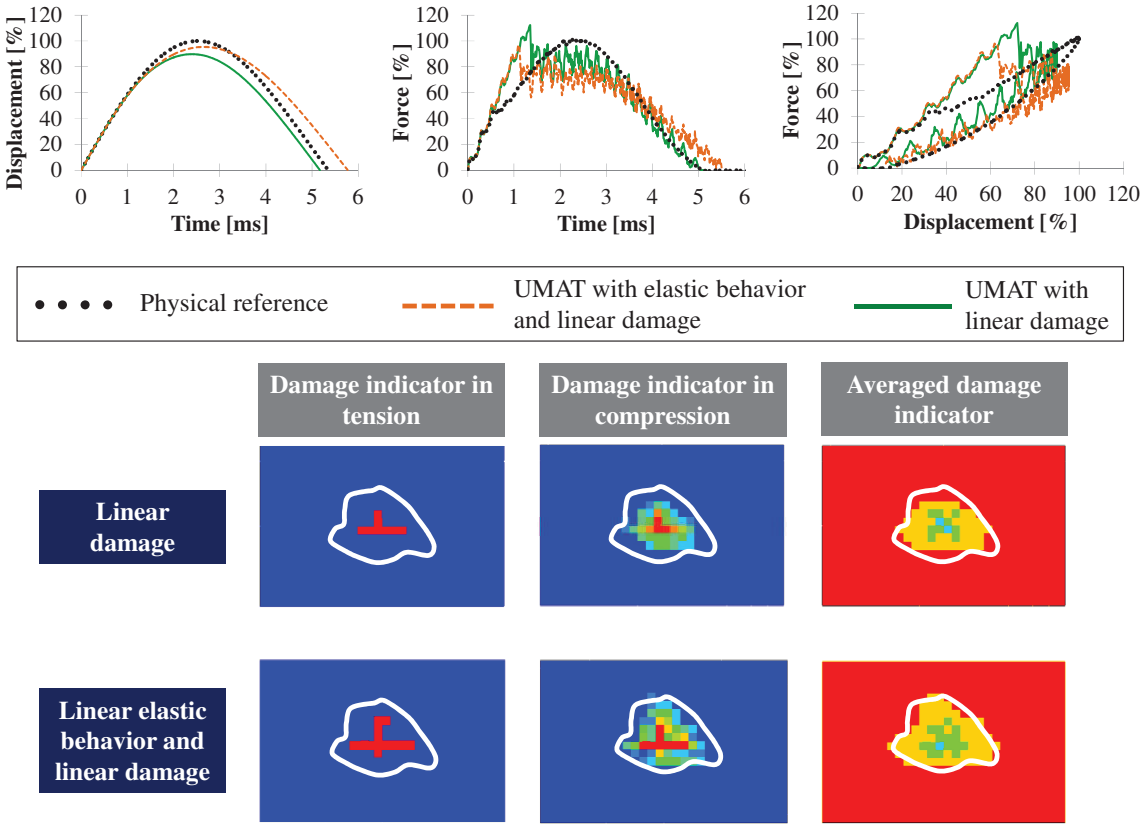

Figure 6.14: Influence of nonlinearity on the correlation for the carbon twill-weave PREPREG composite: 25J impact, a modeling with shell elements and of a linear elastic behavior

Fig. 6.14 presents the results obtained for a 25J impact, when a linear elastic behavior is defined for the longitudinal and transverse in-plane directions. They are compared with the predictions involving a nonlinear pre-failure behavior. A mesh size of 5mm and a linear post-failure damage are used for this comparison. The nonlinear behavior in tension and compression has been replaced by a common linear behavior having the same initial stiffness, the same strengths and the same strains at failure. Regarding the material response, the modeling using a linear behavior predicts a premature failure of the material, leading to a too low reaction force level. A higher displacement of the impactor is captured for the linear elastic material behavior, probably caused by the premature beginning of the post-failure damage propagation reducing considerably the stiffness of the composite plate. It implies that the damaged areas predicted with the linear elastic modeling are larger than those obtained with the nonlinear plastic modeling, but a good agreement is observed with the experimental observations. Finally, a better compromise is obtained using a modeling involving a nonlinear plastic pre-failure behavior.

Fig. 6.15 presents the results of the 50J impact and a modeling with shell elements for both linear and nonlinear continuous post-failure damage models. Similarly as for the 25J impact, both damage models give similar results regarding the material response and the damaged zones. A very good agreement is obtained for the displacement of the impactor. A good correlation is observed for the prediction of the reaction force over the time. The light difference comes from the change of the slope about 40% of the maximal force peak, due to a sudden delamination propagation. The predicted damaged surfaces show a higher but more localized damage distribution in tension than in compression, which corresponds very well

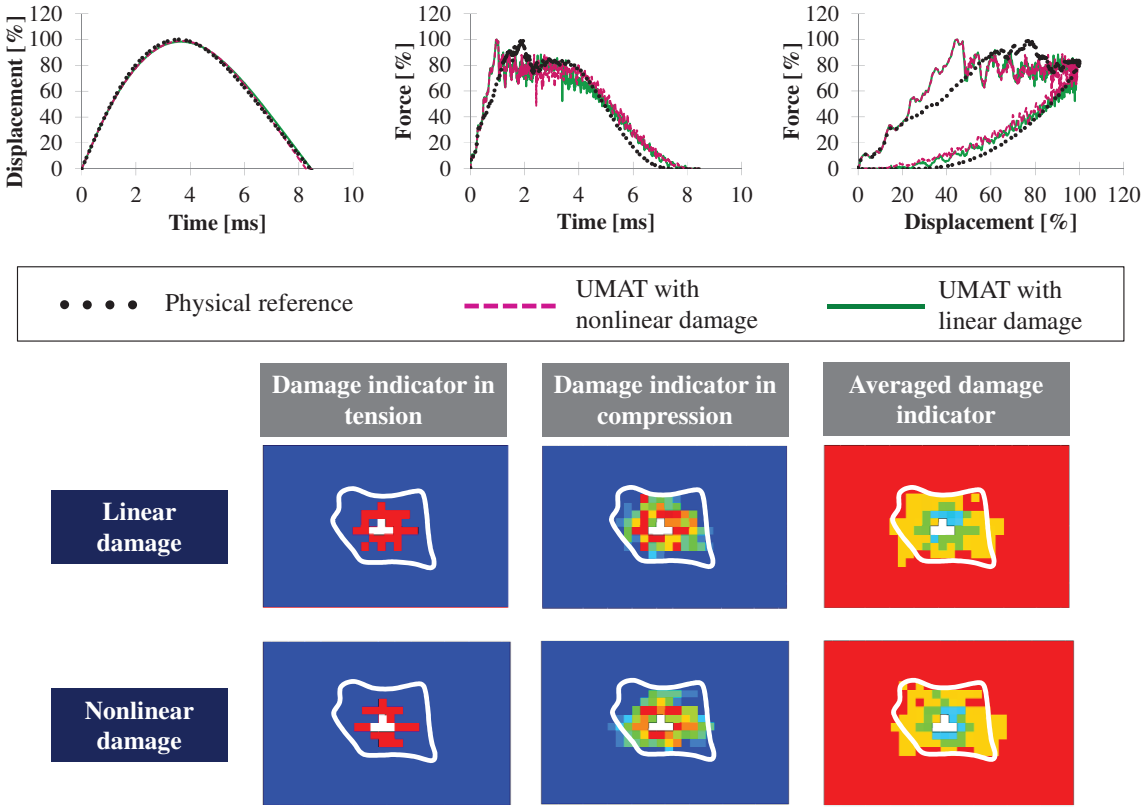

Figure 6.15: Correlation for the carbon twill-weave PREPREG composite: 50J impact and a modeling with shell elements

to the experimental observations presented on Fig. 3.40, where a diffuse damage of the material is visible on the impacted side of the plate whereas a localized damage appears on the back side. The element deletion occurring in the simulations corresponds to the quite perforated plates observed experimentally for a 50J impact. Finally, the predicted maximal damaged surface over the specimen referring to the averaged damage indicator is in good agreement with the experimental observations.

Fig. 6.16 presents an overview of the results for the three impact energies, both continuous post-failure damage models and the 45° orientation. As no failure and no damage are predicted for the 5J impact, both damage evolution laws give similar predictions and only the results obtained by using the nonlinear damage model are reported. As already noticed, too stiff numerical results are obtained for the 5J impact as the modeling with a unique element layer and a mesh size about 5mm does not allow to capture the very localized phenomenon occurring for such low impact energy. For both 25J and 50J impacts, the change of the slope at 40% of the maximal force peak, due to a sudden delamination propagation, is not numerically predicted, which explains the non-optimal agreement with the experimental results. Finally, the maximal damage surfaces represented by the fringe plots of the averaged damage indicator show an acceptable agreement with experiments. The load distribution for the 5J is here not reported, as the results were similar as those already presented on Fig. 6.12

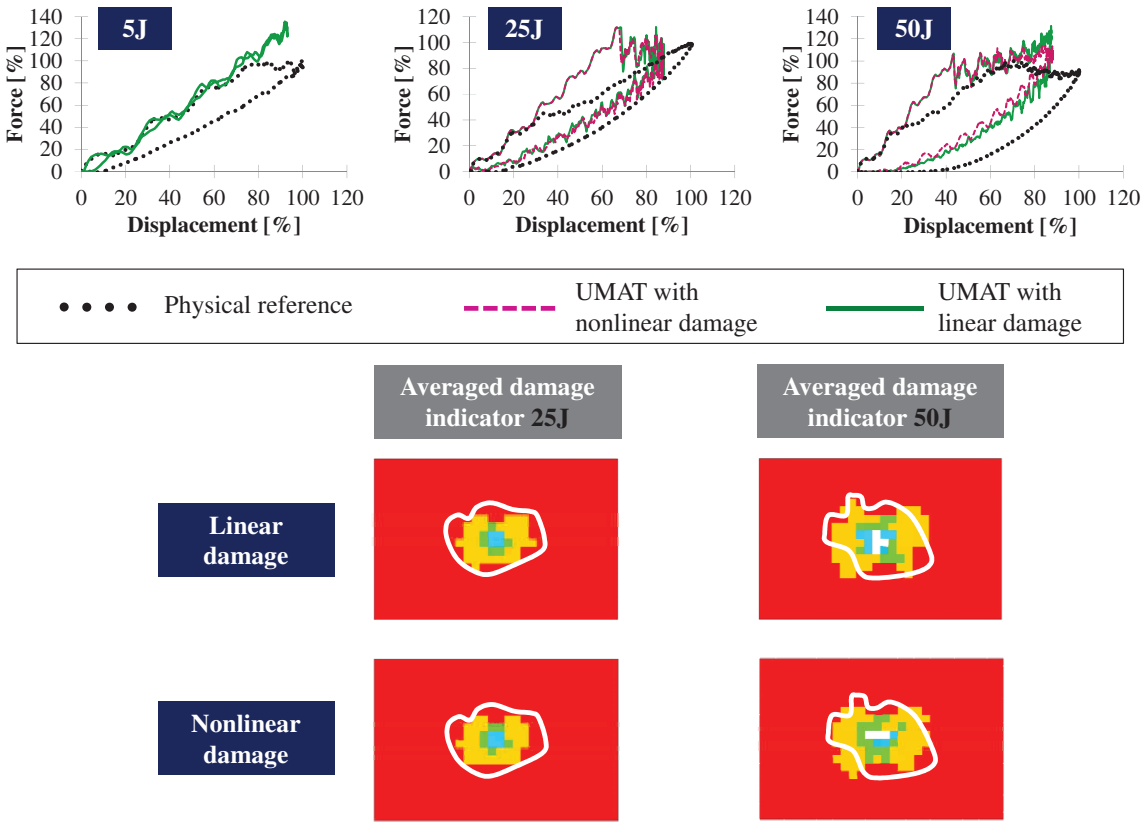

Figure 6.16: Correlation for the carbon twill-weave PREPREG composite: overview of the 5J, 25J and 50J impacts for the 45° orientation and a modeling with shell elements

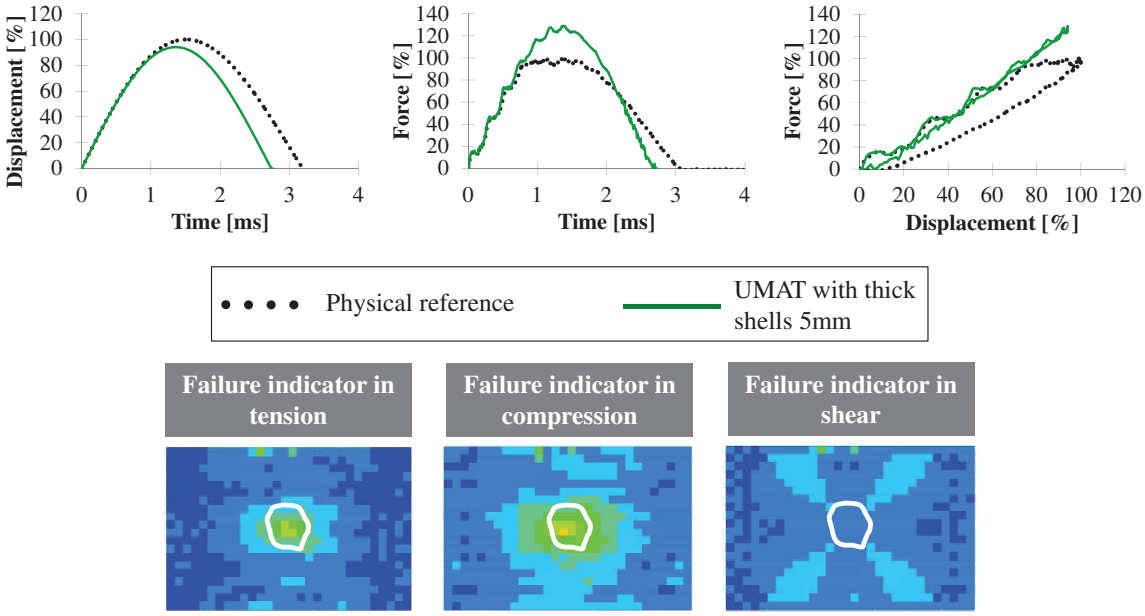

Figure 6.17: Correlation for the carbon twill-weave PREPREG composite: 5J impact and a modeling with thick shell elements

6.3.2 Modeling with thick shell elements

Fig. 6.17 presents the results for the 5J impact, a modeling with thick shell elements and the nonlinear post-failure damage model. Similar remarks as for shell elements can be made regarding the quantitative analysis of the material response. A higher compressive than tensile load distribution is observed, which is in agreement with experimental observations. As no failure occurred and as no damage has been involved, both linear and nonlinear post-failure damage models give similar results.

Fig. 6.18 presents the results for the 25J impact and a modeling with thick shell elements. Both damage models give similar results in terms of material response and damaged surfaces. Moreover, the use of thick shell elements does not have here a high effect on the quantitative analysis of the impact tests. A higher difference between both element types has been observed for the RTM material. Consequently, it seems that the RTM material is more sensitive to 3D stress state than the PREPREG material. This could be explained by the fact that the PREPREG composite studied here seems to delaminate easier than the RTM material. The delamination propagation reduces the effects of damage, cracks distribution and material degradation though the thickness. This could justify the lower effect of the use of thick shell elements for the impact on the PREPREG composite. However, the cross-shape of the damaged zones predicted using thick shell elements is not acceptable, as it has already been remarked for the RTM material.

Fig. 6.19 presents the results for the 50J impact and a modeling with thick shell elements. Both damage models give similar results and only the averaged damage indicator is reported for the evaluation of the damaged surfaces. A similar good correlation as using shell elements is observed concerning the quantitative analysis of the material response. The cross-shape of the damaged zones given by a modeling with thick shell elements is not suitable, even if the maximal damaged zones observed experimentally meet the extremities of the cross branches.

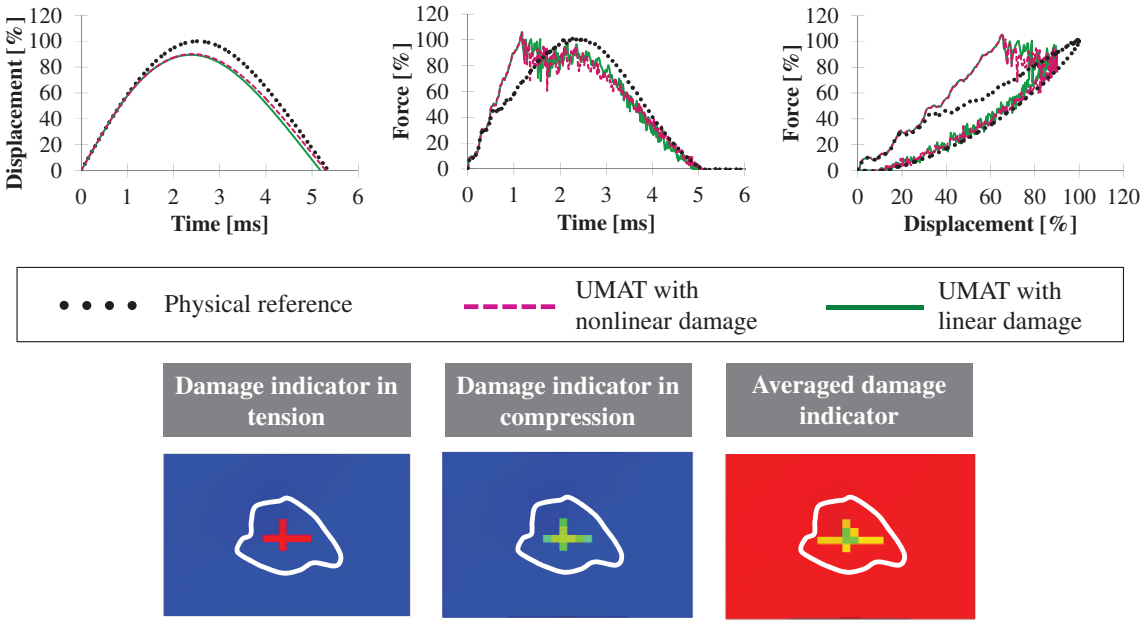

Figure 6.18: Correlation for the carbon twill-weave PREPREG composite: 25J impact and a modeling with thick shell elements

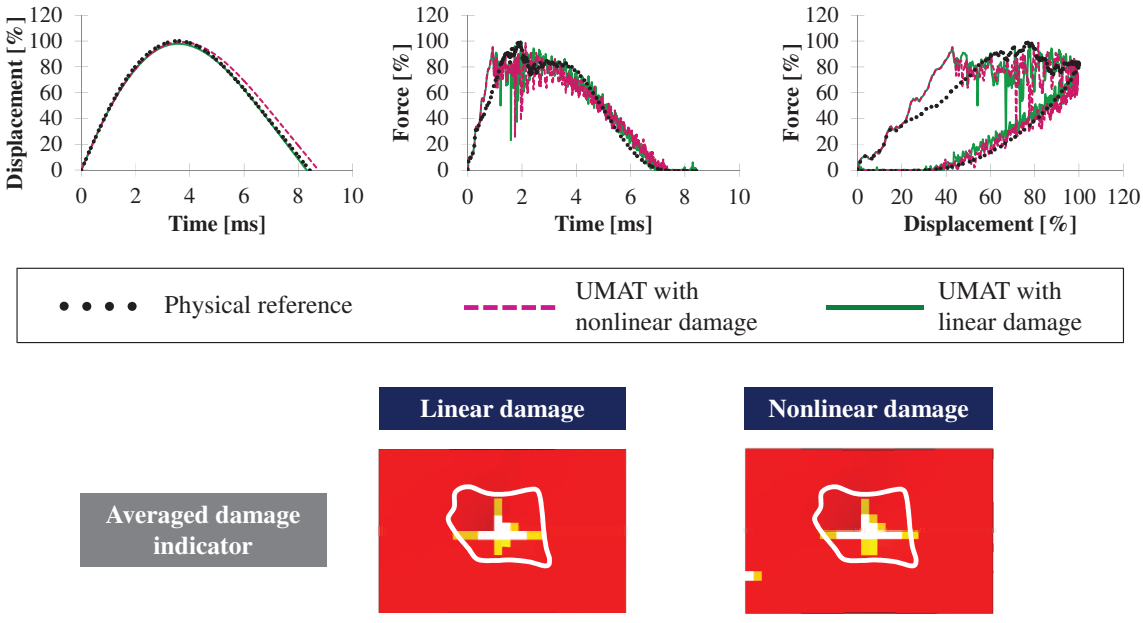

Figure 6.19: Correlation for the carbon twill-weave PREPREG composite: 50J impact and a modeling with thick shell elements

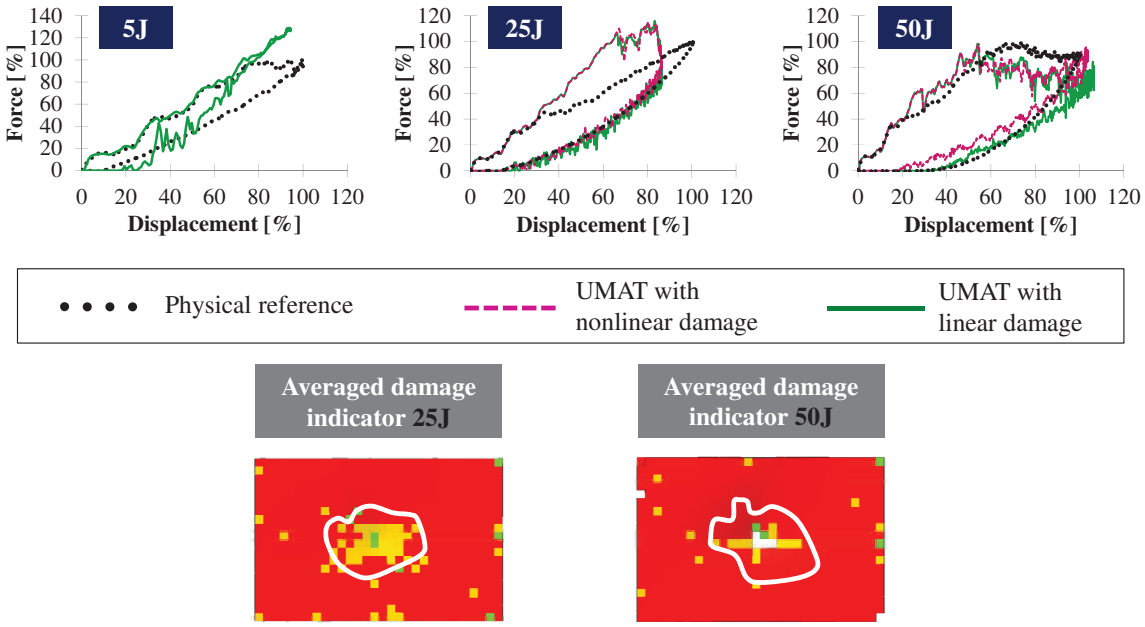

Figure 6.20: Correlation for the carbon twill-weave PREPREG composite: overview of the 5J, 25J and 50J impacts for the 45° orientation and a modeling with thick shell elements

Fig. 6.20 presents an overview of the results for the three impact energies, a modeling with thick shell elements, both continuous post-failure damage models and the 45° orientation. As no failure and no damage is predicted for the 5J impact, both damage evolution laws give similar predictions and only the results obtained by using the nonlinear damage model are reported. Regarding the curves of the material responses, a better agreement is observed than for a modeling with shell elements, particularly due to a better prediction of the maximal impactor's displacement. An acceptable predicted damaged zone is observed for the 25J impact but not for the 50J energy. Finally, some numerical instabilities appearing using thick shell elements (and the LS-DYNA R5 release) are clearly visible, as some elements underwent a kind of a random distributed unexpected damage away from the impacted zone. The *BOUNDARY_NON_REFLECTING keyword has been used in order to reduce the artificial stress wave reflections, that can be generated at the boundaries of the model and, that are likely to reenter the model and contaminating the results. Unfortunately, it did not considerably improve the results and a more recent LS-DYNA release should be tested. The load distribution for the 5J is here not reported, as the results are close to those presented on Fig. 6.17.

6.4 Drop tower tests on hat-profiles

This section presents the numerical results and their correlation for the drop tower tests on 2mm and 4mm thick PREPREG hat-profiles. The experimental results have been described in the section 3.3.3. The simulations have been conducted with under-integrated shell elements. Due to too much numerical instability, no numerical result obtained using a modeling with thick shell elements is reported. Once the hat-profile failed, a quite constant force level is experimentally observed corresponding in a large part to the material response of the steel plate and to the friction at the fracture plane. For this reason, all

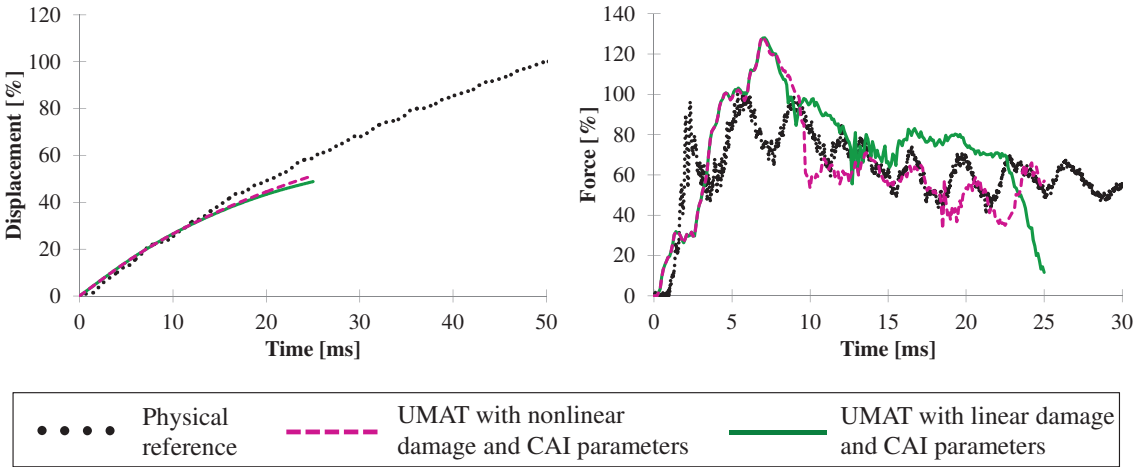

Figure 6.21: Correlation for the carbon twill-weave 2mm thick PREPREG hat-profiles: 100J impact, comparison between the linear and nonlinear post-failure damages using the previous validated material parameters

simulations have been stopped after 25ms.

6.4.1 Drop tower tests on 2mm thick hat-profiles

This section presents the numerical results and their correlation for the 100J impact on 2mm thick hat-profiles having a unidirectional stacking sequence. Experimental results have been described in the section 3.3.3.1.

Fig. 6.21 presents the results for the linear and nonlinear post-failure damage models, based on the material parameters set for the impact tests on elementary plates (C.A.I). An acceptable agreement is observed for the displacement of the impactor. Regarding the reaction force, a unique peak is predicted, whereas three force peaks have been experimentally observed. Moreover, the numerical results show a too high maximal force peak. A good correlation is observed concerning the post-failure behavior (quite constant force level after the force peak), particularly for the nonlinear material degradation. The failure and damage distributions over the hat-profile for the linear post-failure material degradation are presented on Fig. 6.22. The failure indicators show a larger distribution of the compressive loads than of the tensile loads. The localized element erosion is in agreement with the experimental observations. The damage indicators show a localized distribution of post-failure damage around the impacted zone. As no C-SCAN analysis is available for these impact tests, it is difficult to assess the accuracy of these fringe plots. Nevertheless, the maximal damaged zone represented by the averaged damage indicator seems to be relatively plausible.

Fig. 6.23 presents the failure and damage distributions over the hat-profile for the nonlinear post-failure material degradation. Similarly as the linear damage, a larger distribution of the compressive loads than of the tensile loads is observed. Moreover, a larger element erosion occurred for the nonlinear post-failure material degradation, which is responsible for the lower post-failure stress level observed on the curve of the reaction force. Finally, the maximal damaged zone represented by the averaged damage indicator seems to be suitable but a lower element erosion would be preferable.

The previous results show an over-estimation of the force peak about 30%. It has been found that a

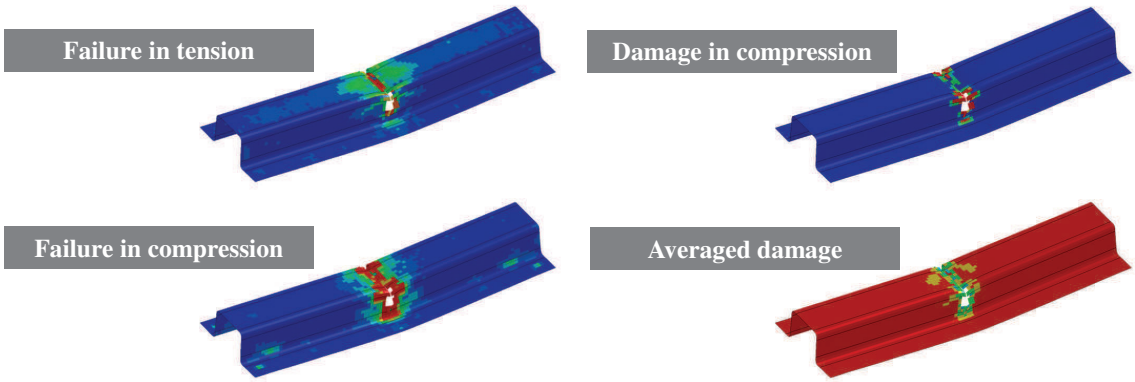

Figure 6.22: Failure and damage distribution for the 100J impact on 2mm thick PREPREG hat-profiles and a linear post-failure damage model

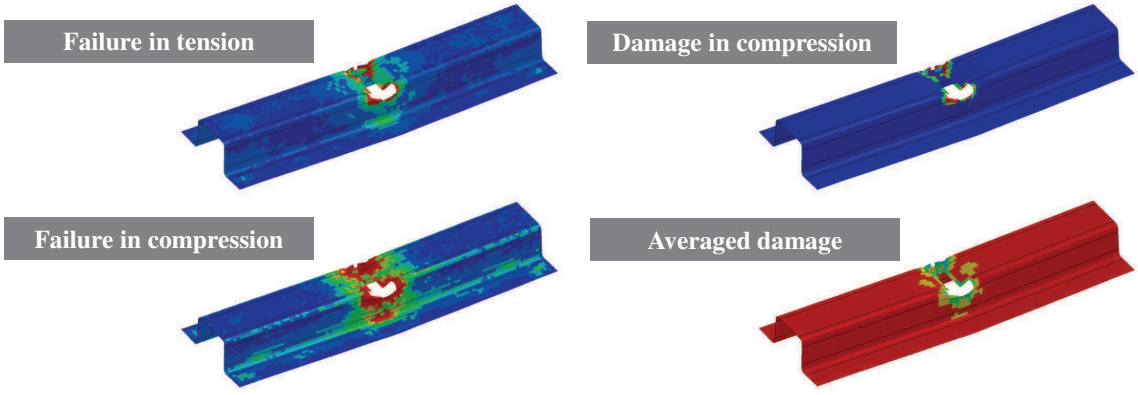

Figure 6.23: Failure and damage distribution for the 100J impact on 2mm thick PREPREG hat-profiles and a nonlinear post-failure damage model

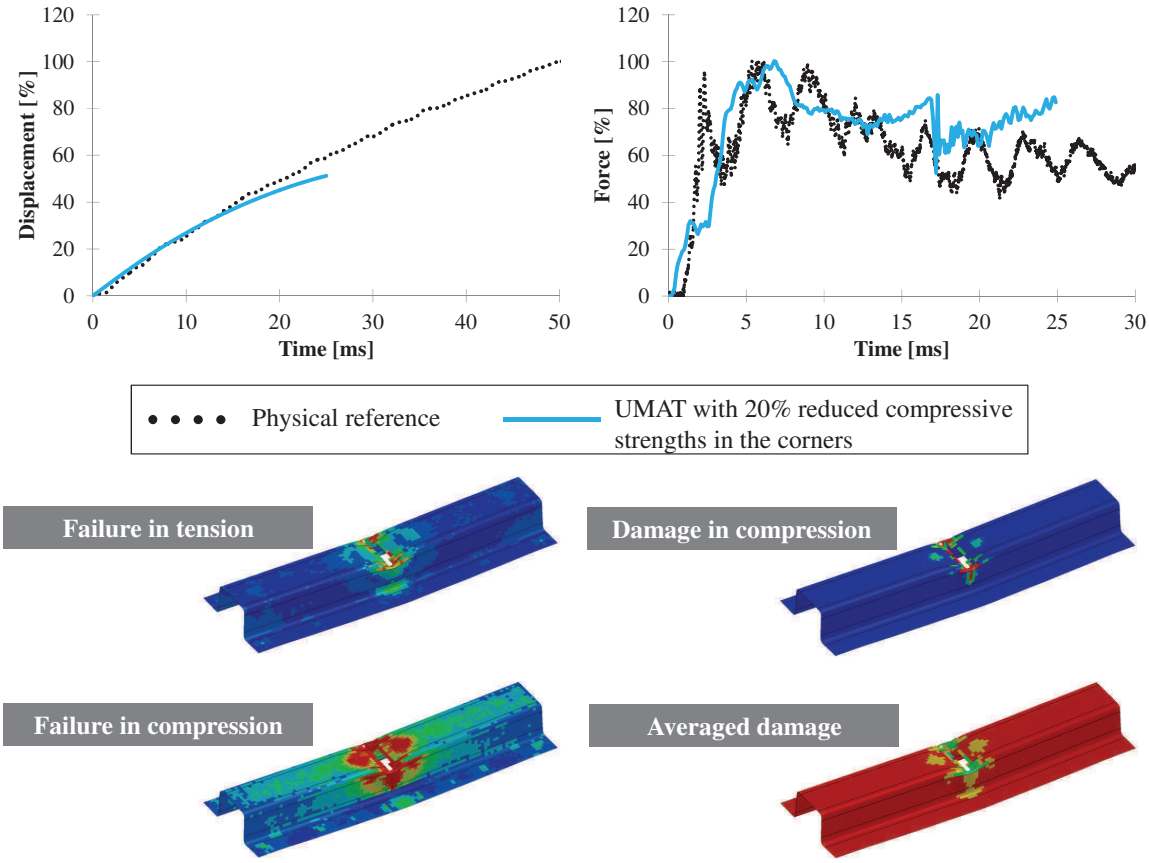

Figure 6.24: Correlation for the carbon twill-weave 2mm thick PREPREG hat-profiles: 100J impact, the linear post-failure damage using the previous validated material parameters and a 25% reduction of the compressive strength in the corners

reduction about 25% of the compressive strength in the corners of the hat-profile tends to improve the material response, as presented on Fig. 6.24. This reduction can be justified by the fact that a resin rich region has been observed in the corners of the hat-profile, due to the manufacturing process. It is naturally difficult to determine accurately the real value of the strength at this place, but such a relatively law reduction should be acceptable. A good correlation is observed regarding both curves and adequate failure and damage distributions are predicted (see Fig. 6.24). Moreover, element erosion is concentrated on the top flat surface of the specimen and the averaged damage indicator shows a damage propagation on the vertical sides of the hat-profile, which corresponds very well to the experimental observations. Finally, the reduction of the compressive strength in the corners (the other material parameters being unchanged) allowed to improve the agreement with experimental results regarding the maximal force peak. Suitable results are obtained regarding the failure and damage distributions. Results close to those reported here are also obtained for the nonlinear damage evolution law.

In order to improve the predictions concerning the impacts on RTM hat-profiles, some updates of the material parameters have been made. Indeed, the previous validated material parameters including the reduction of the compressive strength are kept in the corners of the hat-profile. On the flat side of the specimen, the strains at failure ε_f material parameters are set to high values defining thus a long post-failure material degradation. An effective strain failure criterion is then used (*MAT_ADD_EROSION

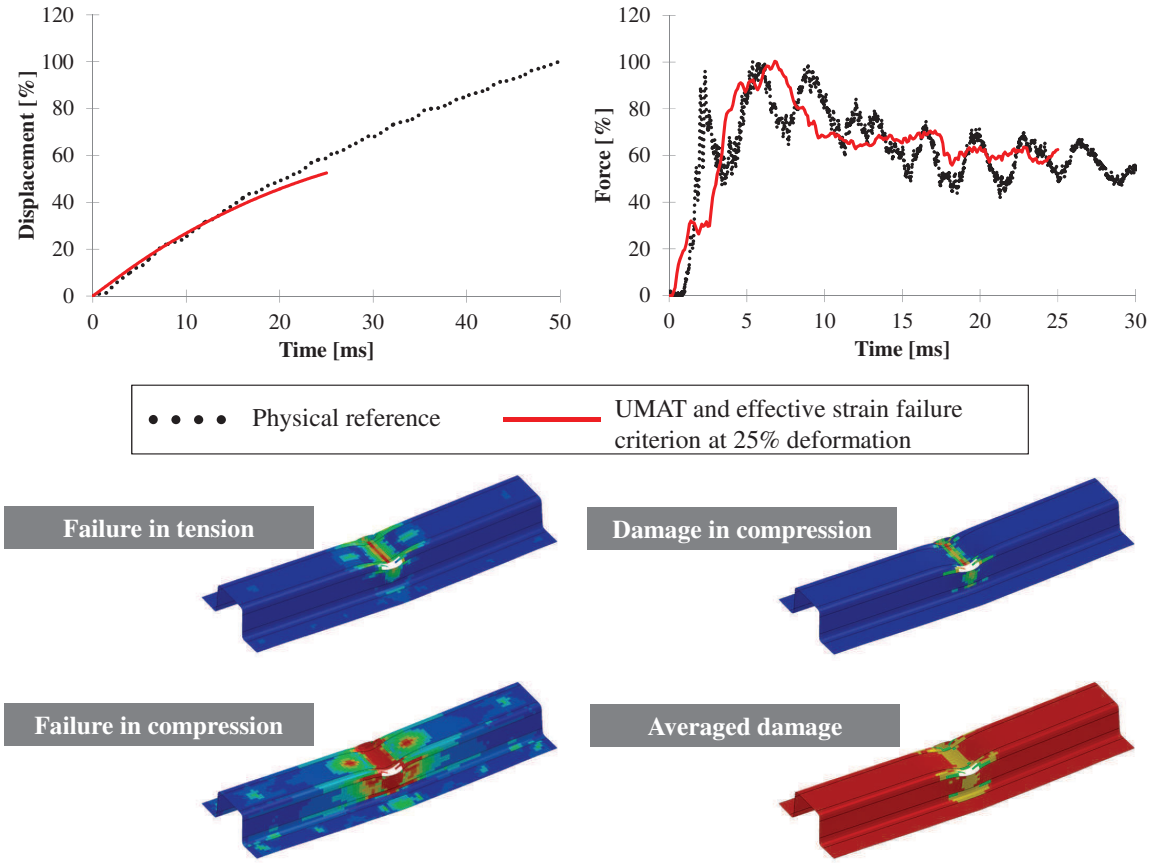

Figure 6.25: Correlation for the carbon twill-weave 2mm thick PREPREG hat-profiles: updated strains at ultimate failure

keyword) to avoid too large element deformations, that are likely to be nonphysical and to increase dramatically the computing time. The deletion of element occurs when an effective strain about 25% in the element is detected. The results corresponding to such a modeling are presented on Fig. 6.25. An acceptable correlation is obtained for the material response, as shown by both graphs. Failure in tension is localized following a line on the top flat side of the specimen, which is acceptable. Failure and damage in compression are distributed around the impacted zone and on the vertical sides of the hat-profiles. The maximal damaged zone represented by the averaged damage indicator seems to be acceptable. Element erosion is localized only in the corners of the specimen, as large post-failure damage and deformations are authorized on the flat side. Similar results are obtained for both continuous post-failure damage models.

6.4.2 Drop tower tests on 4mm thick hat-profiles

6.4.2.1 Impact energy of 350J

This section presents the numerical results and their correlation for the 350J impact on 4mm thick hat-profiles having a unidirectional stacking sequence. Experimental results have been described in the section 3.3.3.2.

Fig. 6.26 presents the results for the linear and nonlinear post-failure damage models, based on the

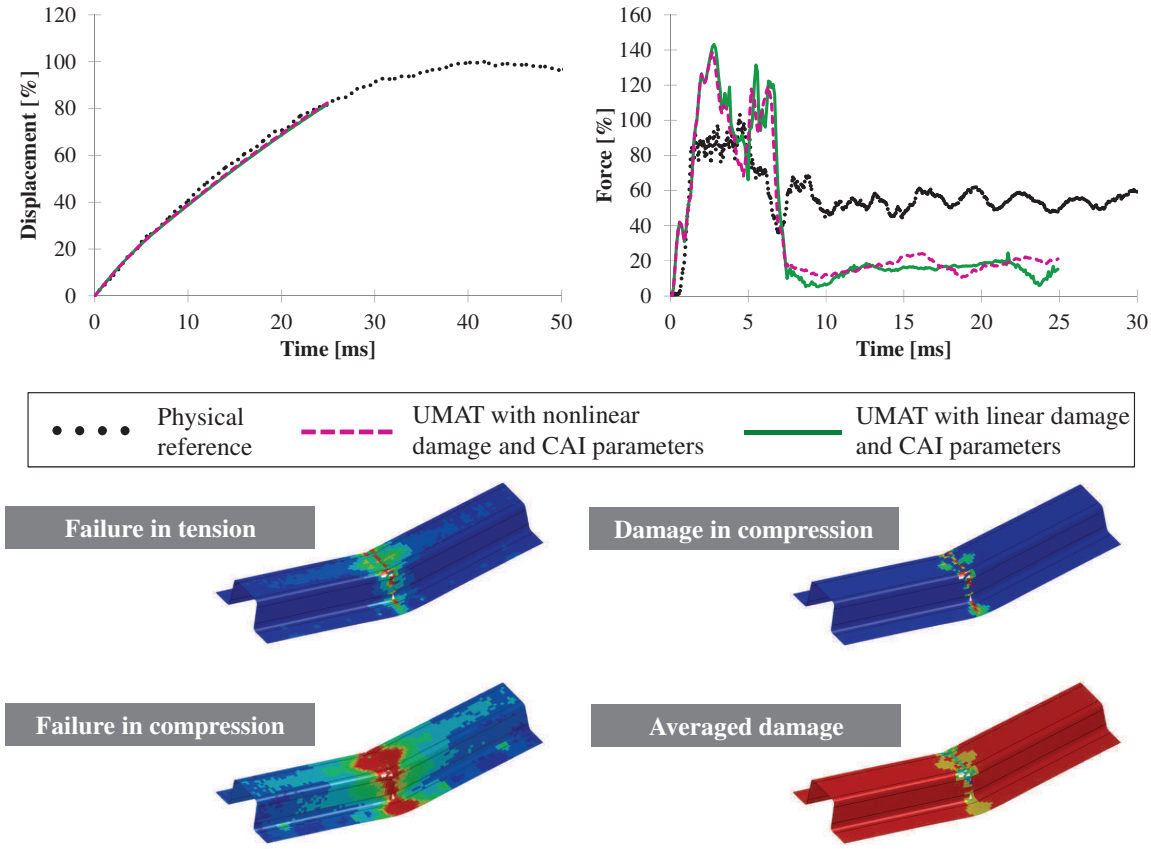

Figure 6.26: Correlation for the carbon twill-weave 4mm thick PREPREG hat-profiles: 350J impact, comparison between the linear and nonlinear post-failure damages using the previous validated material parameters

material parameters set for the impact tests on elementary plates (C.A.I). An acceptable agreement is observed for the displacement of the impactor but too high force peaks are predicted. The sudden fall in the force is caused by a localized element deletion below the impacting mass. As both post-failure damage models gave similar results, only the fringe plots concerning the linear damage are presented. They show that the elements are deleted following a line over the width of the hat-profile. Such a failure is also observed experimentally but it implies a huge loss of reaction force in the simulations, as the fragmentation of the material and the friction between both sides of the hat-profiles are not modeled. The failure indicators show a larger distribution of the compressive loads than of the tensile loads, which seems to be realistic due to the low value of the compressive strength. The damage indicators show a localized distribution of post-failure damage around the impacted zone. As no C-SCAN analysis is available for these impact tests, it is difficult to assess the accuracy of these fringe plots. Nevertheless, the maximal damaged zone represented by the averaged damage indicator seems to be relatively plausible.

The previous results show an over-estimation of the force peak about 40%. Similarly to the 2mm thick hat-profiles, it has been found here that a reduction about 50% of the compressive strength in the corners of the hat-profile tends to improve the material response, as presented on Fig. 6.27. In addition to the consideration of resin rich region in the corners, the considerable thickness of the material and the

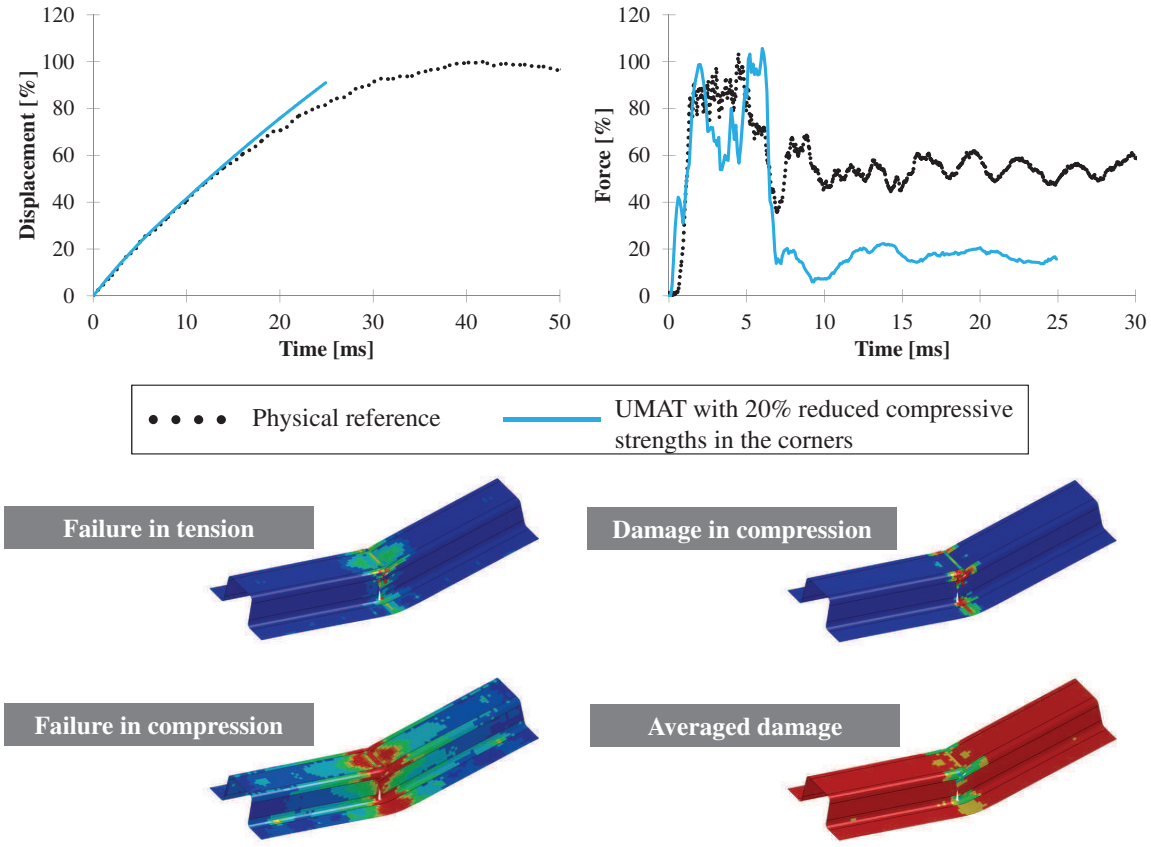

Figure 6.27: Correlation for the carbon twill-weave 4mm thick PREPREG hat-profiles: 350J impact, the linear post-failure damage using the previous validated material parameters and a 50% reduction of the compressive strength in the corners

low radius of the corners increase the risk to suffer from high stress concentrations there. Coupling these potential stress concentrations to the relatively high ply-thickness, premature delamination is likely to happen at these places. It contributes to explain the necessity to reduce considerably the compressive strength in the corners to reach an acceptable force peak. A good correlation is obtained regarding the displacement of the impactor and the maximal force peak but the post-failure material response is not acceptable due to the deletion of elements following a line over the width of the hat-profile. The localization of damage only in the corners is not optimal, as damage should be distributed in the flat sides of the specimen too.

As described previously for the 2mm thick hat-profiles, a modeling involving an effective strain failure criterion has been investigated. Additionally to the reduced compressive strength, the material parameters validated for the impacts on elementary plates are used in the corners. A large post-failure behavior is defined for the flat side of the specimen and an element is deleted, when it undergoes an effective strain about 25%. The numerical results obtained for such a modeling are presented on Fig. 6.28. As both continuous damages gave similar results, only those concerning the linear post-failure material degradation are shown. A good agreement is observed for the reaction force but a too low displacement of the impactor has been captured. The deletion of elements is concentrated in the corners, whereas a collapse of the material should be expected also on the flat sides. This is due to the use of a large value for the effective

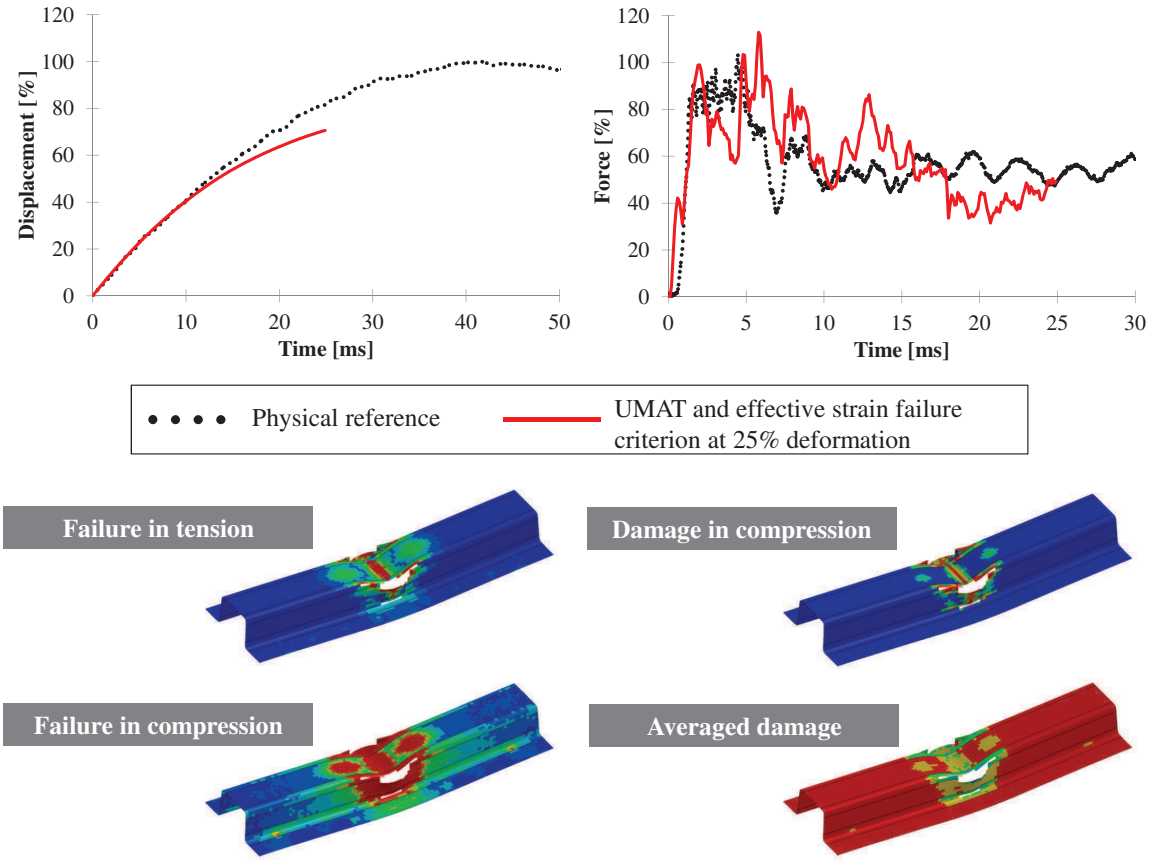

Figure 6.28: Correlation for the carbon twill-weave 4mm thick PREPREG hat-profiles: updated strains at ultimate failure for the 350J impact

strain criterion. Indeed, the elements in the corners are subjected to large deformation, which is not the case for the elements on the flat sides. However, the deletion of elements is replaced by high damage levels at these places. The tensile loads are well localized around the impacted zone and following a transversal line on the top flat side of the hat-profile. A larger distribution of the compressive failure is observed around the impacted area. The compressive damage indicator shows an acceptable localization of the damage in compression on the top and vertical sides of the specimen. Finally, the maximal damaged zone represented by the averaged damage indicator seems to be relatively plausible.

6.4.2.2 Impact energy of 500J

This section presents the numerical results and their correlation for the 500J impact on 4mm thick hat-profiles having a multidirectional stacking sequence. Experimental results have been described in the section 3.3.3.2.

Fig. 6.29 presents the results for the linear and nonlinear post-failure damage models, based on the material parameters set for the impact tests on elementary plates (C.A.I). Similarly to the 350J energy of impact, an acceptable agreement is observed for the displacement of the impactor but too high force peaks are predicted. The sudden fall in the force is still here caused by the element deletion following a line over the width of the hat-profile. As both post-failure damage models gave similar results, only the fringe plots concerning the linear damage are presented. A similar distribution of the failure and damage

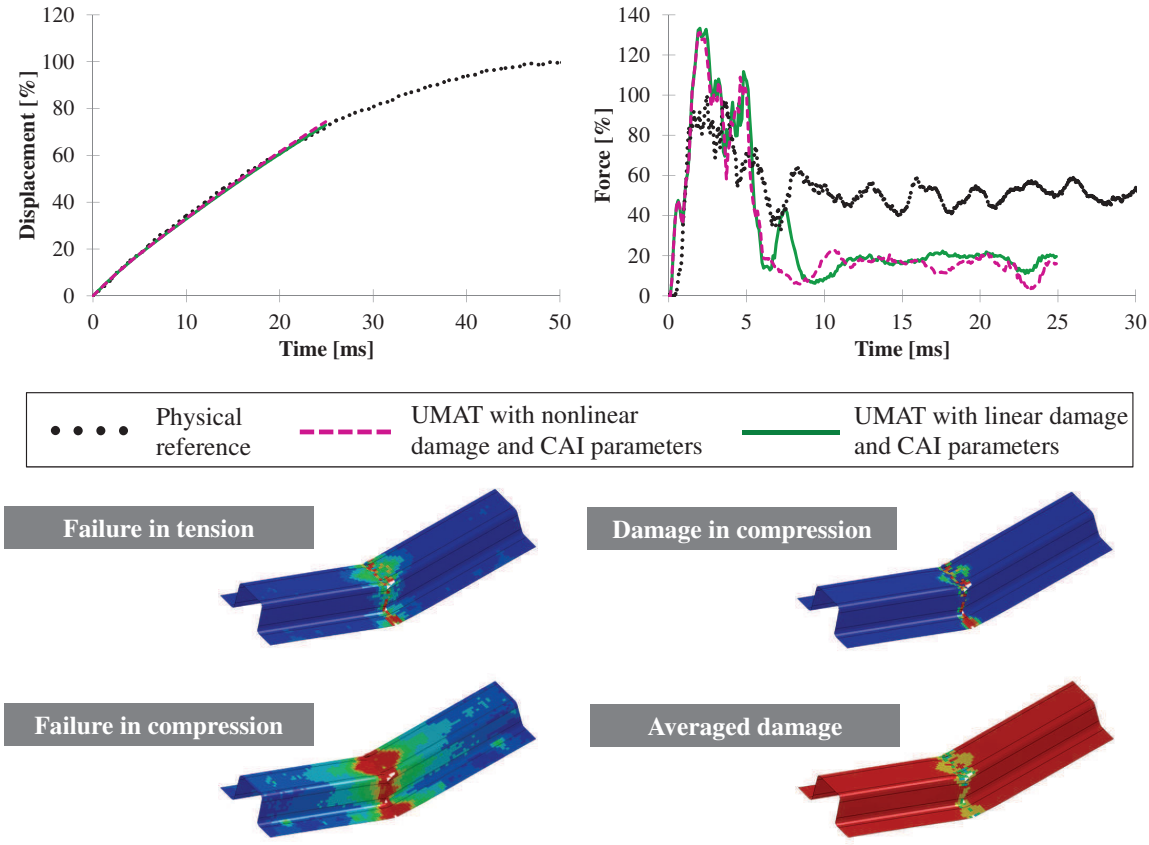

Figure 6.29: Correlation for the carbon twill-weave 4mm thick PREPREG hat-profiles: 500J impact, comparison between the linear and nonlinear post-failure damages using the previous validated material parameters

indicators as for the 350J drop tower tests is observed. It is due to the element deletion that annihilates the damage propagation, as the hat-profile lost its integrity. An assessment of the maximal damaged zone represented by the averaged damage indicator is here unfortunately very difficult. However, regarding the width of the collapse observed in experiments, it seems that the maximal damaged zone represented by the averaged damage indicator is here too concentrated around the impacted zone. Similarly to the 350J impact energy, a reduction about 50% of the compressive strength in the corners has been investigated. It allows to obtain a better correlation regarding the maximal force peak. Similar conclusions and remarks as for the 350J impact are also valid here.

The modeling using the effective strain failure criterion has been also investigated here. The set of material parameters is similar as the one described previously and element deletion occurs, when an element undergoes an effective strain about 25%. The results for the nonlinear post-failure damage are presented on Fig. 6.30. Similarly to the 350J impact energy, a good agreement is observed for the reaction force but a too low displacement of the impactor has been captured. A large deletion of elements occurred, which is in a relative good agreement with the width of the damaged zone observed experimentally (see Fig. 3.45). Due to the considerable element deletion, the analysis of each failure or damage indicator is not judicious, that is why only the maximal damaged areas represented by the averaged damage indicator are showed here. Finally, the distribution of damage around the impacted zone seems to be plausible.

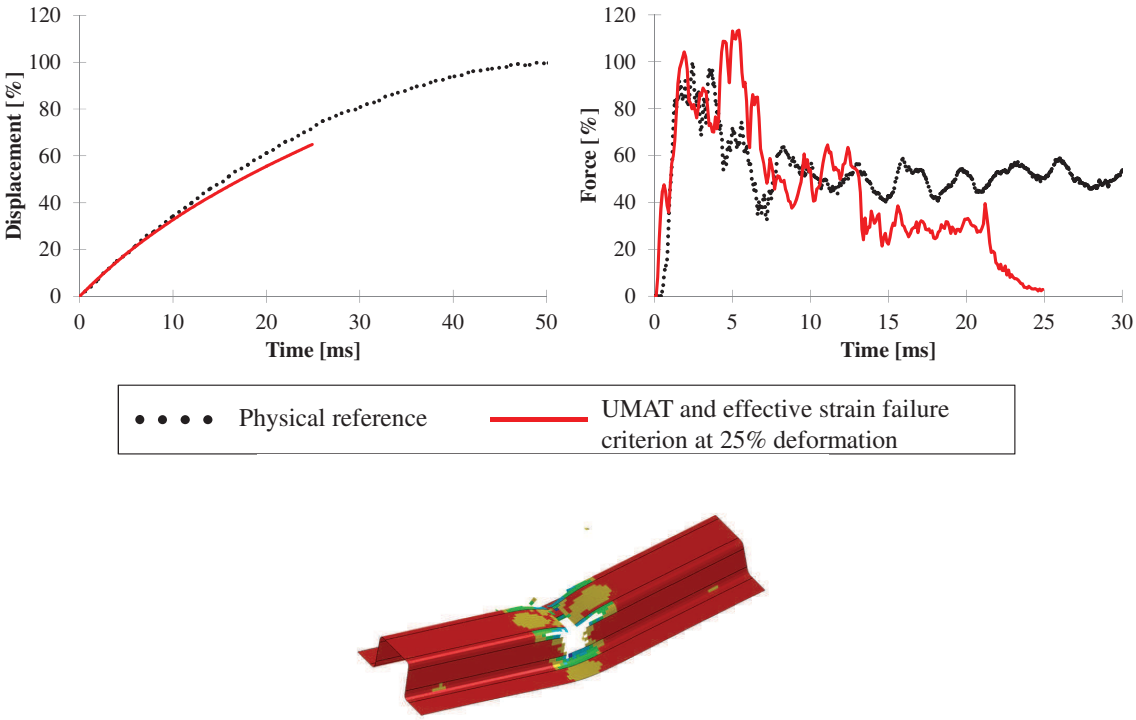

Figure 6.30: Correlation for the carbon twill-weave 4mm thick PREPREG hat-profiles: updated ultimate strains at failure for the 500J impact

6.5 Partial conclusions and outlooks

The previous sections presented the comparison between numerical and experimental results for a T700 twill-weave PREPREG composite. Models built up with shell and thick shell elements have been used in association with the developed UMAT to conduct the simulations of the different experimental tests. A very good correlation is obtained regarding the in-plane unidirectional quasi-static tensile and compressive load cases. The unidirectional longitudinal four-point bending showed generally a light too stiff behavior and the use of post-failure material degradation has been tested to match the strain at failure observed experimentally. On the contrary, the predictions for the unidirectional diagonal bending are acceptable. In the case of a multidirectional stacking sequence, a very good agreement has been obtained in term of stiffness for all in-plane tests. The Tsai-Wu failure criterion gave better predictions of failure than the maximal stress criterion. A kind of constraining or stabilizing effect of the outer 45° woven plies has been observed for the multidirectional diagonal compression, as the numerical model predict a too premature failure compared to experimental results. A too high bending stiffness has been also predicted for bending loads on a multidirectional stacking sequence. The use of the post-failure damage models offered a better correlation in term of nonlinearity and maximal deformation at failure for the multidirectional longitudinal bending. Similar results have been obtained using thick shell elements for the in-plane load cases but a lightly higher bending stiffness has been predicted compared to a modeling with shell elements. Regarding failure, both element types gave similar results, as only 2D failure criteria have been used.

The simulations of the 5J impact showed a too stiff behavior compared to experimental observations. Regarding the displacement of the impactor, the predictions were quite acceptable. However, the reaction

force peak was about 30% over-predicted. Acceptable load distributions, assessed using the analysis of failure indicators, have been observed. The simulations of the 25J impact showed an acceptable correlation. Regarding the reaction force, the change of slope observed about 50% of the force peak could not be numerically captured. It is caused by a sudden delamination propagation in the material that is difficult to model using a unique element layer. It tends to confirm that delamination has to be explicitly modeled using some interface models, as the use of post-failure material degradation seems to be not sufficient to consider this particular material damage. Acceptable damaged surfaces were despite predicted analyzing the fringe plots of the different damage indicators. Similar observations could be made concerning the simulations of the 50J impact. For this energy, a very good agreement has been observed regarding the displacement of the impactor. Finally, similar results concerning the material response have been obtained using both shell and thick shell elements and a mesh size about 5mm, except considering the 45° orientation, where thick shell elements gave a better correlation. Similarly to the simulations made for the RTM composite, the cross-shape of the damaged zones predicted by thick shells elements was still not yet acceptable. It should rely on the intern element formulation and not on the UMAT implementation.

The simulations of the drop tower tests on 2mm thick PREPREG hat-profiles showed an acceptable correlation for both continuous linear and nonlinear post-failure damage models using the material parameters set previously for the impact tests on elementary plates. A reduction about 25% of the compressive strength only in the corners of the hat-profiles allowed to predict a better force peak. Finally, an update of the strains at ultimate failure and the use of a maximal effective strain criterion gave an acceptable agreement regarding the material response and the predicted damaged zones.

The simulations of the 350J drop tower tests on 4mm thick PREPREG hat-profiles showed a too high force peak and a brittle failure of the specimen leading to the absence of an adequate post-failure behavior. A reduction about 50% of the compressive strength in the corners allowed to obtain a better correlation concerning the maximal reaction force peak but it did not improve the post-failure behavior. For these both cases, due to the deletion of elements following a line along the width of the hat-profile, a limited damage distribution has been observed, which did not seem to be realistic enough. Finally, the modeling using the effective strain criterion and the definition of high final strain values leading to large post-failure material degradation improved the material response, even if a lightly too low displacement of the impactor has been predicted. This is caused by a deletion of elements only in the corners, offering a sufficient load-bearing capability to the flat sides of the specimen. The damage localization and distribution were acceptable but a collapse of the flat sides of the specimen should still be obtained. Using the material parameters set previously for the impact tests on elementary plates, the simulations of the 500J drop tower tests on 4mm thick PREPREG hat-profiles showed similar results as for the 350J impact and similar conclusions and remarks could be also made. A sudden large element deletion occurred at the end of the simulation, which was in relative good agreement with experimental observations.

The work presented in this chapter resulted in the following publications [253][3].

[3]This publication includes work from other chapters of this thesis and therefore features again in the corresponding chapters

Conclusion

Summary

In the development process of automotive structural parts in composite, numerical simulations play a major role firstly in a technical aspect by optimizing the shape of the structures and secondly in an economical aspect by limiting the fabrication of hardware and the conduction of expensive experimental tests. Due to the complex behavior and the internal structure of composite materials, a multi-scale characterization method based on a building-block approach has been used in order to understand the real material behavior from a microscopic to a macroscopic level. Simultaneously to this experimental study, the corresponding and adequate modeling techniques have been developed and assessed in order to ensure a reliable prediction of the material behavior. The main objectives of the present study were to characterize numerically and experimentally the macroscopic behavior of carbon fiber woven composite materials for crash simulations and automotive applications. The stiffness, strengths, failure, and damage propagation observed experimentally have been numerically represented to validate the numerical models. The main difficulty relied on the development of accurate but user-friendly modeling techniques being able to give reliable predictions considering the different limitations (element size, single layer models, low computing costs) imposed by the industrial and engineering fields. In this way, the present study aimed also at contributing to the validation of suitable material models for the modeling of the macroscopic crash behavior of composite materials.

Most of the studies reported in the literature and concerning the woven composites are based on microscopic or multi-scale analysis using analytic or numerical finite elements modeling. Moreover, most of the material models implemented in the explicit finite element solver LS-DYNA have been developed to predict the linear behavior and failure of non-crimp fabric laminated structures. The *MAT_058 model is able to predict a nonlinear behavior up to failure but without consideration of any permanent deformation. Finally, the post-failure behavior is modeled either by a constant stress level or by a progressive linear material degradation.

The quasi-static experimental coupon tests conducted for a carbon plain-weave epoxy RTM composite showed a linear tensile behavior but a nonlinear behavior in compression and in shear. Using similar tests for a carbon twill-weave epoxy PREPREG material, a large delamination occurring about 50% of the stress at ultimate failure has been observed for tensile loads. A nonlinear behavior has been also captured in compression and in shear. For both materials, longitudinal four-point bending tests showed a linear behavior and an expected nonlinear behavior has been reported for a shear bending load case.

Low velocity impact tests showed a similar macroscopic material response for both composite materials but larger delaminated and damaged zones have been observed for the PREPREG composite. Finally, drop tower tests on hat-profiles have been conducted to investigate the behavior of both composites on a more complex geometry and to assess the material parameters and the modeling techniques validated previously.

Based on these experimental observations, an orthotropic mesh-insensitive numerical material model predicting nonlinearity, failure and post-failure material degradation has been developed and implemented as a UMAT in the explicit FE-solver LS-DYNA. A unidimensional plasticity model has been coupled to the nonlinearity in order to account for the irreversible aspect of micro-cracks and damage evolution up to failure onset. The nonlinear behavior in each in-plane material direction up to failure can be predicted using the Ramberg-Osgood model or giving a load curve as an input. Failure can be predicted by a maximum stress criterion or by the 2D Tsai-Wu criterion. Linear and nonlinear continuous post-failure damage models have been developed, as well as a constant stress level and a step-based post-failure material degradation models in order to represent the damage propagation in the material after failure. They define thus the intralaminar fracture toughness of the material. The main input parameters are based on the effective mechanical properties of the materials and the strains at ultimate failure can be determined using specific experimental tests or they can be set to fit with experiments. A smeared formulation ensures an adequate distribution of the post-failure damage and offers the mesh independence in the presence of strain localization. As relatively thick composite structures are likely to be designed in order to fulfill the automotive crash regulations, the material model has been implemented for shell, thick shell and solid elements. In the case of a model involving a 3D stress state (volume elements and thick shells), a linear elastic behavior is assumed in the through-the-thickness direction.

For both composite materials, a very good correlation has been obtained regarding the in-plane quasi-static tests on elementary coupons in terms of stiffness, nonlinearity and failure. The Tsai-Wu criterion showed more suitable failure predictions than those given by the maximum failure criterion for the multidirectional stacking sequences. The bending stiffness of both woven composites has been over-predicted by the simulations compared to the experiments, probably due to the fact that these woven composites present a weaker bending behavior as expected.

Regarding the impact tests on the RTM material, the modeling with shell elements showed a too stiff behavior compared to experimental results for the three impact energies. A good correlation is obtained concerning the damaged areas but the maximal displacement of the impactor is about 12% under-estimated and the maximal reaction force peak was between 15% and 30% over-estimated. The four post-failure material degradation models gave similar results and it has been observed, that a continuous damage evolution law limits the oscillations in the curves and the instabilities in the simulations. A modeling with thick shell elements improved the correlation of the material responses for both 25J and 50J impact energies. However, an unsuitable cross-shape of the damage distribution and of the element deletion is observed for each damage definition and for each impact energy using these elements. This numerical problem should rely on the use of the R5 LS-DYNA release. Finally, a poor agreement has been obtained for the lowest 5J impact energy. It is mostly due to the fact that high localized damage

and deformation induced by such a low energy of impact cannot be easily modeled using a mesh size about 5mm and a single element layer. Moreover, the modeling of the 4mm thick composite plate using 2D shell elements does not allow to take into account the through-the-thickness deformations and the different transverse effects. The simulations of the drop tower tests on hat-profiles using the previously validated material parameters showed a too brittle behavior of the composite material. Some updates of the strains at ultimate failure controlling the post-failure material behavior have been made to reach a better agreement with experimental observations.

Regarding the impact tests on the PREPREG material, a good agreement is obtained concerning both 25J and 50J impact in terms of material response and prediction of the damaged areas using shell elements. However, an unsuitable correlation is observed regarding the material response for the 5J impact. The modeling with the linear and nonlinear post-failure damage models showed similar results. Analogous conclusions and correlations have been obtained for a modeling with thick shell elements regarding the material response but the cross-shape of the damage distribution is still not suitable. Finally, the simulations of the drop tower tests on hat-profiles led to similar conclusions as for the RTM material.

The material characterization method based on the building-block approach allows to progressively set the different input parameters of the UMAT. Further experimental tests are naturally required, particularly regarding the post-failure regime. The results presented previously showed a promising way for the prediction of the behavior of woven composite under different load cases using under-integrated elements and a single element layer model.

Perspectives

Some further works have to be conducted in order to improve the numerical prediction of the macroscopic behavior of woven composites under different load cases. First, it is clear that a modeling using thick shell elements seems to be required to model structures presenting a thickness higher than 4mm and using a single element layer. The UMAT should be implemented for thick shell elements on a more current release of LS-DYNA. Moreover, experimental tests will have to be conducted in order to determine the different through-the-thickness and transverse material properties. Microscopic finite elements analysis could allow to be helpful for these investigations, as the out-of-plane properties are still sometimes difficult to capture experimentally.

The previous conclusions put in evidence that delamination, post-failure material degradation and fragmentation should be separately modeled to obtain a better correlation. An interface modeling should be used to model the delamination propagation. The material fragmentation and the post-failure material behavior could be then investigated based on specific experimental tests like bearing tests and a characterization method should be developed to facilitate the use in industrial applications. A modeling without any post-failure definition showed a perforation of the plate, which confirms the necessity of a post-failure behavior definition by modeling impact and crash load cases, in particular using single element layer models. Moreover, it allows to predict and assess the damage tolerance of the composite material.

Concerning the plasticity model, the current unload parallel to the initial Young's modulus should

be replaced by a formulation defining a degradation of the stiffness. Thus, the high plastic strain level observed in the present study should be avoided, offering a more realistic prediction of the permanent deformation. Then, the unidimensional plasticity model should be tested for off-axis tensile, compressive and bending tests. It will allow to determine if an anisotropic plastic or a coupling between the different directions is absolutely required. Cyclic load paths should be also investigated to validate the numerical models.

Then, the Tsai-Wu failure criterion should be adapted to identify the failure mode and the definition of post-failure damage should be further investigated for this failure criterion.

Regarding the intralaminar fracture toughness, it will be necessary to investigate and conduct experimental tests allowing to determine the post-failure material degradation and the strains at ultimate failure.

As it has been already investigated in the literature, woven composites are likely to present a non-negligible strain rate dependency. Consequently, a rate-dependent formulation should be added to the UMAT implementation in order to account for the potential strength increase or for the visco-(elastic)-plastic behavior of the material.

Finally, the UMAT should be assessed using tests on glass-fiber woven composites, because they present a clear nonlinear behavior in several material directions and because they are more rate-sensitive than similar carbon fiber woven composites.

Bibliography

[1] IPCC. *Climate Change 2007 - Synthesis Report: Contribution of Working Groups I, II and III to the Fourth Assessment Report of the Intergovernmental Panel on Climate Change*. Cambridge University Press, ISBN: 92-9169-122-4, 2008.

[2] Haikun Wang, Lixin Fu, and Jun Bi. Co2 and pollutant emissions from passenger cars in china. *Energy Policy*, 39(5):3005–3011, 2011.

[3] EPA. Global greenhouse gas emissions data. `http://www.epa.gov/climatechange/ghgemissions/global.html`, 2013.

[4] Susan Solomon, Dahe Qin, Martin Manning, Melinda Marquis, Kristen Averyt, Melinda M.B. Tignor, Henry LeRoy Miller Jr., and Zhenlin Chen. *Climate Change 2007 - The Physical Science Basis: Working Group I Contribution to the Fourth Assessment Report of the Intergovernmental Panel on Climate Change (IPCC)*. Cambridge University Press, ISBN: 978-0-521-88009-1, 2007.

[5] Bert Metz, Ogunlade Davidson, Peter Bosch, Rutu Dave, and Leo Meyer. *Climate Change 2007 - Mitigation of Climate Change: Working Group III contribution to the Fourth Assessment Report of the Intergovernmental Panel on Climate Change (IPCC)*. Cambridge University Press, ISBN: 978-0-521-88011-4, 2007.

[6] Martin Parry, Osvaldo Canziani, Jean Palutikof, Paul Van der Linden, and Clair Hanson. *Climate Change 2007 - Impacts, Adaptation and Vulnerability: Working Group II contribution to the Fourth Assessment Report of the Intergovernmental Panel on Climate Change (IPCC)*. Cambridge University Press, ISBN: 978-0-521-88010-7, 2008.

[7] J Drake Hamilton. Climate change and health vulnerabilities. *Minnesota medicine*, 92(11):35, 2009.

[8] Anthony J McMichael, Rosalie E Woodruff, and Simon Hales. Climate change and human health: present and future risks. *The Lancet*, 367(9513):859–869, 2006.

[9] Andy Haines, R Sari Kovats, Diarmid Campbell-Lendrum, and Carlos Corvalán. Climate change and human health: impacts, vulnerability and public health. *Public health*, 120(7):585–596, 2006.

[10] Ichiro Kurane. The effect of global warming on infectious diseases. *Osong Public Health and Research Perspectives*, 1(1):4–9, 2010.

[11] European Parliament. Regulation (EC) No 715/2007 of the European Parliament and of the council of 20 June 2007 on type approval of motor vehicles with respect to emissions from light passenger

and commercial vehicles (Euro 5 and Euro 6) and on access to vehicle repair and maintenance information. *Official Journal of the European Union*, 2007.

[12] G Savage. Composite materials technology in formula 1 motor racing. `http://www.f1-forecast.com/pdf/F1-Files/Composite%20Materials%20Technology%20in%20Formula%201%20Motor%20Racing.pdf`, 2008.

[13] Global New Car Assessment Program Global NCAP. Global standards for safer cars. `http://www.globalncap.org/Global_standards/Pages/Globalstandards.aspx`, 2013.

[14] European New Car Assessment Program EuroNCAP. European standards for safer cars. `http://www.euroncap.com/guidelines.aspx`, 2013.

[15] Crash and safety overview. `http://web.iitd.ac.in/~achawla/public_html/736/11-Crash_Safety_practices.pdf`, 2013.

[16] AG Mamalis, M Robinson, DE Manolakos, GA Demosthenous, MB Ioannidis, and J Carruthers. Crashworthy capability of composite material structures. *Composite structures*, 37(2):109–134, 1997.

[17] NA Warrior, TA Turner, F Robitaille, and CD Rudd. Effect of resin properties and processing parameters on crash energy absorbing composite structures made by rtm. *Composites Part A: applied science and manufacturing*, 34(6):543–550, 2003.

[18] MW Joosten, S Dutton, D Kelly, and R Thomson. Experimental and numerical investigation of the crushing response of an open section composite energy absorbing element. *Composite Structures*, 93(2):682–689, 2011.

[19] Jovan Obradovic, Simonetta Boria, and Giovanni Belingardi. Lightweight design and crash analysis of composite frontal impact energy absorbing structures. *Composite Structures*, 94(2):423–430, 2012.

[20] Saijod TW Lau, MR Said, and Mohd Yuhazri Yaakob. On the effect of geometrical designs and failure modes in composite axial crushing: A literature review. *Composite Structures*, 94(3):803–812, 2012.

[21] S Boria, S Pettinari, and F Giannoni. Theoretical analysis on the collapse mechanisms of thin-walled composite tubes. *Composite Structures*, 2013.

[22] PH Thornton and RA Jeryan. Crash energy management in composite automotive structures. *International Journal of Impact Engineering*, 7(2):167–180, 1988.

[23] PH Thornton, JJ Harwood, and P Beardmore. Fiber-reinforced plastic composites for energy absorption purposes. *Composites Science and Technology*, 24(4):275–298, 1985.

[24] George C Jacob, John F Fellers, Srdan Simunovic, and J Michael Starbuck. Energy absorption in polymer composites for automotive crashworthiness. *Journal of composite Materials*, 36(7):813–850, 2002.

[25] G Savage, I Bomphray, and M Oxley. Exploiting the fracture properties of carbon fibre composites to design lightweight energy absorbing structures. *Engineering Failure Analysis*, 11(5):677–694, 2004.

[26] Simonetta Boria and Giovanni Belingardi. Numerical investigation of energy absorbers in composite materials for automotive applications. *International Journal of Crashworthiness*, 17(4):345–356, 2012.

[27] Serge Abrate. *Impact engineering of composite structures*, volume 526. Springer, 2011.

[28] Alastair F Johnson and Anthony K Pickett. Impact and crash modelling of composite structures: A challenge for damage mechanics. *German Aerospace Center (DLR), Institute of Structures and Design*, 1999.

[29] MA McCarthy and JFM Wiggenraad. Numerical investigation of a crash test of a composite helicopter subfloor structure. *Composite structures*, 51(4):345–359, 2001.

[30] Eric Deletombe, David Delsart, Dieter Kohlgrüber, and Alastair F Johnson. Improvement of numerical methods for crash analysis in future composite aircraft design. *Aerospace science and technology*, 4(3):189–199, 2000.

[31] Hamidreza Zarei, Matthias Kröger, and Henrik Albertsen. An experimental and numerical crashworthiness investigation of thermoplastic composite crash boxes. *Composite structures*, 85(3):245–257, 2008.

[32] V Schultheis, S Fell, H Schuermann, and A Bleier. The hierarchical building-block approach of testing and fe analysis for strength prediction of high pressure wet wound composite vessels. *SIMVEC VDI tagung*, 2008.

[33] Military Handbook MIL-HDBK-17-1F. *Composite Materials Handbook Volume 1: Polymer Matrix Composites Guidelines for Characterization of structural materials*. U.S. Department of Defense, 2002.

[34] Military Handbook MIL-HDBK-17-2F. *Composite Materials Handbook Volume 2: Polymer Matrix Composites Material Properties*. U.S. Department of Defense, 2002.

[35] Military Handbook MIL-HDBK-17-3F. *Composite Materials Handbook Volume 3: Polymer Matrix Composites Materials Usage, Design and Analysis*. U.S. Department of Defense, 2002.

[36] P. Tan, L. Tong, and GP Steven. Modelling for predicting the mechanical properties of textile composites a review. *Composites Part A Applied Science and Manufacturing*, 28(11):903–922, 1997.

[37] B.N. Cox and G. Flanagan. *Handbook of analytical methods for textile composites*, volume 4750. National Aeronautics and Space Administration, 1997.

[38] S.V. Lomov, AV Gusakov, G. Huysmans, A. Prodromou, and I. Verpoest. Textile geometry preprocessor for meso-mechanical models of woven composites. *Composites Science and Technology*, 60(11):2083–2095, 2000.

[39] S.V. Lomov, D. Ivanov, and I. Verpoest. Predictive models for textile composites. *7th International Conference - TEXSCI 2010*, 2010.

[40] M. Nguyen, I. Herszberg, and R. Paton. The shear properties of woven carbon fabric. *Composite structures*, 47(1):767–779, 1999.

[41] E. De Bilbao, D. Soulat, G. Hivet, and A. Gasser. Experimental study of bending behaviour of reinforcements. *Experimental mechanics*, 50(3):333–351, 2010.

[42] MJ King, P. Jearanaisilawong, and S. Socrate. A continuum constitutive model for the mechanical behavior of woven fabrics. *International Journal of Solids and Structures*, 42(13):3867–3896, 2005.

[43] XQ Peng and J. Cao. A continuum mechanics-based non-orthogonal constitutive model for woven composite fabrics. *Composites part A: Applied Science and manufacturing*, 36(6):859–874, 2005.

[44] P. Xue, X. Peng, and J. Cao. A non-orthogonal constitutive model for characterizing woven composites. *Composites part A: Applied Science and manufacturing*, 34(2):183–193, 2003.

[45] H. Ryou, K. Chung, and W.R. Yu. Constitutive modeling of woven composites considering asymmetric/anisotropic, rate dependent, and nonlinear behavior. *Composites Part A: Applied Science and Manufacturing*, 38(12):2500–2510, 2007.

[46] N. Pan. Analysis of woven fabric strengths: Prediction of fabric strength under uniaxial and biaxial extensions. *Composites science and technology*, 56(3):311–327, 1996.

[47] M. Sherburn. *Geometric and mechanical modelling of textiles*. PhD thesis, 2007.

[48] A. Shahkarami and R. Vaziri. A continuum shell finite element model for impact simulation of woven fabrics. *International journal of impact engineering*, 34(1):104–119, 2007.

[49] A. Tabiei and I. Ivanov. Computational micro-mechanical model of flexible woven fabric for finite element impact simulation. *International journal for numerical methods in engineering*, 53(6):1259–1276, 2002.

[50] Savvas Vassiliadis, Argyro Kallivretaki, Dimitra Domvoglou, and Christofer Provatidis. Mechanical analysis of woven fabrics: The state of the art. In Savvas Vassiliadis, editor, *Advances in Modern Woven Fabrics Technology*, pages 41–64. InTech, Rijeka, Croatia, July 2011.

[51] N. Chretien. *Numerical Constitutive Models of Woven and Braided Textile Structural Composites*. PhD thesis, Virginia Polytechnic Institute and State University, 2002.

[52] Molded fiber glass companies. Resin transfer molding. `http://www.moldedfiberglass.com/processes/resin-transfer-molding`, 2013.

[53] MRM Industries Inc. The resin transfer molding (rtm) process. `http://www.mrmindustries.com/rtmprocess.htm`, 2013.

[54] Gary Thomas. Composite prepregs manufacturing, benefits and applications. `http://www.azom.com/article.aspx?ArticleID=8353`, 2013.

[55] Hexcel. Hexply® prepreg technology. `http://www.hexcel.com/Resources/DataSheets/Brochure-Data-Sheets/Prepreg_Technology.pdf#page=15`, 2013.

[56] C. Ayranci and J. Carey. 2d braided composites: A review for stiffness critical applications. *Composite Structures*, 85(1):43–58, 2008.

[57] A.F. Gill, P. Robinson, S. Pinho, and J. Sargent. Effect of rtm defects on mode I and II delamination behaviour of 5hs woven composites. In *16th international conference on composite materials, Kyoto, Japan*, 2007.

[58] M. Ito and T.W. Chou. Elastic moduli and stress field of plain-weave composites under tensile loading. *Composites Science and Technology*, 57(7):787–800, 1997.

[59] JF Mandell, DD Samborsky, and L. Wang. Effects of fiber waviness on composites for wind turbine blades. In *Internation SAMPE Symposium and Exhibition*, pages 2653–2666. SAMPE; 1999, 2003.

[60] J. Hofstee, H. De Boer, and F. Van Keulen. Elastic stiffness analysis of a thermo-formed plain-weave fabric composite - part III: experimental verification. *Composites science and technology*, 62(3):401–418, 2002.

[61] J. Hofstee, H. De Boer, and F. Van Keulen. Elastic stiffness analysis of a thermo-formed plain-weave fabric composite: Part I: geometry. *Composites science and technology*, 60(7):1041–1053, 2000.

[62] J. Hofstee and F. Van Keulen. Elastic stiffness analysis of a thermo-formed plain-weave fabric composite part II: analytical models. *Composites science and technology*, 60(8):1249–1261, 2000.

[63] Y. Miao, E. Zhou, Y. Wang, and B.A. Cheeseman. Mechanics of textile composites: Micro-geometry. *Composites Science and Technology*, 68(7):1671–1678, 2008.

[64] DS. Ivanov. Damage analysis of textile composites, 2009.

[65] S.V. Lomov, D.S. Ivanov, I. Verpoest, M. Zako, T. Kurashiki, H. Nakai, and S. Hirosawa. Meso-fe modelling of textile composites: Road map, data flow and algorithms. *Composites Science and Technology*, 67(9):1870–1891, 2007.

[66] Kuno KU Stellbrink. *Micromechanics of composites: composite properties of fibre and matrix constituents*. Hanser Munich, 1996.

[67] Robert M Jones. Mechanics of composite material. *Taylor & Francis, New York*, 1999.

[68] H.G. Franklin. Classic theories of failure of anisotropic materials. *Fibre Science and Technology*, 1(2):137–150, 1968.

[69] AC Orifici, I. Herszberg, and RS Thomson. Review of methodologies for composite material modelling incorporating failure. *Composite Structures*, 86(1-3):194–210, 2008.

[70] Carlos G Dávila and Pedro P Camanho. Failure criteria for frp laminates in plane stress. *NASA TM*, 212663(613), 2003.

[71] Federico Paris. *A study of failure criteria of fibrous composite materials*. National Aeronautics and Space Administration, Langley Research Center, 2001.

[72] M.J. Hinton, A.S. Kaddour, and P.D. Soden. *Failure criteria in fibre reinforced polymer composites: the world-wide failure exercise*. Elsevier Science, 2004.

[73] Gerald Ernst, Matthias Vogler, Christian Hühne, and Raimund Rolfes. Multiscale progressive failure analysis of textile composites. *Composites Science and Technology*, 70(1):61–72, 2010.

[74] R. Rolfes, M. Vogler, S. Czichon, and G. Ernst. Exploiting the structural reserve of textile composite structures by progressive failure analysis using a new orthotropic failure criterion. *Computers & Structures*, 89(11):1214–1223, 2011.

[75] SP Yushanov and A.E. Bogdanovich. Fiber waviness in textile composites and its stochastic modeling. *Mechanics of composite materials*, 36(4):297–318, 2000.

[76] J. Whitcomb and K. Srirengan. Effect of various approximations on predicted progressive failure in plain weave composites. *Composite structures*, 34(1):13–20, 1996.

[77] HM Hsiao and IM Daniel. Elastic properties of composites with fiber waviness. *Composites Part A: Applied Science and Manufacturing*, 27(10):931–941, 1996.

[78] J.D. Whitcomb et al. Three-dimensional stress analysis of plain weave composites. *Composite materials: Fatigue and fracture.*, 3:417–438, 1991.

[79] M.V. Donadon, B.G. Falzon, L. Iannucci, and J.M. Hodgkinson. A 3-d micromechanical model for predicting the elastic behaviour of woven laminates. *Composites science and technology*, 67(11):2467–2477, 2007.

[80] R.L. Karkkainen and B.V. Sankar. A direct micromechanics method for analysis of failure initiation of plain weave textile composites. *Composites science and technology*, 66(1):137–150, 2006.

[81] P. Chaphalkar and A.D. Kelkar. Classical laminate theory model for twill weave fabric composites. *Composites Part A: Applied Science and Manufacturing*, 32(9):1281–1289, 2001.

[82] M. Pankow, A.M. Waas, C.F. Yen, and S. Ghiorse. A new lamination theory for layered textile composites that account for manufacturing induced effects. *Composites Part A: Applied Science and Manufacturing*, 40(12):1991–2003, 2009.

[83] B. Gommers, I. Verpoest, and P. Van Houtte. The mori-tanaka method applied to textile composite materials. *Acta Materialia*, 46(6):2223–2235, 1998.

[84] T. Ishikawa and T.W. Chou. Stiffness and strength behaviour of woven fabric composites. *Journal of Materials Science*, 17(11):3211–3220, 1982.

[85] NK Naik and VK Ganesh. Prediction of on-axes elastic properties of plain weave fabric composites. *Composites Science and Technology*, 45(2):135–152, 1992.

[86] NK Naik and VK Ganesh. An analytical method for plain weave fabric composites. *Composites*, 26(4):281–289, 1995.

[87] N.F. Dow, V. Ramnath, and B.W. Rosen. Analysis of woven fabrics for reinforced composite materials. 1987.

[88] P. Vandeurzen, J. Ivens, and I. Verpoest. A three-dimensional micromechanical analysis of woven-fabric composites: I. geometric analysis. *Composites science and technology*, 56(11):1303–1315, 1996.

[89] P. Vandeurzen, J. Ivens, and I. Verpoest. A three-dimensional micromechanical analysis of woven-fabric composites: II. elastic analysis. *Composites science and technology*, 56(11):1317–1327, 1996.

[90] T.J. Walsh and O.O. Ochoa. Analytical and experimental mechanics of woven fabric composites. *Mechanics of composite materials and structures.*, 3(2):133–152, 1996.

[91] B.V. Sankar and R.V. Marrey. Analytical method for micromechanics of textile composites. *Composites Science and Technology*, 57(6):703–713, 1997.

[92] NK Naik and PS Shembekar. Elastic behavior of woven fabric composites: 1-lamina analysis. *Journal of Composite Materials*, 26(15):2196–2225, 1992.

[93] NK Naik and PS Shembekar. Elastic behavior of woven fabric composites: 3-laminate design. *Journal of composite materials*, 26(17):2522–2541, 1992.

[94] PS Shembekar and NK Naik. Elastic behavior of woven fabric composites: 2-laminate analysis. *Journal of Composite Materials*, 26(15):2226–2246, 1992.

[95] Z. Huang. The mechanical properties of composites reinforced with woven and braided fabrics. *Composites Science and Technology*, 60(4):479–498, 2000.

[96] Zheng Ming Huang. A unified micromechanical model for the mechanical properties of two constituent composite materials. part I: Elastic behavior. *Journal of Thermoplastic Composite Materials*, 13(4):252–271, 2000.

[97] Z.M. Huang. A unified micromechanical model for the mechanical properties of two constituent composite materials part II: Plastic behavior. *Journal of Thermoplastic Composite Materials*, 13(5):344–362, 2000.

[98] Z.M. Huang. A unified micromechanical model for the mechanical properties of two constituent composite materials. part III: strength behavior. *Journal of Thermoplastic Composite Materials*, 14(1):54–69, 2001.

[99] Z.M. Huang. A unified micromechanical model for the mechanical properties of two constituent composite materials. part V: laminate strength. *Journal of Thermoplastic Composite Materials*, 13(3):190–206, 2000.

[100] Z.M. Huang and S. Ramakrishna. Modeling inelastic and strength properties of textile laminates: a unified approach. *Composites science and technology*, 63(3):445–466, 2003.

[101] D. Scida, Z. Aboura, ML Benzeggagh, and E. Bocherens. Prediction of the elastic behaviour of hybrid and non-hybrid woven composites. *Composites science and technology*, 57(12):1727–1740, 1998.

[102] D. Scida, Z. Aboura, ML Benzeggagh, and E. Bocherens. A micromechanics model for 3d elasticity and failure of woven-fibre composite materials. *Composites Science and Technology*, 59(4):505–517, 1999.

[103] VK Ganesh and NK Naik. Failure behaviour of plain weave fabric laminates under in-plane shear loading: effect of fabric geometry. *Composite structures*, 30(2):179–192, 1995.

[104] T. Matsuda, Y. Nimiya, N. Ohno, and M. Tokuda. Elastic-viscoplastic behavior of plain-woven gfrp laminates: Homogenization using a reduced domain of analysis. *Composite structures*, 79(4):493–500, 2007.

[105] A. Gupta and J. Raghavan. Parametric study of the effect of microstructure on creep of plain weave composites. *Composites Part A: Applied Science and Manufacturing*, 42(5):511–520, 2011.

[106] S.V. Lomov, L. Dufort, P. De Luca, and I. Verpoest. Meso-macro integration of modelling of stiffness of textile composites. In *Proceedings of the 28th International Conference of SAMPE Europe*, pages 403–408, 2007.

[107] Ö. Soykasap. Analysis of plain-weave composites. *Mechanics of Composite Materials*, 47(2):161–176, 2011.

[108] O. Soykasap. Micromechanical models for bending behavior of woven composites. *Journal of spacecraft and rockets*, 43(5):1093–1100, 2006.

[109] BD Allison and JL Evans. Effect of fiber waviness on the bending behavior of s-glass/epoxy composites. *Materials & Design*, 2011.

[110] WS Chan and CJ Chou. Effect of delamination and ply fiber waviness on effective axial and bending stiffness in composite laminates. In *The Second International Symposium on Composite Materials and Structures*, pages 105–111, 1992.

[111] U. A. Khashaba, S.M. Aldousari, and I.M.R. Najjar. Behavior of [0]8 woven composites under combined bending and tension loading: Part I experimental and analytical. *Journal of Composite Materials*, 2011.

[112] BN Cox, WC Carter, and NA Fleck. A binary model of textile composites: I. formulation. *Acta metallurgica et materialia*, 42(10):3463–3479, 1994.

[113] J. Xu, B.N. Cox, MA McGlockton, and WC Carter. A binary model of textile composites - part II. the elastic regime. *Acta metallurgica et materialia*, 43(9):3511–3524, 1995.

[114] V. Carvelli and C. Poggi. A homogenization procedure for the numerical analysis of woven fabric composites. *Composites Part A: Applied Science and Manufacturing*, 32(10):1425–1432, 2001.

[115] Y. Jiang, A. Tabiei, and G.J. Simitses. A novel micromechanics-based approach to the derivation of constitutive equations for local/global analysis of a plain-weave fabric composite. *Composites science and technology*, 60(9):1825–1833, 2000.

[116] A. Tabiei and W. Yi. Comparative study of predictive methods for woven fabric composite elastic properties. *Composite Structures*, 58(1):149–164, 2002.

[117] J.D. Whitcomb. Iterative global/local finite element analysis. *Computers & structures*, 40(4):1027–1031, 1991.

[118] P. Tan, L. Tong, and G.P. Steven. Micromechanics models for the elastic constants and failure strengths of plain weave composites. *Composite structures*, 47(1):797–804, 1999.

[119] S.P. Ng, P.C. Tse, and K.J. Lau. Numerical and experimental determination of in-plane elastic properties of 2/2 twill weave fabric composites. *Composites Part B: Engineering*, 29(6):735–744, 1998.

[120] NV De Carvalho, ST Pinho, and P. Robinson. Numerical modelling of woven composites: Biaxial loading. *Composites Part A: Applied Science and Manufacturing*, 2012.

[121] BH Le Page, FJ Guild, SL Ogin, and PA Smith. Finite element simulation of woven fabric composites. *Composites Part A: Applied Science and Manufacturing*, 35(7):861–872, 2004.

[122] EJ Barbero, J. Trovillion, JA Mayugo, and KK Sikkil. Finite element modeling of plain weave fabrics from photomicrograph measurements. *Composite structures*, 73(1):41–52, 2006.

[123] P. Badel. *Analyse mésoscopique du comportement mécanique des renforts tissés de composites utilisant la tomographie aux rayons X*. PhD thesis, Institut National des Sciences Appliquées de Lyon, 2008.

[124] W. Ruijter. *Analysis of mechanical properties of woven textile composites as a function of textile geometry*. PhD thesis, Univiersity of Nottingham, 2008.

[125] G. Couégnat. *Approche multiéchelle du comportement mécanique de matériaux composites à renfort tissé*. PhD thesis, Université Sciences et Technologies-Bordeaux I, 2008.

[126] J. Hofstee and F. Van Keulen. 3-d geometric modeling of a draped woven fabric. *Composite structures*, 54(2):179–195, 2001.

[127] DM Blackketter, DE Walrath, and AC Hansen. Modeling damage in a plain weave fabric-reinforced composite material. *Journal of composites technology and research*, 15(2):136–142, 1993.

[128] T. Ishikawa, M. Matsushima, Y. Hayashi, and T.W. Chou. Experimental confirmation of the theory of elastic moduli of fabric composites. *Journal of Composite Materials*, 19(5):443–458, 1985.

[129] N. Jēkabsons and J. Byström. On the effect of stacked fabric layers on the stiffness of a woven composite. *Composites Part B: Engineering*, 33(8):619–629, 2002.

[130] T. Fuj, S. Amijima, F. Lin, and T. Sagami. Study on strength and nonlinear stress-strain response of plain woven glass fiber laminates under biaxial loading. *Journal of composite materials*, 26(17):2493–2510, 1992.

[131] Y. Wang, J. Li, and D. Zhao. Mechanical properties of fiber glass and kevlar woven fabric reinforced composites. *Composites Engineering*, 5(9):1159–1175, 1995.

[132] A. Adumitroaie and E.J. Barbero. Beyond plain weave fabrics - II. mechanical properties. *Composite Structures*, 93(5):1449–1462, 2011.

[133] E. D'Amato. Nonlinearities in mechanical behavior of textile composites. *Composite structures*, 71(1):61–67, 2005.

[134] D. Goyal and J.D. Whitcomb. Effect of fiber properties on plastic behavior of 2×2 biaxial braided composites. *Composites Science and Technology*, 68(3):969–977, 2008.

[135] Z.M. Huang. Effect of matrix plasticity on ultimate strength of composite laminates. *Journal of reinforced plastics and composites*, 20(4):304–320, 2001.

[136] M. Vogler, R. Rolfes, and P.P. Camanho. Modeling the inelastic deformation and fracture of polymer composites - part I: Plasticity model. *Mechanics of Materials*, 59(0):50 – 64, 2013.

[137] P.P. Camanho, M.A. Bessa, G. Catalanotti, M. Vogler, and R. Rolfes. Modeling the inelastic deformation and fracture of polymer composites - part II: Smeared crack model. *Mechanics of Materials*, 59(0):36 – 49, 2013.

[138] S. Ogihara and K.L. Reifsnider. Characterization of nonlinear behavior in woven composite laminates. *Applied composite materials*, 9(4):249–263, 2002.

[139] CT Sun and JL Chen. A simple flow rule for characterizing nonlinear behavior of fiber composites. *Journal of Composite Materials*, 23(10):1009–1020, 1989.

[140] C. Hochard, P.A. Aubourg, and J.P. Charles. Modelling of the mechanical behaviour of woven-fabric cfrp laminates up to failure. *Composites Science and Technology*, 61(2):221–230, 2001.

[141] G. Odegard, K. Searles, and M. Kumosa. A continuum elastic–plastic model for woven-fabric/polymer-matrix composite materials under biaxial stresses. *Composites science and technology*, 61(16):2501–2510, 2001.

[142] A. Tabiei and Y. Jiang. Woven fabric composite material model with material nonlinearity for nonlinear finite element simulation. *International Journal of Solids and Structures*, 36(18):2757–2771, 1999.

[143] G. Nicoletto, G. Anzelotti, and E. Riva. Mesoscopic strain fields in woven composites: Experiments vs. finite element modeling. *Optics and Lasers in Engineering*, 47(3):352–359, 2009.

[144] G. Anzelotti, G. Nicoletto, and E. Riva. Mesomechanic strain analysis of twill-weave composite lamina under unidirectional in-plane tension. *Composites Part A: Applied Science and Manufacturing*, 39(8):1294–1301, 2008.

[145] T.L. Norman, P. Allison, J.W. Baldwin, B.K. Gracias, and D. Seesdorf. Effect of tow alignment on the mechanical performance of 3d woven textile composites. *Composites Manufacturing*, 4(4):209–215, 1993.

[146] NK Naik and VK Ganesh. Failure behavior of plain weave fabric laminates under on-axis uniaxial tensile loading: 1. analytical predictions. *Journal of Composite Materials*, 30(16):1779–1822, 1996.

[147] VK Ganesh and NK Naik. Failure behavior of plain weave fabric laminates under on-axis uniaxial tensile loading: 3. effect of fabric geometry. *Journal of composite materials*, 30(16):1823–1856, 1996.

[148] J. Kim, M. Shioya, H. Kobayashi, J. Kaneko, and M. Kido. Mechanical properties of woven laminates and felt composites using carbon fibers. part I: in-plane properties. *Composites science and technology*, 64(13):2221–2229, 2004.

[149] B. Yang, V. Kozey, S. Adanur, and S. Kumar. Bending, compression, and shear behavior of woven glass fiber–epoxy composites. *Composites Part B: Engineering*, 31(8):715–721, 2000.

[150] ST Pinho, L. Iannucci, and P. Robinson. Physically-based failure models and criteria for laminated fibre-reinforced composites with emphasis on fibre kinking: Part I: Development. *Composites Part A: Applied Science and Manufacturing*, 37(1):63–73, 2006.

[151] ST Pinho, L. Iannucci, and P. Robinson. Physically based failure models and criteria for laminated fibre-reinforced composites with emphasis on fibre kinking. part II: Fe implementation. *Composites Part A: Applied Science and Manufacturing*, 37(5):766–777, 2006.

[152] NK Naik and R.S. Kumar. Compressive strength of unidirectional composites: evaluation and comparison of prediction models. *Composite structures*, 46(3):299–308, 1999.

[153] S. Song, A.M. Waas, K.W. Shahwan, X. Xiao, and O. Faruque. Braided textile composites under compressive loads: Modeling the response, strength and degradation. *Composites Science and Technology*, 67(15):3059–3070, 2007.

[154] NK Naik, SI Tiwari, and RS Kumar. An analytical model for compressive strength of plain weave fabric composites. *Composites science and technology*, 63(5):609–625, 2003.

[155] NA Fleck, PM Jelf, and PT Curtis. Compressive failure of laminated and woven composites. *Journal of composites technology & research*, 17(3):212–220, 1995.

[156] JCH Yee and S. Pellegrino. Folding of woven composite structures. *Composites Part A: Applied Science and Manufacturing*, 36(2):273–278, 2005.

[157] X.L. Gao, K. Li, and S. Mall. A mechanics-of-materials model for predicting young's modulus of damaged woven fabric composites involving three damage modes. *International journal of solids and structures*, 40(4):981–999, 2003.

[158] NK Naik and R. Kuchibhotla. Analytical study of strength and failure behaviour of plain weave fabric composites made of twisted yarns. *Composites Part A: Applied Science and Manufacturing*, 33(5):697–708, 2002.

[159] R.A. Naik. Failure analysis of woven and braided fabric reinforced composites. *Journal of Composite Materials*, 29(17):2334–2363, 1995.

[160] A. Adumitroaie and E.J. Barbero. Beyond plain weave fabrics - I. geometrical model. *Composite Structures*, 93(5):1424–1432, 2011.

[161] S.W. Tsai. *Theory of composites design*. Think composites Dayton, OH., 1992.

[162] M. Kollegal, SN Chatterjee, and G. Flanagan. Progressive failure analysis of plain weaves using damage mechanics based constitutive laws. *International journal of damage mechanics*, 10(4):301–323, 2001.

[163] R. Zahari, A.H. Azmee, F. Mustapha, M.S. Salit, R. Varatharajoo, and A. Shakrine. Prediction of progressive failure in woven glass/epoxy composite laminated panels. *Jurnal mekanikal*, 25:80–91, 2008.

[164] TE Tay, G. Liu, VBC Tan, XS Sun, and DC Pham. Progressive failure analysis of composites. *Journal of composite materials*, 42(18):1921–1966, 2008.

[165] M. Zako, Y. Uetsuji, and T. Kurashiki. Finite element analysis of damaged woven fabric composite materials. *Composites Science and Technology*, 63(3):507–516, 2003.

[166] O. Hoffman. The brittle strength of orthotropic materials. *Journal of Composite Materials*, 1(2):200–206, 1967.

[167] A. Tabiei and I. Ivanov. Materially and geometrically non-linear woven composite micro-mechanical model with failure for finite element simulations. *International journal of non-linear mechanics*, 39(2):175–188, 2004.

[168] I. Ivanov and A. Tabiei. Three-dimensional computational micro-mechanical model for woven fabric composites. *Composite structures*, 54(4):489–496, 2001.

[169] J.J. Crookston. *Prediction of elastic behaviour and initial failure of textile composites*. PhD thesis, University of Nottingham, 2004.

[170] JM Whitney and RJ Nuismer. Stress fracture criteria for laminated composites containing stress concentrations. *Journal of Composite Materials*, 8(3):253–265, 1974.

[171] RJ Nuismer and JM Whitney. Uniaxial failure of composite laminates containing stress concentrations. *Fracture mechanics of composites, ASTM STP*, 593:117–142, 1975.

[172] S.D. Pandita, K. Nishiyabu, and I. Verpoest. Strain concentrations in woven fabric composites with holes. *Composite structures*, 59(3):361–368, 2003.

[173] HJ Lin, CC Tsai, and JS Shie. Failure analysis of woven-fabric composites with moulded-in holes. *Composites science and technology*, 55(3):231–239, 1995.

[174] R. Zitoune, L. Crouzeix, F. Collombet, T. Tamine, and Y.H. Grunevald. Behaviour of composite plates with drilled and moulded hole under tensile load. *Composite Structures*, 93(9):2384–2391, 2011.

[175] L.W. Chang, S.S. Yau, and T.W. Chou. Notched strength of woven fabric composites with moulded-in holes. *Composites*, 18(3):233–241, 1987.

[176] NK Naik and PS Shembekar. Notched strength of fabric laminates I: Prediction. *Composites science and technology*, 44(1):1–12, 1992.

[177] PS Shembekar and NK Naik. Notched strength of fabric laminates. II: Effect of stacking sequence. *Composites science and technology*, 44(1):13–20, 1992.

[178] S.P. Ng, P.C. Tse, and K.J. Lau. Progressive failure analysis of 2/2 twill weave fabric composites with moulded-in circular hole. *Composites Part B: Engineering*, 32(2):139–152, 2001.

[179] HJ Lin and YJ Lee. Strength of composite laminates with continuous fiber around a circular hole. *Composite structures*, 21(3):155–162, 1992.

[180] Björn Van Den Broucke, P Middendorf, Stepan Vladimirovitch Lomov, and Ignace Verpoest. Modelling of damage in textile reinforced composites: micro-meso approach. In *Proceedings of Symposium on Finite Element Modeling of Textiles and Textile Composites, St. Petersburg, Russia*, 2007.

[181] EJ Barbero, P. Lonetti, and KK Sikkil. Finite element continuum damage modeling of plain weave reinforced composites. *Composites Part B: Engineering*, 37(2):137–147, 2006.

[182] Zhi-gang Hu and Yan Zhang. Continuum damage mechanics based modeling progressive failure of woven-fabric composite laminate under low velocity impact. *Journal of Zhejiang University SCIENCE A*, 11:151–164, 2010.

[183] T. Kurashiki, M. Zako, H. Nakai, M. Imura, and S. Hirosawa. Damage development of woven composites based on multi-scale analysis. In *Proceedings of the 16th International Conference on Composite Materials (ICCM-16)*, 2007.

[184] Y. Thollon and C. Hochard. A general damage model for woven fabric composite laminates up to first failure. *Mechanics of Materials*, 41(7):820–827, 2009.

[185] P. Ladevèze. A damage computational method for composite structures. *Computers & Structures*, 44(1):79–87, 1992.

[186] S. Miot, C. Hochard, and N. Lahellec. A non-local criterion for modelling unbalanced woven ply laminates with stress concentrations. *Composite Structures*, 92(7):1574–1580, 2010.

[187] C. Hochard, N. Lahellec, and C. Bordreuil. A ply scale non-local fibre rupture criterion for cfrp woven ply laminated structures. *Composite structures*, 80(3):321–326, 2007.

[188] K.S. Pandya, C. Veerraju, and NK Naik. Hybrid composites made of carbon and glass woven fabrics under quasi-static loading. *Materials & Design*, 32(7):4094–4099, 2011.

[189] C.T. Key, S.C. Schumacher, and A.C. Hansen. Progressive failure modeling of woven fabric composite materials using multicontinuum theory. *Composites Part B: Engineering*, 38(2):247–257, 2007.

[190] C.T. Key, R.W. Six, and A.C. Hansen. A three-constituent multicontinuum theory for woven fabric composite materials. *Composites science and technology*, 63(13):1857–1864, 2003.

[191] JN Baucom and MA Zikry. Low-velocity impact damage progression in woven e-glass composite systems. *Composites Part A: Applied Science and Manufacturing*, 36(5):658–664, 2005.

[192] JN Baucom, MA Zikry, and AM Rajendran. Low-velocity impact damage accumulation in woven s2-glass composite systems. *Composites science and technology*, 66(10):1229–1238, 2006.

[193] Cesim Atas and Dahsin Liu. Impact response of woven composites with small weaving angles. *International Journal of Impact Engineering*, 35(2):80–97, 2008.

[194] Mehmet Aktaş, H Ersen Balcıoğlu, Alaattin Aktaş, Erkan Türker, and M Emin Deniz. Impact and post impact behavior of layer fabric composites. *Composite Structures*, 94(9):2809–2818, 2012.

[195] MA Hassan, S Naderi, and AR Bushroa. Low-velocity impact damage of woven fabric composites: Finite element simulation and experimental verification. *Materials & Design*, 2013.

[196] B Vieille, VM Casado, and C Bouvet. About the impact behavior of woven-ply carbon fiber-reinforced thermoplastic–and thermosetting–composites: a comparative study. *Composite Structures*, 2013.

[197] NK Naik, Y. Chandra Sekher, and S. Meduri. Damage in woven-fabric composites subjected to low-velocity impact. *Composites Science and Technology*, 60(5):731–744, 2000.

[198] Jang-Kyo Kim and Man-Lung Sham. Impact and delamination failure of woven-fabric composites. *Composites Science and Technology*, 60(5):745–761, 2000.

[199] Cesim Atas and Onur Sayman. An overall view on impact response of woven fabric composite plates. *Composite Structures*, 82(3):336–345, 2008.

[200] Ghasemi Nejhad and A Parvizi-Majidi. Impact behaviour and damage tolerance of woven carbon fibre-reinforced thermoplastic composites. *Composites*, 21(2):155–168, 1990.

[201] S. Babu Aminjikarai and A. Tabiei. A strain-rate dependent 3-d micromechanical model for finite element simulations of plain weave composite structures. *Composite structures*, 81(3):407–418, 2007.

[202] J López-Puente and S Li. Analysis of strain rate sensitivity of carbon/epoxy woven composites. *International Journal of Impact Engineering*, 48:54–64, 2012.

[203] NK Naik, Parimi Jaya Shankar, Venkateswara Rao Kavala, G Ravikumar, Jayaram R Pothnis, and H Arya. High strain rate mechanical behavior of epoxy under compressive loading: Experimental and modeling studies. *Materials Science and Engineering: A*, 528(3):846–854, 2011.

[204] Hansun Ryou, Kwansoo Chung, and Ji-Ho Lim. Mechanical analysis of woven composites at high strain rates and its application to predicting impact behavior. *Metals and materials international*, 14(6):679–687, 2008.

[205] NK Naik, P Yernamma, NM Thoram, R Gadipatri, and VR Kavala. High strain rate tensile behavior of woven fabric e-glass/epoxy composite. *Polymer testing*, 29(1):14–22, 2010.

[206] David R Hufner and Michael L Accorsi. A progressive failure theory for woven polymer-based composites subjected to dynamic loading. *Composite Structures*, 89(2):177–185, 2009.

[207] Patrick Rozycki. *Contribution au développement de lois de comportement pour matériaux composites soumis à l'impact*. PhD thesis, 2000.

[208] Rana Foroutan. *High strain rate behaviour of woven composite materials*. PhD thesis, Department of Mechanical Engineering, McGill University, Montreal, 2009.

[209] Srikanth V Thiruppukuzhi and CT Sun. Models for the strain-rate-dependent behavior of polymer composites. *Composites Science and Technology*, 61(1):1–12, 2001.

[210] X. Zheng. *Nonlinear strain rate dependent composite model for explicit finite element analysis*. PhD thesis, The Graduate Faculty of The University of Akron, 2006.

[211] J.0 Hallquist. LS-Dyna Theory Manual. *Livermore Software Technology Corporation*, March 2006.

[212] Dynamore. Einfuehrung in LS-Dyna. *Stuttgart - Vaihingen*, 18-19 Juni 2008.

[213] Ivan Oskarsson. A new h-adaptive method for shell elements in ls-dyna.

[214] Ls-Dyna Support. Time integration. `http://www.dynasupport.com/tutorial/ls-dyna-users-guide/time-integration`, 2013.

[215] Suri Bala. Time integration. `http://blog2.d3view.com/wp-content/uploads/2007/04/timeintegration_v1.pdf`, 2007.

[216] Livermore Software Technology Corporation LSTC. *LS-DYNA keyword user's manual R6.1.0 Vol I.* 2012.

[217] Hourglass. `http://www.dynasupport.com/howtos/element/hourglass`.

[218] Fu-Kuo Chang and Kuo-Yen Chang. A progressive damage model for laminated composites containing stress concentrations. *Journal of Composite Materials*, 21(9):834–855, 1987.

[219] Livermore Software Technology Corporation LSTC. *LS-DYNA keyword user's manual R6.1.0 Vol II.* 2012.

[220] Stephen W Tsai and Edward M Wu. A general theory of strength for anisotropic materials. *Journal of composite materials*, 5(1):58–80, 1971.

[221] K Schweizerhof, K Weimar, T Muenz, and T Rottner. Crashworthiness analysis with enhanced composite material models in ls-dyna: Merits and limits. In *LS-Dyna World Conference, Detroit, Michigan, USA*, 1998.

[222] A. Matzenmiller, J. Lubliner, and RL Taylor. A constitutive model for anisotropic damage in fiber-composites. *Mechanics of Materials*, 20(2):125–152, 1995.

[223] P. Deslauriers, D. Cronin, and A. Duquette. Numerical modeling of woven carbon composite failure. In *8th International LS-Dyna Users Conference*, pages 11–33.

[224] P. Maimi, P.P. Camanho, JA Mayugo, and CG Davila. A continuum damage model for composite laminates: Part I-Constitutive model. *Mechanics of Materials*, 39(10):897–908, 2007.

[225] P. Maimi, P.P. Camanho, JA Mayugo, and CG Davila. A continuum damage model for composite laminates: Part II-Computational implementation and validation. *Mechanics of Materials*, 39(10):909–919, 2007.

[226] Z Hashin. Failure criteria for unidirectional fiber composites. *Journal of Applied Mechanics*, 47:329–334, 1980.

[227] Chian-Fong Yen. Ballistic impact modeling of composite materials. In *7th International LS-DYNA Users Conference*, pages 22060–6218, 2002.

[228] S.V. Lomov, D.S. Ivanov, I. Verpoest, M. Zako, T. Kurashiki, H. Nakai, J. Molimard, and A. Vautrin. Full-field strain measurements for validation of meso-fe analysis of textile composites. *Composites Part A: Applied Science and Manufacturing*, 39(8):1218–1231, 2008.

[229] J. Littell and The University of Akron. *The Experimental and Analytical Characterization of the Macromechanical Response for Triaxial Braided Composite Materials*. The University of Akron, 2008.

[230] Travis A Bogetti, Christopher PR Hoppel, Vasyl M Harik, James F Newill, and Bruce P Burns. Predicting the nonlinear response and progressive failure of composite laminates. *Composites science and technology*, 64(3):329–342, 2004.

[231] Travis A Bogetti, Christopher PR Hoppel, Vasyl M Harik, James F Newill, and Bruce P Burns. Predicting the nonlinear response and failure of composite laminates: correlation with experimental results. *Composites science and technology*, 64(3):477–485, 2004.

[232] WR Osgood and W Ramberg. Description of stress-strain curves by three parameters. *Tech. Notes Nat. Adv. Comm. Aeronaut*, 1943:13, 1943.

[233] Louie L. Yaw. Nonlinear static - 1d plasticity - various forms of isotropic hardening, walla walla university. `http://people.wallawalla.edu/~louie.yaw/plasticitypublications/1Dplasticity.pdf`, 2012.

[234] JC Simo and Thomas JR Hughes. *Computational inelasticity*. Springer, 1998.

[235] Fionn Dunne and Nik Petrinic. *Introduction to computational plasticity*. Oxford University Press New York, 2005.

[236] Kuo-Shih Liu and Stephen W Tsai. A progressive quadratic failure criterion for a laminate. *Composites Science and Technology*, 58(7):1023–1032, 1998.

[237] J Majak and S Hannus. Orientational design of anisotropic materials using the hill and tsai–wu strength criteria. *Mechanics of composite materials*, 39(6):509–520, 2003.

[238] Zdeněk P Bažant and BH Oh. Crack band theory for fracture of concrete. *Materials and structures*, 16(3):155–177, 1983.

[239] FXC Andrade, M Vogler, JMA Cesar de Sa, and FM Andrade Pires. User-defined nonlocal models in ls-dyna. In *7th European LS-DYNA Users Conference*, 2011.

[240] Amar C Garg. Intralaminar and interlaminar fracture in graphite/epoxy laminates. *Engineering fracture mechanics*, 23(4):719–733, 1986.

[241] Maurício V Donadon and Sérgio Frascino Muller de Almeida. Intralaminar fracture toughness characterization of composite laminates. In *Advances in Composite Materials - Analysis of Natural and Man-Made Materials*, pages 389–410. InTech, 2011.

[242] RW Truss, PJ Hine, and RA Duckett. Interlaminar and intralaminar fracture toughness of uniaxial continuous and discontinuous carbon fibre/epoxy composites. *Composites Part A: Applied Science and Manufacturing*, 28(7):627–636, 1997.

[243] S Jose, R Ramesh Kumar, MK Jana, and G Venkateswara Rao. Intralaminar fracture toughness of a cross-ply laminate and its constituent sub-laminates. *Composites science and technology*, 61(8):1115–1122, 2001.

[244] Kevin D Cowley and Peter WR Beaumont. The interlaminar and intralaminar fracture toughness of carbon-fibre/polymer composites: the effect of temperature. *Composites science and technology*, 57(11):1433–1444, 1997.

[245] Silvestre T Pinho, Paul Robinson, and Lorenzo Iannucci. Fracture toughness of the tensile and compressive fibre failure modes in laminated composites. *Composites Science and Technology*, 66(13):2069–2079, 2006.

[246] Ben IG Barr, Hadi F Abusiaf, and Siddik Sener. Size effect and fracture energy studies using compact compression specimens. *Materials and Structures*, 31(1):36–41, 1998.

[247] Ulrich Hansen and John W Gillespie. Dependence of intralaminar fracture toughness on direction of crack propagation in unidirectional composites. *Journal of composites technology & research*, 20(2):89–99, 1998.

[248] ST Pinho, P Robinson, and L Iannucci. Developing a four point bend specimen to measure the mode I intralaminar fracture toughness of unidirectional laminated composites. *Composites Science and Technology*, 69(7):1303–1309, 2009.

[249] Masaharu Iwamoto, Qing-Qing Ni, Teruhiko Fujiwara, and Ken Kurashiki. Intralaminar fracture mechanism in unidirectional cfrp composites: Part I: Intralaminar toughness and ae characteristics. *Engineering Fracture Mechanics*, 64(6):721–745, 1999.

[250] Maajid Chishti, Chun H Wang, Rodney S Thomson, and Adrian C Orifici. Characterising fibre compression fracture toughness of composites using bearing tests. *Composites Part A: Applied Science and Manufacturing*, 43(10):1775–1782, 2012.

[251] Olivier Cousigné, David Moncayo, Daniel Coutellier, and Hakim Naceur. Numerical modeling of cfrp-woven composites for crash simulations. In *1st International Conference on Composite Dynamics (DYNACOMP), Arcachon, France*, 2012.

[252] Olivier Cousigné, David Moncayo, Daniel Coutellier, Pedro Camanho, and Hakim Naceur. Numerical modeling of nonlinearity, plasticity and damage in cfrp-woven composites for crash simulations. In *17th International Conference on Composite Structures (ICCS17), Porto, Portugal*, 2013.

[253] Olivier Cousigné, David Moncayo, Daniel Coutellier, Pedro Camanho, Hakim Naceur, and Steffen Hampel. Development of a new nonlinear numerical material model for woven composite materials accounting for permanent deformation and damage. *Composite Structures*, 106(0):601 – 614, 2013.

[254] HM Hsiao and IM Daniel. Effect of fiber waviness on stiffness and strength reduction of unidirectional composites under compressive loading. *Composites science and technology*, 56(5):581–593, 1996.

[255] Michael R Piggott. The effect of fibre waviness on the mechanical properties of unidirectional fibre composites: a review. *Composites science and technology*, 53(2):201–205, 1995.

[256] Vijay K Stokes. Random glass mat reinforced thermoplastic composites. part I: phenomenology of tensile modulus variations. *Polymer composites*, 11(1):32–44, 1990.

[257] Vijay K. Stokes. Random glass mat reinforced thermoplastic composites. part II: Analysis of model materials. *Polymer Composites*, 11(1):45–55, 1990.

[258] Vijay K Stokes. Random glass mat reinforced thermoplastic composites. part III: Characterization of the tensile moudulus. *Polymer composites*, 11(6):342–353, 1990.

[259] Vijay K Stokes. Random glass mat reinforced thermoplastic composites. part IV: Characterization of the tensile strength. *Polymer composites*, 11(6):354–367, 1990.

[260] WC Bushko and VK Stokes. Random glass mat reinforced thermoplastic composites. part V: Statistical characterization of the tensile modulus. *Polymer composites*, 13(4):295–308, 1992.

[261] Gayle D Tomkinson-Walles. Performance of random glass mat reinforced thermoplastics. *Journal of Thermoplastic Composite Materials*, 1(1):94–106, 1988.

[262] F Meraghni, F Desrumaux, and ML Benzeggagh. Implementation of a constitutive micromechanical model for damage analysis in glass mat reinforced composite structures. *Composites science and technology*, 62(16):2087–2097, 2002.

[263] Mats L Ericson and Lars A Berglund. Processing and mechanical properties of orientated preformed glass-mat-reinforced thermoplastics. *Composites science and technology*, 49(2):121–130, 1993.